Universidad de Oviedo
Universidá d'Uviéu
University of Oviedo

Electrical and Electronic, Computers and Systems Engineering Department

PhD Programme in Electrical and Electronic Engineering

SWITCHING-MODE POWER CONVERTERS FOR VISIBLE LIGHT COMMUNICATION TRANSMITTERS

Doctoral thesis presented by

Juan Rodríguez Méndez

DECEMBER 2018

Universidad de Oviedo
Universidá d'Uviéu
University of Oviedo

Departamento de Ingeniería Eléctrica, Electrónica, de Computadores y Sistemas

Programa de doctorado en Ingeniería Eléctrica y Electrónica

CONVERTIDORES CONMUTADOS DE POTENCIA PARA TRANSMISORES DE COMUNICACIÓN POR LUZ VISIBLE

Tesis doctoral presentada por

Juan Rodríguez Méndez

DICIEMBRE 2018

Universidad de Oviedo
Universidá d'Uviéu
University of Oviedo

SWITCHING-MODE POWER CONVERTERS FOR VISIBLE LIGHT COMMUNICATION TRANSMITTERS

A doctoral thesis submitted to University of Oviedo for the degree of Doctor of Philosophy in Electrical Engineering

presented by

Juan Rodríguez Méndez

Supervisors:

Francisco Javier Sebastián Zúñiga

Pablo Fernández Miaja

DECEMBER 2018

Universidad de Oviedo
Universidá d'Uviéu
University of Oviedo

CONVERTIDORES CONMUTADOS DE POTENCIA PARA TRANSMISORES DE COMUNICACIÓN POR LUZ VISIBLE

Tesis doctoral presentada en la Universidad de Oviedo para la obtención del Grado de Doctor Ingeniero de Telecomunicación

Presentada por

Juan Rodríguez Méndez

Directores de tesis:

Francisco Javier Sebastián Zúñiga

Pablo Fernández Miaja

DICIEMBRE 2018

A Lelo y Lala

Agradecimientos

Javier Sebastián Zúñiga y Pablo Fernández Miaja han sido imprescindibles para la realización de esta tesis. Javier siempre ha estado ahí para atender mis dudas, revisar los trabajos y siempre ha buscado lo mejor para mí. Pablo, además de ser el responsable del tema de la tesis, ha sacado siempre tiempo para resolver mis dudas y revisar los avances a pesar de la distancia. Diego González Lamar también ha tenido un peso fundamental en la realización de mi tesis, así como en todos los trabajos de investigación que he hecho hasta la fecha. Muchas gracias a los tres por todo ello, por vuestro tiempo y por todos los consejos que me habéis dado.

No me quiero olvidar de los comienzos, ni de cómo Alberto Rodríguez Alonso me ayudó con el proyecto fin de carrera, mis primeras tareas cuando entré en el grupo, la estancia en On Semiconductor, los primeros artículos… Muchas gracias Alberto.

Echando de nuevo la vista atrás, tengo que agradecerle a Marta María Hernando Álvarez que me diese la oportunidad de hacer el proyecto fin de carrera y el doctorado con el grupo. Todavía me acuerdo del día en que Javier y tú me estabais explicando en qué consistía hacer un doctorado y de que mi gran duda en ese momento era si en "eso" había exámenes. En aquellos días, el estrés por acabar la carrera me había hecho obsesionarme por irme a una empresa cuanto antes y olvidarme de seguir estudiando. Siguiendo vuestro consejo, aquel día decidí comenzar este "viaje" y a día de hoy puedo decir que aquella apuesta ha sido una de una de las más acertadas de mi vida, no sólo por lo que he aprendido de electrónica de potencia y por trabajar en algo que me gusta, sino por las experiencias que me ha permitido vivir (los viajes a otros países, ver cómo son los congresos, las presentaciones de los trabajos, las estancias…).

Por su puesto, este "viaje" de casi cuatro años no habría sido lo mismo sin el resto de miembros del grupo: Manu, Aitor, Nacho, Kevin, María, Dani, Marián y Abraham. Muchas gracias por los consejos, ayuda y momentos divertidos que hemos pasado.

También quiero agradecer a Jaume Roig la estancia realizada en On Semiconductor (Bélgica) y todo lo que aprendí allí con él. Muchas gracias Jaume. También gracias a Dragan Maksimovic por permitirme realizar la estancia en el CoPEC (E.E.U.U.). No me olvido de toda la buena gente que conocí en Boulder y que hicieron de aquellos tres meses una experiencia para toda la vida.

Gracias a mis padres. Gracias por todo el cariño que me habéis dado, por los sacrificios, los valores que me habéis inculcado y por siempre estar ahí para escucharme. Todo lo que soy es gracias a vosotros. Os quiero.

Gracias también a Gelu y Neli. Siempre me habéis tratado como a un hijo y eso nunca lo olvidaré. Os quiero (a los guajes también, aunque sean un poco canallas).

Abstract

Nowadays, the use of wireless communication systems is essential for the present and future society. For instance, the mobile data traffic has grown exponentially during last decade and it is expected that it will keep growing at similar rates at least until 2021. Moreover, emerging topics, such as the Internet of Things (IoT) or the smart cities, show that the current trend is to interconnect wirelessly humans and different kinds of items placed in the environment (clothes, cars, city lighting, home appliances, etc.). In addition, the speed demanded by each communication link is growing very quickly due to the high bit rate required by mainstream services, such as video streaming, video calls, cloud-based computing, etc. As a result, the Radio Frequency (RF) spectrum is already close to congestion and, as a consequence, enabling the data traffic predicted for upcoming years needs for further research on new technologies. The problem becomes critical in indoor scenarios (home, office, etc.) where the channel capacity is shared between several users, leading to a reduction of the bit rate for each user. Furthermore, it is estimated that more than 70% of the wireless traffic takes place in indoor environments.

Visible Light Communication (VLC) is one of the most promising solutions for alleviating the saturation of the RF spectrum. This wireless communication system uses the wide and unlicensed visible light spectrum (430-750 THz) to transmit information. The strength of this approach arises when the communication is combined with the lighting functionality of High-Brightness Light-Emitting Diode (HB-LED) bulbs. Thus, the exiting lighting infrastructure can be partially modified to incorporate the communication capability. Since its introduction in 2004, VLC has gained attention due to the increasing use of HB-LEDs in Solid State Lighting (SSL). Besides the longer lifetime and higher power efficiency than other lamp technologies, HB-LEDs are able to change the light intensity rapidly, which enables the communication functionality. As a consequence, VLC is being considered nowadays to supplement existing RF wireless communications systems of indoor environments.

The HB-LED driver is one of the cornerstones of the VLC transmitter. It is responsible for two tasks: controlling the bias level of the HB-LEDs in order to guarantee the desired lighting level, and reproducing the communication signal component with high accuracy. A key point that, in general, is not taken into account in VLC literature is that the high efficiency of HB-LED lighting is not only due to the high efficiency of HB-LEDs converting electrical power into optical power, but also due to the high efficiency achieved by the HB-LED driver that delivers the electrical power. Therefore, the HB-LED driver for VLC must fulfill the two aforementioned tasks achieving high power efficiency. The HB-LED drivers that have been proposed so far can be classified into two subsets: HB-LED drivers based on switching on and off the HB-LEDs and HB-LED drivers for reproducing advanced modulation schemes.

The first subset of HB-LED drivers is made up of a slow-response DC-DC converter that is responsible for the biasing, and a MOSFET that switches on and off the HB-LED string. This method is simple and it achieves high power efficiency. The main drawback of this approach is that pulse-based modulation schemes are not the best choice for providing high data rates.

The second subset of HB-LED drivers are focused on reproducing advanced modulation schemes that allow us to provide higher data rates than pulse-based modulation schemes. In this case, the HB-LED driver is made up of a slow-response DC-DC converter that is responsible for the biasing of the HB-LEDs and a Linear Power Amplifier (LPA) that delivers the AC component (i.e., the communication signal). The use of a LPA has been adopted because it provides the linearity and bandwidth required to reproduce the communication signal component. However, it jeopardizes the main advantage of HB-LED lighting: the power efficiency. The problem is that a Class A or AB LPA offers very low power efficiency (between 10% and 40%).

In summary, reproducing advanced modulation schemes is mandatory for enabling the massive data traffic predicted for upcoming years by using VLC. However, the low power efficiency of the HB-LED drivers used to achieve high bit rates is an important limitation that must be overcome. Therefore, the objective of this dissertation is the development of power efficient solutions that can reproduce advanced modulation schemes. In order to reach this target, the HB-LED drivers for VLC that are proposed in the dissertation are fully based on the use of Switching-Mode Power Converters (SMPCs).

After having introduced VLC and the target of the dissertation, a brief description of each chapter is included below:

Chapter 1: Fundamentals of Visible Light Communication.

This chapter is an introduction to visible light communication where the key points of this new technology are reviewed. The chapter includes the description of the operating principle, the modulation schemes and the characterization of HB-LEDs from the transmission point of view. Moreover, the chapter explains one of the bottlenecks that is slowing down the deployment of VLC: the low power efficiency achieved by the HB-LED drivers that have been proposed for providing high data rates. Finally, the objective of this dissertation and the document organization are described.

Chapter 2: Considering the Use of SMPCs as the HB-LED Drivers of VLC Transmitters.

In this chapter, the use of SMPCs for driving the HB-LEDs of VLC transmitters is explored in order to alleviate the efficiency problem. The chapter studies the relationship between light intensity, current and voltage across an HB-LED, and details the requirements for driving it. After that, the way to incorporate VLC to the existing SSL infrastructure is studied. Finally, the use of Pulse-Width Modulated SMPCs (PWM-SMPCs) is proposed not only to bias the HB-LEDs, but also to amplify the communication signal.

Chapter 3: PWM-SMPCs Derived from the Buck Converter.

Designing a PWM-SMPC able to provide the features that a HB-LED driver for VLC requires is not trivial. Although from a theoretical point of view, the buck converter could be used for driving the HB-LEDs of VLC transmitters, it has some drawbacks that make the practical implementation very difficult. The two main problems are the high switching frequency required for providing the demanded bandwidth, and the capability to perform very small voltage changes that is required in order to reproduce the communication signal. This chapter studies three

buck-derived topologies that are very interesting for VLC because they can alleviate the aforementioned problems. After that, a HB-LED driver architecture based on these three strategies is proposed to be used in VLC. This architecture is fully studied both in the time domain and in the frequency domain. In the experimental section, the implemented prototype is described and three main tests are carried out: evaluation of the trade-off between communication efficiency and power efficiency, evaluation of the communication capability, and feedback loop tests.

Chapter 4: The Ripple Modulation Technique.

Using a PWM-SMPC is an interesting approach for driving the HB-LEDs of a VLC transmitter avoiding the use of a power inefficient LPA. However, the recommended topologies for enabling an affordable switching frequency and for fulfilling the required output voltage accuracy lead to quite complex designs. In this chapter, a novel approach that is especially conceived for VLC is presented. The idea is to use the output voltage ripple of a SMPC in order to reproduce the communication signal. This strategy allows us to reduce both the required switching frequency and the complexity of the power stage. The chapter describes in detail the ripple modulation technique by studying different points: the operating principle of the driver that is proposed for using the output voltage ripple, how to reproduce both single-carrier modulation and multi-carrier modulation schemes, control system required for applying the technique, etc.

Chapter 5: Conclusions, Contributions and Future Work.

The main conclusions of the dissertation are included in this chapter. Moreover, the contributions of the research are also described. Finally, different points that could be studied in the future are explained in order to stablish a possible roadmap to continue the research line.

Resumen

El uso de sistemas de comunicación inalámbrica es esencial para la sociedad actual y futura. Por ejemplo, el tráfico de datos móviles ha crecido exponencialmente durante la última década y se espera que este ritmo se mantenga hasta al menos el año 2021. Además, temas emergentes, como internet de las cosas (*Internet of Things*, IoT) o *smart cities*, muestran una tendencia a interconectar de forma inalámbrica a las personas y distintos elementos colocados en su entorno (ropa, coches, iluminación, etc.). Por otra parte, la velocidad demandada en cada enlace de comunicación está creciendo muy rápidamente debido al alto *bit rate* exigido por servicios de uso general, como el video bajo demanda, las videollamadas, servicios basados en la nube, etc. Como consecuencia, el espectro radioeléctrico (*Radio Frequency*, RF) está saturándose, lo que lleva a la necesidad de investigar nuevas tecnologías que posibiliten el tráfico de datos previsto para los próximos años. El problema es especialmente crítico en entornos cerrados (casas, oficias, etc.), donde la capacidad del canal de comunicación es compartida por varios usuarios, lo cual lleva a la reducción del *bit rate* para cada uno. Además, se estima que el 70% del tráfico inalámbrico tiene lugar en entornos cerrados.

La comunicación por luz visible (*Visible Light Communication*, VLC) es una de las opciones más prometedoras para reducir la saturación de espectro RF. Este sistema de comunicación inalámbrica utiliza el amplio y libre espectro de luz visible (430-750 THz) para transmitir la información. El punto fuerte de esta idea aparece cuando se combina la comunicación con la función de iluminación mediante diodos emisores de luz de alto brillo (*High-Brightness Light-Emitting Diodes*, HB-LEDs). De esta manera, la infraestructura de iluminación existente se puede modificar parcialmente para incorporar la capacidad de comunicación. Desde su presentación en 2004, VLC ha ido recibiendo cada vez más atención gracias al mayor uso de HB-LEDs para la iluminación en estado sólido (*Solid State Lighting*, SSL). Además del mayor tiempo de vida y rendimiento energético con respecto a otras tecnologías de iluminación, los HB-LEDs son capaces de cambiar muy rápidamente la intensidad de la luz, posibilitando así la comunicación. Como consecuencia, en la actualidad se está considerando el uso de VLC para apoyar los sistemas de comunicación inalámbrica por RF en entornos cerrados.

El *driver* de HB-LEDs es una de las partes más importantes del transmisor VLC. Es responsable de dos tareas: controlar la polarización de los HB-LEDs para garantizar el nivel de iluminación deseado, y reproducir la señal de comunicación de forma precisa. Un punto clave que en general no se tiene en cuenta en la literatura de VLC es que el alto rendimiento energético de la iluminación HB-LED se debe tanto al alto rendimiento del HB-LED al convertir la potencia eléctrica en potencia óptica, como al alto rendimiento del *driver* que procesa la potencia eléctrica. Por tanto, el *driver* de HB-LEDs para VLC debe cumplir las dos tareas anteriormente mencionadas consiguiendo un alto rendimiento energético. Los *drivers* de HB-LEDs que han sido propuestos hasta la fecha se pueden clasificar en dos categorías: *drivers* basados en encender y apagar completamente los HB-LEDs, y *drivers* concebidos para reproducir esquemas de modulación avanzados.

En la primera categoría, el *driver* está formado por un convertidor CC/CC de respuesta lenta que polariza los HB-LEDs, y un MOSFET que los enciende y apaga para generar pulsos de luz. Este método es simple y ofrece un alto rendimiento energético. EL mayor problema es que únicamente permite reproducir esquemas de modulación basados en pulsos, y éstos no son la mejor opción para VLC si se quiere lograr un alto *bit rate*.

En la segunda categoría, los *drivers* se centran en reproducir esquemas de modulación avanzados que nos permitan alcanzar altos valores de *bit rate*. En este caso, el *driver* está formado por un convertidor CC/CC de respuesta lenta que polariza los HB-LEDs y un amplificador de potencia lineal (*Linear Power Amplifier*, LPA) que reproduce la señal de comunicación. El uso del LPA se debe a que proporciona una linealidad y un ancho de banda suficientemente altos como para reproducir fielmente la señal de comunicación. Sin embargo, el uso del LPA daña uno de los mayores beneficios de la iluminación HB-LED: el alto rendimiento energético. El problema es que un LPA Clase A o AB alcanza un rendimiento energético muy bajo (entre el 10% y el 40%).

En resumen, es necesario reproducir esquemas de modulación avanzados en VLC para posibilitar el tráfico de datos inalámbricos previsto para los próximos años. Sin embargo, el bajo rendimiento energético de los *drivers* de HB-LEDs usados para alcanzar altos valores de *bit rate* es una limitación importante que se debe superar. Por tanto, el objetivo de la tesis es desarrollar soluciones que alcancen un alto rendimiento energético y que sean capaces de reproducir esquemas de modulación avanzados. Para alcanzar dicho objetivo, los *drivers* que se proponen están basados exclusivamente en el uso de convertidores de potencia conmutados (*Switching-Mode Power Converters*, SMPCs).

Después de haber introducido VLC y el objetivo de la tesis se incluye a continuación una breve descripción de cada uno de los capítulos que la componen:

Capítulo 1: Fundamentos de la Comunicación por Luz Visible.

Este capítulo es una introducción a VLC en el que se explican los puntos más importantes de esta tecnología. El capítulo incluye la descripción del principio de operación, los esquemas de modulación empleados y la caracterización de los HB-LEDs desde el punto de vista de la transmisión. Además, en el capítulo se explica uno de los cuellos de botella que está ralentizando la implantación de VLC: el bajo rendimiento energético de los *drivers* de HB-LEDs que han sido propuestos hasta la fecha para alcanzar altos valores de *bit rate*. Por último, se describe el objetivo de la tesis y la organización del documento.

Capítulo 2: Considerando el Uso de SMPCs como *Drivers* de HB-LEDs para transmisores VLC.

En este capítulo se explora el uso de SMPCs como *drivers* de HB-LEDs para transmisores VLC con el objetivo de mejorar el rendimiento energético. Se estudia la relación entre la intensidad de luz, la corriente y la tensión de un HB-LED, y se detallan los requisitos para controlarlo. Después se estudia cómo incorporar el *driver* a la infraestructura SSL existente. Por último se propone el uso de SMPCs modulados por ancho de pulso (PWM-SMPCs) para polarizar los HB-LEDs y amplificar la señal de comunicación.

Capítulo 3: PWM-SMPCs Derivados del Convertidor Reductor

Diseñar un PWM-SMPC capaz de cumplir los requisitos de un *driver* de HB-LEDs para VLC no es trivial. Aunque desde un punto de vista teórico se podría utilizar un convertidor reductor como *driver*, éste presenta varios problemas que dificultan su implementación práctica. Los dos mayores inconvenientes son la alta frecuencia de conmutación requerida para alcanzar el ancho de banda demandado, y la capacidad de realizar cambios muy pequeños de la tensión sobre los HB-LEDs para reproducir fielmente la señal de comunicación. En este capítulo se estudian tres topologías derivadas del convertidor reductor que son muy interesantes para VLC puesto que pueden aliviar los dos problemas comentados anteriormente. Después, se presenta el diseño de un *driver* basado en esas tres topologías. La arquitectura propuesta es estudiada tanto en el dominio del tiempo como de la frecuencia. En la sección experimental se describe el prototipo implementado y las tres pruebas que han sido llevadas a cabo: evaluación del compromiso entre rendimiento energético y rendimiento de la comunicación, evaluación de la capacidad de comunicación y validación del lazo de realimentación.

Capítulo 4: Técnica de Modulación del Rizado.

Emplear un PWM-SMPC como *driver* es una opción interesante para evitar el uso de LPAs, los cuales causan un bajo rendimiento energético. Sin embargo, las topologías recomendadas para conseguir una frecuencia de conmutación no excesivamente elevada y para lograr la precisión exigida en la tensión de salida conllevan el empleo de diseños muy complejos. En este capítulo se presenta un método que ha sido especialmente concebido para su uso en VLC. Consiste en utilizar el rizado de la tensión de salida de un SMPC para reproducir la señal de comunicación. Esta estrategia permite reducir la frecuencia de conmutación y la complejidad de la etapa de potencia. En el capítulo se describe en detalle la técnica de modulación del rizado (*Ripple Modulation*, RM) estudiando varios puntos: el principio de operación del *driver* propuesto para usar su rizado, cómo reproducir tanto esquemas de modulación mono-portadora como multi-portadora, el sistema de control que se emplea para aplicar la técnica, etc.

Capítulo 5: Conclusiones, Contribuciones y Trabajo Futuro.

Las principales conclusiones de esta tesis doctoral se recogen en este capítulo, además de una descripción de las contribuciones logradas por la investigación que se ha llevado a cabo. Finalmente, se explican diferentes puntos que pueden ser estudiados en el futuro para continuar con la línea de investigación.

Contents

List of Figures

List of Tables

List of Acronyms and Symbols

$\alpha(t)$	Control parameter used to determine the phase-shift in the RM technique
α_{OP}	$\alpha(t)$ value in the operating point
$\beta(t)$	Control parameter used to determine the average phase in the RM technique
$\gamma(t)$	Control parameter used to determine the phase of a switch-node voltage in the RM technique
$\gamma_1(t)$, $\gamma_2(t)$	$\gamma(t)$ of each phase of the two-phase buck converter that is based on the RM technique
$\Delta\alpha$	Minimum change of $\alpha(t)$ that can be performed
$\Delta\beta$	Minimum change of $\beta(t)$ that can be performed
$\Delta\gamma$	Minimum change of $\gamma(t)$ that can be performed
$\Delta\phi_V$	Minimum change of $\phi_V(t)$ that can be performed
ΔA_V	Minimum change of $A_V(t)$ that can be performed
Δd	Minimum change of $d(t)$ that can be performed
$\Delta f_{MCM\text{-}k}$	Difference between f_{MCM} and the k^{th} carrier of a MCM scheme
Δt	Temporal resolution of the FPGA that is responsible for controlling a SMPC
Δv_O	Minimum change of $v_O(t)$ that can be performed
η	Power efficiency or overall power efficiency
η_H	Power efficiency of the high-side converter
η_L	Power efficiency of the low-side converter
µ-LEDs	micro-LEDs
$\tau(f)$	Group delay of $H_H(f)$
$\tau_{R\text{-}Ref}(f)$	Relative variation of the group delay with respect to the group delay at f_{Ref}
$\phi_{k\text{-}Th}(t)$	Theoretical phase modulation of the k^{th} carrier of a MCM scheme
$\phi_{k\text{-}RX}(t, L_D)$	Received phase modulation of the k^{th} carrier of a MCM scheme
$\phi_{RX}(t)$	Phase modulation (receiver signal)
$\phi_{S\text{-}MCM\text{-}k}(t)$	Phase modulation of the k^{th} carrier of a MCM scheme (light intensity signal)
$\phi_{S\text{-}SCM}(t)$	Phase modulation of a SCM scheme (light intensity signal)
$\phi_{Th}(t)$	Theoretical phase modulation

$\phi_{V}(t)$	Phase modulation (voltage signal)
$\phi_{V\text{-}MCM\text{-}k}(t)$	Phase modulation of the k^{th} carrier of a MCM scheme (voltage signal)
$\phi_{V\text{-}Ref}(t)$	Reference of the phase modulation for the voltage signal
$\phi_{V\text{-}SCM}(t)$	Phase modulation of a SCM scheme (voltage signal)
A_i	Amplitude identifier of the 64-QAM scheme detailed in Section 4.3.1
$A_{k\text{-}Th}(t)$	Theoretical amplitude modulation of the k^{th} carrier when the communication signal is normalized to have energy equal to 1 J
$A_{k\text{-}RX\text{-}Nor}(t, L_D)$	Amplitude modulation of the received k^{th} carrier when the communication signal is normalized to have energy equal to 1 J
$A_{RX}(t)$	Amplitude modulation (receiver signal)
ASK	Amplitude-Shift Keying
$A_{S\text{-}MCM\text{-}k}(t)$	Amplitude modulation of the k^{th} carrier of a MCM scheme (light intensity signal)
$A_{S\text{-}SCM}(t)$	Amplitude modulation of a SCM scheme (light intensity signal)
$A_{Th\text{-}Nor}(t)$	Normalized amplitude modulation of the theoretical communication signal
$A_V(t)$	Amplitude modulation (voltage signal)
$A_{V\text{-}MCM\text{-}k}(t)$	Amplitude modulation of the k^{th} carrier of a MCM scheme (voltage signal)
$A_{V\text{-}Nor}(t)$	Normalized amplitude modulation (voltage signal)
$A_{V\text{-}Ref}(t)$	Reference of the amplitude modulation for the voltage signal
$A_{V\text{-}SCM}(t)$	Amplitude modulation of a SCM (voltage signal)
BR_{ASK}	Bit rate of an ASK scheme
BR_{MCM}	Bit rate of a MCM scheme
$BR_{MCM\text{-}k}$	Bit rate provided by the k^{th} carrier of a MCM scheme
BR_{OOK}	Bit rate of an OOK scheme
BR_{PAM}	Bit rate of a PAM scheme
BR_{PPM}	Bit rate of a PPM scheme
BR_{PSK}	Bit rate of a PSK scheme
BR_{QAM}	Bit rate of a QAM scheme
BR_{VPPM}	Bit rate of a VPPM scheme
c_i	i^{th} carrier of a MCM scheme
CCM	Continuous Conduction Mode
CSK	Color-Shift Keying

$d(t)$	Duty cycle
DAC	Digital to Analog Converter
$d_{AC}(t)$	AC component of d(t)
d_{DC}	DC component of d(t)
$d_H(t)$	d(t) of the high-side converter
$d_{H\text{-}Max}$	Maximum value of $d_H(t)$
$d_{H\text{-}Min}$	Minimum value of $d_H(t)$
d_L	d(t) of the low-side converter
d_{OP}	d(t) value in the operating point
$\bar{e}$	Error vector
$\bar{e}_{i,j}$	$\bar{e}$ of the symbol transmitted by the j^{th} carrier during the i^{th} symbol period
EA	Error Amplifier
$E_e(L_D)$	Energy of $\bar{e}_{Nor}(t, L_D)$
$E_{e\text{-}MCM}(L_D)$	Average energy of $\bar{e}_{k\text{-}Nor}(t, L_D)$
$E_{e\text{-}MCM\text{-}k}(L_D)$	Energy of $\bar{e}_{k\text{-}Nor}(t, L_D)$
$\bar{e}_{k\text{-}Nor}(t, L_D)$	$\bar{e}_{Nor}(t, L_D)$ of the k^{th} carrier of a MCM scheme
$\bar{e}_{Nor}(t, L_D)$	Normalized temporal error vector
ESR	Equivalent Series Resistance
ET	Envelope Tracking
EVM_{RMS}	Root Mean Square value of the Error Vector Magnitude
f_C	Cut-off frequency of a filter
$f_{C\text{-}H}$	Cut-off frequency of the output filter of the high-side converter
$f_{C\text{-}L}$	Cut-off frequency of the output filter of the low-side converter
$f_{e\text{-}a1}(t)$, $f_{e\text{-}a2}(t)$	Provisional falling edge positions of phases 1 and 2
$f_{e\text{-}b1}(t)$, $f_{e\text{-}b2}(t)$	Definitive falling edge positions of phases 1 and 2
f_{MCM}	Center frequency of a MCM scheme
$f_{MCM\text{-}1}$, $f_{MCM\text{-}2}$, …, $f_{MCM\text{-}N}$	Carrier frequencies of a MCM scheme
$f_{MCM\text{-}k}$	Frequency of the k^{th} carrier of a MCM scheme
$f_{O\text{-}Max}$	Maximum frequency of a communication signal
FPGA	Field Programmable Gate Array

f_{Ref}	Center frequency of a modulation scheme
f_S	Switching frequency
f_{SCM}	Carrier frequency of a SCM scheme
f_{S-H}	f_S of the high-side converter
f_{S-L}	f_S of the low-side converter
f_V	Frequency of the cosine waveforms used in Section 4.2.2.1
GaN	Gallium Nitride
$G_{dL-i}(f)$	Transfer function between d_L and $i_O(t)$
HB-LED	High-Brightness Light-Emitting Diode
$H_H(f)$	Transfer function between $v_{S-1}(t)$ ad $v_O(t)$
$H_{H-F}(f)$	Transfer function between $v_{S-E}(t)$ and $v_{O-H}(t)$
$H_{H-L}(f)$	Transfer function between $v_{O-H}(t)$ and $v_O(t)$
$H_{H-P}(f)$	$H_P(f)$ of the high-side converter
$H_P(f)$	Transfer function between $v_{S-1}(t)$ and $v_{S-E}(t)$
I_{Amp}	Current amplitudes of the 64-QAM detailed in Section 4.3.1
IM/DD	Intensity Modulation/Direct Detection
$i_O(t)$	Current through the HB-LEDs or output current
$i_{O-AC}(t)$	AC component of $i_O(t)$
$i_{O-AC-Max}(t)$	$i_{O-AC}(t)$ for the highest communication power
$i_{O-AC-Ref}(t)$	Reference of $i_{O-AC}(t)$
i_{O-DC}	DC component of $i_O(t)$
$i_{O-DC-Ref}$	Reference of $i_{O-DC}(t)$
i_{O-PP}	Peak to peak value of $i_O(t)$
$i_{O-Ref}(t)$	Reference of $i_O(t)$
IoT	Internet of Things
$i_Q(t)$	Current that flows through a MOSFET
$i_{S-E}(t)$	Current through the equivalent phase inductor
$i_{S-i}(t)$	Current through the i^{th} phase
K_{S-I}	Proportionality coefficient between light intensity and current though a HB-LED
K_{S-V}	Proportionality coefficient between light intensity and voltage across a HB-LED

L_l	Equivalent phase inductor of a multi-phase buck converter
$L_{l\text{-}i}$	Inductor of the i^{th} phase of the converter
L_D	Link distance
LPA	Linear Power Amplifier
LPF	Low-Pass Filter
MCM	Multi-Carrier Modulation
MIMO	Multiple-Input Multiple-Output
n	Number of HB-LEDs used in a string
N	Number of carriers of a MCM scheme
NS	Number of Symbols
NSP	Number of Symbol Periods
OC	Optical Communication
OOK	On-Off Keying
OWC	Optical Wireless Communication
P	Number of phases of a converter
PAM	Pulse Amplitude Modulation
PBM	Pulse-Based Modulation
PCW	Pure Cosine Waveforms
PFC	Power Factor Correction
P_i	Phase identifier of the 64-QAM scheme detailed in Section 4.3.1
$P_{O\text{-}H}$	Power delivered by the high-side converter
$P_{O\text{-}L}$	Power delivered by the low-side converter
PPM	Pulse Position Modulation
PSK	Phase-Shift Keying
PWM	Pulse-Width Modulation
PWM-SMPC	SMPC based on the PWM technique
PWPPM	Pulse-Width and Pulse-Phase Modulation
QAM	Quadrature Amplitude Modulation
R_D	Dynamic resistance of a HB-LED
$r_{e\text{-}a1}(t)$, $r_{e\text{-}a2}(t)$	Provisional rising edge positions of phases 1 and 2

$r_{e\text{-}b1}(t)$, $r_{e\text{-}b2}(t)$	Definitive rising edge positions of phases 1 and 2
RF	Radio Frequency
RGB HB-LEDs	Red, Green and Blue HB-LEDs
RM	Ripple Modulation
RM-SMPC	SMPC based on the RM technique
R_{Sen}	Precision resistor used to measure the current through the HB-LEDs
$s(t)$	Light intensity
$s_{AC}(t)$	AC component of the light intensity (i.e., communication signal)
SCM	Single-Carrier Modulation
s_{DC}	DC component of the light intensity (i.e., lighting level)
$s_{DC\text{-}Max}$	Maximum value of s_{DC}
$s_{MCM}(t)$	$s_{AC}(t)$ when the modulation scheme is a MCM scheme
$s_{MCM\text{-}k}(t)$	k^{th} carrier of $s_{MCM}(t)$
SMPC	Switching-Mode Power Converter
$s_{SCM}(t)$	$s_{AC}(t)$ when the modulation scheme is a SCM scheme
SSL	Solid State Lighting
$s_w(t)$	Sawtooth signal
$t_{D\text{-}i}$	Delay of $v_{S\text{-}i}(t)$ with respect to $v_{S\text{-}1}(t)$
t_{Fil}	Filter delay
TIA	Transimpedance Amplifier
T_J	Junction temperature of a HB-LED
T_S	Switching period
$T_{S\text{-}H}$	T_S of the high-side converter
$T_{S\text{-}L}$	T_S of the low-side converter
T_{Sy}	Symbol period
V	Amplitude of the cosine waveforms used in Section 4.2.2.1
v_1, v_2, v_3	Cosine waveforms used in Section 4.2.2.1 to explain the theoretical base of the RM technique
V_1, V_2, V_3	Phasors used in Section 4.2.2.1 to explain the theoretical base of the RM technique
$\bar{V}$	Ideal symbol

$\bar{V}(t)$	Ideal symbol (temporal expression used in Section 4.3.2)
$V_{\gamma\text{-}I}$	Knee voltage of a HB-LED considering the relationship between $i_O(t)$ and $v_O(t)$
$V_{\gamma\text{-}S}$	Knee voltage of a HB-LED considering the relationship between $s_O(t)$ and $v_O(t)$
$\bar{V}_{i,j}$	$\bar{V}$ of the symbol transmitted by the j^{th} carrier during the i^{th} symbol period
V_G	Input voltage of a SMPC
$V_{G\text{-}H}$	V_G of the high-side converter
$V_{G\text{-}H\text{-}Min}$	Minimum value of $V_{G\text{-}H}$
$v_{Gi\text{-}j}(t)$	Gate signal of the i^{th} MOSFET of the j^{th} phase
$V_{G\text{-}L}$	V_G of the low-side converter
$v_I(t)$	In-phase component of $\bar{V}(t)$
VLC	Visible Light Communication
$v_O(t)$	Voltage across the HB-LEDs or output voltage
$v_{O\text{-}1}(t)$, $v_{O\text{-}2}(t)$	Voltages provided by each phase of the two-phase buck converter that is based on the RM technique
$v_{O\text{-}1\text{-}AC}(t)$, $v_{O\text{-}2\text{-}AC}(t)$	AC components of $v_{O\text{-}1}(t)$ and $v_{O\text{-}2}(t)$
$V_{O\text{-}1\text{-}AC}(t)$, $V_{O\text{-}1\text{-}AC}(t)$	Phasors of $v_{O\text{-}1}(t)$ and $v_{O\text{-}2}(t)$
$v_{O\text{-}AC}(t)$	AC component of $v_O(t)$
$V_{O\text{-}AC}(t)$	Phasor of $v_{O\text{-}AC}(t)$
$v_{O\text{-}AC\text{-}Max}(t)$	$v_{O\text{-}AC}(t)$ for the highest communication power
$v_{O\text{-}AC\text{-}Ref}(t)$	Reference of $v_{O\text{-}AC}(t)$
$v_{O\text{-}DC}$	DC component of $v_O(t)$
$v_{O\text{-}DC\text{-}Ref}$	Reference of $v_{O\text{-}DC}(t)$
$v_{O\text{-}H}(t)$	$v_O(t)$ of the high-side converter
$v_{O\text{-}H\text{-}AC}(t)$	AC component of $v_{O\text{-}H}(t)$
$v_{O\text{-}H\text{-}DC}$	DC component of $v_{O\text{-}H}(t)$
$v_{O\text{-}H\text{-}DC\text{-}Max}$	$v_{O\text{-}H\text{-}DC}$ for the highest communication power
$v_{O\text{-}L}(t)$	$v_O(t)$ of the low-side converter
$v_{O\text{-}MCM}(t)$	$v_O(t)$ when a MCM scheme is reproduced
$v_{O\text{-}MCM\text{-}I}(t)$	In-phase component of $v_O(t)$ when a MCM scheme is reproduced
$v_{O\text{-}MCM\text{-}I\text{-}k}(t)$	In-phase component of the k^{th} carrier of $v_O(t)$ when a MCM scheme is reproduced

$v_{O\text{-}MCM\text{-}k}(t)$	k^{th} carrier of $v_O(t)$ when a MCM scheme is reproduced
$v_{O\text{-}MCM\text{-}Q}(t)$	Quadrature component of $v_O(t)$ when a MCM scheme is reproduced
$v_{O\text{-}MCM\text{-}Q\text{-}k}(t)$	Quadrature component of the k^{th} carrier of $v_O(t)$ when a MCM scheme is reproduced
$v_{O\text{-}PP}$	Peak to peak value of $v_O(t)$
$v_{O\text{-}PP\text{-}Max}$	$v_{O\text{-}PP}$ for the highest communication power
$v_{O\text{-}Ref}(t)$	Reference of $v_O(t)$
$v_{O\text{-}SCM}(t)$	$v_O(t)$ when a SCM scheme is reproduced
VPPM	Variable Pulse Position Modulation
$v_Q(t)$	Quadrature component of $\bar{V}(t)$
$V_{Rec}(t)$	Rectified voltage (i.e., voltage after a diode bridge fed by the line voltage)
$v_S(t)$	Switch-node voltage
$v_{S\text{-}E}(t)$	Equivalent $v_S(t)$
$v_{Sen}(t)$	Voltage across R_{Sen}
$v_{Sen\text{-}DC}$	DC component of $v_{Sen}(t)$
$v_{S\text{-}i}(t)$	$v_S(t)$ of the i^{th} phase
$v_{S\text{-}L}(t)$	$v_S(t)$ of the low-side converter
$v_{RX}(t)$	Receiver signal
$v_{RX\text{-}DC}$	DC component of $v_{RX}(t)$
$v_{RX\text{-}I}(t)$	In-phase component of $v_{RX}(t)$
$v_{RX\text{-}I\text{-}0}(t)$	$v_{RX\text{-}I}(t)$ before being filtered
$v_{RX\text{-}PP}$	Peak to peak value of $v_{RX}(t)$
$v_{RX\text{-}Q}(t)$	Quadrature component of $v_{RX}(t)$
$v_{RX\text{-}Q\text{-}0}(t)$	$v_{RX\text{-}Q}(t)$ before being filtered
$\bar{W}$	Received symbol
WDM	Wavelength Division Multiplexing

Chapter 1:
Fundamentals of Visible Light Communication

The saturation of wireless communication systems that is predicted for upcoming years has boost the research on new frequency bands different from the radiofrequency spectrum during the last decade. Making use of the wide and unlicensed visible light spectrum is one of the most promising methods for alleviating the problem. This chapter is an introduction to visible light communication where the key points of this new technology are reviewed. The chapter includes the description of the operating principle, the modulation schemes and the characterization of high-brightness light emitting diodes from the transmission point of view. Moreover, the chapter explains one of the bottlenecks that is slowing down the implementation of visible light communication: the low power efficiency achieved by the high-brightness light emitting diode drivers that have been proposed for providing high data rates. Finally, the objective of this dissertation and the document organization are described.

1.1 Introduction

Nowadays, the use of wireless communication systems is essential for the present and future society. For instance, the mobile data traffic has grown exponentially during last decade and it is expected that it will keep growing at similar rates at least until 2021 [1.1]. Moreover, emerging topics, such as the Internet of Things (IoT) or the smart cities, show that the current trend is to interconnect wirelessly humans and different kinds of items placed in the environment (clothes, cars, city lighting, home appliances, etc.) [1.2], [1.3]. In addition, the speed demanded by each communication link is growing very quickly due to the high bit rate required by mainstream services, such as video streaming, video calls, cloud-based computing, etc. As a result, the Radio Frequency (RF) spectrum is already close to congestion and, as a consequence, enabling the data traffic predicted for upcoming years needs for further research on new technologies. The problem becomes critical in indoor scenarios (home, office, etc.) where the channel capacity is shared between several users, leading to a reduction of the bit rate for each user. Furthermore, it is estimated that more than 70% of the wireless traffic takes place in indoor environments [1.4].

Looking at higher and unexplored frequency bands is a logical step to alleviate the saturation of the RF wireless communication systems. As Fig. 1.1 shows, this reasoning leads to the use of the light as the transmission medium. Optical Communication (OC) involves any kind of telecommunication system that uses the light (i.e., infrared, visible or ultraviolet light) to transmit the information. OC includes very simple systems, such as smoke signals and ship flags; but also advanced telecommunication systems, such as fiber-optic communication. Optical Wireless Communication (OWC) is a subset of OC where unguided light is used as the transmission medium. Although the first optical telegraph network was built more than two hundred years ago [1.5], OWC has remained rather unexplored. However, the aforementioned RF congestion has boosted the interest in OWC during the last years.

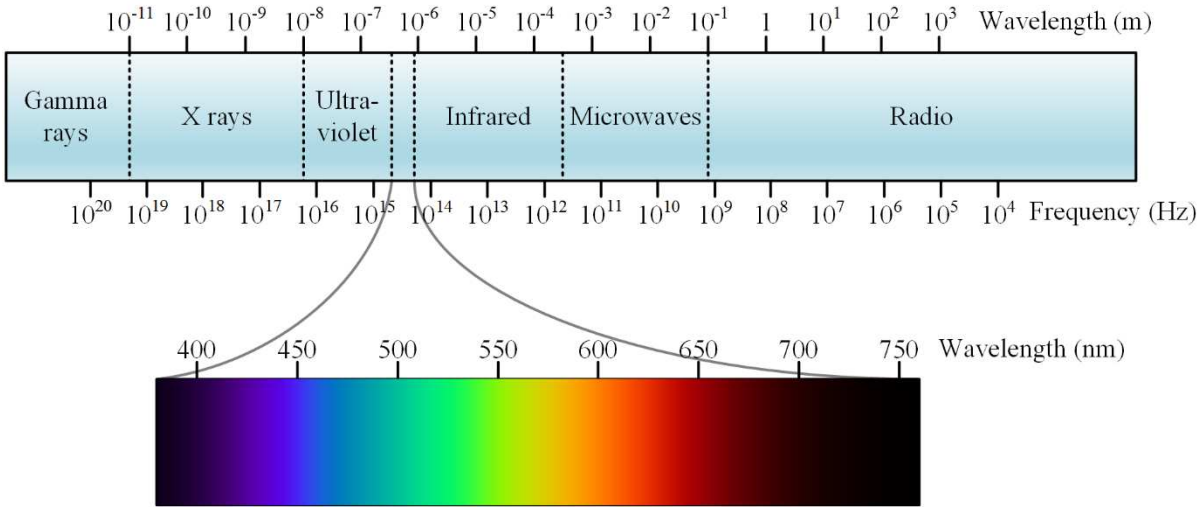

Fig. 1.1. Electromagnetic spectrum.

Visible Light Communication (VLC) is an OWC subset that has caught the attention of many communication researchers [1.6]-[1.11]. This wireless communication system uses the wide and unlicensed visible light spectrum (430-750 THz) to transmit information. The strength of this approach arises when the communication is combined with the lighting functionality of High-Brightness Light-Emitting Diode (HB-LED) bulbs. Thus, the exiting lighting infrastructure can be partially modified to incorporate the communication capability. Since its introduction in 2004 [1.12], VLC has gained attention due to the increasing use of HB-LEDs in Solid State Lighting (SSL). Besides the

longer lifetime and higher power efficiency than other lamp technologies, HB-LEDs are able to change the light intensity rapidly, which enables the communication functionality. As a consequence, VLC is being considered nowadays to supplement existing RF wireless communications systems of indoor environments because of its main benefits:

- VLC opens up a large unlicensed visible region for wireless communication in comparison to the restricted and expensive RF spectrum.
- No special facilities are needed to implement VLC systems because, in principle, they can be integrated into the existing lighting ones.
- Since visible light cannot penetrate building walls, VLC provides communication security and avoids naturally the interference with other VLC systems from adjacent rooms. Therefore, the whole available bandwidth is provided for each closed environment.

Obviously, VLC has some drawbacks that should be pointed out:

- Although line-of-sight is not mandatory for enabling VLC (reflected beams keep transmitting the information), the performance falls and it is strongly jeopardized by the presence of obstacles.
- The range of VLC systems is lower than that of RF systems.

Taking into account the aforementioned characteristics, VLC has been proposed to be used in several applications:

- Internet connectivity in indoor scenarios, where the existing lighting infrastructure can be adapted [1.9]-[1.10].
- Vehicle to vehicle communications, where VLC can be implemented using cars headlights [1.13]-[1.14].
- Underwater communications, where light is less attenuated than RF signals [1.15]-[1.16].
- Wireless communications in scenarios where RF communication is dangerous, such as airplanes, mines or hospitals [1.17].

1.2 Operating Principle of VLC

HB-LEDs generate light based on electroluminescence phenomenon that occurs when an electric field is applied to a P-N junction, promoting the recombination of electrons and holes. Since HB-LEDs are made with direct semiconductor materials, part of the recombination generates photons in a determined wavelength (the other part is wasted by generating heat).

The most common semiconductor material used in HB-LEDs for lighting is Gallium Nitride (GaN), which emits blue light. The HB-LED encapsulation includes a phosphor layer that is excited by the blue light. As a result, a part of the blue photons travel through the phosphor layer without alteration, whereas the rest ones are converted into yellow photons. Therefore, the white light that is finally emitted by the HB-LED is a combination of blue and yellow photons.

In VLC, the transmission of the information is performed by modulating the light intensity waveform emitted by the HB-LEDs (s(t)). After that, s(t) is demodulated by using a photodetector-based receiver. This technique, where the optical power is modulated to transmit the information, is referred as Intensity Modulation/Direct Detection (IM/DD)

[1.18]. Therefore, s(t) is made up of a DC component (s_{DC}) that fixes the lighting level and an AC component ($s_{AC}(t)$) that is determined by the modulation scheme that is being reproduced:

$$s(t) = s_{DC} + s_{AC}(t). \tag{1.1}$$

It is important to note that the light intensity modulation must be fast enough to be unappreciable to the human eye due to safety reasons (i.e., above 100 Hz approximately [1.19]-[1.20]).

Fig. 1.2 shows the general schematic of a VLC systems. Note that the receiver is made up of a photodiode that converts the optical input power into a current signal, a Transimpedance Amplifier (TIA) that transforms the current signal into a voltage signal, a band-pass filter and a demodulator.

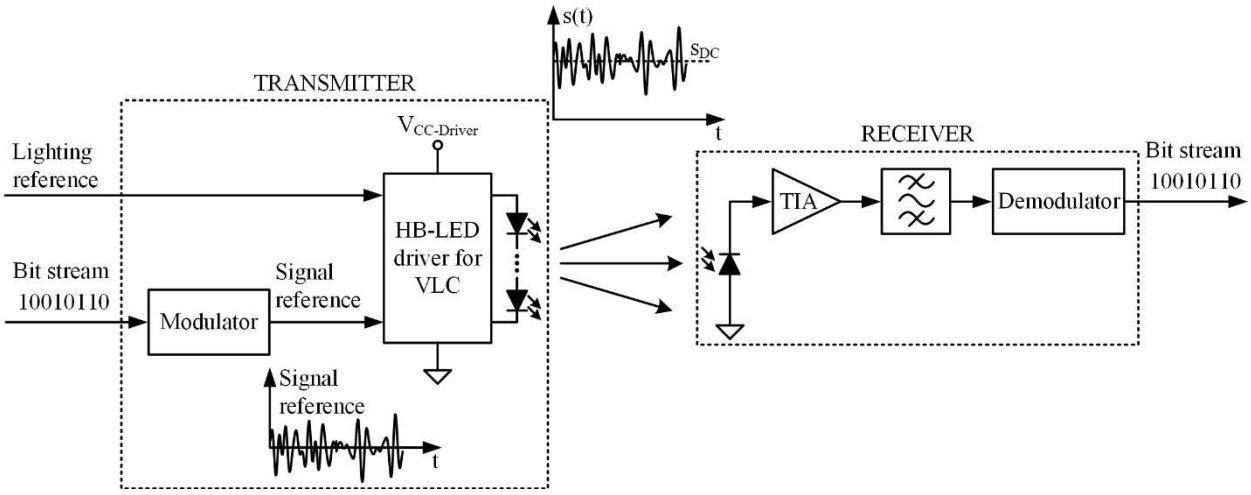

Fig. 1.2. General scheme of a VLC system.

1.3 Features of the HB-LED for Performing VLC

As previously explained, the HB-LED is overcoming traditional lighting in the market due to its long lifetime and high power efficiency. However, in a VLC system, the HB-LED is also responsible for most of the tasks that are performed by the different parts of a conventional RF transmitter: the HB-LED is the antenna because it introduces the information in the transmission medium, it is the local oscillator because it transforms the current modulation in a light modulation (not light intensity) that appears in the THz range, etc. Therefore, the linearity and the bandwidth are two features purely related to the communication functionality that must be taken into account.

1.3.1 HB-LED Linearity

In order to minimize the distortion of the communication signal, it is desired to have a linear relationship between the input and the output of the HB-LED. Traditionally, the HB-LEDs have been driven by controlling the current that flows through them ($i_O(t)$). Therefore, the HB-LED linearity should be evaluated by considering the current and the emitted light intensity (i.e., s(t)) as the input and output, respectively. Fig. 1.3 shows the ideal scheme of a VLC transmitter according to the previous reasoning.

Considering (1.1) and a linear relationship between $i_O(t)$ and s(t), the modulation of the current is translated into a proportional modulation of the light intensity:

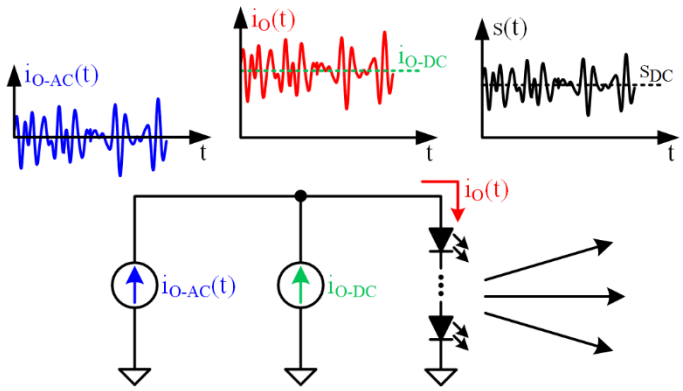

Fig. 1.3. Ideal scheme of a VLC transmitter that is based on controlling the current through the HB-LEDs.

$$i_O(t) = i_{O-DC} + i_{O-AC}(t), \tag{1.2}$$

$$s(t) = s_{DC} + s_{AC}(t), \tag{1.3}$$

$$s_{DC} \cong n \cdot K_{S-I} \cdot i_{O-DC}, \tag{1.4}$$

$$s_{AC}(t) \cong n \cdot K_{S-I} \cdot i_{O-AC}(t). \tag{1.5}$$

where $K_{S\text{-}I}$ is the proportionality coefficient, n is the number of HB-LEDs used in the string, and i_{DC} and $i_{AC}(t)$ are the DC and AC components of the current through them, respectively. In practice, and as Fig. 1.4 shows, the transfer function is not perfectly linear, which leads to some distortion of the communication signal component and to the need of linearizing the transfer function over the biasing point [1.21]. As a result, the non-linear characteristic of the transfer function limits the linear dynamic range of the HB-LED, which jeopardizes the amount of information that can be encoded in the amplitude of s(t).

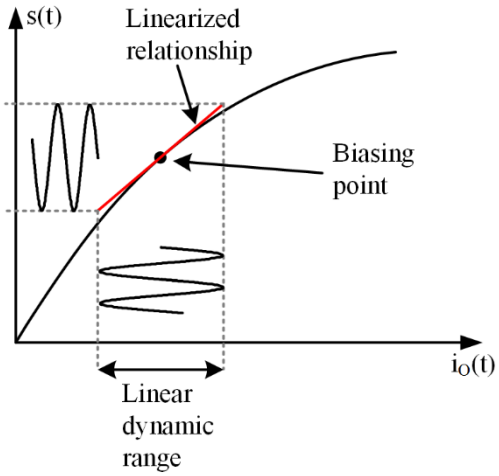

Fig. 1.4. Linearization of the relationship between the current and the emitted optical power of a HB-LED.

1.3.2 HB-LED Bandwidth

The bandwidth of the HB-LED for the electrical to optical power conversion is another fundamental parameter that must be taken into account for performing VLC. The higher the HB-LED bandwidth, the faster the modulation schemes that can be reproduced and, as a result, the higher the bit rate achieved. As previously explained, a blue GaN HB-LED in combination with a yellow phosphor is the preferred approach for obtaining white light in SSL. However,

this phosphor layer is optimized for color conversion, but not for achieving a very rapid response to changes of the light intensity. In fact, it limits the HB-LED bandwidth to a few MHz (3-5 MHz) [1.22]-[1.23]. A more expensive approach for obtaining white light is to combine the red, green and blue light of RGB HB-LEDs. In this way, a bandwidth around 10-20 MHz per color could be achieved [1.24]. In any case, since the available bandwidth is quite limited, achieving high data rates is a challenging task.

1.3.3 Techniques to Overcome the HB-LED Limitations

During last years, several techniques have been proposed to increase the bandwidth provided by HB-LEDs and to improve their linearity in order to archive higher bit rates and to reduce the distortion of the communication signal:

- *Pre-distortion and post-distortion*. In order to increase the linear dynamic range, a non-linear transfer function that compensates the non-linear characteristics of the HB-LED can be incorporated into the VLC system. Typically, this non-linear transfer function is located after the modulator of the transmitter (i.e., just after generating the reference of the communication signal component). This approach is referred as pre-distortion [1.25]. Another possibility is to incorporate the transfer function before the demodulator of the receiver [1.26]. In this case, the approach is known as post-distortion.
- *Blue light filtering*. As previously explained, the yellow phosphor of GaN HB-LEDs limits the bandwidth to a few MHz. Using a blue filter at the receiver to reject the yellow component increases the bandwidth to the range of 10-20 MHz [1.22].
- *Post-equalization and pre-equalization*. A post-equalizer is a band-pass filter placed in the receiver that boosts a certain frequency band. In VLC, it is frequently used for compensating the attenuation introduced by the HB-LEDs in the tens of MHz range (i.e., just above the available bandwidth). In combination with the blue light filtering technique, this option enables a bandwidth above 50 MHz [1.23]-[1.24]. Similarly, a pre-equalizer is a band-pass filter placed in the transmitter side (just after generating the communications signal reference that feeds the HB-LED driver). In combination with the use of micro-LEDs (μ-LEDs), which is an alternative lighting technology that is described below, pre-equalization enables bit rates up to several Gbps [1.27].
- *Color exploitation*. The transmitter bandwidth can also be improved by taking advantage of the light color. However, this feature is only possible when RGB HB-LEDs are used. Basically, there are two possible approaches. The first one is referred as Wavelength Division Multiplexing (WDM) and considers each HB-LED as an independent transmitter, thus achieving three channels with a bandwidth of around 20 MHz for each one [1.28]-[1.33]. The second approach is known as Color-Shift Keying (CSK) and is a modulation scheme that transmits data by performing small variations of the light color [1.34]-[1.36].
- *Alternative lighting devices*. Replacing HB-LEDs by other lighting devices is one of the most controversial methods for increasing the available bandwidth. It implies giving up the power efficiency, power density, cost, maturity and reliability of widely adopted HB-LEDs. The researchers that study this strategy are mainly focused on a technology referred as μ-LEDs, which consists in reducing the HB-LED size to increase the bandwidth [1.37]-[1.39]. Obviously, the amount of optical power that each device can deliver also decreases and, therefore, μ-LEDs arrays must be employed.

- *Multiple-Input Multiple-Output (MIMO)*. In general, several HB-LED bulbs can be found in an indoor environment and each one can be considered as an independent transmitter. Moreover, a bulb is frequently made up of several HB-LEDs and, therefore, each bulb can be splitted into smaller VLC transmitters. However, since all the communication channels are using the same frequency band, the difficulty is to differentiate the data streams of each channel at the receiver. The MIMO technique exploits this idea considering several transmitters and several receivers [1.40]-[1.43]. The key point is that each transmitter has a different orientation, thus transmitting most of the optical power to only one of the receivers. Therefore, the distinguishing criterion is based on the multipath propagation. Through the use of this technique, the link capacity is multiplied by the number of transmitters.

1.4 Modulations Schemes for VLC

Regardless the particular bandwidth provided by the light source, maximizing the bit rate for that bandwidth is a main target. It is important to note that the bit rate depends not only on the available bandwidth, but also on the modulation scheme that is being reproduced. In this sense, three main approaches can be found in the literature: Pulse-Based Modulation (PBM) schemes, Single-Carrier Modulation (SCM) schemes and Multi-Carrier Modulation (MCM) schemes.

1.4.1 Pulse-Based Modulation Schemes

PBM schemes use light pulses to transmit the information. The main PBM schemes that have been proposed for VLC are reviewed in this section.

In Pulse Amplitude Modulation (PAM) schemes, the information is encoded in the amplitude of the light pulses (see Fig. 1.5). The number of amplitudes and the symbol period (T_{Sy}) determine the bit rate:

$$BR_{PAM} = \frac{log_2(Number\ of\ amplitudes)}{T_{Sy}}. \tag{1.6}$$

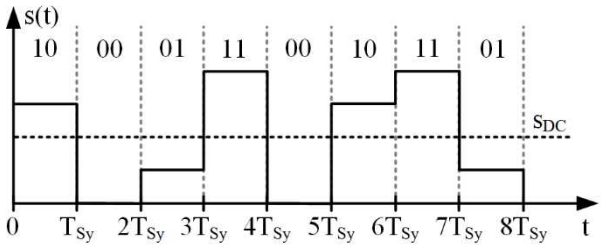

Fig. 1.5. Example of PAM scheme that considers four amplitudes (4-PAM scheme).

On-Off Keying (OOK) is a PAM subset that is widely used in VLC due to its simplicity. In this case, the transmission of a high level is understood as '1' and the transmission of a low level represents a '0' (see Fig. 1.6). Hence, the bit rate can be deduced from (1.6) by considering two amplitudes:

$$BR_{OOK} = \frac{1}{T_{Sy}}. \tag{1.7}$$

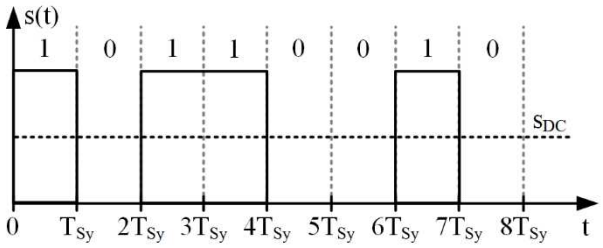

Fig. 1.6. Example of OOK scheme.

The problem of PAM and OOK schemes is that s_{DC} (i.e., the lighting level) depends on the sequence of symbols that is being transmitted. Therefore, several symbols that do not send any information should be included in order to guarantee the desired lighting level. As a result, the effective bit rate of the modulation scheme is reduced.

In Pulse Position Modulation (PPM) schemes, T_{Sy} is splitted into smaller time slots. In this case, the information is encoded in the time slot where the light pulse is performed (see Fig. 1.7). The number of time slots and T_{Sy} determine the bit rate as follows:

$$BR_{PPM} = \frac{log_2(Number\ of\ time\ slots)}{T_{Sy}}. \tag{1.8}$$

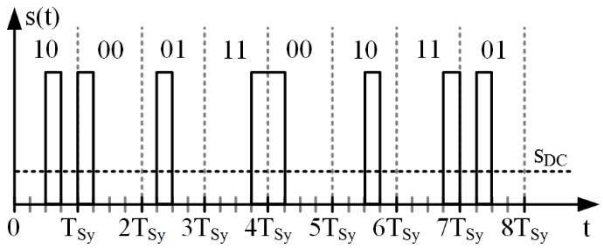

Fig. 1.7. Example of PPM scheme.

In PPM schemes, the amplitude of the pulses and the number of time slots determines s_{DC}. Therefore, this modulation scheme is not valid for performing dimming.

Variable Pulse Position Modulation (VPPM) is a scheme derived from PPM schemes that is widely used in VLC because it is compatible with dimming. VPPM only considers two possible positions of the light pulses over T_{Sy}: at the beginning or at the end (see Fig. 1.8). In this case, s_{DC} is controlled independently by adjusting the width of the light pulses. Since VPPM only considers two possible positions of the light pulses, the bit rate is:

$$BR_{VPPM} = \frac{1}{T_{Sy}}. \tag{1.9}$$

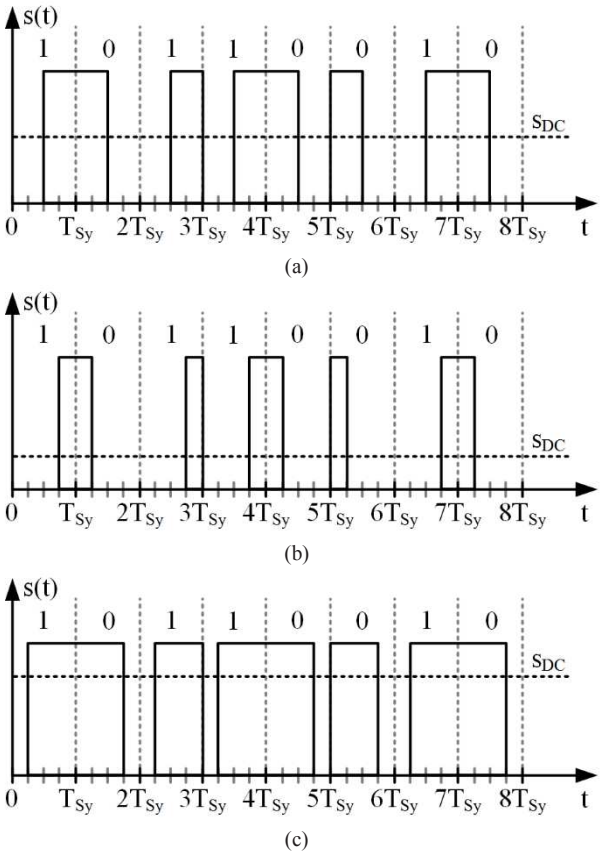

Fig. 1.8. Example of VPPM scheme: (a) 50% dimming. (b) 25% dimming. (c) 75% dimming.

1.4.2 Single-Carrier Modulation Schemes

SCM schemes are better options than PBM schemes for reaching high bit rates [1.4], [1.6], [1.44]. They consist in changing the amplitude or/and the phase of a cosine waveform (i.e., the carrier) whose frequency is f_{SCM}:

$$s(t) = s_{DC} + s_{SCM}(t), \tag{1.10}$$

$$s_{SCM}(t) = A_{S-SCM}(t) \cdot cos(2 \cdot \pi \cdot f_{SCM} \cdot t + \phi_{S-SCM}(t)), \tag{1.11}$$

where $s_{SCM}(t)$ is the AC component of s(t) when the modulation scheme is a SCM scheme. Moreover, $A_{S\text{-}SCM}(t)$ and $\phi_{S\text{-}SCM}(t)$ are the amplitude modulation and phase modulation of $s_{SCM}(t)$, respectively. Since $s_{SCM}(t)$ is a purely alternating waveform, it does not modify the lighting level (i.e., s_{DC}) and, therefore, it can be adjusted independently. The three main SCM schemes are Amplitude-Shift Keying (ASK), where the amplitude changes over time (see Fig. 1.9(a)); Phase-Shift Keying (PSK), where the phase changes over time (see Fig. 1.9(b)); and Quadrature Amplitude Modulation (QAM), where both the amplitude and the phase change over time (see Fig. 1.9(c)). The bit rate achieved by each SCM scheme can be found below:

$$BR_{ASK} = \frac{log_2(Number\ of\ amplitudes)}{T_{Sy}}, \tag{1.12}$$

$$BR_{PSK} = \frac{log_2(Number\ of\ phases)}{T_{Sy}}, \tag{1.13}$$

$$BR_{QAM} = \frac{log_2(Number\ of\ amplitudes - phases\ combinations)}{T_{Sy}}. \tag{1.14}$$

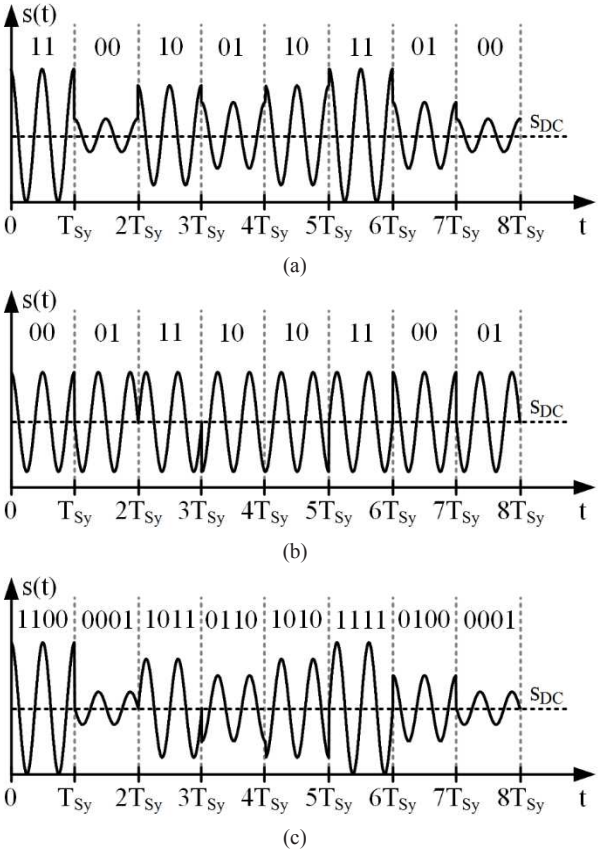

Fig. 1.9. Example of SCM schemes: (a) 4-ASK. (b) 4-PSK. (c) 16-QAM scheme.

1.4.3 Multi-Carrier Modulation Schemes

MCM schemes are also better options than PBM schemes for reaching high bit rates [1.4], [1.6], [1.44]. They are made up of N cosine waveforms (i.e., the carriers) with different frequencies ($f_{MCM\text{-}1}$, $f_{MCM\text{-}2}$, …, $f_{MCM\text{-}N}$) that change their amplitudes and phases over time:

$$s(t) = s_{DC} + s_{MCM}(t), \tag{1.15}$$

$$\begin{aligned} s_{MCM}(t) = s_{MCM-1}(t) + s_{MCM-2}(t) + \cdots + s_{MCM-N}(t) = \\ \frac{A_{S-MCM-1}(t)}{N} \cdot cos\big(2 \cdot \pi \cdot f_{MCM-1} \cdot t + \phi_{S-MCM-1}(t)\big) + \\ \frac{A_{S-MCM-2}(t)}{N} \cdot cos\big(2 \cdot \pi \cdot f_{MCM-2} \cdot t + \phi_{S-MCM-2}(t)\big) + \cdots + \\ \frac{A_{S-MCM-N}(t)}{N} \cdot cos\big(2 \cdot \pi \cdot f_{MCM-N} \cdot t + \phi_{S-MCM-N}(t)\big) = \\ = \frac{1}{N}\sum_{k=1}^{N} A_{S-MCM-k}(t) \cdot cos(2 \cdot \pi \cdot f_{MCM-k} \cdot t + \phi_{S-MCM-k}(t)), \end{aligned} \tag{1.16}$$

where $s_{MCM}(t)$ is the AC component of s(t) when the modulation scheme is a MCM scheme. Moreover, $f_{MCM\text{-}k}$, $A_{S\text{-}MCM\text{-}k}(t)$ and $\phi_{S\text{-}MCM\text{-}k}(t)$ are the frequency, the amplitude modulation and phase modulation of the k^{th} carrier, respectively.

As in the case of SCM schemes, the communication signal component (i.e., $s_{MCM}(t)$) is a purely alternating waveform and, therefore, it does not affect the lighting level (i.e., s_{DC}). Fig. 1.10 shows an example of a MCM scheme that is made up of four 16-QAM schemes.

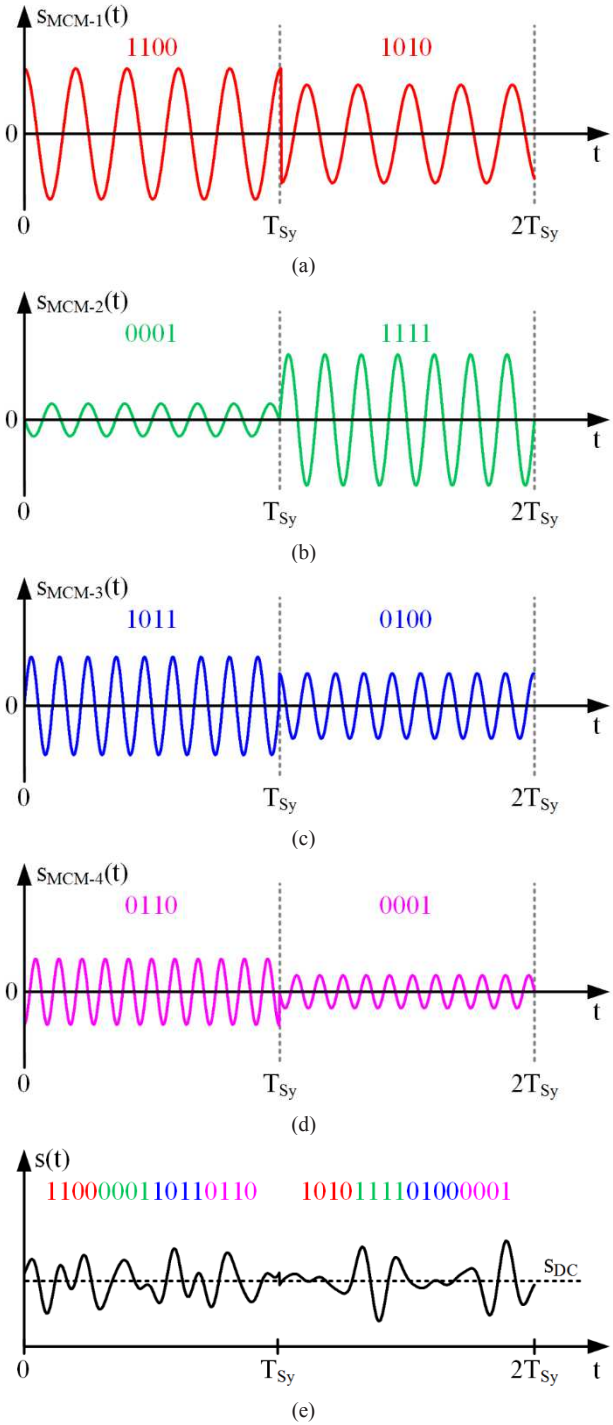

Fig. 1.10. Example of a MCM scheme that is made up of four 16-QAM schemes: (a) $s_{MCM\text{-}1}(t)$. (b) $s_{MCM\text{-}2}(t)$. (c) $s_{MCM\text{-}3}(t)$. (d) $s_{MCM\text{-}4}(t)$. (e) s(t) of a MCM scheme.

The bit rate achieved by a MCM scheme is the sum the bit rates provided by each modulated carrier:

$$BR_{MCM} = \sum_{k=1}^{N} BR_{MCM-k}. \tag{1.17}$$

One of the greatest benefits of MCM schemes is that they are robust against the multipath fading. This phenomenon is caused by the different propagation paths of the signal over the wireless scenario. This factor is translated into different time delays of the light beams that reach the receiver, which increases the error during the demodulation process. Since the error rises for low T_{Sy} values, the multipath fading becomes critical for PBM schemes and SCM schemes when they are conceived for providing high data rates. They key point is that since MCM schemes are made-up of several carriers that are modulated with a low T_{Sy} value (compare Fig. 1.9 to Fig. 1.10), the multipath fading in not as critical as in the case of PBM and SCM schemes, and the bitrate can be improved by considering a higher number of carriers. For this reason, MCM schemes are the preferred modulation schemes for the VLC applications that require high bit rates [1.4], [1.9].

1.5 The HB-LED Driver for VLC

The HB-LED driver is one of the cornerstones of the VLC transmitter. It is responsible for two tasks: controlling the bias level of the HB-LEDs in order to guarantee the desired lighting level, and reproducing the communication signal with high accuracy. A key point that, in general, is not taken into account in the VLC literature is that the high efficiency of HB-LED lighting is not only due to the high efficiency of HB-LEDs converting electrical power into optical power, but also due to the high efficiency achieved by the HB-LED driver that delivers the electrical power. Therefore, the HB-LED driver for VLC must fulfill the two aforementioned tasks achieving high power efficiency. The HB-LED drivers that have been proposed so far can be classified into two subsets: HB-LED drivers based on switching on and off the HB-LEDs and HB-LED drivers for reproducing PAM, SCM and MCM schemes.

1.5.1 HB-LED Drivers Based on Switching On and Off the HB-LEDs

The HB-LED drivers of the first subset are made up of a slow-response DC-DC converter responsible for the biasing and a MOSFET that switches on and off the HB-LED string (see Fig. 1.11). These HB-LED drivers are only able to reproduce PBM schemes that consider 0 and a high level as the possible pulses amplitudes. Therefore, they have been proposed for reproducing OOK, PPM and VPPM schemes [1.45]-[1.49]. This method is simple and it achieves high power efficiency. The main drawback of this approach is that according to the Section 1.4, the aforementioned modulation schemes are not the best choice for providing high data rates. The highest data rate obtained by using this approach is 266 kbps [1.49]. It is important to note that although [1.46] claims that the method can reach a bit rate up to 2 Mbps, the error of the communication is not evaluated in that work and the sequence selected to demonstrate the communication capability is not representative.

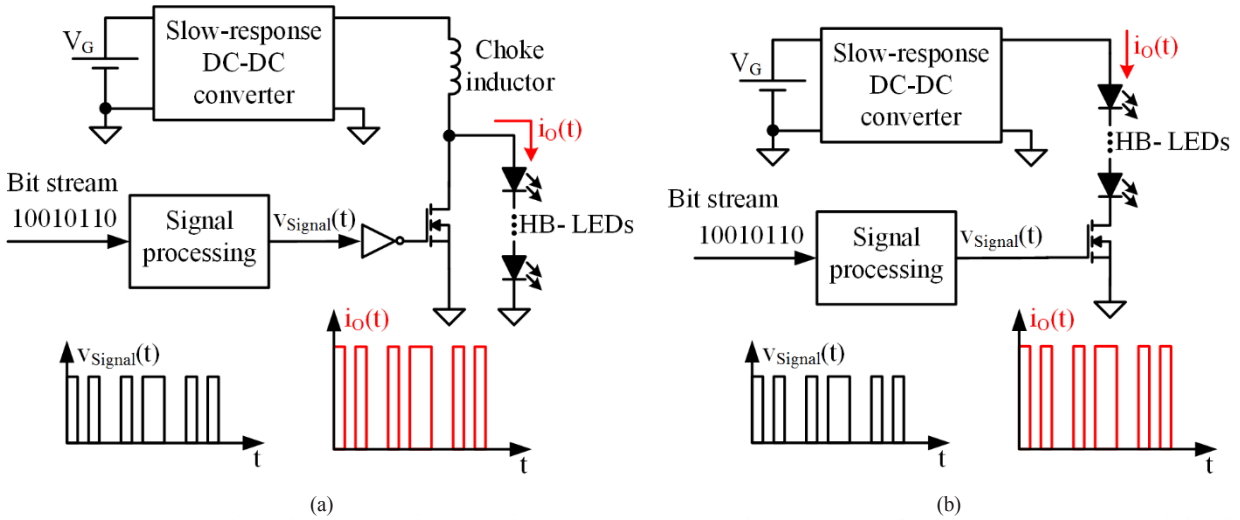

Fig. 1.11. HB-LED drivers based on switching on and off the HB-LEDs: (a) Implementation with the MOSFET connected in parallel with the HB-LED string. (b) Implementation with the MOSFET connected in series with the HB-LED string.

1.5.2 HB-LED Drivers for Reproducing PAM, SCM and MCM Schemes

The HB-LED drivers of the second subset are focused on reproducing advanced modulation schemes (i.e., SCM and MCM schemes) that allow us to provide higher data rates than PBM schemes. It is important to note that although the strength of this approach arises when SCM and MCM schemes are used, this approach is also able to reproduce any kind of PBM schemes, including PAM schemes. As Fig. 1.12 shows, the HB-LED driver is made up of a slow-response DC-DC converter that is responsible for the biasing of the HB-LEDs and a Linear Power Amplifier (LPA) that delivers the AC component. The use of a LPA has been adopted because it provides the linearity and bandwidth that is required for reproducing the communication signal. However, it jeopardizes the main advantage of HB-LED lighting: the power efficiency. The problem is that a Class A or AB LPA offers very low power efficiency (between 10% and 40%). The use of this kind of HB-LED driver for VLC is reported in [1.11], [1.29]-[1.33] and [1.50]-[1.55].

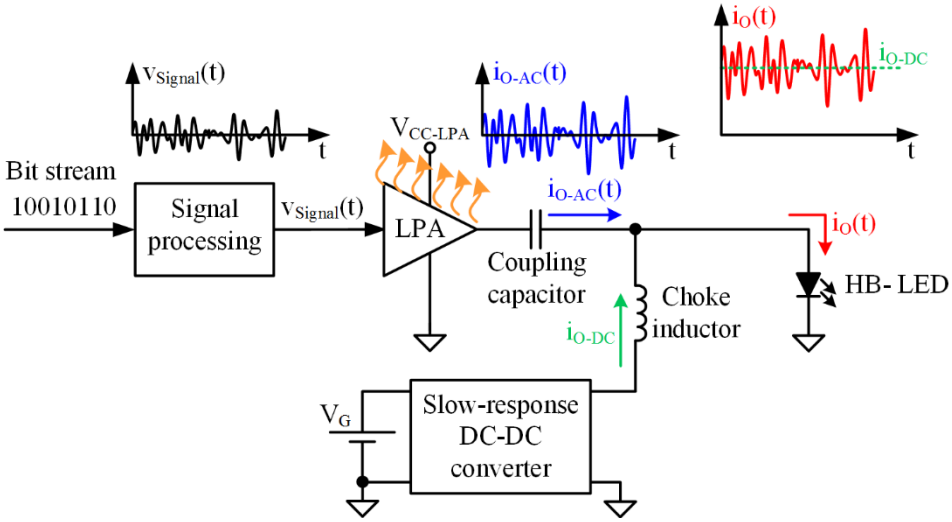

Fig. 1.12. HB-LED driver for reproducing PAM, SCM and MCM schemes.

It is important to note that the overall efficiency of the HB-LED driver for VLC is determined by both the LPA and the slow-response DC-DC power converter, which actually achieves high power efficiency (similar to a conventional HB-LED driver for lighting applications). Therefore, the straightforward method for increasing the

efficiency is to reduce the power delivered by the LPA in order to mitigate the impact of its low efficiency on the overall efficiency. However, this strategy is counterproductive because reducing the communication signal power strongly jeopardizes the range of the communication system. A more intelligent method is to design advanced modulation schemes that demand less communication signal power for achieving the same range [1.56]-[1.57]. Nevertheless, this benefit is obtained at the expense of damaging other characteristics and the improvement is not as high as desired. Another approach can be found in [1.58], where a Digital to Analog Converter (DAC) is used as HB-LED driver for VLC. However, since the proposed DAC is made up of several transistors that operate in linear mode (i.e., similar to a LPA), the efficiency is lower than 70%.

1.6 Objectives and Document Organization

As is explained in this chapter, reproducing advanced modulation schemes is mandatory for enabling the massive data traffic predicted for upcoming years by using VLC. However, the low power efficiency of the HB-LED drivers used to achieve high bit rates is an important limitation that must be overcome. Therefore, the objective of this dissertation is the development of power efficient solutions that are able to reproduce advanced modulation schemes (i.e., SCM and MCM schemes). In order to reach this target, the HB-LED drivers for VLC that are introduced in the following chapters are fully based on the use of Switching-Mode Power Converters (SMPCs).

The dissertation is organized as follows. The use of SMPCs that are based on the Pulse-Width Modulation (PWM) technique is explored in Chapter II. Three strategies for addressing the design challenges that appear when a SMPC is developed to drive the HB-LED of a VLC transmitter are presented in Chapter III. This chapter also includes the SMPC based on the PWM technique that is proposed for VLC. A novel approach for designing SMPCs is described in Chapter IV. This method uses the output voltage ripple to reproduce the communication signal. Finally, Chapter V is focused on presenting a “road map” to keep reducing the trade-off between bandwidth and power efficiency. Moreover, the conclusions and the contributions of the dissertation are included in this chapter.

1.7 References

[1.1] Cisco Systems, “Cisco visual networking index: global mobile data traffic forecast update, 2016-2021”, Feb. 2017. [Online]. Available: http://www.cisco.com/c/en/us/solutions/collateral/service-provider/visual-networking-index-vni/mobile-white-paper-c11-520862.htmlasdsad

[1.2] L. Atzori, A. Iera, and G. Morabito, “The internet of things: a survey,” Comput. Netw., vol. 54, no. 15, pp. 2787–2805, 2010.

[1.3] J. Gubbi, R. Buyya, S. Marusic, and M. Palaniswami, “Internet of Things (IoT): a vision, architectural elements, and future directions,” Future Generat. Comput. Syst., vol. 29, no. 7, pp. 1645-1660, Sep. 2013. [Online]. Available: http://dx.doi.org/10.1016/j.future.2013.01.010

[1.4] Z. Ghassemlooy, L. N. Alves, S. Zvanovec, and A. Khalighi, *Visible light communications: theory and applications*. CRC Press, 2017.

[1.5] The Flag Press, “History behind semaphore flags,” retrieved from https://flagexpressions.wordpress.com/2010/03/23/history-behind-semaphore-flags/, Nov. 17, 2012.

[1.6] S. Dimitrov, and H. Haas, *Principles of LED light communications. Towards networked Li-Fi*. Cambridge University Press, 2015.

[1.7] "IEEE standard for local and metropolitan area networks--part 15.7: short-range wireless optical communication using visible light," in IEEE Std 802.15.7-2011, vol., no., pp.1-309, Sept. 6 2011.

[1.8] GBI Research, "Visible Light Communication (VLC)—a potential solution to the global wireless spectrum shortage", Sep. 2011 [Online]. Available: http://www.gbiresearch.com

[1.9] H. Elgala, R. Mesleh, and H. Haas, "Indoor optical wireless communication: potential and state-of-the-art," IEEE Commun. Mag., vol. 49, no. 9, pp. 56–62, Sep. 2011.

[1.10] H. Haas, C. Chen, and D. O'Brien, "A guide to wireless networking by light," In Progress in Quantum Electronics, vol. 55, pp. 88-111, Sep. 2017.

[1.11] A. Jovicic, J. Li and T. Richardson, "Visible light communication: opportunities, challenges and the path to market," in IEEE Communications Magazine, vol. 51, no. 12, pp. 26-32, December 2013.

[1.12] T. Komine and M. Nakagawa, "Fundamental analysis for visible-light communication system using LED lights," in IEEE Transactions on Consumer Electronics, vol. 50, no. 1, pp. 100-107, Feb 2004.

[1.13] D. R. Kim, S. H. Yang, H. S. Kim, Y. H. Son and S. K. Han, "Outdoor visible light communication for inter-vehicle communication using controller area network," 2012 Fourth International Conference on Communications and Electronics (ICCE), Hue, 2012, pp. 31-34.

[1.14] J. H. Yoo *et al*., "Demonstration of vehicular visible light communication based on LED headlamp," 2013 Fifth International Conference on Ubiquitous and Future Networks (ICUFN), Da Nang, 2013, pp. 465-467.

[1.15] N. Farr, A. Bowen, J. Ware, C. Pontbriand, and M. Tivey, "An integrated, underwater optical /acoustic communications system," OCEANS 2010 IEEE - Sydney, Sydney, NSW, 2010, pp. 1-6.

[1.16] Z. Zeng, S. Fu, H. Zhang, Y. Dong and J. Cheng, "A survey of underwater optical wireless communications," in IEEE Communications Surveys & Tutorials, vol. 19, no. 1, pp. 204-238, 2017.

[1.17] X. Weing, and W. T. Chung, "VLC-based medical healthcare information system," Biomed. Eng.: Appl. Basis Commun., 24 (2) (2012), pp. 155-163.

[1.18] J. M. Kahn and J. R. Barry, "Wireless infrared communications," in Proceedings of the IEEE, vol. 85, no. 2, pp. 265-298, Feb 1997.

[1.19] J. A. J. Roufs and F. J. J. Blommaizt, "Temporal impulse and step responses of the human eye obtained psychophysically by means of a drift-correction perturbation technique," Vision Research, vol. 21, no. 8, pp. 1203-21, 1981.

[1.20] A. Wilkins, J. Veitch and B. Lehman, "LED lighting flicker and potential health concerns: IEEE standard PAR1789 update," 2010 IEEE Energy Conversion Congress and Exposition, Atlanta, GA, 2010, pp. 171-178.

[1.21] D. Tsonev, S. Sinanovic and H. Haas, "Complete modeling of nonlinear distortion in OFDM-based optical wireless communication," in Journal of Lightwave Technology, vol. 31, no. 18, pp. 3064-3076, Sept.15, 2013.

[1.22] J. Grubor, S. C. J. Lee, K. D. Langer, T. Koonen and J. W. Walewski, "Wireless high-speed data transmission with phosphorescent white-light LEDs," 33rd European Conference and Exhibition of Optical Communication - Post-Deadline Papers (published 2008), Berlin, Germany, 2007, pp. 1-2.

[1.23] H. Le Minh et al., "100-Mb/s NRZ visible light communications using a postequalized white LED," in IEEE Photonics Technology Letters, vol. 21, no. 15, pp. 1063-1065, Aug.1, 2009.

[1.24] H. Li, X. Chen, B. Huang, D. Tang and H. Chen, "High bandwidth visible light communications based on a post-equalization circuit," in IEEE Photonics Technology Letters, vol. 26, no. 2, pp. 119-122, Jan.15, 2014.

[1.25] H. Elgala, R. Mesleh and H. Haas, "Predistortion in optical wireless transmission using OFDM," 2009 Ninth International Conference on Hybrid Intelligent Systems, Shenyang, 2009, pp. 184-189.

[1.26] H. Qian, S. J. Yao, S. Z. Cai and T. Zhou, "Adaptive postdistortion for nonlinear LEDs in visible light communications," in IEEE Photonics Journal, vol. 6, no. 4, pp. 1-8, Aug. 2014.

[1.27] X. Li et al., "Wireless visible light communications employing feed-forward pre-equalization and PAM-4 Modulation," in Journal of Lightwave Technology, vol. 34, no. 8, pp. 2049-2055, April, 2016.

[1.28] S. K. Liaw, H. H. Chou, C. J. Wu, M. J. Chien and C. Teng, "500 Mb/s OOK visible light communications using RGB-based LEDs," 2015 International Symposium on Next-Generation Electronics (ISNE), Taipei, 2015, pp. 1-2.

[1.29] J. Vučić, C. Kottke, K. Habel and K. D. Langer, "803 Mbit/s visible light WDM link based on DMT modulation of a single RGB LED luminary," Optical Fiber Communication Conference and Exposition (OFC/NFOEC), 2011 and the National Fiber Optic Engineers Conference, Los Angeles, CA, 2011, pp. 1-3.

[1.30] F. Wu, C. Lin, C. Wei, C. Chen, Z. Chen and H. Huang, "3.22-Gb/s WDM visible light communication of a single RGB LED employing carrier-less amplitude and phase modulation," 2013 Optical Fiber Communication Conference and Exposition and the National Fiber Optic Engineers Conference (OFC/NFOEC), Anaheim, CA, 2013, pp. 1-3.

[1.31] Y. Wang, X. Huang, J. Zhang, Y. Wang, N. Chi, "Enhanced performance of visible light communication employing 512QAM N-SC-FDE and DD-LMS," Opt. Exp., vol. 22, no. 13, pp. 15328-15334, Jun. 2014.

[1.32] Y. Wang, L. Tao, X. Huang, J. Shi and N. Chi, "8-Gb/s RGBY LED-based WDM VLC system employing high-order CAP modulation and hybrid post equalizer," in IEEE Photonics Journal, vol. 7, no. 6, pp. 1-7, Dec. 2015.

[1.33] H. Chun et al., "LED based wavelength division multiplexed 10 Gb/s visible light communications," in Journal of Lightwave Technology, vol. 34, no. 13, pp. 3047-3052, July1, 1 2016.

[1.34] R. Singh, T. O'Farrell and J. P. R. David, "Performance evaluation of IEEE 802.15.7 CSK physical layer," 2013 IEEE Globecom Workshops (GC Wkshps), Atlanta, GA, 2013, pp. 1064-1069.

[1.35] E. Monteiro and S. Hranilovic, "Design and implementation of color-shift keying for visible light communications," in Journal of Lightwave Technology, vol. 32, no. 10, pp. 2053-2060, May15, 2014.

[1.36] R. Singh, T. O'Farrell and J. P. R. David, "An enhanced color shift keying modulation scheme for high-speed wireless visible light communications," in Journal of Lightwave Technology, vol. 32, no. 14, pp. 2582-2592, July15, 15 2014.

[1.37] R. X. G. Ferreira et al., "High bandwidth GaN-based micro-LEDs for multi-Gb/s visible light communications," in IEEE Photonics Technology Letters, vol. 28, no. 19, pp. 2023-2026, Oct.1, 1 2016.

[1.38] Y. F. Yin, W. Y. Lan, T. C. Lin, C. Wang, M. Feng and J. J. Huang, "High-speed visible light communication using GaN-based light-emitting diodes with photonic crystals," in Journal of Lightwave Technology, vol. 35, no. 2, pp. 258-264, Jan.15, 15 2017.

[1.39] M. S. Islim, R. X. Ferreira, X. He, E. Xie, S. Videv, S. Viola, S. Watson, N. Bamiedakis, R. V. Penty, I. H. White, and A. E. Kelly, "Towards 10 Gb/s orthogonal frequency division multiplexing-based visible light communication using a GaN violet micro-LED," Photon. Res. 5(2), 35–43 (2017).

[1.40] L. Zeng et al., "High data rate Multiple Input Multiple Output (MIMO) optical wireless communications using white LED lighting," in IEEE Journal on Selected Areas in Communications, vol. 27, no. 9, pp. 1654-1662, December 2009.

[1.41] A. H. Azhar, T. A. Tran and D. O'Brien, "A Gigabit/s indoor wireless transmission using MIMO-OFDM visible-light communications," in IEEE Photonics Technology Letters, vol. 25, no. 2, pp. 171-174, Jan.15, 2013.

[1.42] A. Burton, H. Le Minh, Z. Ghassemlooy, E. Bentley and C. Botella, "Experimental demonstration of 50-Mb/s visible light communications using 4 x 4 MIMO," in IEEE Photonics Technology Letters, vol. 26, no. 9, pp. 945-948, May1, 2014.

[1.43] S. Rajbhandari, A. V. N. Jalajakumari, H. Chun; G. Faulkner, K. Cameron, D. Tsonev, H. Haas, E. Xie, J. J. D. McKendry, J. J. D. Herrnsdorf, R. Ferreira, E. Gu, M. D. Dawson, D. C. O'Brien, "A multi-Gigabit/sec integrated multiple input multiple output VLC demonstrator," in Journal of Lightwave Technology , vol.PP, no.99, pp.1-1

[1.44] J. G. Proakis, *Digital communications*, 4th ed. New York: McGrawHill, 2000.

[1.45] S. Zhao, J. Xu and O. Trescases, "Burst-mode resonant LLC converter for an LED luminaire with integrated visible light communication for smart buildings," in IEEE Transactions on Power Electronics, vol. 29, no. 8, pp. 4392-4402, Aug. 2014.

[1.46] K. Modepalli and L. Parsa, "Dual-purpose offline LED driver for illumination and visible light communication," in IEEE Transactions on Industry Applications, vol. 51, no. 1, pp. 406-419, Jan.-Feb. 2015.

[1.47] X. Deng, K. Arulandu, Y. Wu, G. Zhou and J. P. M. G. Linnartz, "Performance analysis for joint illumination and visible light communication using buck driver," in IEEE Transactions on Communications, vol. PP, no. 99, pp. 1-1, 2018.

[1.48] S. Haese, L. Mtimet and M. Hélard, "LED driver performance analysis for joint visible light communication and illumination," 2016 IEEE 59th International Midwest Symposium on Circuits and Systems (MWSCAS), Abu Dhabi, pp. 1-4, 2016.

[1.49] B. Hussain et al., "A fully integrated IEEE 802.15.7 visible light communication transmitter with on-chip 8-W 85% efficiency boost LED driver," 2015 Symposium on VLSI Circuits (VLSI Circuits), Kyoto, 2015, pp. C216-C217, 2015.

[1.50] H. Haas, C. Chen and D. O'Brien, "A guide to wireless networking by light", in Progress in Quantum Electronics, vol. 55, pp. 88-111, Sep. 2017.

[1.51] J. Vucic, C. Kottke, S. Nerreter, A. Buttner, K. D. Langer and J. W. Walewski, "White light wireless transmission at 200+Mb/s net data rate by use of discrete-multitone modulation," in IEEE Photonics Technology Letters, vol. 21, no. 20, pp. 1511-1513, Oct.15, 2009.

[1.52] J. Vucic, C. Kottke, S. Nerreter, K. D. Langer and J. W. Walewski, "513 Mbit/s visible light communications link based on DMT-modulation of a white LED," in Journal of Lightwave Technology, vol. 28, no. 24, pp. 3512-3518, Dec.15, 2010.

[1.53] A. M. Khalid et al., "1-Gb/s transmission over a phosphorescent white LED by using rate-adaptive discrete multitone modulation," IEEE Photon. J., vol. 4, no. 5, pp. 1465–73, Oct. 2012.

[1.54] C. Kottke, J. Hilt, K. Habel, J. Vučić and K. D. Langer, "1.25 Gbit/s visible light WDM link based on DMT modulation of a single RGB LED luminary," 2012 38th European Conference and Exhibition on Optical Communications, Amsterdam, pp. 1-3, 2012.

[1.55] S. Fuada, T. Adiono, A. P. Putra and Y. Aska, "LED driver design for indoor lighting and low-rate data transmission purpose," Optik - International Journal for Light and Electron Optics, vol. 156, pp. 847-856, 2018.

[1.56] P. Ge, X. Liang, J. Wang and C. Zhao, "Modulation order selection and power allocation for energy efficient VLC-OFDM systems," 2017 9th International Conference on Wireless Communications and Signal Processing (WCSP), Nanjing, pp. 1-6, 2017.

[1.57] C. R. Kumar and R. K. Jeyachitra, "Power efficient generalized spatial modulation MIMO for indoor visible light communications," in IEEE Photonics Technology Letters, vol. 29, no. 11, pp. 921-924, June 1 2017.

[1.58] A. V. N. Jalajakumari, D. Tsonev, K. Cameron, H. Haas and R. Henderson, "An energy efficient high-speed digital LED driver for visible light communications," 2015 IEEE International Conference on Communications (ICC), London, pp. 5054-5059, 2015.

Chapter 2:
Considering the Use of SMPCs as the HB-LED Drivers of VLC Transmitters

Although VLC is an application with high potential for alleviating the congestion of the RF spectrum, it has some bottlenecks that are slowing down its deployment. One of the most important problems is the low power efficiency of the HB-LED drivers proposed for reproducing advanced modulation schemes. In this chapter, the use of SMPCs for driving the HB-LEDs of VLC transmitters is explored in order to alleviate the efficiency problem. The chapter studies the relationship between light intensity, current and voltage across a HB-LED, and details the requirements for driving it. After that, the way to incorporate VLC to the existing SSL infrastructure is studied. Finally, the use of SMPCs based on the PWM technique (PWM-SMPCs) is proposed not only to bias the HB-LEDs, but also to amplify the communication signal.

2.1 Introduction

In order to alleviate the power efficiency problem of VLC transmitters and to enable higher power levels, the present dissertation explores the use of SMPCs for driving the HB-LEDs of VLC transmitters. SMPCs are much more efficient from the power perspective than LPAs. Hence, it is expected that they will allow us to increase the power delivered to the HB-LEDs while minimizing the power consumption and, as a consequence, the heat dissipation. However, and as will be shown along the dissertation, designing a SMPC for driving the HB-LEDs of a VLC transmitter is not straightforward because it requires several features that are not usually provided by conventional SMPCs. For instance, the bandwidth of conventional SMPCs is much narrower than that of LPAs.

This section is focused on identifying the requirements of a HB-LED driver for performing VLC. Analyzing the transformation from the electrical domain (i.e., voltage and current) to the optical domain (i.e., light intensity) is essential to address this point. Hence, the first step is the study of the relationship between the light intensity (i.e., s(t)), the current that flows through the HB-LEDs string (i.e., $i_O(t)$) and the applied voltage ($v_O(t)$). The behavior depends on the particular HB-LED that is used, but certain general characteristics can be identified. Fig. 2.1 shows the aforementioned relationship including the impact of the HB-LED junction temperature (T_J).

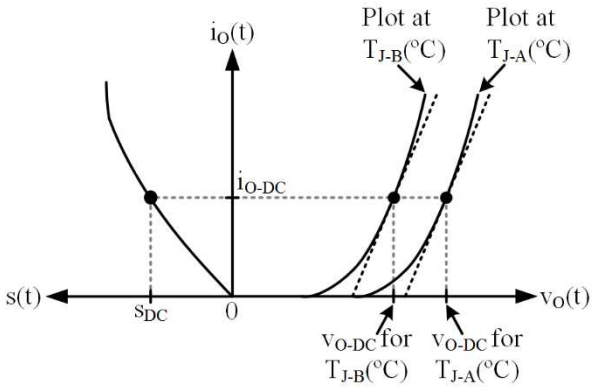

Fig. 2.1. Relationship between s(t), $i_O(t)$ and $v_O(t)$ considering the impact of T_J ($T_{J\text{-}B} > T_{J\text{-}A}$). Note that the black dashed lines are the linear approximations.

Typically, VLC transmitters generate the desired s(t) by controlling $i_O(t)$ and assuming the linear relationship obtained from (1.1)-(1.5) :

$$s(t) \cong n \cdot K_{S-I} \cdot i_O(t). \tag{2.1}$$

Regarding the relationship between $i_O(t)$ and $v_O(t)$, the behavior of a single HB-LED has been traditionally modeled as an ideal diode in series with the dynamic resistance (R_D) and a constant voltage source that represents the knee voltage ($V_{\gamma\text{-}I}$). As Fig. 2.1 shows, the relationship between $i_O(t)$ and $v_O(t)$ strongly depends on T_J. Basically, $V_{\gamma\text{-}I}$ falls when T_J rises while R_D remains constant [2.1]-[2.3]. Consequently, ensuring a certain voltage level does not guarantee the desired lighting level. This is the reason why the HB-LED drivers used for lighting applications need to control the current that flows through the HB-LEDs. In any case, the relationship between $i_O(t)$ and $v_O(t)$ can be modeled as follows:

$$i_O(t) \cong \frac{1}{n \cdot R_D} \cdot \left(v_O(t) - n \cdot V_{\gamma-I}(T_J)\right). \tag{2.2}$$

It is important to note that $V_{\gamma\text{-}I}$ denotes the knee voltage of the linear approximation, not the knee voltage of the real relationship between $i_O(t)$ and $v_O(t)$, which is typically defined as the threshold voltage between conduction and no conduction of the HB-LED.

Moreover, the relationship between s(t) and $v_O(t)$ is quite linear because the non-linear relationship between s(t) and $i_O(t)$ tends to compensate the non-linear relationship between $i_O(t)$ and $v_O(t)$. Therefore, Fig. 2.2 shows a good representation of the relationship between s(t) and $v_O(t)$. It can be seen that the relationship is quite linear once $v_O(t)$ overcomes the knee voltage between s(t) and $v_O(t)$ ($V_{\gamma\text{-}S}$). As in the previous case, $V_{\gamma\text{-}S}$ denotes the knee voltage of the linear approximation, not the knee voltage of the real relationship between s(t) and $v_O(t)$.Therefore, the relationship between s(t) and $v_O(t)$ can be modeled as:

$$s(t) \cong K_{S-V} \cdot \left(v_O(t) - n \cdot V_{\gamma-S}(T_J)\right), \tag{2.3}$$

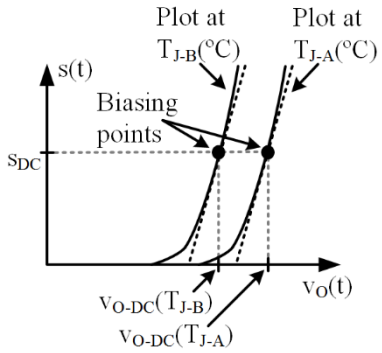

Fig. 2.2. Relationship between s(t) and $v_O(t)$ considering the impact of T_J ($T_{J\text{-}B} > T_{J\text{-}A}$). Note that the black dashed lines are the linear approximations.

where $K_{S\text{-}V}$ is the proportionality coefficient.

Fig. 2.3 shows s(t), $i_O(t)$ and $v_O(t)$ when a modulation scheme is reproduced for the same $s_{O\text{-}DC}$ value and considering the impact of T_J. There are three important facts that should be highlighted. The first one is that DC component of $v_O(t)$ ($v_{O\text{-}DC}$) changes with T_J. The second fact is that the AC component of $v_O(t)$ ($v_{O\text{-}AC}(t)$) does not change with T_J. Finally, the third fact is that the amplitude of $v_{O\text{-}AC}(t)$ is around one order of magnitude lower than $v_{O\text{-}DC}$. These points will be taken into account along the following sections of the chapter.

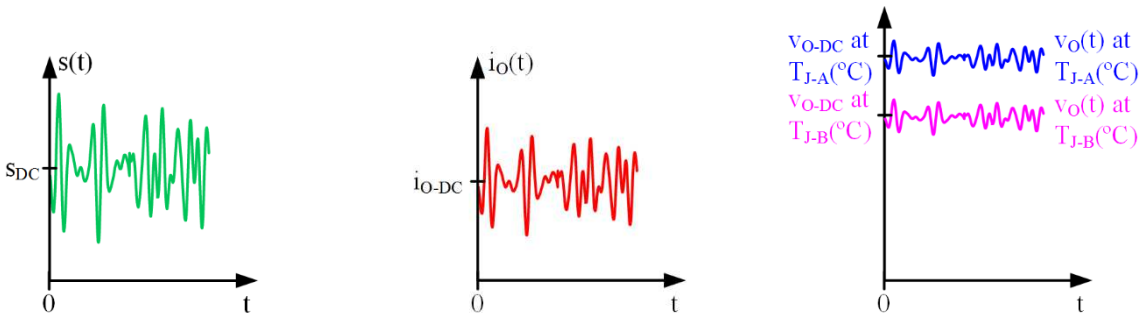

(a) (b) (c)

Fig. 2.3. Waveforms of the HB-LEDs when VLC is performed for the same $s_{O\text{-}DC}$ value and considering the impact of T_J: (a) s(t). (b) $i_O(t)$. (c) $v_O(t)$.

Once the relationship between the optical domain and the electrical domain of the HB-LEDs has been characterized, the requirements for driving the HB-LEDs of a VLC transmitter can be stated:

Capability to reproduce a fast current reference. The HB-LED driver must exploit all the bandwidth provided by the HB-LEDs in order to maximize the bit rate. Consequently, the HB-LED driver must be able to reproduce current waveforms of several MHz.

Temperature compensation. As was previously explained, the relation between $i_O(t)$ and $v_O(t)$ strongly depends on T_J. Therefore, implementing some kind of current feedback loop is mandatory to ensure the proper reproduction of s(t).

High output voltage accuracy. As Fig. 2.2 shows, the current through the HB-LEDs does not start until the applied voltage overcomes $n \cdot V_{\gamma\text{-}I}$. After that, a small voltage increase is translated into a high current increase and, consequently, a high increase of the light intensity. Therefore, the HB-LED driver must be able to perform very small voltage variations in comparison to the DC voltage that it must provide (i.e., $|v_{O\text{-}AC}(t)| << |v_{O\text{-}DC}|$, see Fig. 2.3). Another consequence is that the HB-LED driver must minimize the output voltage ripple in order to reduce distortion of the communication signal.

Low/medium power. The power that the HB-LED driver must deliver strongly depends on the application scenario. For instance, the power of a HB-LED bulb for office environments is in the order of tens of watts, whereas it can attain thousands of watts in the case of a football stadium.

High power efficiency. Low power dissipation in the HB-LED driver is essential to extend the use of VLC for providing services such as Internet connection. In this sense, a 90% efficiency target seems to be reasonable.

Dimming capability. This last feature is recommended, but not mandatory.

2.2 Incorporating VLC to SSL

This section is focused on discussing how VLC could be incorporated to the existing SSL infrastructure. The AC-DC architectures that have been proposed for SSL can be classified into several subsets (passive topologies, one-stage switching topologies, two-stage switching topologies, etc.) [2.4]. For the sake of simplicity, the incorporation of VLC is exemplified with two subsets: one-stage switching topologies with or without Power Factor Correction (PFC).

Fig. 2.4 shows the general scheme and the main voltage waveforms of a one-stage switching topology without PFC. It is made up of a rectifier, an electrolytic capacitor and a SMPC. Thanks to the electrolytic capacitor, the voltage after the diode bridge (V_{Rec}) is almost constant and equal to the peak value of the line voltage ($v_{Line}(t)$). Since V_{Rec} is too high for directly driving the HB-LEDs, a step-down SMPC is used to convert V_{Rec} into the required constant voltage (i.e., V_O). According to Section 2.1, the SMPC typically controls the output current in order to drive properly the HB-LEDs.

At this point, there are two options for incorporating VLC to this SSL architecture. The first one is to replace the existing SMPC by a SMPC specially designed for VLC. As a consequence, the new SMPC must be able to provide the bias level (i.e., $v_{O\text{-}DC}$) and the small voltage variations related to the communication signal (i.e., $v_{O\text{-}AC}(t)$) from V_{Rec}. However, this is quite challenging for two reasons. The first one is that $v_{O\text{-}AC}(t)$ is around two levels of magnitude

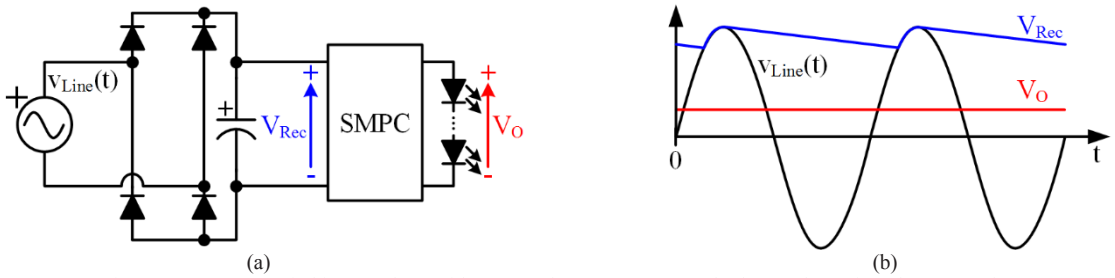

(a) (b)

Fig. 2.4. One-stage switching topology without PFC for SSL: (a) General scheme. (b) Main voltage waveforms.

lower than V_{Rec}. As a result, the output voltage accuracy that the SMPC should provide is unaffordable. The second problem is that the voltage ripple of V_{Rec} could be not negligible and, as a consequence, the new SMPC must take it into account in order to reproduce $v_{O\text{-}AC}(t)$ with high accuracy. The second option for incorporating VLC to the SSL architecture is to connect a SMPC specially designed for VLC between the existing SMPC and the string of HB-LEDs (see Fig. 2.5). In this way, the task of the SMPC is to feed the SMPC specially designed for VLC with a very constant input voltage (V_G). Since V_G is closer to $v_O(t)$ than V_{Rec}, this approach greatly facilitates the design of the special SMPC for VLC. It is important to note that since all the SMPCs for VLC that are proposed in this dissertation are derived from the buck converter (i.e., step down converters), V_G must be higher than $v_O(t)$.

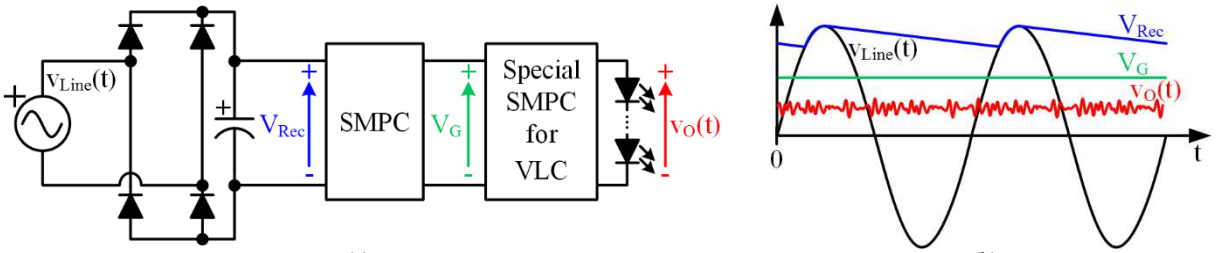

(a) (b)

Fig. 2.5. Incorporating VLC to a one-stage switching topology without PFC for SSL: (a) General scheme. (b) Main voltage waveforms.

Fig. 2.6 shows the general scheme and the main voltage waveforms of a one-stage switching topology with PFC. It is made up of a rectifier, a SMPC and an electrolytic capacitor. The voltage after the diode bridge (i.e., $V_{Rec}(t)$) is the rectified line voltage. In this case, the SMPC has two tasks. The first one is to reduce the voltage and to control the output current in order to properly drive the HB-LEDs. The second task is to ensure that the input current is proportional to $v_{Line}(t)$ to ensure power factor correction. In this case, incorporating VLC by using a one-stage approach is more difficult than in the previous case because $V_{Rec}(t)$ is not constant and the SMPC specially designed for VLC should remove the frequency line ripple and perform power factor correction. Therefore, using two switching stages and connecting the special SMPC for VLC between the SMPC and the string of HB-LEDs is the most suitable approach (see Fig. 2.7).

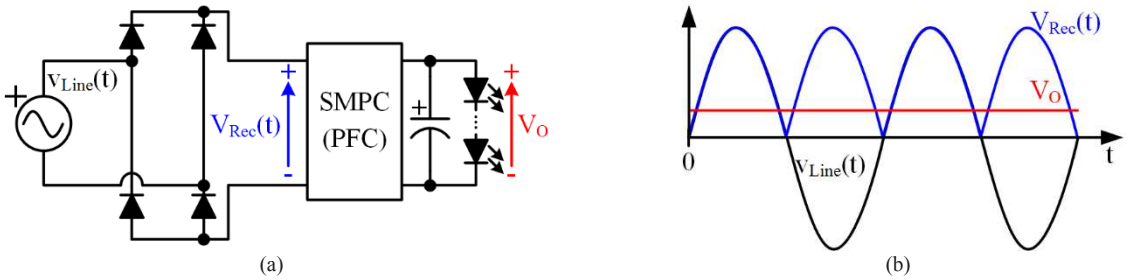

(a) (b)

Fig. 2.6. One-stage switching topology with PFC for SSL: (a) General scheme. (b)Main voltage waveforms.

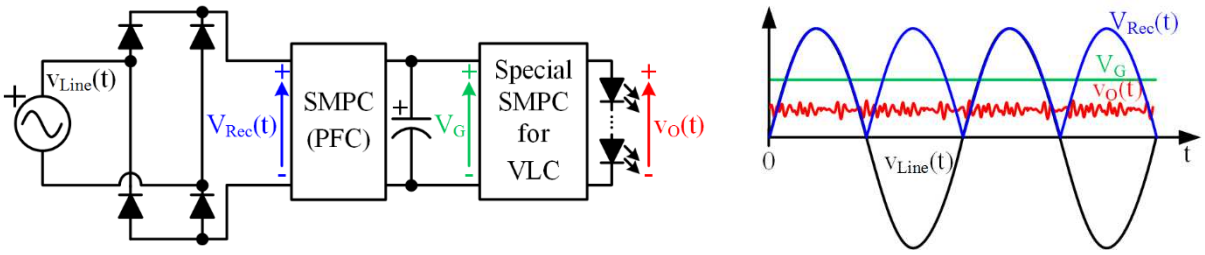

(a) (b)

Fig. 2.7. Incorporating VLC to a one-stage switching topology with PFC for SSL: (a) General scheme. (b) Main voltage waveforms.

2.3 Pulse-Width Modulated SMPC Seen as Power Amplifiers

Although SMPCs are used mostly to provide a constant output voltage, they are also able to generate a variable output voltage. Typically, a SMPC controls the output voltage by adjusting the width of a pulsating waveform that is subsequently filtered. It means that these SMPCs are controlled by means of the PWM technique and, according to that, are noted as Pulse-Width Modulated SMPCs (PWM-SMPCs) along the dissertation. Since the buck converter is the cornerstone of the topologies that are studied in this dissertation, it will be used to explain how a PWM-SMPC can be used to provide a variable voltage and, as a result, how it can be seen as a power amplifier (i.e., an electronic device that increases the power of a signal).

It is well known that the buck converter transforms the input voltage (i.e., V_G) into a lower one (i.e., $V_O < V_G$). Fig. 2.8 shows the conventional buck converter topology and the main voltage waveforms when the target is to provide a constant output voltage. When the MOSFET is activated (state 1), it behaves as a short-circuit and, as a consequence, the voltage applied to the input of the L-C filter ($v_S(t)$) is equal to V_G. Note that in this state, the diode is deactivated and blocks V_G. Moreover, when the MOSFET is deactivated (state 2), the diode operates as a short-circuit and conducts the inductor current. Therefore, $v_S(t)$ is equal to 0 V during the state. As a conclusion, the MOSFET and the diode operate as complementary switches (see Fig. 2.9(a)) and the buck converter has two operating states (see Fig. 2.9 (b)). Since the buck converter continually alternates between state 1 and state 2, the switch-node voltage (i.e., $v_S(t)$) is a

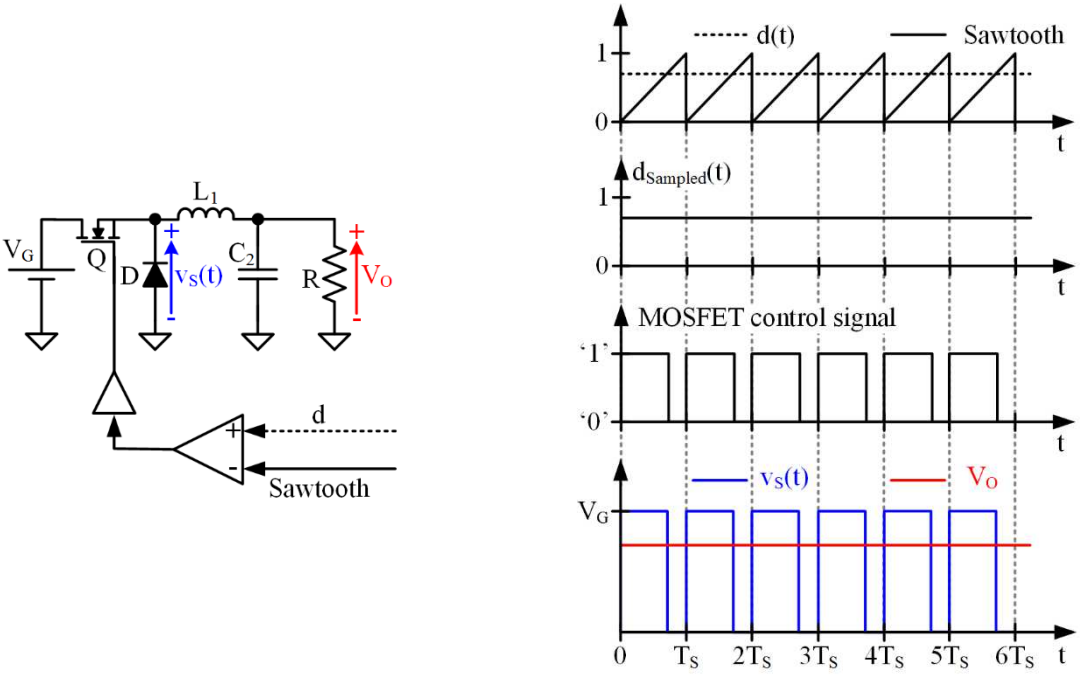

(a) (b)

Fig. 2.8. (a) Buck converter. (b) Main voltage waveforms for a constant output voltage.

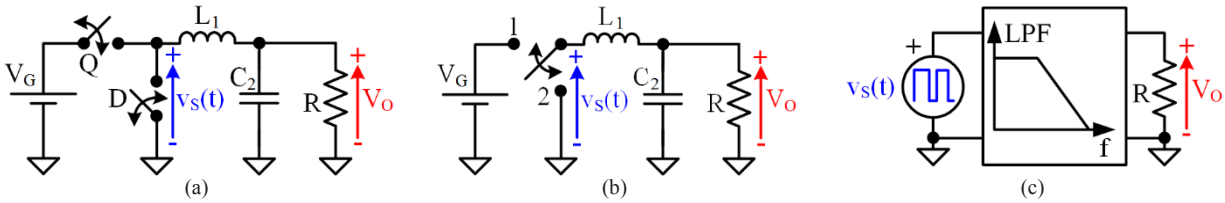

Fig. 2.9. Equivalent circuits of the buck converter: (a) Considering ideal complementary switches. (b) Considering the two possible operating states. (c) The buck converter seen as a pulse-width modulator.

pulse voltage waveform with amplitude V_G that is applied to a Low-Pass Filter (LPF). Essentially, the operating principle of the buck converter is based on the PWM technique (see Fig. 2.9 (c)). In this way, the ratio between the time that the buck converter remains in state 1 and the switching period (T_S) determines the output voltage:

$$V_O = d \cdot V_G, \tag{2.4}$$

where d is the duty cycle, which is the term commonly used to denote the aforementioned ratio. It is important to note that (2.4) is valid if the buck converter operates in Continuous Conduction Mode (CCM). Along the rest of the dissertation, it is assumed that the SMPCs operate in CCM.

Changing the duty cycle over time (i.e., d(t) instead of d) allows us to provide a variable output voltage (i.e., $v_O(t)$ instead of V_O). Therefore, if d(t) tracks the desired reference, the buck converter can be seen as a power amplifier, thus redefining (2.4) as:

$$v_O(t) = d(t) \cdot V_G, \tag{2.5}$$

As Fig. 2.10 shows, d(t) is a continuous-time signal that is sampled once per switching period. According to the Nyquist-Shannon sampling theorem, the switching frequency (f_S), which is equal to the sampling frequency, should accomplish:

$$f_S \geq 2 \cdot f_{O-Max}, \tag{2.6}$$

where $f_{O\text{-}Max}$ is the maximum frequency of the time-varying voltage that is going to be reproduced.

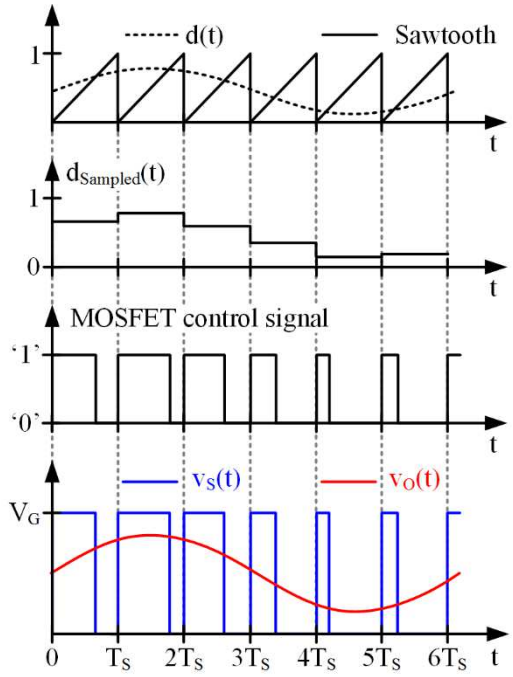

Fig. 2.10. Main voltage waveforms for a time-varying output voltage.

In summary, the buck converter can be seen as a power amplifier considering d(t) and $v_O(t)$ as the input and output, respectively. In this way, the buck converter can be used for reproducing the desired light intensity waveform by making d(t) proportional to the time-varying output voltage that must be provided (i.e., providing the voltage waveform of Fig. 2.3(c) in order to reproduce the light intensity waveform of Fig. 2.3(a)).

2.4 Using a PWM-SMPC for Driving the HB-LEDs of a VLC Transmitter

As was explained in Chapter 1, either the light intensity waveform of a SCM scheme or a MCM scheme can be described as:

$$s(t) = s_{DC} + s_{AC}(t). \tag{2.7}$$

According to (2.3), the PWM-SMPC should provide the following voltage:

$$v_O(t) = n \cdot V_{\gamma-S}(T_J) + \frac{s(t)}{K_{S-V}}, \tag{2.8}$$

$$v_{O-DC} = n \cdot V_{\gamma-S}(T_J) + \frac{s_{DC}}{K_{S-V}}, \tag{2.9}$$

$$v_{O-AC}(t) = \frac{s_{AC}(t)}{K_{S-V}}. \tag{2.10}$$

Fig. 2.11 shows the general scheme of a PWM-SMPC that drives the HB-LEDs of the VLC transmitter in open-loop. The voltage reference that is amplified ($v_{O\text{-}Ref}(t)$) is obtained by summing communication voltage reference ($v_{O\text{-}AC\text{-}Ref}(t)$) and the biasing voltage reference ($v_{O\text{-}DC\text{-}Ref}$). $v_{O\text{-}AC\text{-}Ref}(t)$ is generated by considering the information (usually in the form of bit sequence) that is going to be transmitted, the voltage gain of the PWM-SMPC and (2.10). Moreover, $v_{O\text{-}DC\text{-}Ref}$ can be calculated by considering the desired lighting level (i.e., s_{DC}), the voltage gain of the PWM-SMPC and (2.9). The problem of this approach is that since the HB-LEDs are driven with a voltage waveform, the correct reproduction of the light intensity waveform is not guaranteed. Remind that the voltage required for properly biasing the HB-LEDs depends on T_J (see (2.8)). As was explained in Section 2.1, $V_{\gamma\text{-}S}$ falls with T_J and, as a consequence, implementing some kind of feedback loop is mandatory to compensate that dependence.

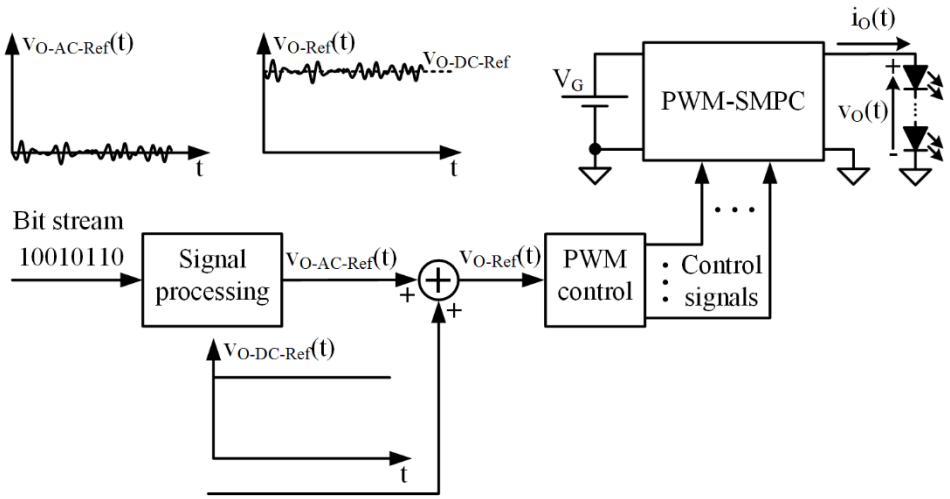

Fig. 2.11. PWM-SMPC for driving the HB-LEDs of a VLC transmitter in open-loop.

Since the relationship between light intensity and current is quite independent of T_J, the straightforward method for solving the issue is to incorporate a feedback loop to regulate $i_O(t)$ (see Fig. 2.12). In this way, the PWM-SMPC drives the HB-LEDs with a current proportional to the desired light intensity waveform according to (2.1):

$$i_O(t) = \frac{s(t)}{n \cdot K_{S-I}}, \tag{2.11}$$

$$i_{O-DC} = \frac{s_{DC}}{n \cdot K_{S-I}}, \tag{2.12}$$

$$i_{O-AC}(t) = \frac{s_{AC}(t)}{n \cdot K_{S-I}}. \tag{2.13}$$

In this case, there is an output current reference ($i_{O\text{-}Ref}(t)$) that is made up of the biasing current reference ($i_{O\text{-}DC\text{-}Ref}$) and the communication current reference ($i_{O\text{-}AC\text{-}Ref}(t)$). $i_{O\text{-}AC\text{-}Ref}(t)$ is generated by considering the bit sequence that is

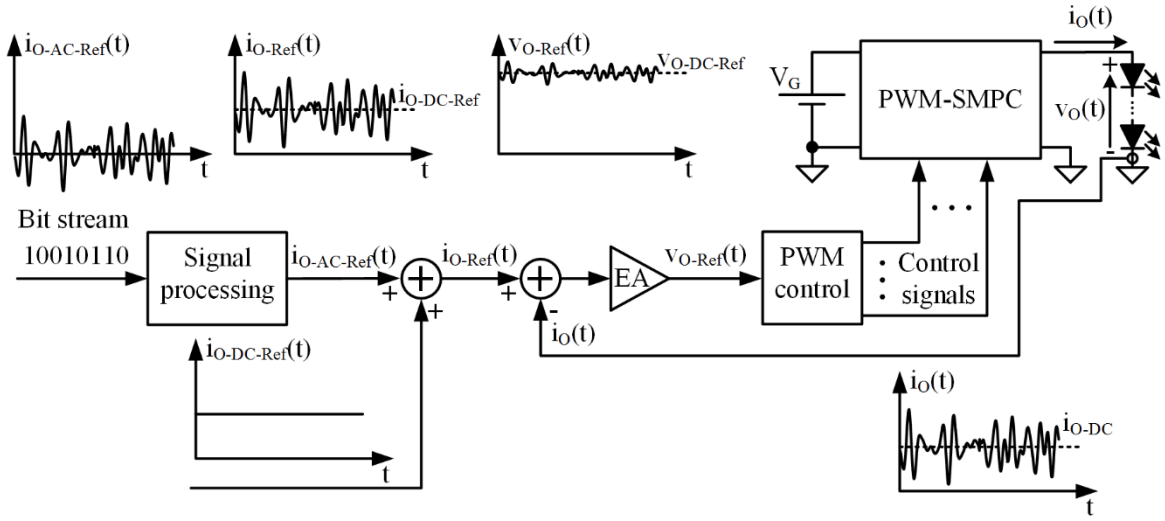

Fig. 2.12. PWM-SMPC for driving the HB-LEDs of a VLC transmitter by regulating $i_O(t)$.

going to be transmitted and (2.13). Moreover, $i_{O\text{-}Ref\text{-}DC}$ can be calculated by considering the desired lighting level (i.e., s_{DC}) and (2.12).Then, $i_{O\text{-}Ref}(t)$ is compared to $i_O(t)$. The result is processed by the Error Amplifier (EA), which provides $v_{O\text{-}Ref}(t)$. This signal feeds the PWM block that generates the gate signals of the MOSFETs.

The simplicity constitutes the major advantage of this approach. Unfortunately, the high f_S required for implementing this method is a significant problem. Take into account that f_S must be high enough to ensure a bandwidth equal or higher than the maximum frequency of the communication signal (i.e., $f_{O\text{-}Max}$). As was previously explained, the theoretical minimum value of f_S is twice $f_{O\text{-}Max}$ according to the Nyquist-Shannon sampling theorem. However, this limit rises when the reactive elements of the power stage and the dynamics related to the current feedback loop, such as the EA response, are considered. Therefore, f_S would be much higher than $f_{O\text{-}Max}$ in practice. The key point is that since $f_{O\text{-}Max}$ is in the order of MHz, f_S would be extremely high, which will be translated into an impractical design because of the switching losses, the difficulty of generating the gate signals, etc.

A more intelligent approach is to use a feedback loop to regulate $i_{O\text{-}DC}$ instead of $i_O(t)$. As explained in Section 2.1, the relationship between $s_{AC}(t)$, $i_{O\text{-}AC}(t)$ and $v_{O\text{-}AC}(t)$ does not depend on T_J. Hence, regulating $i_{O\text{-}DC}$ and, after that, providing $v_{O\text{-}AC}(t)$ in open-loop is enough to guarantee the proper reproduction of s(t) (Fig. 2.2 and Fig. 2.3 may help to understand this statement). In this way, the feedback loop does not limit the speed of the HB-LED driver for reproducing the communication component of the light intensity and, as a result, the required fs can be reduced in comparison to the previous approach. Fig. 2.13 shows the scheme of a PWM-SMPC for driving the HB-LEDs of a VLC transmitter by regulating $i_{O\text{-}DC}$. In this case, the measured output current is filtered in order to obtain $i_{O\text{-}DC}$. Since this value determines the lighting level, it is compared to $i_{O\text{-}DC\text{-}Ref}$. Thus, the EA provides the biasing voltage reference (i.e., $v_{O\text{-}DC\text{-}Ref}$) that ensures the desired lighting level. After that, $v_{O\text{-}AC\text{-}Ref}(t)$ is added to $v_{O\text{-}DC\text{-}Ref}$ to obtain $v_{O\text{-}Ref}(t)$, which feeds the PWM block in order to generate the gate signal of the MOSFETs.

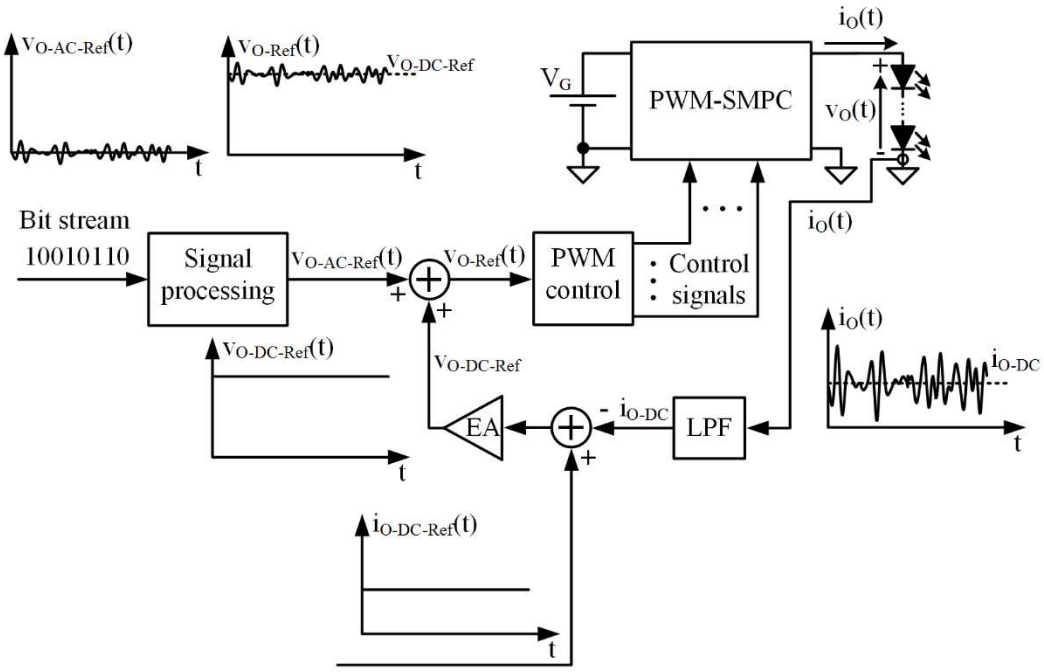

Fig. 2.13. PWM-SMPC for driving the HB-LEDs of a VLC transmitter by regulating $i_{O\text{-}DC}$.

2.5 Using a Buck Converter for Driving the HB-LEDs of a VLC Transmitter

The buck converter has several characteristics that are very interesting for driving the HB-LEDs of a VLC transmitter. The main benefits are the high bandwidth and efficiency in comparison to other topologies that have a similar number of elements. Moreover, it is a simple solution thanks to the low number of elements and to the linear relationship between d(t) and $v_O(t)$ (see (2.5)). This last point facilitates a lot the control of the converter because d(t) is proportional to the voltage reference that must be amplified (i.e., $v_{O\text{-}Ref}(t)$). Fig. 2.14 shows the scheme of a buck converter for driving the HB-LEDs of a VLC transmitter by regulating $i_{O\text{-}DC}$. That scheme is the basis of the different designs that will be proposed along the rest of the dissertation.

From a theoretical point of view, the basic design depicted in Fig. 2.14 can be used as the HB-LED driver of a VLC transmitter. However, in practice, it has several drawbacks that hinders the implementation. Any SMPC is made up of real components that include parasitic elements. Hence, SMPCs have several sources of power losses and, as a result, the 100% theoretical efficiency is never reached. In the case of using a buck converter to drive the HB-LEDs of a VLC transmitter, the switching losses of the switching-mode semiconductor devices are the most critical problem.

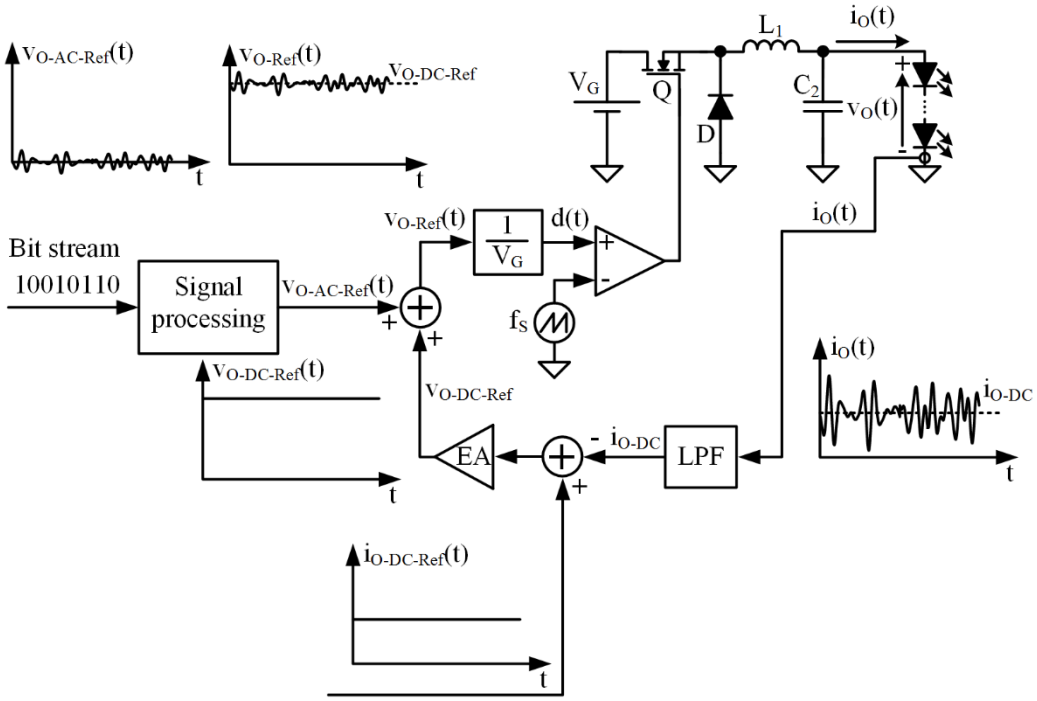

Fig. 2.14.Buck converter for driving the HB-LEDs of a VLC transmitter by regulating $i_{O\text{-}DC}$.

The transition of a real switching-mode semiconductor device (either a MOSFET or a diode) between on-state (i.e., the device is activated) and off-state (i.e., the device is deactivated) is not instantaneous. During transitions, the switching-mode semiconductor device dissipates power since it is blocking voltage and driving current at the same time. Therefore, the higher the f_S value of the SMPC, the higher the switching losses and, as a consequence, the lower the power efficiency. This is not a problem in the case of conventional SMPCs used is SSLs, where f_S ranges between the tens and the hundreds of kHz. However, switching losses become critical when f_S reaches the MHz range and, as will be explained below, this is the situation that occurs when a buck converter is used to drive the HB-LED string of a VLC transmitter.

As was previously explained, since the buck converter is a PWM-SMPC, the theoretical minimum f_S is $2 \cdot f_{O\text{-}Max}$ (see (2.6)). Note that in the case of using a buck converter for driving the HB-LEDs of a VLC transmitter, $f_{O\text{-}Max}$ is the maximum frequency of the communication signal. Therefore, and according to Section 2.4, the approach depicted in Fig. 2.14 allows us to reproduce the desired light intensity waveform and to use f_S equal to $2 \cdot f_{O\text{-}Max}$. However, using a buck converter with the theoretical minimum f_S is impractical because it will cause too much output voltage ripple. This is because the output filter of the buck converter, which is a second order one, does not reject enough the switching-related harmonics of $v_S(t)$. Note that this output voltage ripple is translated into distortion of the communication signal. In order to solve the problem, f_S must be around $20 \cdot f_{S\text{-}Max}$ [2.5]. Unfortunately, the required f_S is unaffordable because $f_{O\text{-}Max}$ could reach units or tens of MHz. It is important to note that the problem is not only the low power efficiency that would be achieved because of the high switching losses (probably below 80%), but also the malfunction that the power dissipation would cause to the switching-mode semiconductor devices, the difficulty of generating properly the gate signals of the MOSFETs, etc.

Fig. 2.15 exemplifies the problem in the frequency domain by considering two f_S values ($f_{S\text{-}B} < f_{S\text{-}A}$) in order to highlight the impact of reducing f_S. As can be seen, $v_S(f)$ is made up of the bias level (i.e., the DC component), the communication signal that is reproduced thanks to the PWM technique, and the switching-related harmonics. The output filter of the buck converter allows us to provide an output voltage that is made up of the desired components $v_S(f)$: the bias voltage level and the communication signal. However, since the filter is not an ideal LPF, part of the switching-related harmonics appear at the output. Basically, this is the output voltage ripple seen in the frequency domain. If f_S is reduced (i.e., from $f_{S\text{-}A}$ to $f_{S\text{-}B}$), switching losses fall and, as a result, the efficiency of the buck converter rises. However, since the switching-related harmonics are closer to the cut-off frequency of the filter (f_C), they are rejected in a minor manner and, as a consequence, the distortion of the signal will be higher. Note that in order to maximize the rejection of the switching harmonics, f_C must be the lowest value that allows the pass of the communication signal without distorting it (regardless the selected f_S).

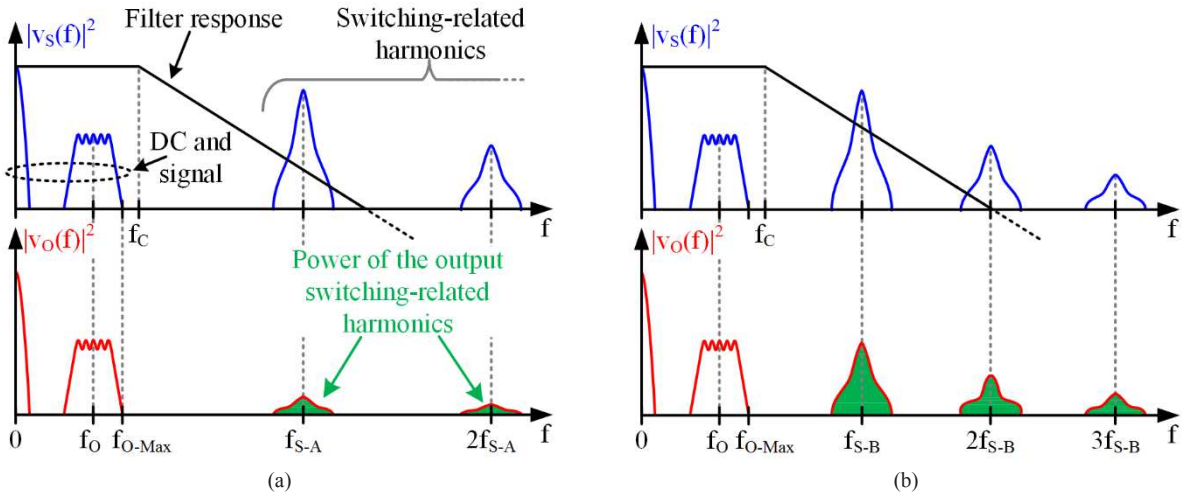

Fig. 2.15. Analysis in the frequency domain of the distortion caused by the reduction of f_S ($f_{S\text{-}B} < f_{S\text{-}A}$).

As was previously indicated, another problem caused by the high f_S value is the difficulty of generating properly the gate signals of the MOSFETs. This point is linked to one of the requirements for driving the HB-LEDs of a VLC transmitter that are detailed in Section 2.1: achieving high output voltage accuracy. As is described in that section, the HB-LED driver must be able to perform very small voltage changes around a much higher voltage level (i.e., $|v_{O\text{-}AC}(t)| >> v_{O\text{-}DC}$). In the case of PWM-SMPC, the capability to perform very small voltage changes around a much higher voltage level is translated into the capability to perform very small duty cycle changes around a much higher duty cycle level (i.e., $|d_{AC}(t)| << d_{DC}$, where $d_{AC}(t)$ and d_{DC} are the AC component and DC component of d(t), respectively). According to (2.5), the minimum output voltage change (Δv_O) that can be performed with a buck converter around the bias voltage can be analyzed as follows:

$$v_{O-DC} + \Delta v_O = d_{DC} \cdot V_G + \Delta d \cdot V_G, \tag{2.14}$$

where Δd is the minimum duty cycle change that can be performed. It is important to note that Δd depends on the temporal resolution (Δt) of the converter control system and that the capability to perform small duty cycle changes falls with f_S:

$$\Delta d = \frac{\Delta t}{T_S} = f_S \cdot \Delta t. \tag{2.15}$$

Substituting (2.15) into (2.14) and focusing on Δv_O leads to:

$$\Delta v_O = f_S \cdot \Delta t \cdot V_G. \tag{2.16}$$

Hence, for a given Δt, the higher the f_S value, the lower the minimum output voltage change that can be performed and, as a consequence, the lower the output voltage accuracy.

2.6 Conclusion

The use of a SMPCs is an interesting approach to increase the power and the efficiency of the VLC transmitters that are conceived to reproduce advanced modulation schemes (i.e., SCM and MCM schemes). However, driving the HB-LEDs of VLC transmitters leads to very challenging requirements, such as a bandwidth of units to tens of MHz and the capability to perform very small voltage changes. In particular, the high f_S required for providing such a high bandwidth is the main problem that jeopardizes not only the power efficiency, but also the proper amplification of the communication signal. It is concluded that using a buck converter that regulates $i_{O\text{-}DC}$ with a feedback loop and that reproduces the communication signal in open loop is an interesting approach for alleviating the problem. However, the required f_S keeps being unaffordable and, as a consequence, more complex solutions should be explored.

2.7 References

[2.1] A. Keppens, W. R. Ryckaert, G. Deconinck, and P. Hanselaer, "High power light-emitting diode junction temperature determination from current-voltage characteristics," in J. Appl. Phys., vol. 104, no. 9, pp. 093104-1–093104-8, Nov. 2008.

[2.2] Osram Opto Semiconductors, "LED fundamentals. Thermal characteristics of LEDs", Aug. 2011. [Online]. Available: https://ledlight.osram-os.com/wp-content/uploads/2013/01/OSRAM-OS_LED-FUNDAMENTALS_Thermal-Characteristics-of-LEDs_v2_08-16-11_SCRIPT.pdf

[2.3] On Semiconductor, "LED lighting. Definitions and characteristics", TND3228/D, Sep. 2007. [Online]. Available: https://www.onsemi.com/pub/Collateral/TND328-D.PDF

[2.4] M. Arias, A. Vázquez, and J. Sebastián, "An overview of the AC-DC and DC-DC converters for LED lighting applications," Automatika – Journal for Control, Measurement, Electronics, Computing and Communication, vol. 53, p. 17, 2012 2012.

[2.5] V. Yousefzadeh, Narisi Wang, Z. Popovic and D. Maksimovic, "A digitally controlled DC/DC converter for an RF power amplifier," in IEEE Transactions on Power Electronics, vol. 21, no. 1, pp. 164-172, Jan. 2006.

Chapter 3:
PWM-SMPCs Derived from the Buck Converter

Designing a PWM-SMPC able to provide the features that a HB-LED driver for VLC requires is not trivial. Although from a theoretical point of view, the buck converter could be used for driving the HB-LEDs of VLC transmitters, it has some drawbacks that make the practical implementation very difficult. The two main problems are the high f_S required for providing the demanded bandwidth, and the capability to perform very small voltage changes that is required in order to reproduce the communication signal. This chapter studies three buck-derived topologies that are very interesting for VLC because they can alleviate the aforementioned problems. After that, a HB-LED driver architecture based on these three strategies is proposed to be used in VLC. This architecture is fully studied both in the time domain and in the frequency domain. In the experimental section, the implemented prototype is described and three main tests are carried out: evaluation of the trade-off between communication efficiency and power efficiency, evaluation of the communication capability, and feedback loop tests.

3.1 Introduction

According to Chapter 2, there are two main problems that jeopardize the use of a conventional buck converter for driving the HB-LEDs of a VLC transmitter. The first one is the high f_S that is required in order to provide the bandwidth that is needed to reproduce the communication signal, which is typically of several MHz. Using lower f_S values than the recommended minimum one, which is around $20 \cdot f_{O\text{-}Max}$, leads to an increase of the output voltage ripple. As a result, the distortion of the communication signal rises and, consequently, the performance of the communication link falls because of the higher number of communication errors. The second problem of the buck converter is the high duty cycle accuracy that is required for reproducing the communication signal. As was explained Chapter 2, the HB-LED driver must be able to perform very small voltage changes because of the relationship between s(t) and $v_O(t)$. Hence, the buck converter must be able to perform very small duty cycle changes. However, it is quite difficult when f_S reaches the MHz range because of the low Δt value that is required. In order to alleviate both problems, more sophisticated solutions than the conventional buck converter are needed. At this point, the target is to find topologies able to alleviate the two aforementioned problems in order to enable the practical use of PWM-SMPCs as HB-LED drivers of VLC transmitters.

3.2 Three Buck-Derived Converters that Are Interesting for VLC

In this section, three buck-derived topologies that were proposed for other power electronics applications are reviewed. The design modifications add certain features that make the topologies very interesting to be used as the HB-LED driver of a VLC transmitter [3.1].

3.2.1 Multi-Phase Buck Converter

The multi-phase buck converter (see Fig. 3.1) [3.2] was conceived to be used as voltage regulator modules for supplying microprocessors because of the high efficiency and bandwidth achieved by this topology [3.3]-[3.4]. In addition, the multi-phase buck converter is widely used as envelope amplifier when the Envelope Tracking (ET) technique is used to increase the efficiency of a RF LPA [3.7]-[3.12].

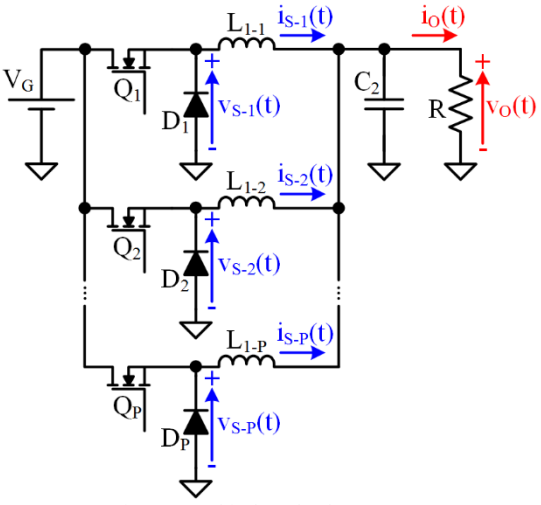

Fig. 3.1. Multi-phase buck converter.

The operating principle of the multi-phase buck converter is to sum several pulse-width modulated voltages in order to obtain a new voltage waveform whose switching-related harmonics have less power and, moreover, they are placed at higher frequencies. In this way, the new pulse-width modulated voltage can be filtered more easily and, consequently, the output voltage ripple is lower than in the case of a single-phase approach. Note that P denotes the number of phases of the multi-phase buck converter and that the pulse-width modulated voltages are the switch-node voltages ($v_{S\text{-}1}(t)$, $v_{S\text{-}2}(t)$,…, $v_{S\text{-}P}(t)$) of the topology. All the pulse-width modulated voltages are equal, but they are phase-shifted. In this way, and as will be demonstrated later, the harmonic content of the equivalent switch-node voltage ($v_{S\text{-}E}(t)$) around certain switching harmonics is much lower than in the case of the conventional buck converter.

Fig. 3.2(a) shows the equivalent circuit of the multi-phase buck converter where the switch-node voltages are modelled as ideal pulse-width modulated voltage sources. Each one has a particular delay ($t_{D\text{-}1}$, $t_{D\text{-}2}$,…, $t_{D\text{-}P}$) with respect to the switch-node voltage of the first phase (i.e., $v_{S\text{-}1}(t)$). Then, each ideal pulse voltage source can be expressed in the following way:

$$v_{S-i}(t) = v_{S-1}(t - t_{D-i}). \tag{3.1}$$

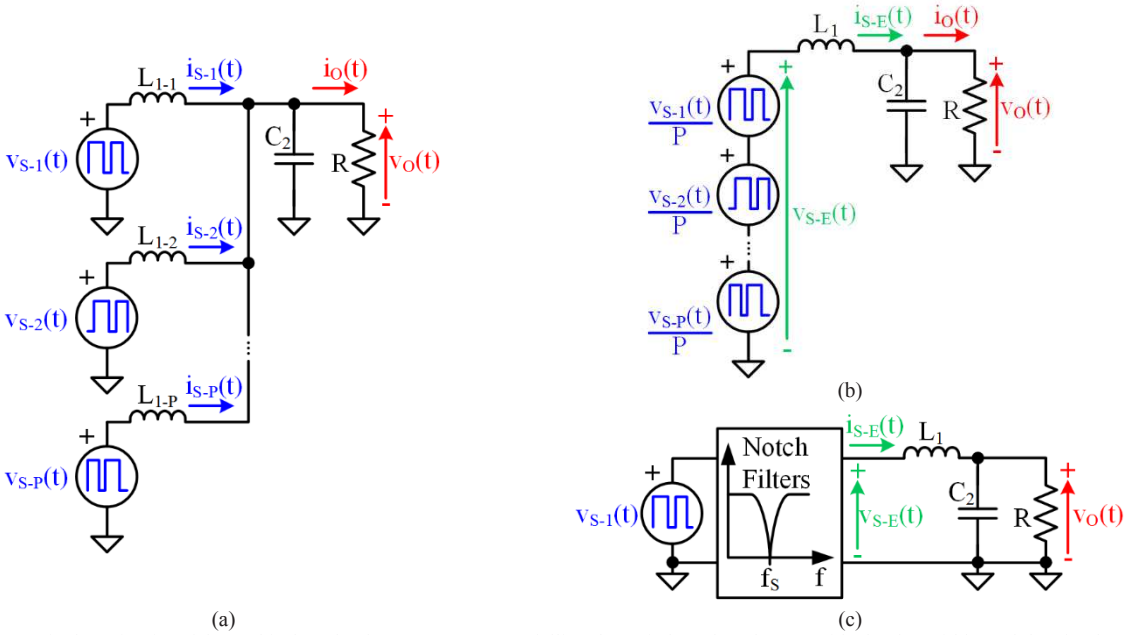

Fig. 3.2. Equivalent circuits of the multi-phase buck converter: (a) Modelling the switch-node voltages as ideal pulse-width modulated voltage sources. (b) Applying the superposition and the Thevenin's theorems to obtain the equivalent filter and $v_{S\text{-}E}(t)$. (c) Taking into account the transfer function between $v_{S\text{-}1}(t)$ and $v_{S\text{-}E}(t)$.

Using a suitable delay pattern leads to a reduction of the output voltage ripple. In this way, the benefit of the multi-phase structure arises when the delay pattern defined below is used:

$$t_{D-i} = \frac{(i-1)\cdot T_S}{P}. \tag{3.2}$$

The superposition and the Thevenin's theorems are applied to obtain the schematic depicted in Fig. 3.2(b). Note that the phase inductors ($L_{1\text{-}1}$, $L_{1\text{-}2}$, …, $L_{1\text{-}P}$) are identical and, consequently, L_1 is equal to $L_{1\text{-}1}/P$. In this way, the equivalent switch-node voltage at the input of the equivalent filter can be defined as:

$$v_{S-E}(t) = \frac{1}{P}\sum_{i=1}^{P} v_{S-i}(t) = \frac{1}{P}\sum_{i=1}^{P} v_{S-1}(t - t_{D-i}). \tag{3.3}$$

In the frequency domain, (3.3) leads to the following relationship:

$$v_{S-E}(f) = v_{S-1}(f) \cdot \frac{1}{P} \cdot \frac{\sin(\pi \cdot T_S \cdot f)}{\sin\left(\pi \cdot \frac{T_S}{P} \cdot f\right)} \cdot e^{-j\cdot\pi\cdot\left(\frac{P-1}{P}\right)\cdot T_S \cdot f}. \tag{3.4}$$

Therefore, a transfer function between $v_{S\text{-}1}(t)$ and $v_{S\text{-}E}(t)$ can be defined as follows (see Fig. 3.2 (c)):

$$H_P(f) = \frac{v_{S-E}(f)}{v_{S-1}(f)} = \frac{1}{P} \cdot \frac{\sin(\pi \cdot T_S \cdot f)}{\sin\left(\pi \cdot \frac{T_S}{P} \cdot f\right)} \cdot e^{-j\cdot\pi\cdot\left(\frac{P-1}{P}\right)\cdot T_S \cdot f}. \tag{3.5}$$

Note that $H_P(f)$ introduces notch filters at some switching frequency harmonics, contributing to reduce the output voltage ripple.

In order to facilitate the understanding of the multi-phase buck converter, an example with two phases will be addressed below. According to (3.3), $v_{S\text{-}E}(t)$ can be written as follows:

$$v_{S-E}(t) = \frac{1}{2} \cdot \left(v_{S-1}(t) + v_{S-2}(t)\right). \tag{3.6}$$

Taking into account (3.1) and (3.2), $v_{S\text{-}2}(t)$ can be written as a function of $v_{S\text{-}1}(t)$ and, consequently, (3.6) can be rewritten as follows:

$$v_{S-E}(t) = \frac{1}{2} \cdot \left(v_{S-1}(t) + v_{S-1}\left(t - \frac{T_S}{2}\right)\right). \tag{3.7}$$

In the frequency domain, (3.7) can be expressed as:

$$v_{S-E}(f) = v_{S-1}(f) \cdot H_P(f), \tag{3.8}$$

where $H_P(f)$ is:

$$H_P(f) = \frac{v_{S-E}(f)}{v_{S-1}(f)} = \frac{1}{2} \cdot \frac{\sin(\pi \cdot T_S \cdot f)}{\sin\left(\pi \cdot \frac{T_S}{2} \cdot f\right)} \cdot e^{-j\cdot\frac{\pi\cdot T_S}{2}\cdot f}. \tag{3.9}$$

Fig. 3.3(a) shows the main voltage waveforms of a two-phase buck converter. It can be seen that $v_{S\text{-}E}(t)$ can be filtered more easily than $v_{S\text{-}1}(t)$ because the switching harmonics are placed at higher frequencies and they have less power (note that the amplitude of the pulses of $v_{S\text{-}E}(t)$ is lower than that of $v_{S\text{-}1}(t)$). As was previously explained, the effect of the two-phase structure can be modeled as the incorporation of notch filters (see Fig. 3.3(b)).

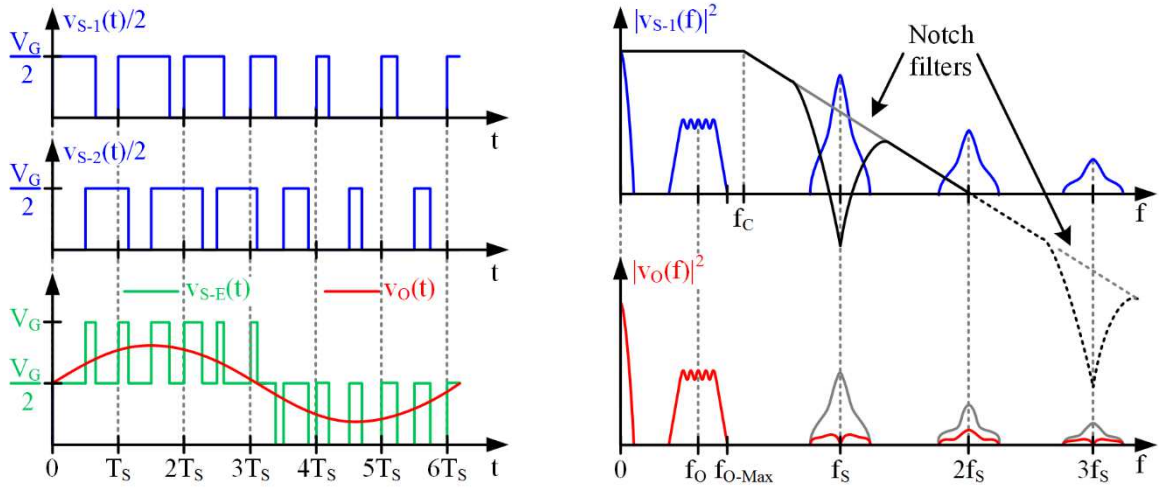

(a) (b)

Fig. 3.3. Two-phase buck converter example: (a) Main voltage waveforms. (b) Effect of the multi-phase structure in the frequency domain.

3.2.2 Buck Converter with High Order Output Filter

A straightforward method to reduce the required f_S without increasing the output voltage ripple is to increase the order of the buck converter output filter (see Fig. 3.4(a)). The use of a fourth or higher order output filter was already proposed in ET for reducing the output voltage ripple of the envelope amplifier [3.9]-[3.17]. For a given f_C value, the higher the order of the output filter, the higher the rejection of the switching-related harmonics and, consequently, the lower the required f_S (see Fig. 3.4(b)).

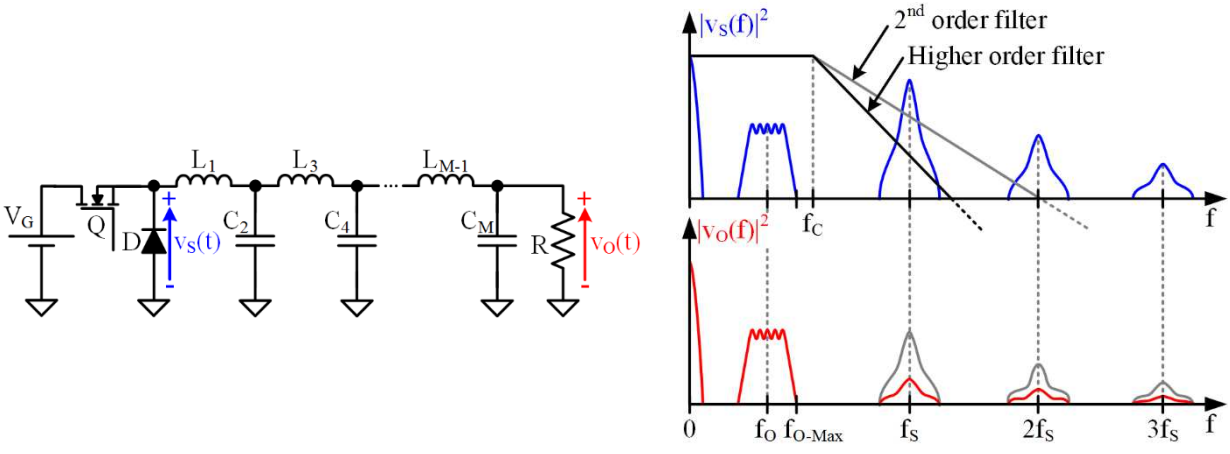

(a) (b)

Fig. 3.4. Buck converter with M[th] order output filter: (a) Topology. (b) Effect of the M[th] order output filter in the frequency domain.

3.2.3 Floating Buck Converter

The floating buck converter is a buck converter whose output is connected in series with a constant voltage source (see Fig. 3.5). This buck-derived converter is similar to two topologies that were proposed as envelope amplifiers: the multiple-input buck converter [3.18] and the multi-level converter [3.19] (see Fig. 3.6). As in those cases, the output voltage is made up of the contribution of different voltage sources:

$$v_O(t) = V_L + V_{G-H} \cdot d(t), \tag{3.10}$$

where V_L and $V_{G\text{-}H}$ are the voltage provided by the low-side constant voltage source and the input voltage of the floating buck converter, respectively.

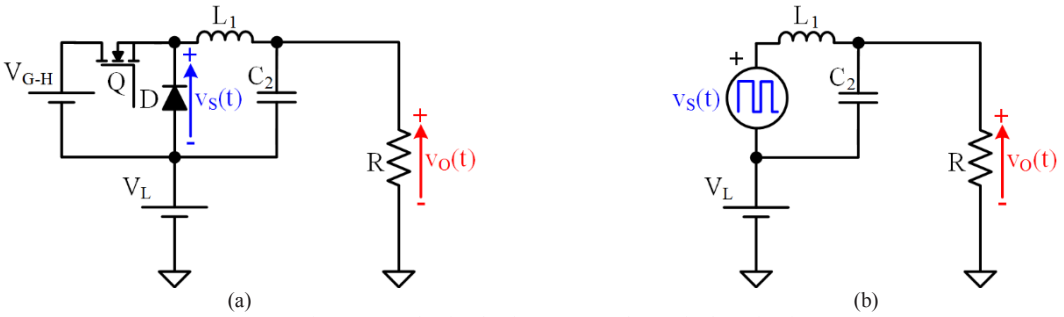

Fig. 3.5. (a) Floating buck converter. (b) Equivalent circuit.

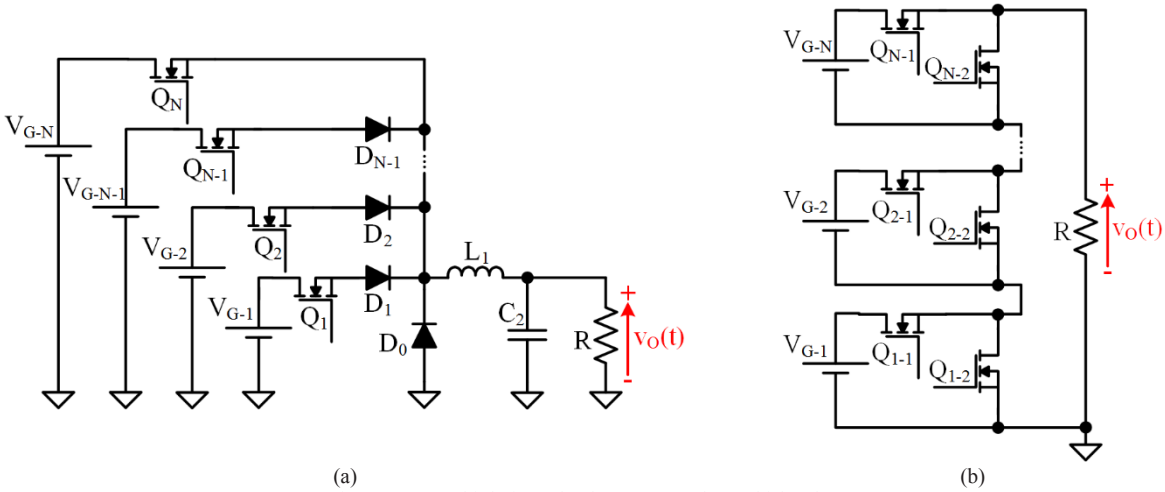

Fig. 3.6. (a) Multiple-input buck converter. (b) Multi-level converter.

The floating buck converter has three benefits that are very interesting for VLC. The first one is that it reduces the output voltage ripple because the amplitude of the pulses at the input of the filter is lower (see Fig. 3.7(a)-(b)). As a consequence, the power of the switching-related harmonics at the input of the filter is lower than that in the case of a conventional buck converter (see Fig. 3.7 (c)). In this way, the required f_S is lower.

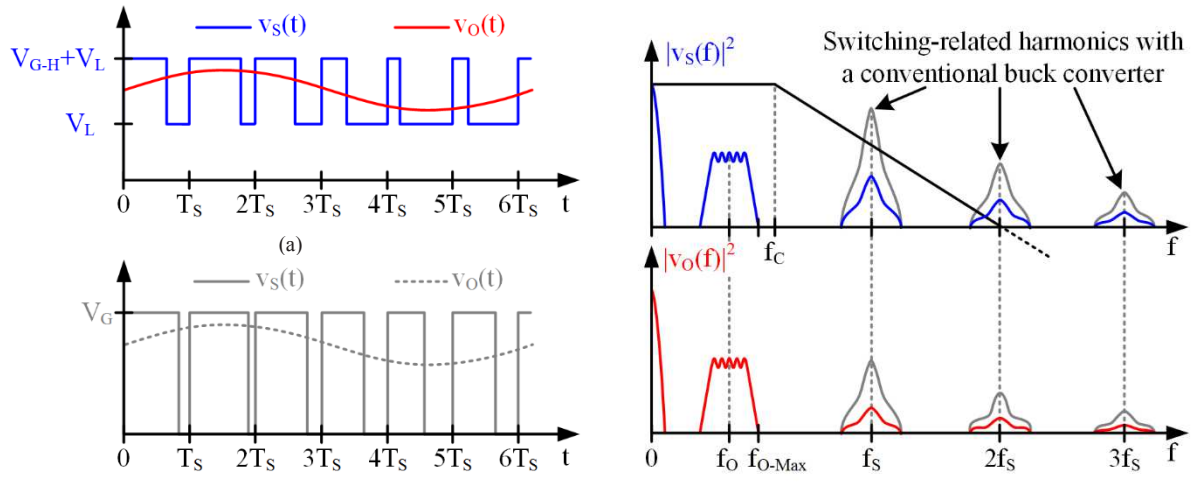

Fig. 3.7. (a) Main voltage waveforms of a floating buck converter. (b) Main voltage waveforms of a conventional buck converter. (c) Effect of the floating structure in the frequency domain.

The second benefit is that the operating range of the duty cycle is wider than that of a conventional buck converter. As was explained in Section 2.5 and summarized in Section 3.1, VLC requires a HB-LED driver able to perform very small voltage changes. In the case of a buck converter, this requirement implies having the capability to perform very small duty cycle changes, which is very difficult when f_S is very high. This problem is alleviated in the case of the floating buck converter because $V_{G\text{-}H}$ can be chosen with a value close to the voltage variations that need to be performed. In this way, and according to (3.10), the duty cycle changes that must be performed are higher. In order to make these reasoning more consistent, a simple mathematical analysis will be carried out (equivalent to the one made in Section 2.5 of Chapter 2). According to (3.10), the minimum output voltage change that can be performed with a floating buck converter around the bias voltage can be expressed as follows:

$$v_{O-DC} + \Delta v_O = V_L + d_{DC} \cdot V_{G-H} + \Delta d \cdot V_{G-H}. \tag{3.11}$$

Substituting (2.15) into (3.11) and focusing on Δv_O leads to:

$$\Delta v_O = f_S \cdot \Delta t \cdot V_{G-H}. \tag{3.12}$$

As in the case of a conventional buck converter (see (2.16)), for a given Δt, the higher the f_S value, the lower the minimum output voltage change that can be performed and, as a consequence, the lower the output voltage accuracy. However, the floating buck converter can perform smaller voltage changes than a conventional buck converter because of two reasons: the required f_S is lower and $V_{G\text{-}H}$ is lower than V_G.

Finally, the third benefit of the floating buck converter is that it minimizes the power processed with high f_S, which reduces the impact of the switching losses. Note that the voltage that the MOSFET and the diode have to block is equal to $V_{G\text{-}H}$ which, as was previously indicated, is lower than V_G, reducing the energy dissipated during the switching transitions.

3.3 Floating Multi-Phase Buck Converter with High Order Output Filter

Taking into account the benefits of the topologies described in Section 3.2, a floating multi-phase buck converter with high order output filter is proposed for acting as the HB-LED driver of VLC transmitters (see Fig. 3.8) [3.20]-[3.22]. Moreover, the constant voltage source that is connected in series with the output of the multi-phase buck converter will be provided by a synchronous buck converter. As will be explained later, the synchronous buck converter allows us to control $i_{O\text{-}DC}$ and, consequently, to perform dimming. Furthermore, it is well known that driving floating MOSFETs is difficult when f_S is high. This problem appears in the conventional multi-phase buck converter, where the source terminals of the MOSFETs are connected to non-constant voltage points. However, in the proposed configuration, the source terminals of the MOSFETs are connected to the input voltage source negative terminal of the multi-phase buck converter (see Fig. 3.8). In this way, the MOSFETs driving task becomes easier if $V_{G\text{-}H}$ is used to supply the MOSFETs drivers of the multi-phase buck converter. Note that the position of the other multi-phase buck converter elements should be modified with respect to the conventional one in order to properly perform the buck converter function.

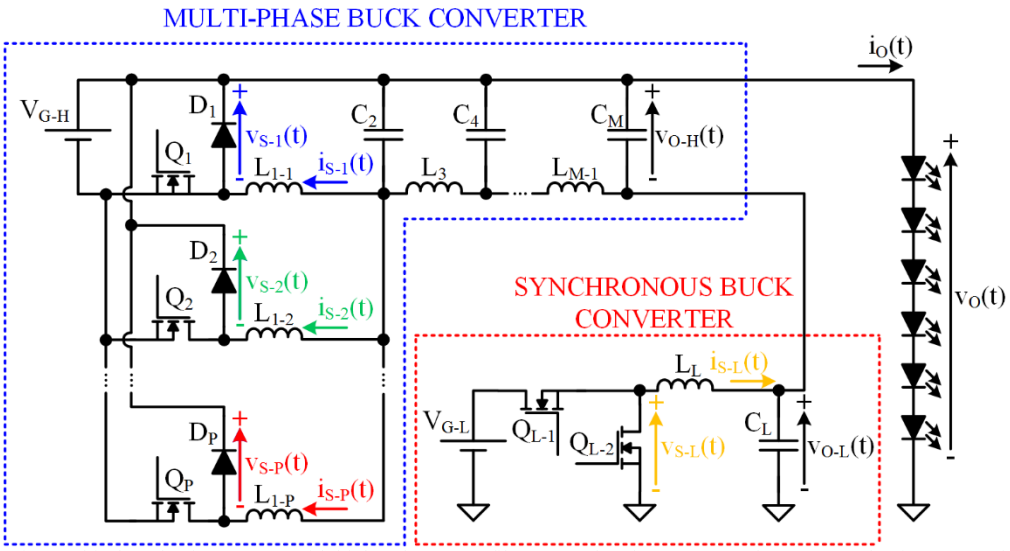

Fig. 3.8. Floating multi-phase buck converter with high order output filter. Note that the constant voltage source that is connected in series with the output of the multi-phase buck converter is provided by a synchronous buck converter.

3.3.1 Operation Description: Controlling $i_{O\text{-}DC}$ and Splitting the Power

The operation of the proposed HB-LED driver for VLC is derived from the recommended approach that was presented in Section 2.4: controlling $i_{O\text{-}DC}$. In this case, the synchronous buck converter (i.e., the low-side converter in Fig. 3.8) operates in close-loop and it is responsible for regulating $i_{O\text{-}DC}$. Regarding the multi-phase buck converter (i.e., the high-side converter in Fig. 3.8), it operates in open-loop performing the small voltage variations that are required for reproducing the communication signal. The set of PWM-SMPCs works in the following way. The multi-phase buck converter provides $v_{O\text{-}AC}(t)$ (i.e., the voltage component responsible for the communication) plus a certain DC voltage ($v_{O\text{-}H\text{-}DC}$) required for the proper operation of the PWM-SMPC. Note that $v_{O\text{-}H\text{-}DC}$ is mandatory to ensure that the total output voltage of the multi-phase buck converter ($v_{O\text{-}H}(t)$) never reaches zero or negative values (i.e., $v_{O\text{-}AC}(t) + v_{O\text{-}H\text{-}DC} > 0$ V). The remaining DC voltage that is required for achieving the desired lighting level is provided by the synchronous buck converter. Therefore, the synchronous buck converter regulates $i_{O\text{-}DC}$ by adjusting its output voltage ($v_{O\text{-}L}$) to ensure that the total DC output voltage of the HB-LED driver (i.e., $v_{O\text{-}DC} = v_{O\text{-}L} + v_{O\text{-}H\text{-}DC}$) achieves the desired biasing point regardless $v_{O\text{-}H\text{-}DC}$ and the $V_{\gamma\text{-}I}$ variations with T_J. Then, the total output voltage of the HB-LED driver is:

$$v_O(t) = v_{O-L} + v_{O-H}(t) = v_{O-L} + v_{O-H-DC} + v_{O-H-AC}(t) = v_{O-DC} + v_{O-AC}(t), \tag{3.13}$$

$$v_{O-DC} = v_{O-L} + v_{O-H-DC}, \tag{3.14}$$

$$v_{O-AC}(t) = v_{O-H-AC}(t), \tag{3.15}$$

where $v_{O\text{-}H\text{-}AC}(t)$ is the AC component of $v_{O\text{-}H}(t)$.

Fig. 3.9 shows the control scheme of the proposed HB-LED driver for VLC. Since the multi-phase buck converter is responsible for reproducing the communication signal, it is the only PWM-SMPC that must ensure a bandwidth equal or higher than $f_{O\text{-}Max}$. As a result, its switching frequency ($f_{S\text{-}H}$) is high and the target is to use a value as close as possible to the theoretical minimum one (i.e., $2 \cdot f_{O\text{-}Max}$ according to the Nyquist-Shannon sampling theorem) without

distorting the communication signal because of the ripple. The use of the multi-phase structure, the floating structure and the high order output filter is focused on reducing the gap. In any case, since $f_{S\text{-}H}$ will be in the MHz range even if it is equal to $2 \cdot f_{O\text{-}Max}$, the multi-phase buck converter will suffer from high switching losses. The key point is that since the multi-phase buck converter only delivers the part of the power determined by the communication signal, which is significantly lower than the total power, the impact of those switching losses in the overall efficiency is mitigated. The rest of the power is delivered by the synchronous buck converter, which can achieve high efficiency because the selection of its switching frequency ($f_{S\text{-}L}$) is not subject to a high bandwidth requirement. Therefore, $f_{S\text{-}L}$ can be significantly lower than $f_{S\text{-}H}$. Note that since the synchronous buck converter only needs to track a constant current reference (i.e., $i_{O\text{-}DC\text{-}Ref}$), its design and efficiency are similar to those of a conventional HB-LED driver for lighting applications. In practice, the synchronous buck converter will typically operate with $f_{S\text{-}L}$ in the range of hundreds of

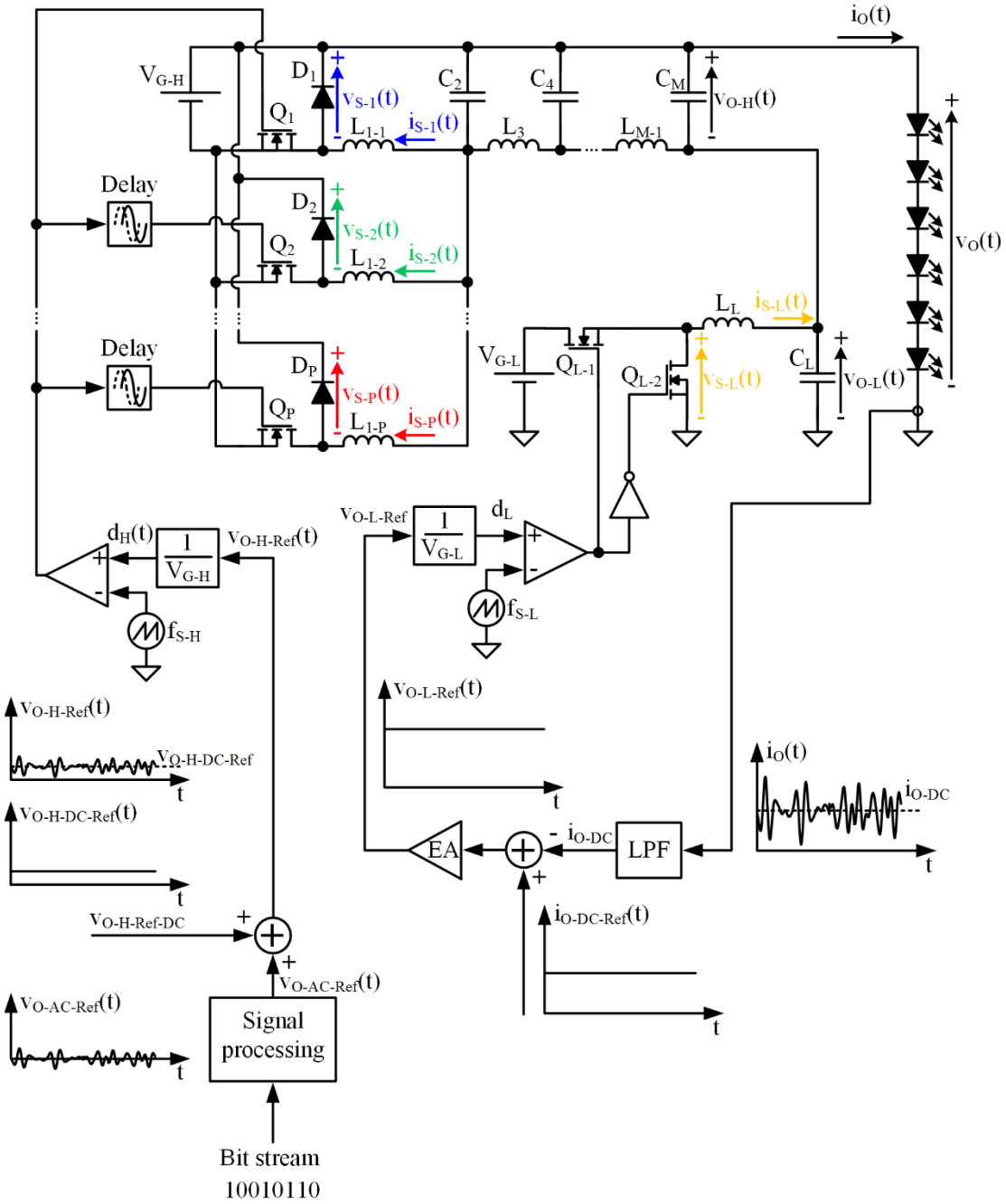

Fig. 3.9. Control scheme of the floating multi-phase buck converter with high order output filter.

kHz while the multi-phase buck converter will operate with $f_{S\text{-}H}$ in the MHz range. In summary, the power delivered by the multi-phase buck converter must be minimized in order to maximize the overall efficiency. It can be performed by selecting $v_{O\text{-}H\text{-}DC}$ barely higher than the one that always ensures $v_{O\text{-}H}(t) > 0$ V.

Another advantage of this approach is that the output-series connection enables an accurate reproduction of $v_{O\text{-}AC}(t)$ with relative ease. Since the multi-phase buck converter is focused on performing the small voltage variations, while the synchronous buck converter provides most of $v_{O\text{-}DC}$, the required duty cycle accuracy for each PWM-SMPC is not as critical as in the case of conventional buck converter. The reasoning is similar to that of the floating buck converter.

Regarding the drawbacks, the two isolated input voltages required for the implementation (i.e., $V_{G\text{-}H}$ and $V_{G\text{-}L}$) is the weakest point of the approach.

In summary, the HB-LED driver proposed for VLC is focused on addressing the two major design challenges that appear when a PWM-SMPC is used to drive the HB-LEDs of a VLC transmitter: the problems caused by the high f_S that is required in order to provide the demanded bandwidth, and the high duty cycle accuracy that is required for reproducing the communication signal. The multi-phase structure, the floating structure and the use of a high order output filter allow us to reduce the required f_S with respect to a conventional buck converter which, in turns, increases the power efficiency. Moreover, the floating structure also allows us to increase the power efficiency more because the synchronous buck converter delivers the major part of the power. Since this PWM-SMPC can reach a very high efficiency, the power that it processes causes few power losses. Finally, the capability of performing very small voltage variations is increased with respect to a conventional buck converter because the multi-phase buck converter does not have to provide the entirely output voltage. It is focused on performing the small voltage variations while the synchronous buck converter delivers most of the DC voltage.

3.3.2 Steady State Operation

Obtaining the equivalent circuits of the proposed HB-LED driver will be helpful to understand the steady state operation. It can be performed by following the methodology explained in Section 3.2.1. Hence, the first step is to consider CCM operation and to model each switch-node voltage as ideal pulse-width modulated voltage source (see Fig. 3.10(a)). It is important to note that $v_{S\text{-}1}(t)$, $v_{S\text{-}2}(t)$, …, $v_{S\text{-}P}(t)$ denote the switch-node voltages of the multi-phase buck converter and that $v_{S\text{-}L}(t)$ is the switch-node voltage of the synchronous buck converter. The second step is to apply the superposition and Thevenin's theorems in order to obtain both the equivalent filter of the multi-phase buck converter and the equivalent voltage (i.e., $v_{S\text{-}E}(t)$) at the input of that filter (see Fig. 3.10(b)). As will be shown later, the circuit can be simplified more. However, at this point it is simple enough to facilitate the understanding of the steady state operation.

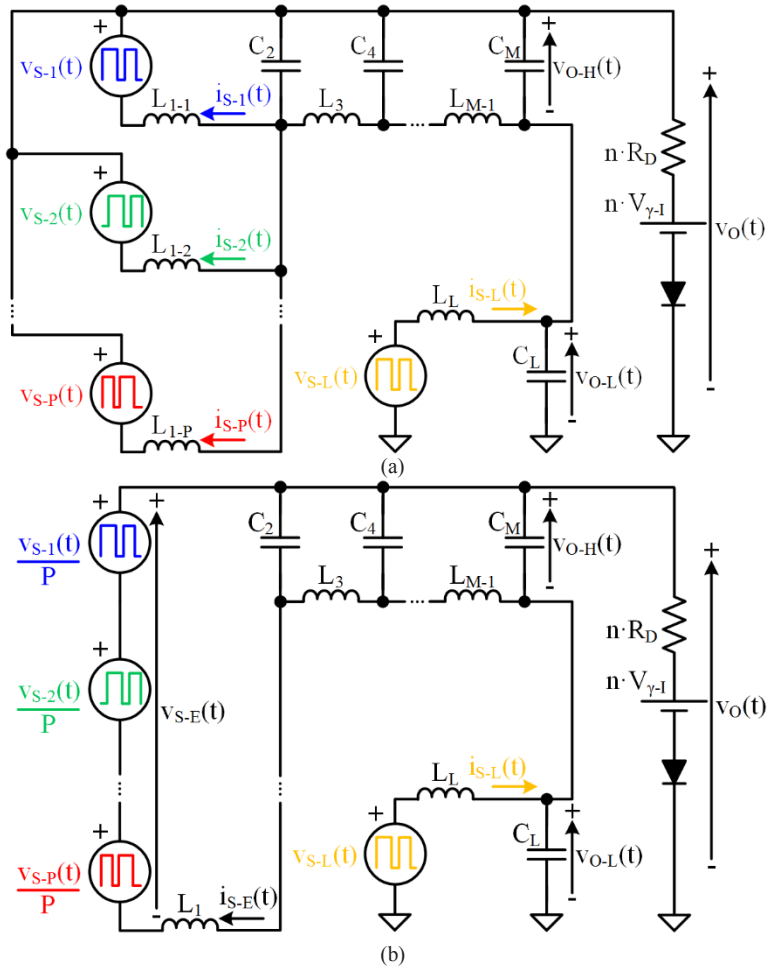

Fig. 3.10. Equivalent circuits of the proposed HB-LED driver: (a) Modeling $v_{S\text{-}1}(t)$, $v_{S\text{-}2}(t)$, …, $v_{S\text{-}P}(t)$ and $v_{S\text{-}L}(t)$ as ideal pulse-width modulated voltage sources. (b) Applying the superposition and the Thevenin's theorems.

Fig. 3.11 shows the main electrical waveforms of the proposed HB-LED driver assuming steady state conditions. Note that $T_{S\text{-}H}$ and $T_{S\text{-}L}$ are the switching period of high-side converter and the low-side converter, respectively. According to Section 3.2.1, and thanks to the delay pattern indicated in (3.2), $v_{S\text{-}E}(t)$ has lower harmonic content than the switch-node voltages and, moreover, it is placed at higher frequencies. Thus, the filtering task is easier than in the case of a single-phase approach.

Another important point is that, as Fig. 3.11(a) shows, the total output voltage ripple is made up of the output voltage ripple of both PWM-SMPCs (i.e., the multi-phase buck converter and the synchronous buck converter). Then, it is essential to reduce not only the output voltage ripple of the multi-phase buck converter, but also the output voltage ripple of the synchronous buck converter in order to minimize the distortion of the communication signal.

The reduction of the output voltage ripple achieved by the multi-phase buck converter in steady state operation can also be understood from the main current waveforms. As Fig. 3.11(b) shows, the current delivered by each PWM-SMPC are identical (i.e., equal to $i_O(t)$) due to the output-series connection. Moreover, it is very important to analyze the current of each phase of the multi-phase buck converter (i.e., $i_{S\text{-}1}(t)$, $i_{S\text{-}2}(t)$, …, $i_{S\text{-}P}(t)$) in order to understand the reduction of the output voltage ripple achieved by the multi-phase structure. Assuming that all phase inductances are identical, the current ripple of each phase of the multi-phase buck converter will be equal. In addition, the DC component of each phase current is $i_{O\text{-}DC}/P$ if the Equivalent Series Resistances (ESRs) of all phase inductors are identical. Then, the inductor current of the i^{th} phase is delayed $t_{D\text{-}i}$ with respect to the inductor current of the first phase

(see Fig. 3.11(b)). As a result, the sum of all phase currents (i.e., $i_{S\text{-}E}(t) = i_{S\text{-}1}(t) + i_{S\text{-}2}(t) + \ldots + i_{S\text{-}P}(t)$) has lower ripple than in the case of a single phase.

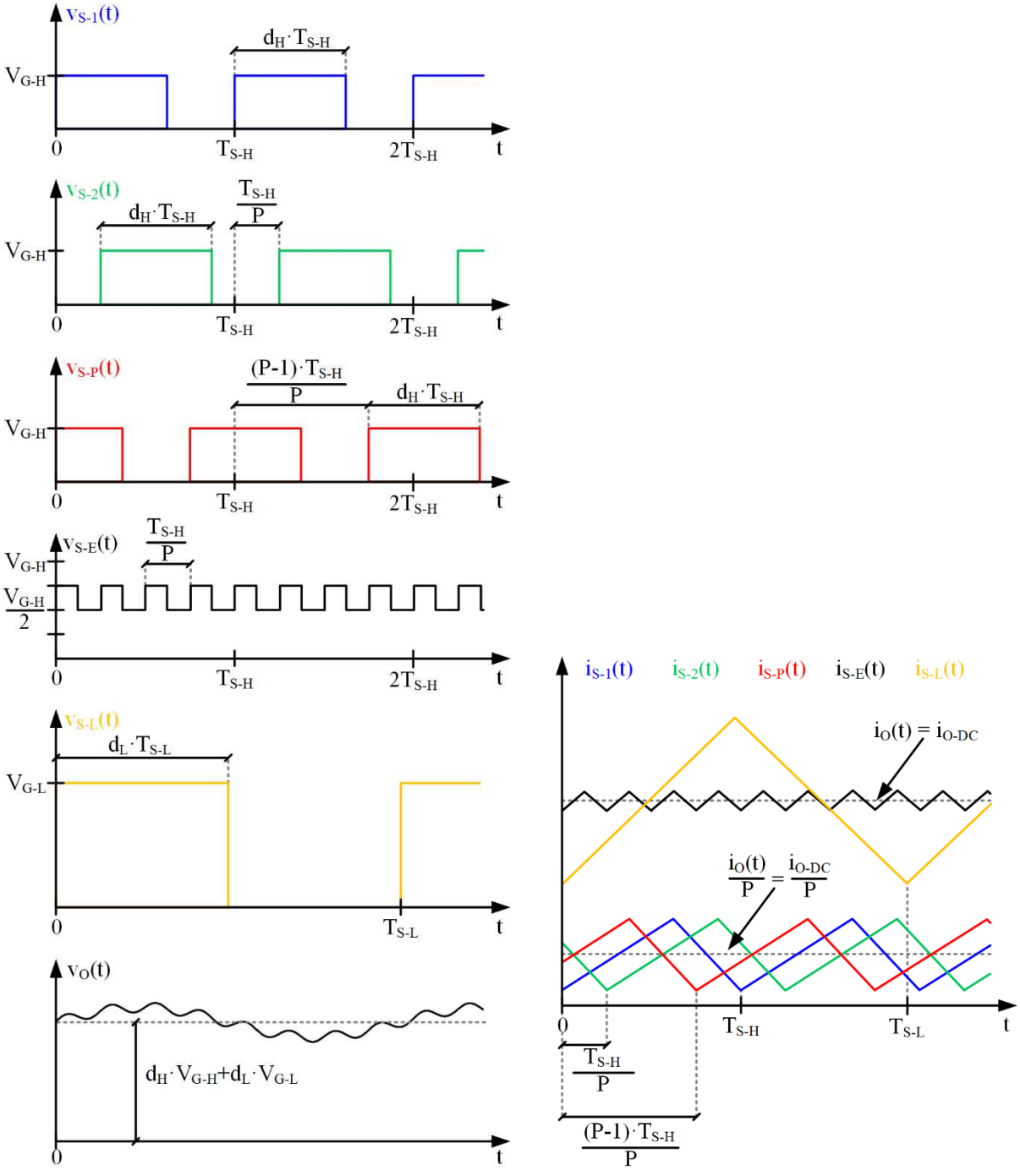

(a) (b)

Fig. 3.11. Main electrical waveforms of the proposed HB-LED driver assuming steady state conditions: (a) Voltage waveforms. (b) Current waveforms.

3.3.3 Frequency Domain Analysis

The steady state analysis is a suitable initial step to study the proposed HB-LED driver. However, the frequency domain analysis must be carried out in order to deeply understand the operation of the multi-phase buck converter, the operation of the synchronous buck converter and their joint operation as a single HB-LED driver for VLC.

As previously explained, the multi-phase buck converter is responsible for reproducing the communication signal with high accuracy. The operating principle is based on providing the desired $v_{O\text{-}AC}(t)$ from $v_{S\text{-}1}(t)$ by carefully filtering this pulse-width modulated voltage. Therefore, the transfer function between $v_{S\text{-}1}(t)$ and $v_O(t)$ (i.e., $H_H(f) = v_O(f)/v_{S\text{-}1}(f)$) must be analyzed. It is important to note that $H_H(f)$ must reject the switching harmonics together with their sidebands (i.e., the switching-related harmonics). Moreover, this transfer function must meet some additional requirements in order to avoid distortion when reproducing the communication signal. Firstly, its magnitude must be flat in the desired frequency bands. Note that these frequency bands include the DC component and the frequency components that appear due to the duty cycle variation over time (i.e., the frequency components related to the communication signal that is being reproduced). Secondly, the phase-shift of $H_H(f)$ must be linear with frequency in those regions, ensuring a constant group delay.

$H_H(f)$ will show the effect of the multi-phase structure, the effect of M^{th} order low-pass filter and the impact of the synchronous buck converter on the multi-phase buck converter:

$$H_H(f) = H_{H-P}(f) \cdot H_{H-F}(f) \cdot H_{H-L}(f), \tag{3.16}$$

where $H_{H\text{-}P}(f)$ is the transfer function between $v_{S\text{-}1}(t)$ and $v_{S\text{-}E}(t)$ (i.e., the effect of multi-phase structure), $H_{H\text{-}F}(f)$ is the transfer function between $v_{S\text{-}E}(t)$ and $v_{O\text{-}H}(t)$ (i.e., the effect of M^{th} order low-pass filter), and $H_{H\text{-}L}(f)$ is the transfer function between $v_{O\text{-}H}(t)$ and $v_O(t)$ (i.e., the impact of the synchronous buck converter). The equivalent circuit depicted in Fig. 3.12 can be used to analyze $H_H(f)$.

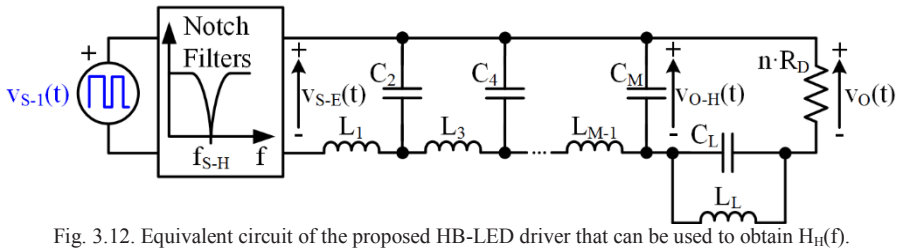

Fig. 3.12. Equivalent circuit of the proposed HB-LED driver that can be used to obtain $H_H(f)$.

Starting with the M^{th} order low-pass filter, it is well-known that it causes a magnitude drop for frequencies higher than the cut-off frequency ($f_{C\text{-}H}$). Therefore, $f_{C\text{-}H}$ must be higher than the highest frequency component of the signal (i.e., $f_{O\text{-}Max}$). There is an important trade-off between $f_{C\text{-}H}$, $f_{S\text{-}H}$, $f_{O\text{-}Max}$ and the order of the filter. $f_{C\text{-}H}$ must be high enough to not distort the frequency components of the signal and, at the same time, it must be low enough to ensure enough rejection of the switching harmonics and their sidebands. In order to alleviate this problem, $f_{S\text{-}H}$ can be increased in exchange for higher switching losses. Another option consists in increasing the filter order. However, this is translated into higher complexity and cost. This issue has been deeply studied in [3.15] and [3.9] for the ET application, and the design guidelines included in these works are valid for the multi-phase buck converter of the proposed HB-LED driver. As in [3.15] and [3.9], the source impedance of the filter is 0 Ω and, consequently, proper filter tables must be used. In this case, $n \cdot R_D$ must be considered as the load impedance of the filter.

Regarding $H_{H\text{-}P}(f)$ and according to (3.1)-(3.5) and to the notation of the floating multi-phase buck converter, it can be defined as:

$$H_{H-P}(f) = \frac{v_{S-E}(f)}{v_{S-1}(f)} = \frac{1}{P} \cdot \frac{\sin(\pi \cdot T_{S-H} \cdot f)}{\sin\left(\pi \cdot \frac{T_{S-H}}{P} \cdot f\right)} \cdot e^{-j \cdot \pi \cdot \left(\frac{P-1}{P}\right) \cdot T_{S-H} \cdot f}. \tag{3.17}$$

As was previous indicated, the multi-phase structure introduces notch filters at several switching frequency harmonics, contributing to reduce the output voltage ripple. As Fig. 3.13 shows, the higher the number of phases, the higher the number of notch filters and the lower the output voltage ripple.

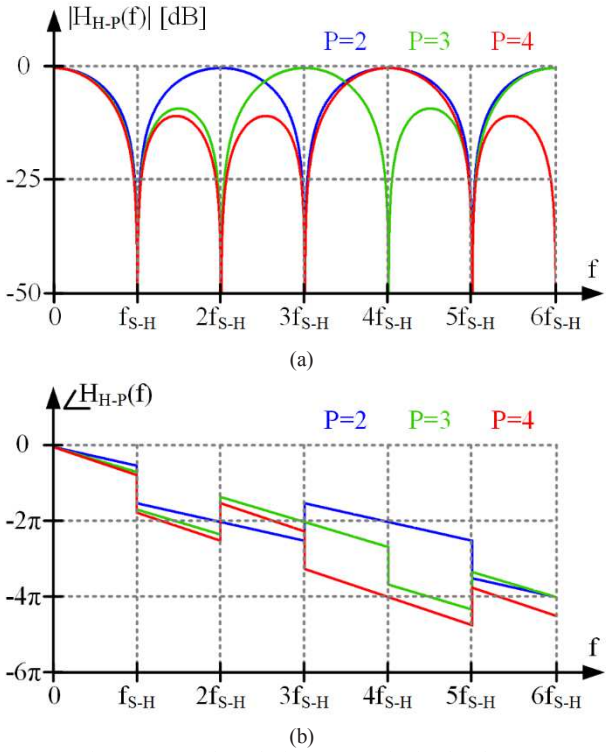

Fig. 3.13. $H_{H\text{-}P}(f)$ analysis: (a) Magnitude. (b) Phase.

Regarding the impact of the synchronous buck converter on the multi-phase buck converter, the output filter of the synchronous buck converter also introduces a notch filter at its cut-off frequency ($f_{C\text{-}L}$). Fig. 3.14 shows $H_{H\text{-}L}(f)$ for different Q values of the synchronous buck converter filter keeping the same $f_{C\text{-}L}$. Note that the expression utilized for the Q factor evaluation is:

$$Q = n \cdot R_D \cdot \sqrt{\frac{C_L}{L_L}}. \tag{3.18}$$

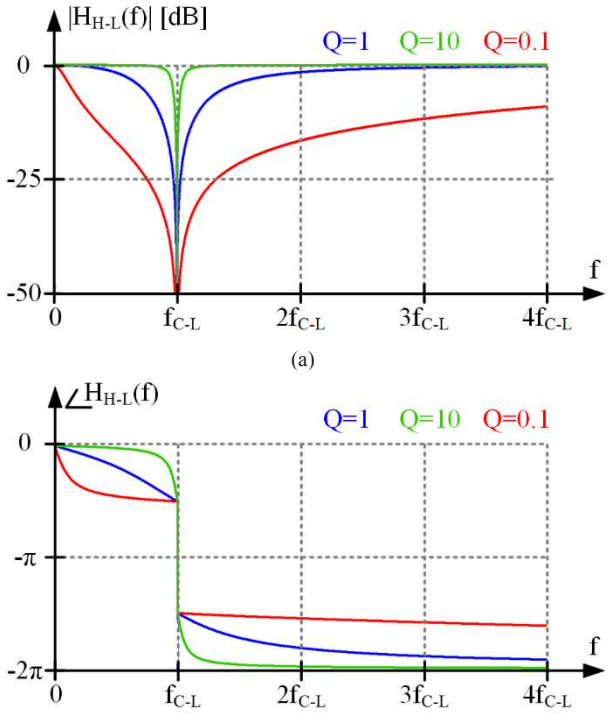

Fig. 3.14. $H_{H\text{-}L}(f)$ analysis: (a) Magnitude. (b) Phase.

Finally, Fig. 3.16(a) shows $|H_H(f)|$ highlighting the different effects. This figure considers different number of phases and different designs of the synchronous buck converter filter that keep the same $f_{C\text{-}L}$ but change the Q factor. It is important to note that f_{Ref} represents the center frequency of the modulation scheme that is going to be reproduced. The rest of signal components would be placed around f_{Ref}. It can be seen that the available frequency band for the communication signal depends on the Q factor of the synchronous buck converter filter. Note that in Fig. 3.16(a), the identification of the available frequency band only considers the amplitude distortion. However, the phase distortion also plays an important role (see Fig. 3.16(b)). Therefore, the relative variation of the group delay with respect to the group delay at f_{Ref} (i.e., $\tau_{R\text{-}Ref}(f)$) must be evaluated:

$$\tau_{R-Ref}(f) = \frac{\tau(f) - \tau(f_{Ref})}{\tau(f_{Ref})}, \tag{3.19}$$

where $\tau(f)$ is the group delay of $H_H(f)$. The actual available frequency band is the smallest of both approaches (i.e., considering the amplitude and the phase distortion) and it depends on the limits employed to identify the bands. In other words, the maximum attenuation permitted in the case of the amplitude distortion, and the maximum relative variation of the group delay permitted in the case of the phase distortion. In any case, it can be concluded that a high Q factor is desirable for maximizing the available frequency band. Moreover, $f_{C\text{-}L}$ must be placed between the DC component and the lowest harmonic of the reproduced modulation scheme.

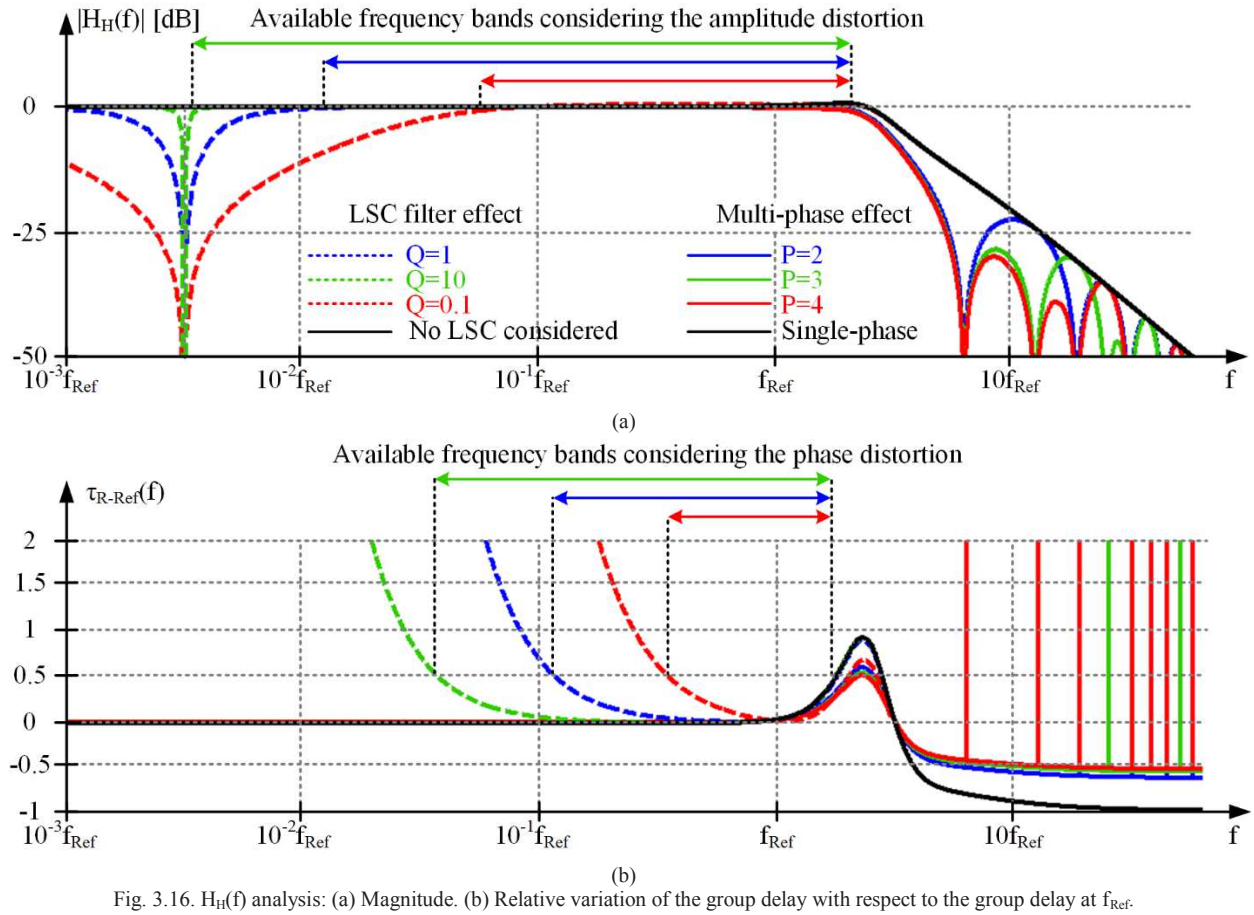

Fig. 3.16. $H_H(f)$ analysis: (a) Magnitude. (b) Relative variation of the group delay with respect to the group delay at f_{Ref}.

Regarding the synchronous buck converter, how it is affected by the multi-phase buck converter when it tries to control $i_{O\text{-}DC}$ must be analyzed. There are several transfer functions that can be calculated in order to address this point. In this paper, the transfer function between the duty cycle (d_L) and $i_O(t)$ ($G_{dL\text{-}i}(f)$) is obtained and studied by using the equivalent circuit depicted in Fig. 3.15.

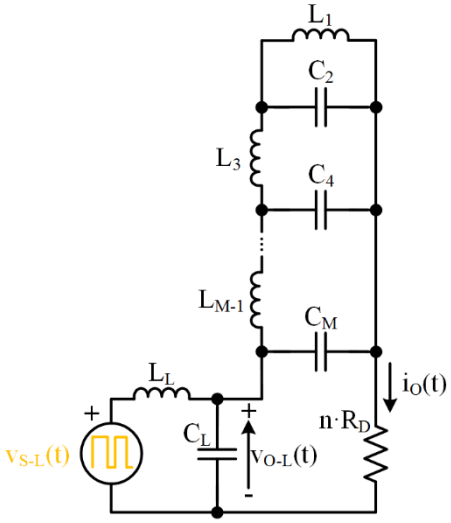

Fig. 3.15. Equivalent circuit of the proposed HB-LED driver that can be used to obtain $G_{dL\text{-}i}(f)$.

Fig. 3.17 shows $G_{dL\text{-}i}(f)$ for different Q values of the synchronous buck converter filter, highlighting the impact of the multi-phase buck converter. It can be seen that the output impedance of the multi-phase buck converter introduces certain notch filters at high frequencies. Fortunately, this fact has minor impact on the current feedback loop

and, consequently, the synchronous buck converter can be designed similarly to a conventional HB-LED driver for lighting applications. It is important to note that the LPF of the feedback loop must be taken into account for designing the regulator. The cut-off frequency of this LPF should be as low as possible but, at the same time, high enough to not jeopardize excessively the bandwidth of the feedback loop. In general, this point is not an issue and, in practice, a cut-off-frequency similar to $f_{C\text{-}L}$ fulfills the application requirements.

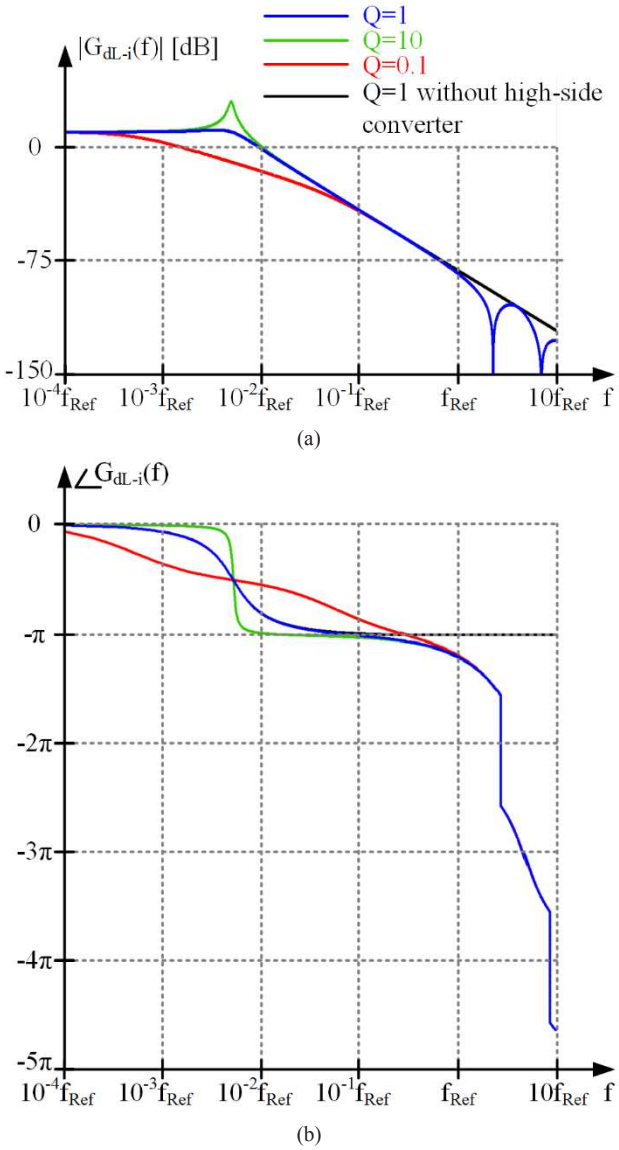

Fig. 3.17. $G_{dL\text{-}i}(f)$ analysis: (a) Magnitude. (b) Phase.

3.3.4 Design Guidelines

The recommended steps for the design of the proposed VLC transmitter are described in this section. The design specifications should include the maximum lighting level ($s_{DC\text{-}Max}$) and the modulation scheme that must be reproduced together with the maximum power of the communication signal, thus defining $s_{AC}(t)$ for the highest communication power. It is important to note that the modulation scheme does not determine the communication signal power because it only determines the shape of the signal. The same signal can be transmitted with different power levels (i.e., more or less amplification) depending on the particular application requirements.

Step 1: dimensioning the HB-LED string. The number of HB-LEDs of the string (i.e., n) that are needed can be calculated by taking into account $s_{DC\text{-}Max}$. Their dynamic resistance (i.e., R_D) and their knee voltage (i.e., $V_{\gamma\text{-}I}$) must be considered to obtain the equivalent model.

Step 2: characterization of $i_{O\text{-}AC}(t)$ and $v_{O\text{-}AC}(t)$ for the highest communication power. $i_{O\text{-}AC}(t)$ and $v_{O\text{-}AC}(t)$ for the highest communication power ($i_{O\text{-}AC\text{-}Max}(t)$ and $v_{O\text{-}AC\text{-}Max}(t)$, respectively) can be obtained by considering (2.1), (2.2) and the equivalent dynamic resistance of the HB-LED string selected in Step 1 (i.e., $n \cdot R_D$). After that, the peak to peak value of $v_O(t)$ ($v_{O\text{-}PP}$) for the highest communication power ($v_{O\text{-}PP\text{-}Max}$) can be calculated from $v_{O\text{-}AC\text{-}Max}(t)$.

Step 3: determining $V_{G\text{-}H}$. It is important to note that the lower the $V_{G\text{-}H}$ value, the lower the duty cycle accuracy required to generate $v_{O\text{-}H}(t)$ and, as a consequence, the lower the demanded time resolution of the Field Programmable Gate Array (FPGA). Therefore, it is essential to determine the minimum $V_{G\text{-}H}$ value ($V_{G\text{-}H\text{-}Min}$) that could to be used. The duty cycle of the multi-phase buck converter ($d_H(t)$) must be always lower than a maximum value ($d_{H\text{-}Max}$) and higher than a minimum value ($d_{H\text{-}Min}$) that are stablished due to safety reasons. For the sake of simplicity, the same safety margin is considered for both duty cycle limits (i.e., $d_{H\text{-}Min} = 1 - d_{H\text{-}Max}$). Note that Fig. 3.18 can be used to understand the reasoning related to Step 3. Under the aforementioned considerations and when the HB-LED driver for VLC operates with the maximum communication power, the following equation can be used to determine $V_{G\text{-}H\text{-}Min}$:

$$d_{Max} \cdot V_{G-H-Min} = d_{Min} \cdot V_{G-H-Min} + v_{O-PP-Max}. \tag{3.20}$$

Therefore, $V_{G\text{-}H}$ must satisfy the following condition:

$$V_{G-H} \geq V_{G-H-Min} = \frac{v_{O-PP-Max}}{1 - 2 \cdot d_{Min}}. \tag{3.21}$$

It is important to note that $v_{O\text{-}H\text{-}DC}$ is defined as:

$$v_{O-H-DC} = d_{Min} \cdot V_{G-H-Min} + \frac{v_{O-PP}}{2}. \tag{3.22}$$

As a result, the following condition is always satisfied:

$$v_{O-H}(t) \geq d_{Min} \cdot V_{G-H} \geq 0\,V. \tag{3.23}$$

The maximum value of $v_{O\text{-}H\text{-}DC}$ is reached when the communication power is the highest one:

$$v_{O-H-DC-Max} = 0.5 \cdot V_{G-H-Min}. \tag{3.24}$$

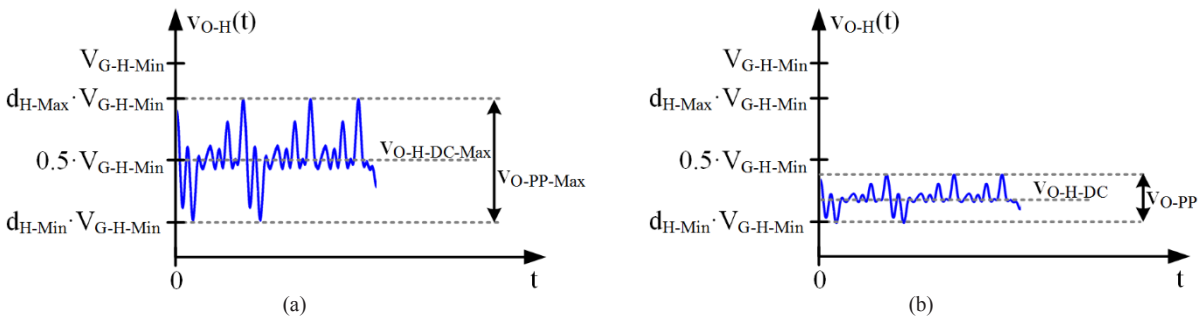

Fig. 3.18. $v_{O\text{-}H}(t)$ for two communication power levels using $V_{G\text{-}H} = V_{G\text{-}H\text{-}Min}$: (a) Maximum communication power. (b) Lower communication power.

Step 4: Selecting the number of phases (i.e., P) and the order of the filter (i.e., M). As is explained in Section 3.3.3, both the multi-phase structure and the high order output filter contribute to reduce the output voltage ripple. Therefore, both points must be addressed together. Obviously, the higher the number of phases, the lower the required order of the filter and vice versa. As a consequence, there are several solutions (i.e., several combinations of P and M) that, showing similar complexity (which could be evaluated using P + M), ensure a certain level of output voltage ripple rejection. In order to select the most appropriate solution for the particular requirements of the VLC transmitter, parameters that are difficult to be measured, such as the dependence of the cost or of the size on P and M, must be taken into account. In any case, it is recommendable to follow the directions of [3.15] and [3.9] for determining M and the cut-off frequency of the filter (i.e., $f_{C\text{-}H}$) once P is selected.

Step 5: Designing the synchronous buck converter. In the case of the synchronous buck converter, the input voltage (i.e., $V_{G\text{-}L}$) can be selected according to standard voltage values such as 24 V or 48 V. As is explained in Section 3.3.3, the cut-off frequency of the filter (i.e., $f_{C\text{-}L}$) should be lower than the minimum frequency of the communication signal that the multi-phase buck converter is going to reproduce. In addition, the Q value of the filter should be high enough to avoid the distortion of the communication signal. The design of the feedback loop is straightforward.

3.3.5 Experimental Results

3.3.5.1 Prototype Details

A two-phase asynchronous buck converter and a single-phase synchronous buck converter were built to test experimentally the proposed HB-LED driver (see Fig. 3.19). The switching frequency of the two-phase buck converter and the synchronous buck converter are 10 MHz and 250 kHz, respectively. The output filter of the two-phase buck converter is a 4^{th} order Butterworth filter with a cut-off frequency equal to 4 MHz. In the case of the synchronous buck converter, the cut-off frequency of the 2^{nd} order filter is 20.5 kHz and the Q value is 1.56. Table III.I shows the passive components used for the filters implementation. The inductors of the two-phase buck converter are implemented with iron powder cores (T50-2) from Micrometals. A SER1390-333MLB inductor from Coilcraft is used for the inductor of the synchronous buck converter. The LPF of the feedback loop is implemented with a RC filter whose cut-off frequency is 15.9 kHz. Silicon MOSFETs are used in both PWM-SMPCs: SSM3K336R in the two-phase buck converter and TK7S10N1Z in the synchronous buck converter. In both cases, the MOSFETs are driven by EL7156 ICs. Schottky diodes DB2430500L are used in the two-phase buck converter. The load is made up of 6 HB-LEDs (W42180 Seoul Semiconductor) connected in series. The input voltage of the two-phase buck converter and the synchronous buck converter are 8.5 V and 24 V, respectively. Commercial receiver PDA10A-EC is used in the VLC setup. Since this device is made up of a photodiode and a transconductance amplifier, its output signal is a voltage waveform proportional to the received light intensity.

Regarding the communication signal, a 64-QAM-OFDM scheme that is made up of 29 carriers is reproduced. It is important to note that the maximum frequency component of the reproduced modulation scheme (i.e., $f_{O\text{-}Max}$) is around 3 MHz. Hence $f_{S\text{-}H}$ is quite close to the theoretical minimum value (i.e., $f_{S\text{-}H} = 3.3 \cdot f_{O\text{-}Max}$). The sequence of duty

cycle values that the multi-phase buck converter requires to reproduce the communication signal (i.e., $d_H(t)$) is stored in the FPGA that controls the two-phase buck converter.

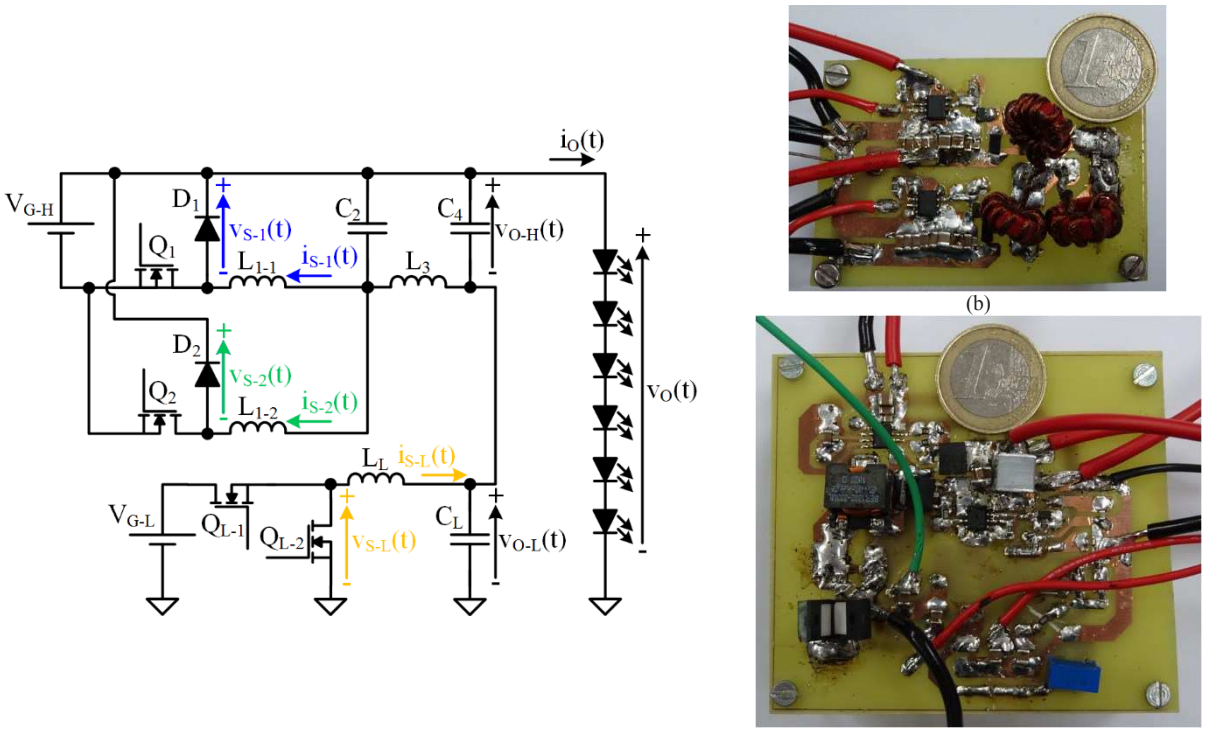

Fig. 3.19. Two-phase buck converter with 4th order Butterworth filter in output-series connection with a synchronous buck converter: (a) Schematic circuit of the implemented HB-LED driver. (b) Two-phase buck converter prototype. (c) Synchronous buck converter prototype.

TABLE III.I. PASSIVE COMPONENTS USED FOR THE OUTPUT FILTERS IMPLEMENTATIONS.

Component	L_{1-1} (nH)	L_{1-2} (nH)	C_2 (nF)	L_3 (nH)	C_4 (nF)	L_L (µH)	C_L (µF)
Value	812	812	9.4	287.1	2.3	33	1.818

3.3.5.2 Evaluation of the Trade-Off between Communication Efficiency and Power Efficiency

The HB-LED driver prototype is tested under different operating conditions in order to deeply evaluate its performance. The test target is to study how the lighting level and the communication signal power affect both the power efficiency and the communication efficiency. Obviously, the lighting level depends on the average current through the HB-LED string (i.e., i_{O-DC}). Regarding the communication signal power, it can be controlled by adjusting the peak to peak value of $v_O(t)$ (i.e., v_{O-PP}).

Two lighting levels (determined by i_{O-DC} = 300 mA and i_{O-DC} = 500 mA) and two levels of the communication signal power (determined by v_{O-PP} = 4.1 V and v_{O-PP} = 2.2 V) are considered. As a result, there are four possible situations (see Table III.II). It is important to note that the distance between the transmitter and the receiver is 20 cm in all situations. Fig. 3.20 exemplifies the performed test and facilitates the understanding of the reasoning that will appear along this section.

Fig. 3.21 shows the main waveforms of the VLC system for each situation. Note that $v_{RX}(t)$ is the receiver signal. The DC component of $v_{RX}(t)$ (v_{RX-DC}) measures the lighting level while the peak to peak value (v_{RX-PP}) is determined by the received communication signal power. Table III.II indicates both the DC component and the peak to peak value

TABLE III.II. MAIN PARAMETERS OF THE TEST PERFORMED TO EVALUATE THE TRADE-OFF BETWEEN COMMUNICATION EFFICIENCY AND POWER EFFICIENCY.

	$i_{O\text{-}DC}$ (mA)	$i_{O\text{-}PP}$ (mA)	$v_{O\text{-}DC}$ (V)	$v_{O\text{-}PP}$ (V)	$v_{O\text{-}L}$ (V)	$v_{RX\text{-}DC}$ (mV)	$v_{RX\text{-}PP}$ (mV)	$P_{O\text{-}L}$ (W)	$P_{O\text{-}H}$ (W)	P_O (W)	η_L (%)	η_H (%)	η (%)	EVM_{RMS} (%)
Situation 1	500	750	19.9	4.1	16.1	34	29	8.19	1.24	10.1	92.8	79.2	91.3	22.3
Situation 2	300	575	19	4.1	15.2	23	25	4.64	1.23	5.87	89.7	84.5	88.6	27.6
Situation 3	500	350	19.9	2.2	18.2	34	15	9.56	0.52	10.08	94.8	75.7	93.6	23.2
Situation 4	300	300	19	2.2	17.3	23	15	5.31	0.51	5.82	92.4	81.3	91.3	24

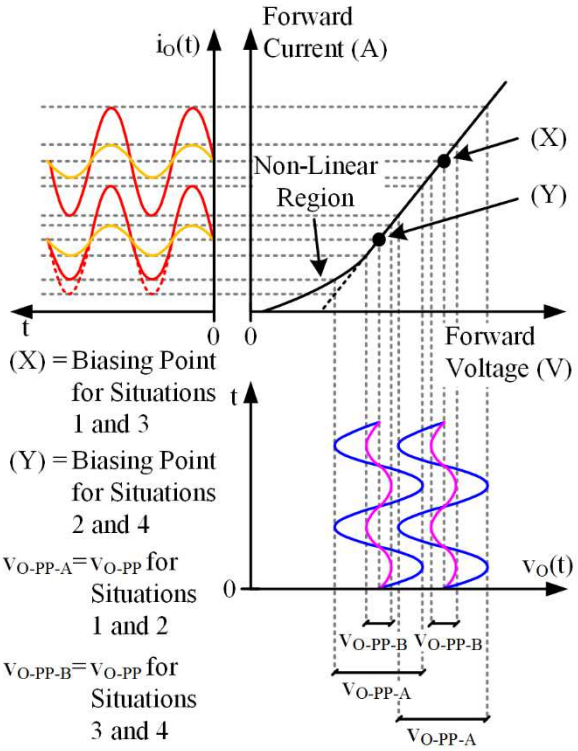

Fig. 3.20. Graphical description of the test considering the I-V curve of the HB-LED string and cosine waveforms.

of each waveform. Note that $i_{O\text{-}PP}$ is the peak to peak value of $i_O(t)$. In addition, it shows the amount of power delivered by the two-phase buck converter ($P_{O\text{-}H}$) and by the synchronous buck converter ($P_{O\text{-}L}$), the efficiency of the two-phase buck converter (η_H), the efficiency of the synchronous buck converter (η_L), the overall efficiency (η) and a figure-of-merit for evaluating the communication efficiency that will be introduced below.

In situation 1, $i_{O\text{-}DC}$ and $v_{O\text{-}PP}$ are 500 mA and 4.1 V, respectively. Note that as indicated in Section 2.1, $v_{O\text{-}AC}(t)$ is small in comparison to $v_{O\text{-}DC}$. It can be seen that most of $v_{O\text{-}DC}$ is delivered by the synchronous buck converter. In this situation, the power of the HB-LED driver is 10.1 W, the 81% of the power is provided by the synchronous buck converter and the overall efficiency is 91.3%.

Comparing situation 2 to situation 1 allows us to study the impact of decreasing the lighting level on the power efficiency of the HB-LED driver ($i_{O\text{-}DC}$ falls from 500 mA to 300 mA). In order to achieve the lower biasing point, the synchronous buck converter decreases its output voltage and, as a result, the amount of power delivered by this PWM-SMPC falls. It is important to note that since the communication signal power is the same, the peak to peak values of the waveforms are the same as in situation 1 and, consequently, the operating conditions of the two-phase

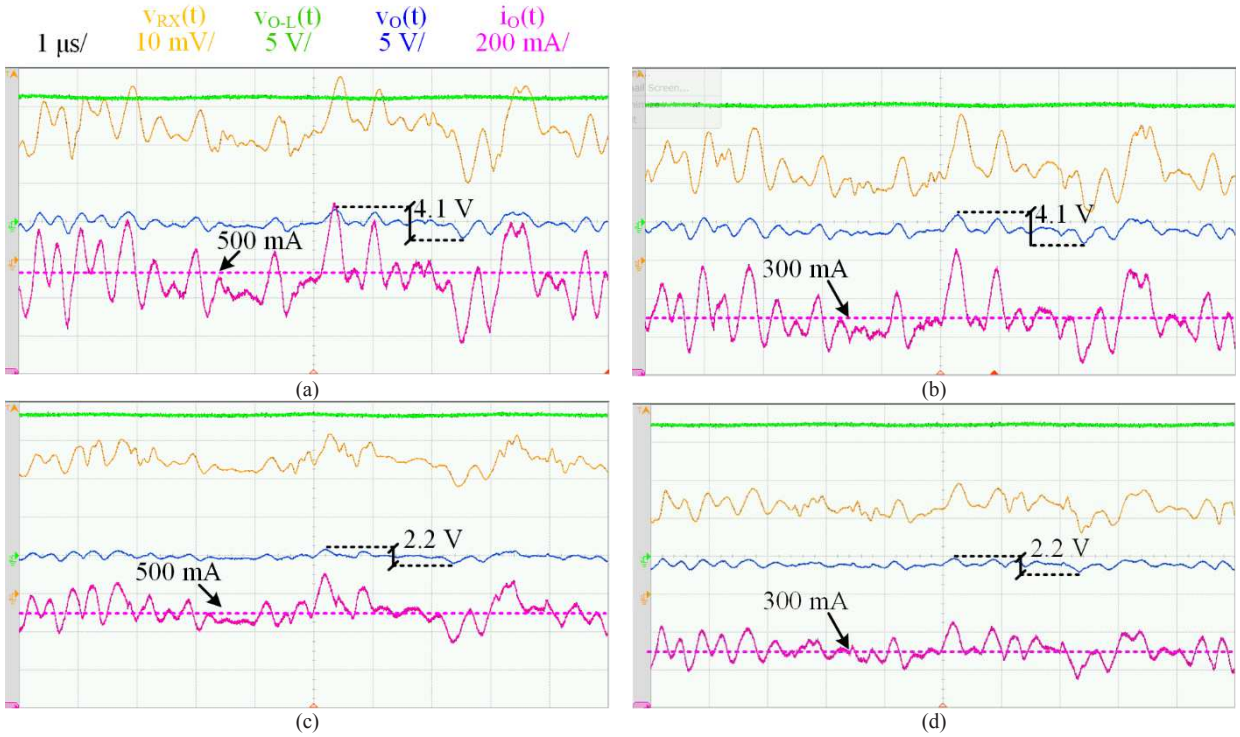

Fig. 3.21. Main experimental waveforms of the VLC system during the test performed to evaluate the trade-off between communication efficiency and power efficiency: (a) Situation 1. (b) Situation 2. (c) Situation 3. (d) Situation 4.

buck converter are almost the same. Actually, $i_{O\text{-}PP}$ and $v_{RX\text{-}PP}$ slightly change because the transmitter partially works in the non-linear region of the HB-LED string. It can be easily understood seeing Fig. 3.20. How this fact affects the communication will be addressed below. Taking into account all these considerations, the weight of the synchronous buck efficiency on the overall efficiency is lower in situation 2 than in situation 1 and, consequently, the overall efficiency falls.

In order to study the impact of reducing the communication signal power on the power efficiency of the HB-LED driver, situation 3 can be compared to situation 1 ($v_{O\text{-}PP}$ falls from 4.1 V to 2.2 V). All the peak to peak values of the waveforms change while the values of $i_{O\text{-}DC}$, $v_{O\text{-}DC}$ and $v_{RX\text{-}DC}$ are the same as in situation 1. However, it is important to note that the output voltage of the synchronous buck converter is higher in the case of situation 3. It is because the AC voltage provided by the two-phase buck converter is lower in this situation, so its DC voltage is reduced to minimize the power that it delivers. Consequently, the synchronous buck converter increases its output voltage to achieve the desired lighting level. As Table III.II shows, the total power of the HB-LED driver is almost the same in situation 1 and in situation 3, but the power share is different. It can be seen that in situation 3, the power provided by the synchronous buck converter (94.8% of the total power) is higher than in situation 1 and, as a result, the overall efficiency rises.

Finally, the remaining case appears in situation 4, where both the lighting level and the communication signal power fall ($i_{O\text{-}DC}$ falls from 500 mA to 300 mA and $v_{O\text{-}PP}$ falls from 4.1 V to 2.2 V). In this situation, the power of the HB-LED driver is 5.82 W, the synchronous buck converter delivers the 91.2% of the total power and the overall efficiency is 91.3%.

Fig. 3.22 shows an estimation of the losses distributed in the components of the experimental prototype for each operating situation. It can be seen that although $P_{O\text{-}H}$ is much lower than $P_{O\text{-}L}$ in all operating situations (see Table III.II), the semiconductor switching losses of the two-phase buck converter is one of the major sources of power losses.

In summary, minimizing the communication signal power and maximizing the lighting level is the best strategy for achieving the highest power efficiency. This conclusion fits in with the efficiency of the PWM-SMPCs because the strategy leads to minimize the power delivered by the multi-phase buck converter and to maximize the power delivered by the synchronous buck converter. In this way, the overall efficiency of the HB-LED driver is mainly determined by the efficiency of the synchronous buck converter.

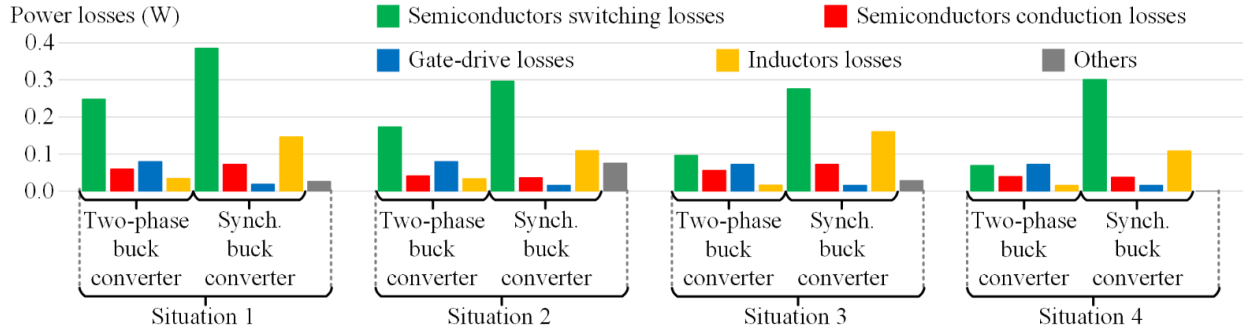

Fig. 3.22. Estimation of the power losses distribution in the components of the experimental VLC transmitter for each operating situation.

However, the impact of both the lighting level and the communication signal power on the communication efficiency must also be evaluated to show a more general vision of the VLC transmitter performance. Basically, the communication efficiency depends on two parameters: the distortion and the power of the received signal. In general, the higher the power of the received signal, the higher the communication efficiency because the signal can be demodulated easier. Obviously, the higher the signal distortion, the lower the communication efficiency.

The error vector ($\bar{e}$) is employed to measure the accuracy of the communications system:

$$\bar{e} = \bar{W} - \bar{V}, \tag{3.25}$$

where $\bar{W}$ is the received symbol and $\bar{V}$ is the ideal symbol. Note that a symbol is a vector whose magnitude and direction are determined by the amplitude and the phase of a certain cosine waveform. The modulation scheme defines the possible symbols (i.e., the amplitude and phase combinations that the cosine waveform can have) and the bit sequence that univocally identify each one. In this way, the transmission of a particular symbol leads to the transmission of a particular bit sequence and, consequently, the transmission of information. The reproduced 64-QAM-OFDM scheme is made up of several carriers (i.e., cosine waveforms with different frequencies), and each one transmits a symbol (i.e., each one has a particular amplitude and a particular phase) during a certain time interval which is referred as symbol period (see Chapter 1). The $\bar{e}$ calculation is used to evaluate the performance of the communication system by evaluating the Root Mean Square value of the Error Vector Magnitude (EVM_{RMS}) [3.23]. This widely used figure-of-merit evaluates $\bar{e}$ for each carrier during a sequence of several symbol periods considering the average power of the involved symbols:

$$EVM_{RMS} = \sqrt{\frac{\sum_{i=1}^{NSP}\sum_{j=1}^{N}|\overline{e_{i,j}}|^2}{\sum_{i=1}^{NSP}\sum_{j=1}^{N}|\overline{V_{i,j}}|^2}}, \tag{3.26}$$

where NSP is the Number of Symbol Periods and N is the number of carriers. The lower the EVM_{RMS} value, the higher the communication efficiency. Typically, a value around 5%-15% is required to fulfill the requirements of commercial wireless communication systems. Table III.II shows the EVM_{RMS} value obtained in each situation. It can be seen that

the measured values do not accomplish with the communication standards. However, as will be explained in the following section, this issue can be solved by adjusting the communication speed to the particular communication scenario where the VLC system is evaluated.

The best result is obtained when $i_{O\text{-}DC}$ is 500 mA and $v_{O\text{-}PP}$ is 4.1 V (i.e., situation 1). If the lighting level is considerably reduced (i.e., the situation changes from 1 to 2), EVM_{RMS} rises dramatically although the communication signal power is the same. The reason is that the HB-LED string must be operating in the current-voltage linear region to properly reproduce the communication signal. However, $v_{O\text{-}PP}$ is too high for the $i_{O\text{-}DC}$ value considered in situation 2 (Fig. 3.20 may help to understand this phenomena). Thus, the HB-LEDs operate close to $V_{\gamma\text{-}I}$, where the non-linear current-voltage relation causes high signal distortion. Then, the communication signal power should be reduced when considering the lighting level of situation 2 in order to avoid the non-linear region. In this way, EVM_{RMS} can be improved by reducing $v_{O\text{-}PP}$. It is equivalent to move from situation 2 to situation 4. It can be seen that, as expected, EVM_{RMS} is lower than in the case of situation 2 because it reduces the distortion caused by the non-linear operation. However, since the communication signal power is lower than in the case of situation 1, EVM_{RMS} is not as low as in that situation. Finally, EVM_{RMS} can be reduced a bit by increasing the lighting level (i.e., moving from situation 4 to situation 3) in order to completely avoid the non-linear operation.

As a conclusion, there is trade-off between power efficiency and communication efficiency. For a particular lighting level, the communication signal power must be the maximum possible without operating in the non-linear region in order to maximize the communication efficiency. However, from the power efficiency perspective, the best results are obtained when the communication signal power is minimized.

3.3.5.3 Evaluation of the Communication Capability

The reproduced 64-QAM-OFDM scheme is made up of 29 carriers. The lowest carrier frequency and the highest carrier frequency are 200 kHz and 3 MHz, respectively. Each carrier provides a bit rate equal to 600 kbps and, consequently, the maximum bit rate achieved by this modulation scheme is 17.4 Mbps. However, the speed of the communication signal must be evaluated together with EVM_{RMS} in order to show a consistent result. It is important to note that, in general, the higher the communications speed, the higher the number of transmission errors. However, the actual values of these two parameters depend on the communication scenario, which, in addition, changes over time. One of the advantages of OFDM schemes is that the communication speed can be dynamically adjusted to reduce EVM_{RMS}. This is performed by deactivating the carriers that are causing more transmission errors.

Fig. 3.23 shows the measured relationship between EVM_{RMS} and bit rate when the VLC system is evaluated in the laboratory setup and it operates in situation 1. It can been seen that EVM_{RMS} is too high for the maximum speed. Therefore, for this particular communication scenario, a bit rate lower than 7.5 Mbps should be used to accomplish with most extended communication standards (i.e., $EVM_{RMS} \leq 15\%$).

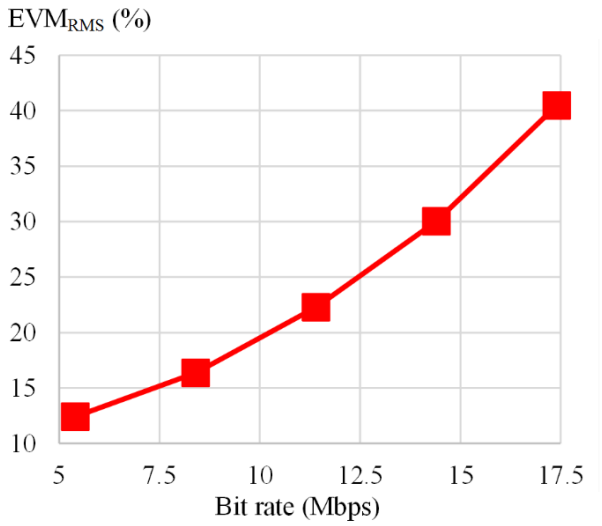

Fig. 3.23. EVM_{RMS} for different bit rates when the VLC system is evaluated in the laboratory setup and it operates in the situation 1.

3.3.5.4 Feedback Loop Tests

Several tests were carried out in order to check the feedback loop behavior of the implemented HB-LED driver. Fig. 3.24(a) shows how the synchronous buck converter reduces its output voltage in order to compensate the fall of $V_{\gamma\text{-}I}$ with T_J. Thus, both $i_{O\text{-}DC}$ and $i_{O\text{-}PP}$ remain constant over time. Note that for this test, the HB-LEDs heat sink was removed to see a considerable change during a short period of time.

Fig. 3.24(b) shows the results when two changes in the communication signal power are performed. When the increase of the communication signal power occurs, the two-phase buck increases not only the AC component of its output voltage, but also the DC component. Remember that the DC component of the two-phase buck converter output voltage is adjusted to provide the minimum value that enables the reproduction of the AC component. As a consequence, the synchronous buck converter reduces its output voltage to compensate the change.

Finally, Fig. 3.24(c) shows the results when two changes in the lighting level are performed. It can be seen how the synchronous buck converter modifies its output voltage to track the desired lighting level.

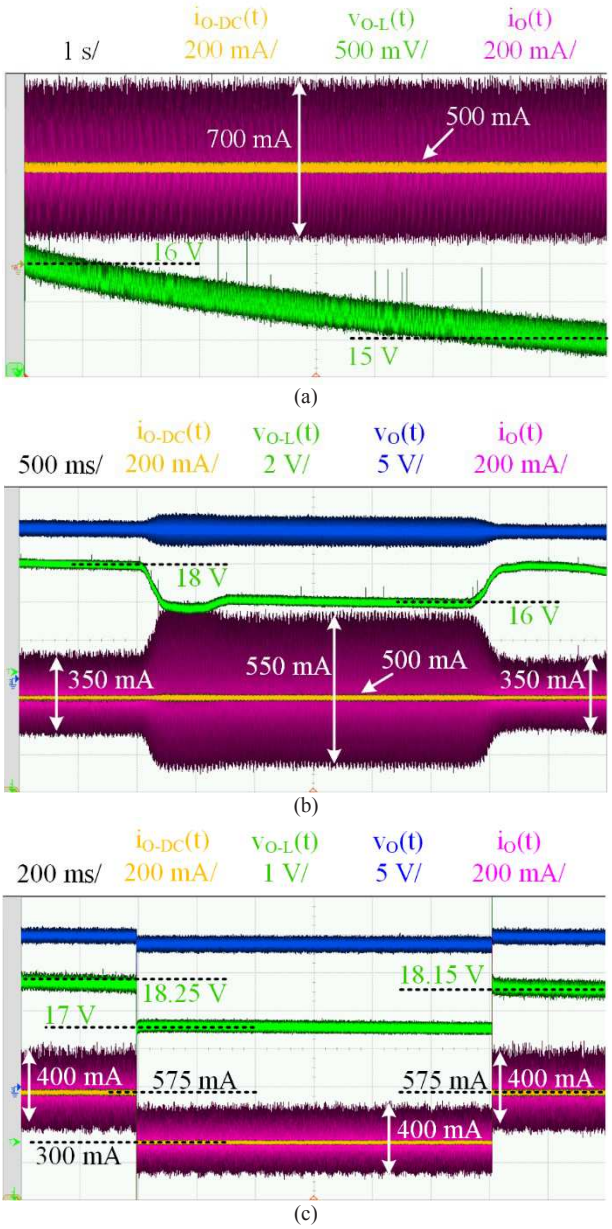

Fig. 3.24. Main experimental waveforms of the VLC system during the feedback loop tests: (a) Compensation of the $V_{\gamma\text{-}I}$ fall with T_J. (b) Response to two changes of the communication signal power. (c) Response to two changes of the lighting level.

3.4 Conclusion

The multi-phase structure, the floating structure and the high order filter are three strategies very interesting for being used in the HB-LED driver of a VLC transmitter. They allow us to reduce the required switching frequency, which is translated into a higher power efficiency and an easier implementation. Furthermore, the floating structure can be used to minimize the power processed with high switching frequency, which increases the power efficiency even more. In addition, this structure also facilitates the reproduction of the communication signal since it increases the operating range of the duty cycle with respect to a conventional buck converter. The proposed HB-LED driver for VLC takes advantage of all these benefits because it is a floating multi-phase buck converter with high order output filter. Moreover, the constant voltage source that is connected in series with the output of the multi-phase buck converter is provided by a synchronous buck converter that enables the dimming capability.

The joint operation of both PWM-SMPCs is studied, focusing the attention on the multi-phase effect, the high order output filter effect and the impact of each PWM-SMPC on the other. It is concluded that the multi-phase structure supports the filtering task by reducing the output voltage ripple, whereas high Q factors of the synchronous buck converter filter are desirable for reducing the signal distortion. Moreover, the multi-phase buck converter has minor impact on the synchronous buck operation and, consequently, its design is similar to conventional HB-LED drivers for lighting applications.

The wide experimental section allows us to analyze the trade-off that exists between communication efficiency and power efficiency. The key point is that for a particular lighting level, the power efficiency falls when the communication signal power rises. However, from the communication perspective, the communication signal power must be the maximum possible without operating in the non-linear region.

In summary, it is demonstrated that the proposed architecture is good approach for alleviating the two main problems that appear when a PWM-SMPC is considered for driving the HB-LEDs of a VLC transmitter: the issues caused by the high switching frequency that is required in order to provide the demanded bandwidth, and the high duty cycle accuracy that is required for reproducing the communication signal.

3.5 References

[3.1] J. Rodríguez, D. G. Lamar, D. G. Aller, P. F. Miaja and J. Sebastián, “Efficient visible light communication transmitters based on switching-mode dc-dc converters,” in Sensors, vol. 18, no. 4, 2018.

[3.2] W. Chen, “High efficiency, high density, polyphase converters for high current applications,” Linear Technology Corporation, Sept. 1999 [Online]. Available: http://www.linear.com/pc/downloadDocument.do?navId=H0,C1,C1003,C1042,C1032,C1062,P1726,D4166

[3.3] X. Zhou, P. L. Wong, P. Xu, F. C. Lee and A. Q. Huang, “Investigation of candidate VRM topologies for future microprocessors,” in IEEE Transactions on Power Electronics, vol. 15, no. 6, pp. 1172-1182, Nov 2000.

[3.4] X. Zhou, P. Xu and F. C. Lee, “A novel current-sharing control technique for low-voltage high-current voltage regulator module applications,” in IEEE Transactions on Power Electronics, vol. 15, no. 6, pp. 1153-1162, Nov 2000.

[3.5] A. Soto, J. A. Oliver, J. A. Cobos, J. Cezon and F. Arevalo, “Power supply for a radio transmitter with modulated supply voltage,” Applied Power Electronics Conference and Exposition. APEC '04. Nineteenth Annual IEEE, vol. 1, pp. 392-398, 2004.

[3.6] M. C. W. Hoyerby and M. E. Andersen, “High-bandwidth, high-efficiency envelope tracking power supply for 40W RF power amplifier using paralleled bandpass current sources,” 2005 IEEE 36th Power Electronics Specialists Conference, Recife, pp. 2804-2809, 2005.

[3.7] O. Garcia, A. de Castro, A. Soto, J. A. Oliver, J. A. Cobos and J. Cezon, “Digital control for power supply of a transmitter with variable reference,” Twenty-First Annual IEEE Applied Power Electronics Conference and Exposition, 2006. APEC '06., Dallas, TX, pp. 6 pp.-, 2006.

[3.8] P. Cheng, M. Vasić, O. García, J. Á. Oliver, P. Alou and J. A. Cobos, “Minimum time control for multiphase buck converter: analysis and application,” in IEEE Transactions on Power Electronics, vol. 29, no. 2, pp. 958-967, Feb. 2014.

[3.9] J. Sebastián, P. Fernández-Miaja, F. J. Ortega-González, M. Patiño and M. Rodríguez, "Design of a two-phase buck converter with fourth-order output filter for envelope amplifiers of limited bandwidth," in IEEE Transactions on Power Electronics, vol. 29, no. 11, pp. 5933-5948, Nov. 2014.

[3.10] P. F. Miaja, A. Rodríguez and J. Sebastián, "Buck-derived converters based on gallium nitride devices for envelope tracking applications," in IEEE Transactions on Power Electronics, vol. 30, no. 4, pp. 2084-2095, April 2015.

[3.11] Y. Zhang, M. Rodríguez and D. Maksimović, "Output filter design in high-efficiency wide-bandwidth multi-phase buck envelope amplifiers," 2015 IEEE Applied Power Electronics Conference and Exposition (APEC), Charlotte, NC, pp. 2026-2032, 2015.

[3.12] Y. Zhang, J. Strydom, M. de Rooij and D. Maksimović, "Envelope tracking GaN power supply for 4G cell phone base stations," 2016 IEEE Applied Power Electronics Conference and Exposition (APEC), Long Beach, CA, pp. 2292-2297, 2016.

[3.13] M. C. W. Hoyerby and M. A. E. Andersen, "Ultrafast tracking power supply with fourth-order output filter and fixed-frequency hysteretic control," in IEEE Transactions on Power Electronics, vol. 23, no. 5, pp. 2387-2398, Sept. 2008.

[3.14] A. Garcia i Tormo, A. Poveda, E. Alarcon and F. Guinjoan, "Design-oriented characterization of adaptive asynchronous ΣΔ modulation switching power amplifiers for bandlimited signals," 2009 IEEE International Symposium on Circuits and Systems, Taipei, pp. 2882-2885, 2009.

[3.15] J. Sebastián, P. Fernández-Miaja, A. Rodríguez and M. Rodríguez, "Analysis and design of the output filter for buck envelope amplifiers," in IEEE Transactions on Power Electronics, vol. 29, no. 1, pp. 213-233, Jan. 2014.

[3.16] P. F. Miaja, J. Sebastián, R. Marante and J. A. García, "A linear assisted switching envelope amplifier for a UHF polar transmitter," in IEEE Transactions on Power Electronics, vol. 29, no. 4, pp. 1850-1861, April 2014.

[3.17] M. Rodríguez, Y. Zhang and D. Maksimović, "High-frequency PWM buck converters using GaN-on-SiC HEMTs," in IEEE Transactions on Power Electronics, vol. 29, no. 5, pp. 2462-2473, May 2014.

[3.18] M. Rodríguez, P. Fernández-Miaja, A. Rodríguez and J. Sebastián, "A multiple-input digitally controlled buck converter for envelope tracking applications in radiofrequency power amplifiers," in IEEE Transactions on Power Electronics, vol. 25, no. 2, pp. 369-381, Feb. 2010.

[3.19] M. Vasic, O. Garcia, J. A. Oliver, P. Alou, D. Diaz and J. A. Cobos, "Multilevel power supply for high-efficiency RF amplifiers," in IEEE Transactions on Power Electronics, vol. 25, no. 4, pp. 1078-1089, April 2010.

[3.20] J. Rodriguez, D. G. Aller, D. G. Lamar and J. Sebastian, "Energy efficient visible light communication transmitter based on the split of the power," 2017 IEEE Energy Conversion Congress and Exposition (ECCE), Cincinnati, OH, pp. 217-224, 2017.

[3.21] J. Rodriguez, D. G. Aller, D. G. Lamar, and J. Sebastian, "Performance evaluation of a VLC transmitter based on the split of the power," 2018 IEEE Applied Power Electronics Conference and Exposition (APEC), San Antonio, TX, 2018.

[3.22] J. Rodriguez, D. G. Lamar, P. Fernandez Miaja, D. G. Aller and J. Sebastian, "Power efficient VLC transmitter based on pulse-width modulated DC-DC converters and the split of the power," in IEEE Transactions on Power Electronics.

[3.23] E. McCune, *Practical digital wireless signals*. Cambridge University Press, 2010.

Chapter 4:
The Ripple Modulation Technique

Using a PWM-SMPC is an interesting approach for driving the HB-LEDs of a VLC transmitter avoiding the use of a power inefficient LPA. However, the recommended topologies for enabling an affordable f_S and for fulfilling the required output voltage accuracy lead to quite complex designs. In this chapter, a novel approach that is especially conceived for VLC is presented. The idea is to use the output voltage ripple of a SMPC to reproduce the communication signal. This strategy allows us to reduce both the required f_S and the complexity of the power stage. The chapter describes in detail the ripple modulation technique by studying different points: the operating principle of the driver that is proposed for using the output voltage ripple, how to reproduce both SCM and MCM schemes, the control system required for applying the technique, etc.

4.1 Introduction

As was shown in Chapter 2, using PWM-SMPCs for driving the HB-LEDs of a VLC transmitter is a promising approach for avoiding the efficiency problem of LPAs. According to Chapter 3, complex topologies (several converters, several phases, isolated input voltages, high number of reactive elements, etc.) are mandatory to achieve the required output voltage accuracy and to exploit the entirely bandwidth provided by a conventional lighting HB-LED (i.e., reproducing communication signals with frequencies up to 3-5 MHz) by using an affordable f_S. However, the current trend is to overcome the bandwidth limitation of conventional lighting HB-LEDs by applying the techniques that are described in Section 1.3.3. In general, these techniques offer higher bit rates because they enable higher available bandwidths. As a result, the communication signals that must be reproduced to exploit the available bandwidths are faster than in the case of a conventional lighting HB-LED (i.e., $f_{O\text{-}Max}$ rises). Hence, using the complex topologies described in Chapter 3 could be not enough to achieve an affordable f_S. Remember that the prototype presented in Chapter 3 must use a f_S value 3.3 times higher than $f_{O\text{-}Max}$, and it could be impractical when $f_{O\text{-}Max}$ is higher than 3-5 MHz because of the switching losses, the required duty cycle accuracy, etc. Note that, for instance, if the available bandwidth is 20 MHz (as in the case of RGB HB-LEDs), the required f_S is 66 MHz. Even if a f_S value equal to the theoretical minimum one of a PWM-SMPC (i.e., $2 \cdot f_{O\text{-}Max}$ according to the Nyquist-Shannon sampling theorem) could be used, f_S would be quite high. Taking into account the previous facts, the logical step is to explore novel approaches different from PWM-SMPCs in order to reduce the ratio between the required f_S and maximum frequency that can be reproduced (i.e., $f_{O\text{-}Max}$).

4.2 Using the Ripple Modulation Technique for Reproducing SCM Schemes

In VLC, the variable voltage that the HB-LED driver must provide is not an unknown waveform. It is a communication signal and, consequently, it can be deeply characterized. It seems reasonable to think that a SMPC especially conceived for reproducing this particular variable voltage will provide better results than a SMPC able to reproduce any kind of variable voltage. Therefore, the next step is to carefully study the variable voltage that the HB-LED driver for VLC must provide in order to reach a method for reducing f_S and the complexity of the power stage. This strategy will allow us to design a SMPC especially conceived to reproduce the variable voltage required by VLC. According to the previous reasoning, this new SMPC could offer better features than the PWM-SMPCs of Chapter 2 and 3, which can reproduce any kind of variable voltage within a range of frequencies and voltages.

The voltage characterization depends on the modulation scheme that is being reproduced. Since the objective is to reproduce advanced modulation schemes, SCM and MCM schemes are considered. For the sake of simplicity, the first target is to develop a SMPC especially conceived to reproduce SCM schemes. According to (1.10) and (2.3), $v_O(t)$ can be expressed in this way when a SCM scheme is reproduced:

$$v_{O-SCM}(t) = v_{O-DC} + A_{V-SCM}(t) \cdot cos\big(2 \cdot \pi \cdot f_{SCM} \cdot t + \phi_{V-SCM}(t)\big), \tag{4.1}$$

where $A_{V\text{-}SCM}(t)$ and $\phi_{V\text{-}SCM}(t)$ are the amplitude and the phase modulation of the voltage, respectively. Both components can be obtained from the amplitude and phase modulation of the light intensity:

$$A_{V-SCM}(t) = \frac{A_{S-SCM}(t)}{K_{S-V}}, \tag{4.2}$$

$$\phi_{V-SCM}(t) = \phi_{S-SCM}(t). \tag{4.3}$$

In summary, a HB-LED driver for VLC must provide a voltage that is made up a DC component (i.e., $v_{O\text{-}DC}$) and a cosine waveform that changes the amplitude and the phase over time in order to reproduce a SCM scheme. Hence, the HB-LED driver must be able to fulfill four requirements:

- Controlling $v_{O\text{-}DC}$ in order to properly bias the HB-LEDs.
- Generating a cosine waveform (i.e., the carrier of the SCM scheme).
- Controlling the amplitude of the cosine waveform in order to perform the amplitude modulation (i.e., $A_{V\text{-}SCM}(t)$).
- Controlling the phase of the cosine waveform in order to perform the phase modulation (i.e., $\phi_{V\text{-}SCM}(t)$).

The novel method that is proposed in this chapter is referred as Ripple Modulation (RM) technique and it meets the aforementioned requirements by using the output voltage ripple of a SMPC to reproduce the communication signal ([4.1]-[4.2]). The SMPCs that are based on the use of the RM technique are referred as RM-SMPC in this dissertation.

4.2.1 Using the 1st Switching Harmonic of a Synchronous Buck Converter with High Order Output Filter

A possible implementation of the RM technique could be the use of the 1st switching harmonic of the output voltage ripple. As a first approach, a synchronous buck converter with high order output filter is considered to implement the idea. Fig. 4.1 shows both the topology (see Fig. 4.1(a)) and the equivalent circuit after considering $v_S(t)$ as an ideal pulse voltage source (see Fig. 4.1(b)). Since the target is to use the 1st switching harmonic, the output filter design differs from the conventional one of a PWM-SMPC: the filter passes not only the DC component of $v_S(t)$, but also its 1st switching harmonic. Hence, f_C must be between f_S and $2 \cdot f_S$.

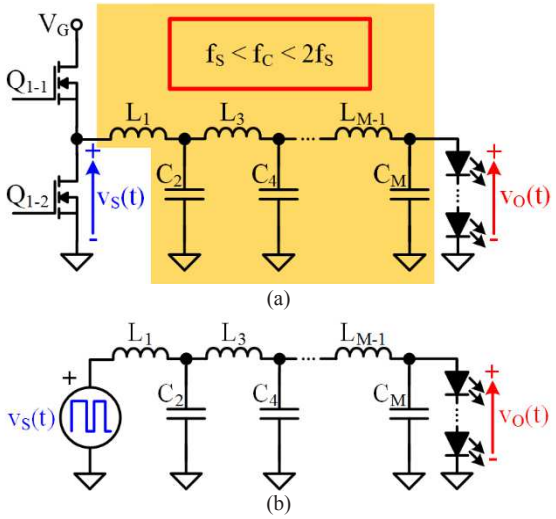

Fig. 4.1. Synchronous buck converter with a high order output filter that passes the DC component and the 1st switching harmonic of $v_S(t)$: (a) Topology. (b) Equivalent circuit after considering $v_S(t)$ as an ideal pulse voltage source.

Another major difference with respect to a conventional buck converter is that the proposed synchronous buck converter is not controlled by means of the PWM technique (i.e., it is not a PWM-SMPC). It is controlled by using a more complex technique that has been called Pulse-Width and Pulse-Phase Modulation (PWPPM) in this dissertation. It implies that not only the width of the pulse is controlled (i.e., d(t)), but also the position over the switching period. Fig. 4.2 shows an example of a pulse-width modulated voltage, and a pulse-width and pulse-phase modulated voltage. It is important to note that controlling the phase of the pulses is equivalent to control their position. The dimensionless parameter that is used to control the phase of a pulse will be noted as $\gamma(t)$ (see Fig. 4.2(b)), and it ranges between 0 and 1. When $\gamma(t)$ is 0, the pulse phase is 0º, and when $\gamma(t)$ is 1, the pulse phase is $-2\cdot\pi$. Therefore, the pulse phase is equal to $-2\cdot\pi\cdot\gamma(t)$ and, consequently, the center of the pulse appears $T_S\cdot\gamma(t)$ after the beginning of the switching period (see Fig. 4.2(b)). Note that the phase is determined by the center of the pulse. As will be demonstrated later, the use of the PWPPM technique and the proposed filter design enable the control of $\phi_V(t)$.

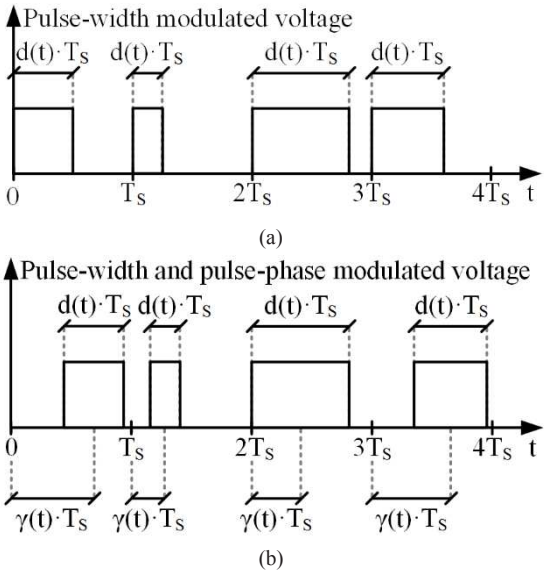

Fig. 4.2. Two strategies for controlling a SMPC: (a) Pulse-width modulation control. (b) Pulse-width and pulse-phase modulation control.

In order to reduce the mathematical complexity of the operating principle description, it is considered that d(t) and $\gamma(t)$ do not change over time (i.e., steady-state conditions). Then, $v_S(t)$ can be expressed as a function of its harmonics by using the Fourier analysis:

$$v_S(t) = d(t)\cdot V_G + \sum_{k=1}^{\infty} \frac{2\cdot V_G}{k\cdot\pi} sin(k\cdot\pi\cdot d(t))\cdot cos(k\cdot 2\cdot\pi\cdot f_S\cdot t - k\cdot 2\cdot\pi\cdot\gamma(t)). \quad (4.4)$$

Taking into account the proposed filter design that was previously described, $v_O(t)$ is equal to the DC component plus the 1st switching harmonic of $v_S(t)$ with a certain delay (t_{Fil}) due to the nature of the filter (note that this delay does not imply any negative effect for the communication):

$$v_O(t + t_{Fil}) = v_{O-DC} + A_V(t)\cdot cos\big(2\cdot\pi\cdot f_S\cdot t + \phi_V(t)\big), \quad (4.5)$$

$$v_{O-DC} = d(t)\cdot V_G, \quad (4.6)$$

$$A_V(t) = \frac{2 \cdot V_G}{\pi} sin(\pi \cdot d(t)), \tag{4.7}$$

$$\phi_V(t) = -2 \cdot \pi \cdot \gamma(t), \tag{4.8}$$

where $v_{O\text{-}DC}$, $A_V(t)$ and $\phi_V(t)$ are the bias voltage, the amplitude and the phase of the cosine waveform, respectively.

According to (4.5)-(4.8), and as Fig. 4.3 shows, $A_V(t)$ and $\phi_V(t)$ can be controlled by using d(t) and $\gamma(t)$, respectively. The problem is that this approach does not enable the implementation of the desired HB-LED driver for a VLC transmitter because it is not able to control independently $A_V(t)$ and $v_{O\text{-}DC}$. Both $A_V(t)$ and $v_{O\text{-}DC}$ depend on d(t) and, consequently, only one of them can be adjusted properly. Therefore, a new design with a higher order of freedom to decouple $A_V(t)$ and $v_{O\text{-}DC}$ is needed.

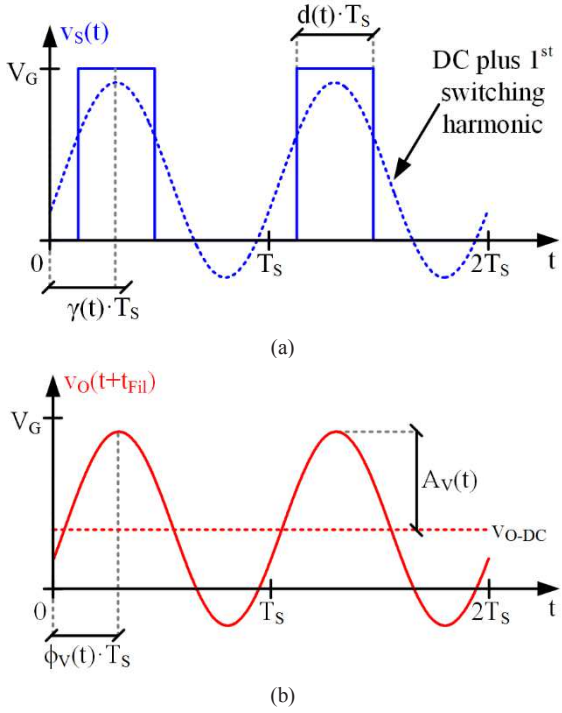

Fig. 4.3. Main voltage waveforms of the synchronous buck conceived to implement the RM technique: (a) Switch-node voltage highlighting the DC component plus the 1st switching harmonic. (b) Output voltage (note that the output voltage representation cancels the filter delay (i.e., t_{Fil}) to facilitate the understanding).

4.2.2 Using the 1st Switching Harmonic of a Two-Phase Synchronous Buck Converter with High Order Output Filter

As was explained in Section 4.2.1, the RM technique cannot be implemented successfully by using the 1st switching harmonic of a synchronous buck converter because $v_{O\text{-}DC}$ and $A_V(t)$ cannot be controlled independently. In order to solve that problem, the use of the 1st switching harmonic of a two-phase synchronous buck converter with high order output filter is studied in this section.

4.2.2.1 Summing Two Cosine Waveforms with Different Phases, the Cornerstone for controlling $A_V(t)$

The decision to use a two-phase buck converter for implementing the RM technique is because of a mathematical property that is explained in this section. Let us consider two cosine waveforms, $v_1(t)$ and $v_2(t)$, that have the same

amplitude (V) and frequency (f_V). The phases of both cosine waveforms are different and they can change over time ($-2\cdot\pi\cdot\gamma_1(t)$ and $-2\cdot\pi\cdot\gamma_2(t)$, respectively). Hence, these two cosine waveforms can be written as follows:

$$v_1(t) = V \cdot cos(2 \cdot \pi \cdot f_V \cdot t - 2 \cdot \pi \cdot \gamma_1(t)), \tag{4.9}$$

$$v_2(t) = V \cdot cos(2 \cdot \pi \cdot f_V \cdot t - 2 \cdot \pi \cdot \gamma_2(t)). \tag{4.10}$$

Although $\gamma_1(t)$ and $\gamma_2(t)$ can vary within 0 and 1, as it will be justified later, the maximum difference allowed between them is 0.5. In addition, it is assumed that $\gamma_2(t)$ is higher or equal to $\gamma_1(t)$. It is known that the sum of these two cosine waveforms is equal to a third cosine waveform that has the same frequency:

$$v_3(t) = v_1(t) + v_2(t) = 2 \cdot V \cdot cos(\pi \cdot \alpha(t)) \cdot cos(2 \cdot \pi \cdot f_V \cdot t - 2 \cdot \pi \cdot \beta(t)), \tag{4.11}$$

where $\alpha(t)$ is the phase-shift between $v_1(t)$ and $v_2(t)$ divided by $2\cdot\pi$, and $\beta(t)$ is the absolute value of the mean phase of $v_1(t)$ and $v_2(t)$ divided by $2\cdot\pi$ (i.e., the mean value of $\gamma_1(t)$ and $\gamma_2(t)$):

$$\alpha(t) = \frac{2 \cdot \pi \cdot \gamma_2(t) - 2 \cdot \pi \cdot \gamma_1(t)}{2 \cdot \pi} = \gamma_2(t) - \gamma_1(t), \tag{4.12}$$

$$\beta(t) = \frac{2 \cdot \pi \cdot \gamma_1(t) + 2 \cdot \pi \cdot \gamma_2(t)}{2 \cdot (2 \cdot \pi)} = \frac{\gamma_1(t) + \gamma_2(t)}{2}. \tag{4.13}$$

Note that both $\gamma_1(t)$ and $\gamma_2(t)$ can be expressed as a function of $\alpha(t)$ and $\beta(t)$ by manipulating (4.12) and (4.13):

$$\gamma_1(t) = \beta(t) - \frac{\alpha(t)}{2}, \tag{4.14}$$

$$\gamma_2(t) = \beta(t) + \frac{\alpha(t)}{2}. \tag{4.15}$$

According to (4.11), $\alpha(t)$ determines the amplitude of $v_3(t)$. When $\alpha(t)$ is 0 (i.e., the phase-shift is 0 radian), the maximum amplitude (i.e., $2\cdot V$) is reached. On the other hand, when $\alpha(t)$ is 0.5 (i.e., the phase-shift is π radian), the amplitude is 0 V. Then, the higher the phase-shift, the lower the amplitude of $v_3(t)$. It is important to note that when $\alpha(t)$ is higher than 0.5 (i.e., the phase-shift is higher than π radians), the sign of $\cos(\pi\cdot\alpha(t))$ changes. Therefore, it is stablished that $\alpha(t)$ must range between 0 and 0.5 limits in order to avoid the phase modification.

Considering (4.11), $\beta(t)$ determines the phase of $v_3(t)$. For instance, if the phases of $v_1(t)$ and $v_2(t)$ are $-\pi/4$ and $-3\cdot\pi/4$, respectively (i.e., $\gamma_1(t)$ and $\gamma_2(t)$ are equal to 1/8 and 3/8, respectively), the phase of $v_3(t)$ is $-\pi/2$ (i.e., $\beta(t)$ is equal to 1/4). Note that $\beta(t)$ can vary within 0 and 1.

Fig. 4.4(a) shows $v_3(t)$ for certain values of $\alpha(t)$ and $\beta(t)$ (i.e., $\alpha(t) = 0.3$ and $\beta(t) = 0.3$). Fig. 4.4(b) demonstrates that the amplitude of $v_3(t)$ rises as $\alpha(t)$ falls. On the other hand, Fig. 4.4(c) shows that the phase of $v_3(t)$ falls as $\beta(t)$ increases.

As a conclusion, any cosine waveform whose amplitude and phase must be independently controllable can be generated by summing two cosine waveforms with both the same amplitude and the same frequency. They key point is that the phases of these two cosine waveforms must be controlled independently.

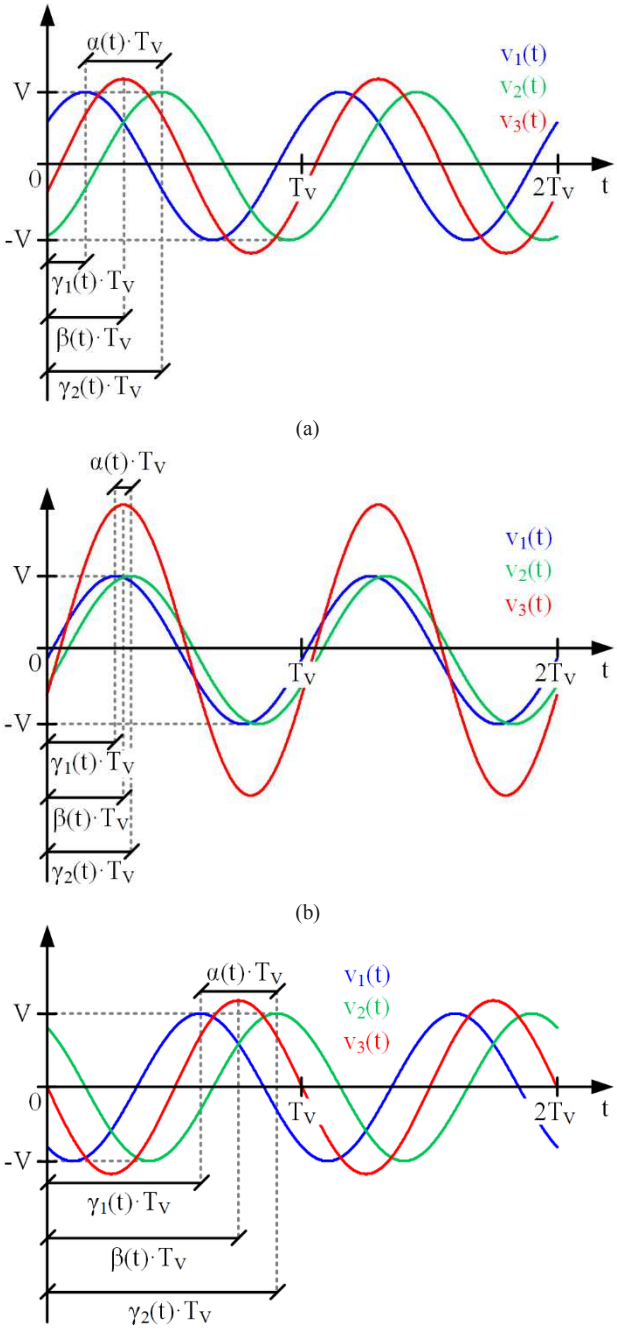

Fig. 4.4. Sum of two cosine waveforms with both the same amplitude and the same frequency but different phases: (a) Initial conditions: α(t) = 0.3 and β(t) = 0.3. (b) Effect of decreasing α(t): α(t) = 0.06 and β(t) = 0.3. (c) Effect of increasing β(t): α(t) = 0.3 and β(t) = 0.75.

Using a phasorial representation is an interesting approach for studying the sum of $v_1(t)$ and $v_2(t)$. Both cosine waveforms can be expressed as:

$$v_1(t) = Re\left\{V \cdot e^{j\cdot 2\cdot\pi\cdot f_V\cdot t} \cdot e^{-j\cdot 2\cdot\pi\cdot\gamma_1(t)}\right\}, \tag{4.16}$$

$$v_2(t) = Re\left\{V \cdot e^{j\cdot 2\cdot\pi\cdot f_V\cdot t} \cdot e^{-j\cdot 2\cdot\pi\cdot\gamma_2(t)}\right\}. \tag{4.17}$$

Therefore, the following two phasors can be defined to represent both cosine waveforms:

$$V_1(t) = V \cdot e^{-j\cdot 2\cdot\pi\cdot\gamma_1(t)}, \tag{4.18}$$

$$V_2(t) = V \cdot e^{-j\cdot 2\cdot\pi\cdot\gamma_2(t)}. \tag{4.19}$$

Note that the frequency component is not included in the definition for the sake of simplicity. Therefore, the relationship between the phasors and the cosine waveforms can be expressed as follows:

$$v_1(t) = Re\{V_1(t) \cdot e^{j\cdot 2\cdot\pi\cdot f_V\cdot t}\}, \tag{4.20}$$

$$v_2(t) = Re\{V_2(t) \cdot e^{j\cdot 2\cdot\pi\cdot f_V\cdot t}\}. \tag{4.21}$$

The phasor of $v_3(t)$ can be calculated by summing the $V_1(t)$ and $V_2(t)$:

$$V_3(t) = V_1(t) + V_2(t) = V \cdot \left(e^{-j\cdot 2\cdot\pi\cdot\gamma_1(t)} + e^{-j\cdot 2\cdot\pi\cdot\gamma_2(t)}\right). \tag{4.22}$$

Following (4.14) and (4.15), $\alpha(t)$ and $\beta(t)$ can be used instead of γ_1 (t) and $\gamma_2(t)$ for calculating $V_3(t)$:

$$\begin{aligned} V_3(t) = V \cdot \left(e^{-j\cdot 2\cdot\pi\cdot\left[\beta(t)-\frac{\alpha(t)}{2}\right]} + e^{-j\cdot 2\cdot\pi\cdot\left[\beta(t)+\frac{\alpha(t)}{2}\right]}\right) &= V \cdot e^{-j\cdot 2\cdot\pi\cdot\beta(t)} \cdot \left(e^{j\cdot\pi\cdot\alpha(t)} + e^{-j\cdot\pi\cdot\alpha(t)}\right) \\ &= 2 \cdot V \cdot cos(\pi \cdot \alpha(t)) e^{-j\cdot 2\cdot\pi\cdot\beta(t)}. \end{aligned} \tag{4.23}$$

The relationship between $V_3(t)$ and $v_3(t)$ can be expressed as follows:

$$\begin{aligned} v_3(t) = v_1(t) + v_2(t) &= Re\{V_1(t) \cdot e^{j\cdot 2\cdot\pi\cdot f_V\cdot t}\} + Re\{V_2(t) \cdot e^{j\cdot 2\cdot\pi\cdot f_V\cdot t}\} \\ &= Re\{V_1(t) \cdot e^{j\cdot 2\cdot\pi\cdot f_V\cdot t} + V_2(t) \cdot e^{j\cdot 2\cdot\pi\cdot f_V\cdot t}\} = Re\{[V_1(t) + V_2(t)] \cdot e^{j\cdot 2\cdot\pi\cdot f_V\cdot t}\} \\ &= Re\{V_3(t) \cdot e^{j\cdot 2\cdot\pi\cdot f_V\cdot t}\}. \end{aligned} \tag{4.24}$$

Fig. 4.5 shows the graphical description of the phasorial interpretation.

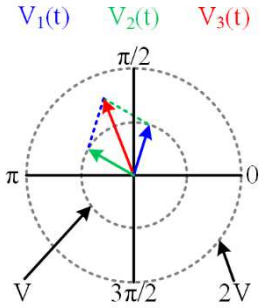

Fig. 4.5. Phasorial interpretation of the sum of two cosine waveforms that have the same amplitude and frequency, but different phases.

4.2.2.2 Operating Principle of the Proposed HB-LED Driver

Fig. 4.6 shows the two-phase synchronous buck converter that is proposed for reproducing a SCM scheme by using the 1st switching harmonic of the output voltage ripple. As in the case of the single-phase synchronous buck converter that is explained in Section 4.2.1, the output filter passes not only the DC component, but also the 1st

switching harmonic of the switch-node voltages (i.e., $v_{S\text{-}1}(t)$ and $v_{S\text{-}2}(t)$). Therefore, f_C must be higher than the 1st switching harmonic and lower than the second one (i.e., $f_S < f_C < 2 \cdot f_S$).

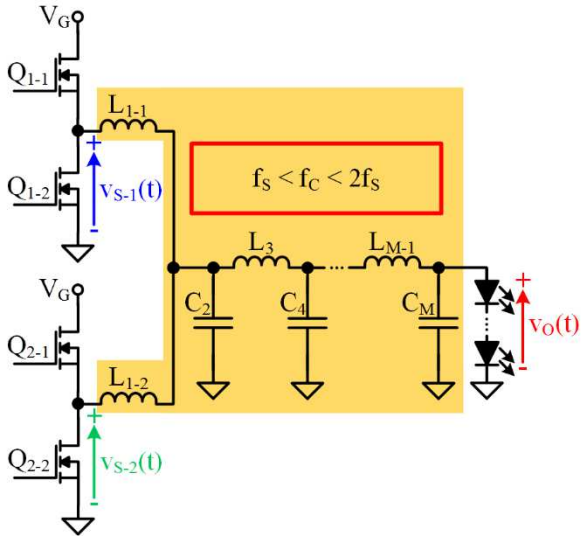

Fig. 4.6. Two-phase synchronous buck converter with a high order output filter that passes the DC component and the 1st switching harmonic of both $v_{S\text{-}1}(t)$ and $v_{S\text{-}2}(t)$.

This approach also uses the PWPPM technique instead of the PWM technique to control the SMPC. In this case, the duty cycle is the same for both phases of the converter (i.e., d(t)) while the phases (i.e., the pulses positions) are modulated independently (i.e., $\gamma_1(t)$ and $\gamma_2(t)$).

As will be seen in this section, the operation of the proposed two-phase synchronous buck converter is based on the mathematical property detailed in Section 4.2.2.1. This strategy will allow us to control independently $v_{O\text{-}DC}$, $A_V(t)$ and $\phi_V(t)$. The equivalent circuits depicted in Fig. 4.7 will support the explanation of how $A_V(t)$ and $\phi_V(t)$ can be controlled by modulating the phases (i.e., the positions) of $v_{S\text{-}1}(t)$ and $v_{S\text{-}2}(t)$. Since $v_{S\text{-}1}(t)$ and $v_{S\text{-}2}(t)$ are pulse voltage waveforms determined by the MOSFETs states ($Q_{1\text{-}1}$ and $Q_{1\text{-}2}$ in the case of $v_{S\text{-}1}(t)$, and $Q_{2\text{-}1}$ and $Q_{2\text{-}2}$ in the case of $v_{S\text{-}2}(t)$), they can be considered as ideal pulse voltage sources (see Fig. 4.7(a)).

In order to facilitate the understanding, it is considered that d(t), $\gamma_1(t)$ and $\gamma_2(t)$ do not change over time (i.e., steady-state conditions). Then, the switch-node voltages can be expressed as a function of their harmonics by using the Fourier analysis:

$$v_{S-1}(t) = d(t) \cdot V_G + \sum_{k=1}^{\infty} \frac{2 \cdot V_G}{k \cdot \pi} sin\big(k \cdot \pi \cdot d(t)\big) \cdot cos\big(k \cdot 2 \cdot \pi \cdot f_S \cdot t - k \cdot 2 \cdot \pi \cdot \gamma_1(t)\big), \tag{4.25}$$

$$v_{S-2}(t) = d(t) \cdot V_G + \sum_{k=1}^{\infty} \frac{2 \cdot V_G}{k \cdot \pi} sin\big(k \cdot \pi \cdot d(t)\big) \cdot cos\big(k \cdot 2 \cdot \pi \cdot f_S \cdot t - k \cdot 2 \cdot \pi \cdot \gamma_2(t)\big). \tag{4.26}$$

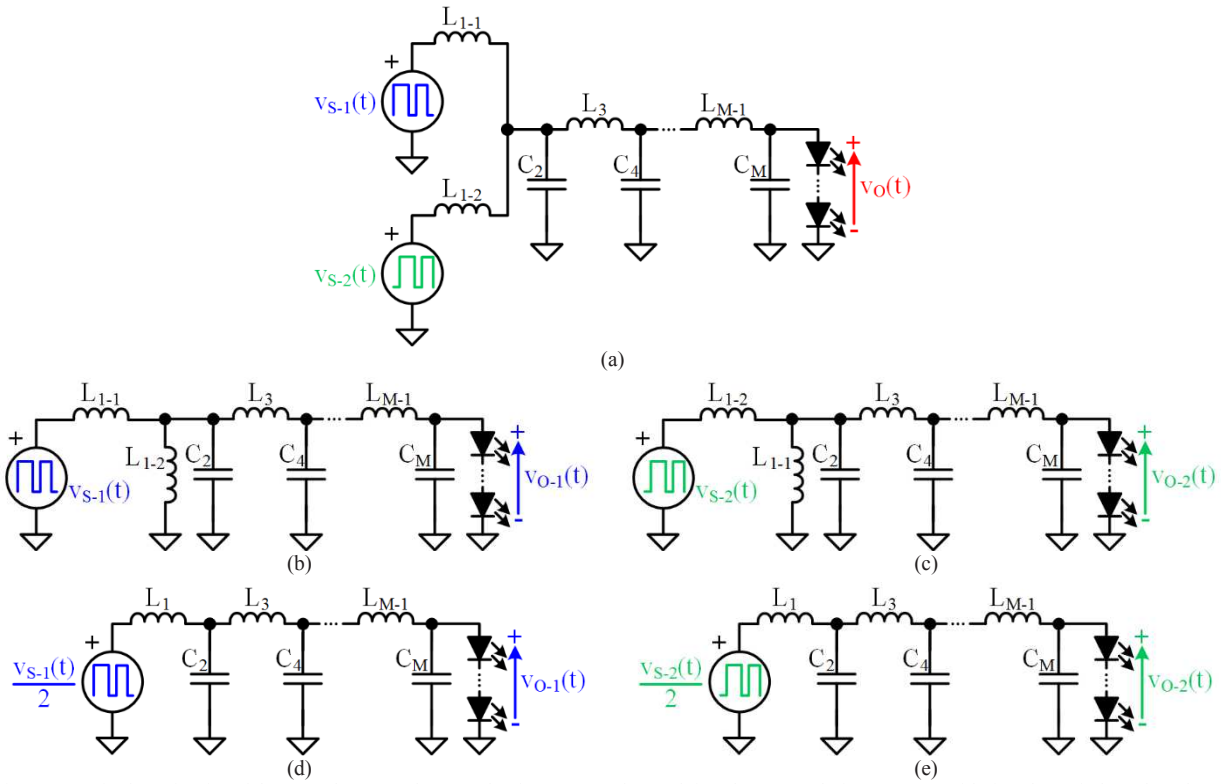

Fig. 4.7. Equivalent circuits of the two-phase synchronous buck converter for applying the RM technique: (a) Considering the switch-node voltages as ideal pulse voltage sources. (b)-(c) Applying the superposition theorem. (d)-(e) Applying the Thevenin's theorem.

The superposition theorem allows us to calculate $v_O(t)$ by analyzing the voltage contribution of each phase (see Fig. 4.7(b)-(c)):

$$v_O(t) = v_{O-1}(t) + v_{O-2}(t). \tag{4.27}$$

where $v_{O-1}(t)$ and $v_{O-2}(t)$ are the voltages provided by phases 1 and 2, respectively. The circuits depicted in Fig. 4.7(d)-(e) can be obtained by considering that the phase inductors (i.e., L_{1-1} and L_{1-2}) are equal and by applying the Thevenin's theorem. These circuits consider the switch-node voltages divided by two and applied to a low-pass filter, where the equivalent first inductor (L_1) is half the phase inductor (i.e., $L_1=0.5 \cdot L_{1-1}$). The voltage contribution of each phase of the converter can be calculated by taking into account that the filter passes the DC component and the 1st switching harmonic, the delay introduced by the filter and (4.25)-(4.26):

$$v_{O-1}(t + t_{Fil}) = \frac{d(t) \cdot V_G}{2} + \frac{V_G}{\pi} sin\big(\pi \cdot d(t)\big) \cdot cos\big(2 \cdot \pi \cdot f_S \cdot t - 2 \cdot \pi \cdot \gamma_1(t)\big), \tag{4.28}$$

$$v_{O-2}(t + t_{Fil}) = \frac{d(t) \cdot V_G}{2} + \frac{V_G}{\pi} sin\big(\pi \cdot d(t)\big) \cdot cos\big(2 \cdot \pi \cdot f_S \cdot t - 2 \cdot \pi \cdot \gamma_2(t)\big). \tag{4.29}$$

Substituting (4.28)-(4.29) into (4.27) and using $\alpha(t)$ and $\beta(t)$ instead of $\gamma_1(t)$ and $\gamma_2(t)$ allow us to expresses $v_O(t)$ in the following way:

$$v_O(t + t_{Fil}) = d(t) \cdot V_G + \frac{2 \cdot V_G}{\pi} sin\big(\pi \cdot d(t)\big) \cdot cos\big(\pi \cdot \alpha(t)\big) \cdot cos\big(2 \cdot \pi \cdot f_S \cdot t - 2 \cdot \pi \cdot \beta(t)\big). \tag{4.30}$$

Similarly to Section 4.2.2.1, $\alpha(t)$ and $\beta(t)$ can be used to control the $A_V(t)$ and the $\phi_V(t)$, respectively. Now, $\alpha(t)$ is the dimensionless parameter that determines the phase-shift between the pulses (i.e., the position difference) and, consequently, $A_V(t)$. Moreover, $\beta(t)$ determines the average phase of the pulses (i.e., the average position) and, as a result, $\phi_V(t)$. Fig. 4.8 shows the main voltage waveforms involved in the process.

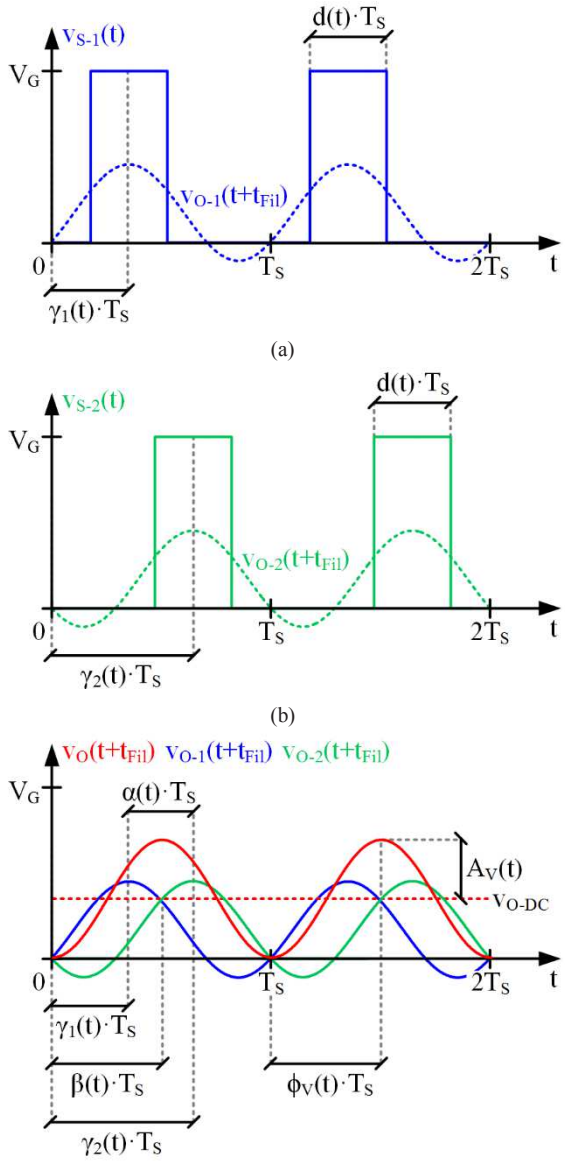

Fig. 4.8. Main voltage waveforms of the two-phase synchronous buck converter conceived for applying the RM technique. Note that the output voltage representations cancel the filter delay (i.e., t_{Fil}) to facilitate the understanding: (a) Switch-node voltage of phase 1 and output voltage component that it provides. (b) Switch-node voltage of phase 2 and output voltage component that it provides. (c) Graphical calculation of the output voltage from the components provided by each phase.

As a conclusion, the RM technique implemented with a two-phase synchronous buck converter with high order output filter fulfills all the requirements indicated in Section 4.2. This approach allows us to provide an output voltage that is made up of a DC component and an amplitude and phase modulated cosine waveform whose frequency is equal to f_S. Therefore, this approach can be used to reproduce SCM schemes in VLC. The following equations indicate the key terms:

$$v_{O-DC}(t) = d(t) \cdot V_G, \tag{4.31}$$

$$A_V(t) = \frac{2 \cdot V_G}{\pi} sin\big(\pi \cdot d(t)\big) \cdot cos\big(\pi \cdot \alpha(t)\big), \tag{4.32}$$

$$\phi_V(t) = -2 \cdot \pi \cdot \beta(t). \tag{4.33}$$

In order to exemplify the operation of the proposed two-phase synchronous buck converter, Fig. 4.9 shows the main voltage waveforms for different d(t), α(t) and β(t) values that are indicated in Table IV.I. In Fig. 4.9(b), a decrease of $A_V(t)$ is performed by increasing α(t). $\phi_V(t)$ is decreased in Fig. 4.9(c) by increasing β(t). Finally, $v_{O\text{-}DC}$ is increased in Fig. 4.9(d) by increasing d(t). Note that in the last case, since d(t) also affects $A_V(t)$ (see (4.32)), α(t) must be recalculated in order to not modify $A_V(t)$.

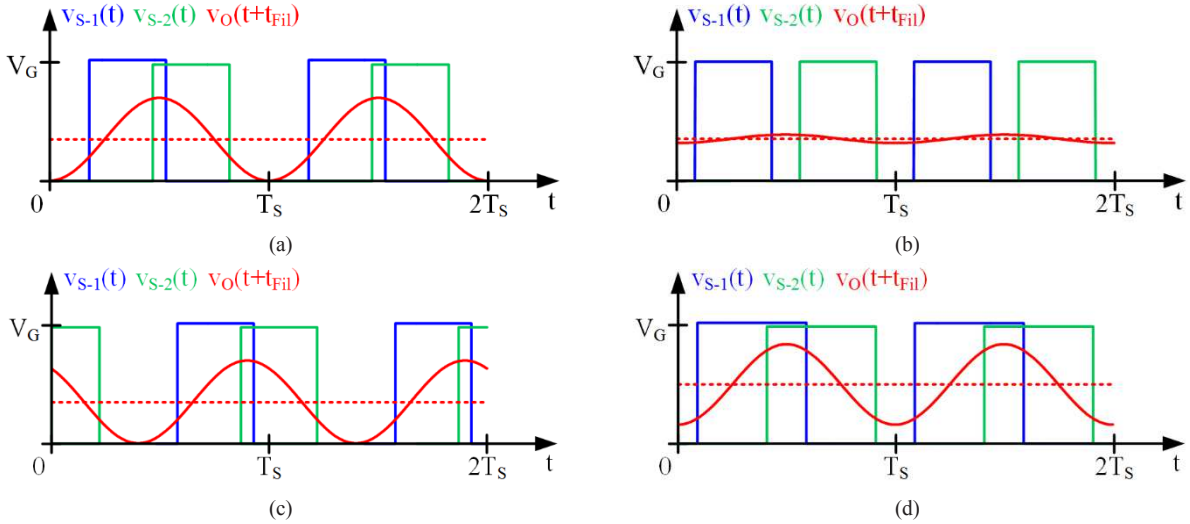

Fig. 4.9. Four examples of pulses situations: (a) Initial conditions. (b) Decrease of $A_V(t)$. (c) Decrease of $\phi_V(t)$. (d) Increase of $v_{O\text{-}DC}$. Note that these examples aim to facilitate the understanding of the RM technique and that the values of the voltages and control parameters do not represent the typical operation of the two-phase synchronous buck converter as a HB-LED driver for VLC, where $A_V(t)$ must be low in comparison to $v_{O\text{-}DC}$ due the HB-LEDs characteristics.

TABLE IV.I. MAIN PARAMETERS OF THE OPERATION EXAMPLE DEPICTED IN Fig. 4.9.

	d(t)	α(t)	β(t)	$\gamma_1(t)$	$\gamma_2(t)$	$v_{O\text{-}DC}$	$A_V(t)$	$\phi_V(t)$
Example 1	0.35	0.29	0.5	0.36	0.64	$0.35 \cdot V_G$	$0.35 \cdot V_G$	$-\pi$
Example 2	0.35	0.48	0.5	0.26	0.74	$0.35 \cdot V_G$	$0.04 \cdot V_G$	$-\pi$
Example 3	0.35	0.29	0.9	0.76	0.04	$0.35 \cdot V_G$	$0.35 \cdot V_G$	$-1.8 \cdot \pi$
Example 4	0.5	0.32	0.5	0.34	0.66	$0.5 \cdot V_G$	$0.35 \cdot V_G$	$-\pi$

As in Section 4.2.2.1, using a phasorial representation is an interesting approach for studying the operation of the proposed RM-SMPC. The phasorial analysis considers the AC components of $v_{O\text{-}1}(t)$ and $v_{O\text{-}2}(t)$:

$$v_{O-1-AC}(t + t_{Fil}) = \frac{V_G}{\pi} sin\big(\pi \cdot d(t)\big) \cdot cos\big(2 \cdot \pi \cdot f_S \cdot t - 2 \cdot \pi \cdot \gamma_1(t)\big), \tag{4.34}$$

$$v_{O-2-AC}(t + t_{Fil}) = \frac{V_G}{\pi} sin\big(\pi \cdot d(t)\big) \cdot cos\big(2 \cdot \pi \cdot f_S \cdot t - 2 \cdot \pi \cdot \gamma_2(t)\big). \tag{4.35}$$

These terms can be expressed as:

$$v_{O-1-AC}(t+t_{Fil}) = Re\left\{\frac{V_G}{\pi} sin\big(\pi \cdot d(t)\big) \cdot e^{j\cdot 2\cdot\pi\cdot f_S\cdot t} \cdot e^{-j\cdot 2\cdot\pi\cdot\gamma_1(t)}\right\}, \tag{4.36}$$

$$v_{O-2-AC}(t+t_{Fil}) = Re\left\{\frac{V_G}{\pi} sin\big(\pi \cdot d(t)\big) \cdot e^{j\cdot 2\cdot\pi\cdot f_S\cdot t} \cdot e^{-j\cdot 2\cdot\pi\cdot\gamma_2(t)}\right\}. \tag{4.37}$$

At this point, two phasors can be defined to represent both cosine waveforms:

$$V_{O-1-AC}(t) = \frac{V_G}{\pi} sin\big(\pi \cdot d(t)\big) \cdot e^{-j\cdot 2\cdot\pi\cdot\gamma_1(t)}, \tag{4.38}$$

$$V_{O-2-AC}(t) = \frac{V_G}{\pi} sin\big(\pi \cdot d(t)\big) \cdot e^{-j\cdot 2\cdot\pi\cdot\gamma_2(t)}. \tag{4.39}$$

Note that the frequency component is not included in the definition for the sake of simplicity. Therefore, the relationship between the phasors and the waveforms can be expressed as follows:

$$v_{O-1-AC}(t+t_{Fil}) = Re\{V_{O-1-AC}(t) \cdot e^{j\cdot 2\cdot\pi\cdot f_S\cdot t}\}, \tag{4.40}$$

$$v_{O-2-AC}(t+t_{Fil}) = Re\{V_{O-2-AC}(t) \cdot e^{j\cdot 2\cdot\pi\cdot f_S\cdot t}\}. \tag{4.41}$$

The phasor of $v_{O\text{-}AC}(t)$ can be calculated by summing $V_{O\text{-}1\text{-}AC}(t)$ and $V_{O\text{-}2\text{-}AC}(t)$:

$$V_{O-AC}(t) = V_{O-1-AC}(t) + V_{O-2-AC}(t) = \frac{V_G}{\pi} sin\big(\pi \cdot d(t)\big) \cdot \left(e^{-j\cdot 2\cdot\pi\cdot\gamma_1(t)} + e^{-j\cdot 2\cdot\pi\cdot\gamma_2(t)}\right). \tag{4.42}$$

Following (4.14) and (4.15), α(t) and β(t) can be used instead of γ_1 (t) and γ_2(t) for calculating $V_{O\text{-}AC}(t)$:

$$\begin{aligned} V_{O-AC}(t) &= \frac{V_G}{\pi} sin\big(\pi \cdot d(t)\big) \cdot \left(e^{-j\cdot 2\cdot\pi\cdot\left[\beta(t)-\frac{\alpha(t)}{2}\right]} + e^{-j\cdot 2\cdot\pi\cdot\left[\beta(t)+\frac{\alpha(t)}{2}\right]}\right) \\ &= \frac{V_G}{\pi} sin\big(\pi \cdot d(t)\big) \cdot e^{-j\cdot 2\cdot\pi\cdot\beta(t)}\left(e^{j\cdot\pi\cdot\alpha(t)} + e^{-j\cdot\pi\cdot\alpha(t)}\right) \\ &= \frac{2\cdot V_G}{\pi} sin\big(\pi \cdot d(t)\big) \cdot cos(\pi\cdot\alpha(t)) e^{-j\cdot 2\cdot\pi\cdot\beta(t)}. \end{aligned} \tag{4.43}$$

The relationship between $V_{O\text{-}AC}(t)$ and $v_{O\text{-}AC}(t)$ can be expressed as follows:

$$\begin{aligned} v_{O-AC}(t+t_{Fil}) &= v_{O-1-AC}(t+t_{Fil}) + v_{O-2-AC}(t+t_{Fil}) \\ &= Re\{V_{O-1-AC}(t) \cdot e^{j\cdot 2\cdot\pi\cdot f_S\cdot t}\} + Re\{V_{O-2-AC}(t) \cdot e^{j\cdot 2\cdot\pi\cdot f_S\cdot t}\} \\ &= Re\{V_{O-1-AC}(t) \cdot e^{j\cdot 2\cdot\pi\cdot f_S\cdot t} + V_{O-2-AC}(t) \cdot e^{j\cdot 2\cdot\pi\cdot f_S\cdot t}\} \\ &= Re\{[V_{O-1-AC}(t) + V_{O-2-AC}(t)] \cdot e^{j\cdot 2\cdot\pi\cdot f_S\cdot t}\} = Re\{V_{O-AC}(t) \cdot e^{j\cdot 2\cdot\pi\cdot f_S\cdot t}\}. \end{aligned} \tag{4.44}$$

Fig. 4.10 shows $V_{O\text{-}1\text{-}AC}(t)$, $V_{O\text{-}2\text{-}AC}(t)$ and $V_{O\text{-}AC}(t)$ for the four examples depicted in Fig. 4.9.

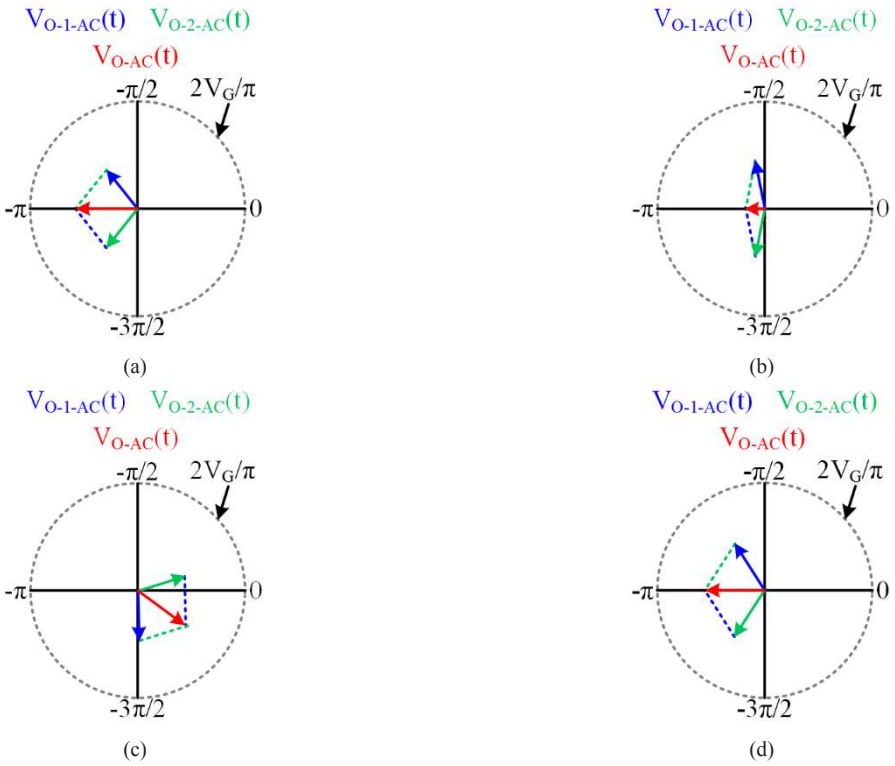

Fig. 4.10. Phasorial interpretation of the four examples of pulses situations: (a) Initial conditions. (b) Decrease of $A_V(t)$. (c) Decrease of $\phi_V(t)$. (d) Increase of $v_{O\text{-}DC}$.

4.2.2.3 Low-Pass Filter Design

In order to exemplify the low-pass filter design process, the filter developed for the prototype detailed in Section 4.3 is explained in this section. The DC component and the 1st switching harmonic of $v_{S\text{-}1}(t)$ and $v_{S\text{-}2}(t)$ constitute the part of the spectrum that must be maintained at the output of the RM-SMPC. Therefore, the design target is to remove the 2nd and higher switching harmonics of $v_{S\text{-}1}(t)$ and $v_{S\text{-}2}(t)$. It is recommended to calculate first the equivalent low-pass filter (i.e., the output filter of the circuits depicted in Fig. 4.7(d)-(e)) and, after that, design the low-pass filter with two phases taking into account that the phase inductors are equal to $2 \cdot L_1$. The equivalent low-pass filter must be calculated considering the equivalent switch-node voltage at its input:

$$v_{S-E}(t) = \frac{1}{2} \cdot [v_{S-1}(t) + v_{S-2}(t)]. \tag{4.45}$$

Obviously, the equivalent low-pass filter must pass both the DC component and the 1st switching harmonic of $v_{S\text{-}E}(t)$. Some considerations must be taken into account to evaluate the spectrum magnitude at the input of the filter (i.e., $|v_{S\text{-}E}(f)|$). Since $A_V(t)$ and $\phi_V(t)$ change over time (it is exemplified in Section 4.2.2.4), $|v_{S\text{-}E}(f)|$ differs from delta functions centered at the switching harmonics. Therefore, $|v_{S\text{-}E}(f)|$ depends on the modulation scheme that is being reproduced. Fig. 4.11(a) shows the spectrum magnitude estimated by using Matlab when considering a 64-QAM scheme and T_{Sy} equal to $3 \cdot T_S$. This means that a single symbol is represented by three carrier periods, which in this case is equal to three switching periods. Since the DC component is a delta function at 0 Hz that does not jeopardize the filter design, the DC component is removed from Fig. 4.11(a) and the result is normalized to the maximum value. Fig. 4.11 also shows the magnitude (see Fig. 4.11(a)) and phase response (see Fig. 4.11(b)) of the filter.

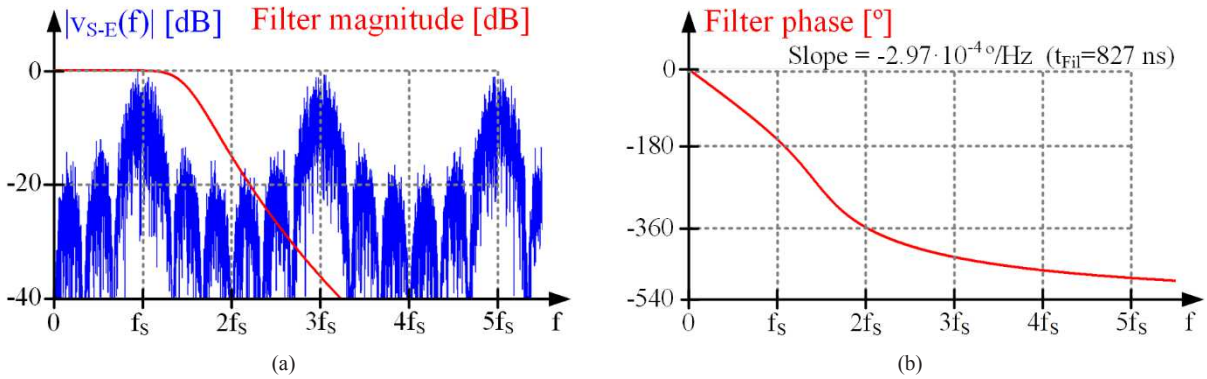

Fig. 4.11. Estimated $v_{S\text{-}E}(t)$ spectrum magnitude and low-pass filter design. Note that the DC component of $v_{S\text{-}E}(f)$ is removed and the result is normalized to the maximum value.

In order to avoid distortion, the magnitude of the filter must be constant and its phase must be linear with frequency (this means a constant group delay) for all the desired frequency components [4.3]-[4.6]. In addition, it must ensure enough rejection of the undesired frequency components. It is important to note that considering the proposed two-phase buck converter, even harmonics are null when the d(t) is 0.5. This fact facilitates the filtering task and, as $|v_{S\text{-}E}(f)|$ shows in Fig. 4.11(a), this potential benefit is used in the example. In any case, the method is also valid without making use of this option. The filter design of the example is a sixth-order Butterworth filter with f_C equal $1.5 \cdot f_S$. The delay introduced by the filter (i.e., t_{Fil}) can be estimated from the slope of the filter phase response for the desired frequency components. The value for this example is around 827 ns.

4.2.2.4 Reproducing SCM schemes by Modifying Dynamically $A_V(t)$ and $\phi_V(t)$

In order to reproduce a modulation scheme, both $A_V(t)$ and $\phi_V(t)$ must be changed over time and, consequently, $\alpha(t)$ and $\beta(t)$ must be updated. Hence, the generation of the amplitude and phase modulated cosine waveform can be seen as a concatenation of different Pure Cosine Waveforms (PCWs) portions (i.e., cosine waveforms whose amplitude, phase and frequency is constant over time). Obviously, each PCW portion has a specific amplitude and phase. From a theoretical point of view, this fact is equivalent to have different PCWs available that have a certain amplitude and phase according to the symbol that each one represents, and some parts of them are extracted in order to build the desired waveform. The concatenation of different PCWs leads to a concatenation of $A_V(t)$ samples ($A_{V\text{-}1}$, $A_{V\text{-}2}$, …) and $\phi_V(t)$ samples ($\phi_{V\text{-}1}$, $\phi_{V\text{-}2}$, …) that, in turns, are translated into a sequence of $\alpha(t)$ samples (α_1, α_2, …) and $\beta(t)$ samples (β_1, β_2, …). Fig. 4.12 shows an example in which three samples that are taken every $2 \cdot T_S$ are considered. The desired amplitude and phase values (i.e., ($A_{V\text{-}1}$, $A_{V\text{-}2}$, $A_{V\text{-}3}$) and ($\phi_{V\text{-}1}$, $\phi_{V\text{-}2}$, $\phi_{V\text{-}3}$)) are reproduced by calculating and updating $\alpha(t)$ and $\beta(t)$ (i.e., (α_1, α_2, α_3) and (β_1, β_2, β_3)) after $2 \cdot T_S$. In the signal processing field it is equivalent to apply a rectangular window to a cosine waveform of infinite time duration. This is the operation that causes the spectral broadening of each harmonic that conditions the output filter design (see Fig. 4.11(a)).

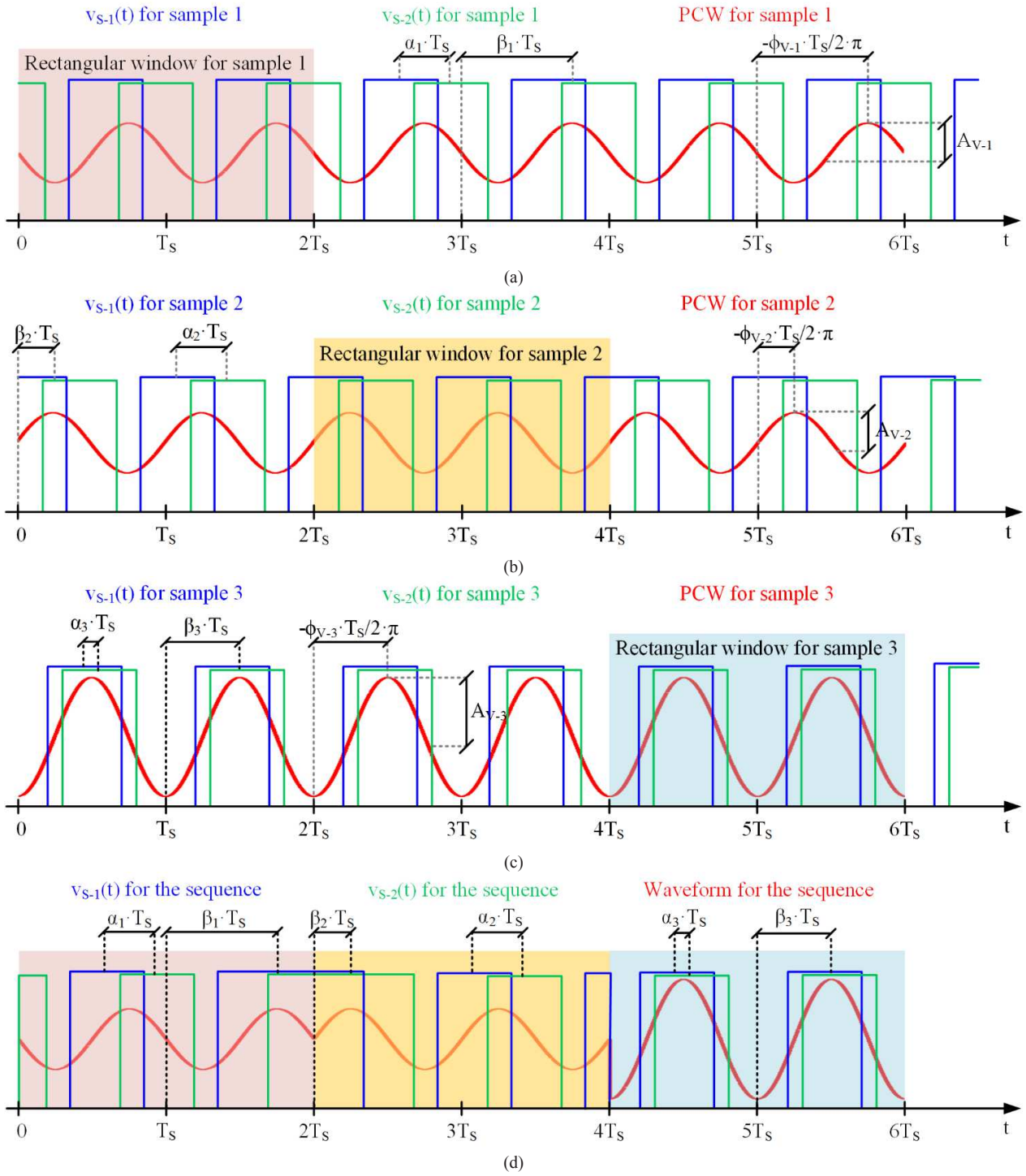

Fig. 4.12. Construction of an amplitude and phase modulated cosine waveform by applying the rectangular windows to three different PCWs: (a) PCW for sample 1 with its rectangular window. (b) PCW for sample 2 with its rectangular window. (c) PCW for sample 3 with its rectangular window. (d) Resultant sequence.

4.3 Prototype 1: SCM Transmitter based on the RM Technique

In order to prove the ideas that have been presented in the previous sections of this chapter, a two-phase synchronous buck converter with sixth-order Butterworth filter was built (see Fig. 4.13). The HB-LED driver supplies six HB-LEDs (W42180 Seoul Semiconductor) connected in series as load and operates in open loop. f_S is 500 kHz, the maximum power is around 10 W and the power efficiency is around 86%. MOSFETs CSD88539ND are used driven by LM5101AMX/NOPB ICs. The control signals are generated by a FPGA. The low-pass filter corresponds to the design detailed in Section 4.2.2.3: sixth-order Butterworth filter with f_C equal to $1.5 \cdot f_S$ (i.e., f_C = 750 kHz). Table IV.II shows the ideal values of the passive components. The delay introduced by the filter is 672 ns. The difference with respect to the value calculated in Section 4.2.2.3 (i.e., 827 ns) is due to the tolerance of the passive components. A precision resistor (R_{Sen}) of 0.25 Ω is connected in series with the HB-LEDs in order to measure the output current by measuring its voltage ($v_{Sen}(t)$). A biasing output voltage of 18.9 V is stablished to impose an average current of 440 mA flowing through the HB-LEDs at the operating conditions. The duty cycle is 0.5 to cancel the even harmonics of $v_{S\text{-}E}(t)$ in order to make less restrictive the output filter design. To achieve all these specifications, the input voltage is defined as 37.8 V.

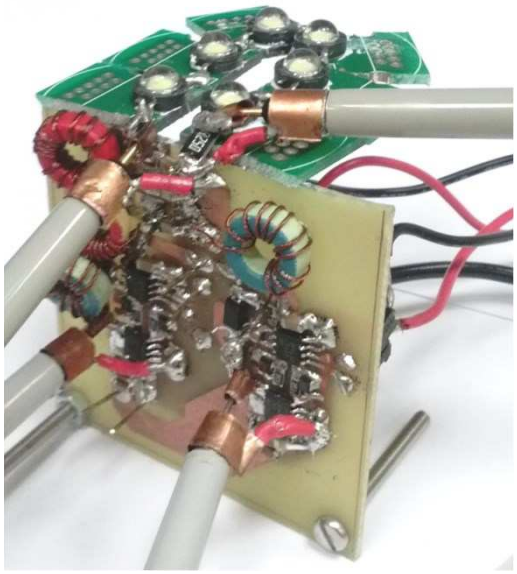

Fig. 4.13. Prototype of the two-phase synchronous buck converter that applies the RM technique for reproducing SCM schemes.

TABLE IV.II. THEORETICAL VALUES OF THE SIXTH ORDER BUTTERWORTH FILTER.

$L_{1\text{-}1}$(µH)	$L_{1\text{-}2}$(µH)	C_2(nF)	L_3(µH)	C_4(nF)	L_5(µH)	C_6(nF)
4.39	4.39	56	2.2	38.25	1.07	8.24

4.3.1 QAM Scheme Demonstration

In order to proof the concept, an example of a 64-QAM scheme is implemented by using the aforementioned prototype. 8 different amplitudes and 8 different phases are stablished. Table IV.III shows the different current amplitudes (I_{Amp}) and phases with the bit code that identifies each one. There are 64 possible symbols and, as a consequence, each symbol transmits 6 bits. The codification example is defined as follows: the 3 bits that identify a certain amplitude are interpreted as the 3 most significant bits of the symbol and the 3 bits that identify a certain phase

are interpreted as the 3 least significant bits of the symbol. Fig. 4.14 shows the constellation diagram (dots in red) of the reproduced 64-QAM scheme. It is important to note that T_{Sy} is equal to $3 \cdot T_S$ (i.e., 3 periods of the carrier) and that the bit rate is 1 Mbps.

TABLE IV.III. AMPLITUDES AND PHASES DEFINITION FOR THE 64-QAM SCHEME.

Amplitudes			**Phases**		
ID	**I_{Amp}(mA)**	**Bit code**	**ID**	**Phase (°)**	**Bit code**
A_1	104.57	000	P_1	0	000
A_2	159.86	001	P_2	-45	001
A_3	203.13	010	P_3	-90	010
A_4	254.81	011	P_4	-135	011
A_5	296.88	100	P_5	-180	100
A_6	349.76	101	P_6	-225	101
A_7	405.05	110	P_7	-270	110
A_8	440	111	P_8	-315	111

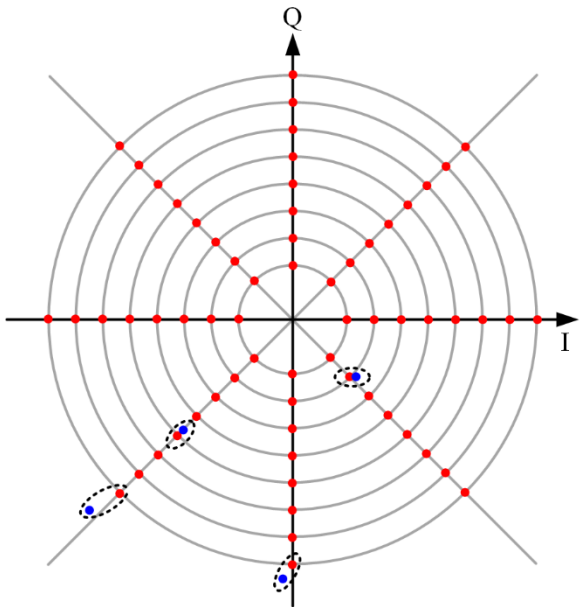

Fig. 4.14. Constellation diagram of the reproduced 64-QAM scheme (dots in red). The received symbols of the example shown in Fig. 4.15 are also included (dots in blue).

Fig. 4.15(a) shows a part of a 64-QAM sequence in which four symbols can be identified. Note that $v_{Sen\text{-}DC}$ is the DC component of $v_{Sen}(t)$ and it is related to the average current that flows through the HB-LEDs. The received symbols of this example are included in Fig. 4.14 (dots in blue). Fig. 4.15(b) shows the fast transition achieved when a change in the amplitude is performed. It can be seen that the transition instant at the output (i.e., $v_O(t)$ and $v_{Sen}(t)$) is delayed t_{Fil} with respect to the transition instant at the input of the filter (i.e., $v_{S\text{-}1}(t)$ and $v_{S\text{-}2}(t)$). Regarding the accuracy achieved, it can be seen that the maximum error appear during the transition. This is the part where the highest difference between the experimental (yellow solid line) and the theoretical (yellow dashed line) appears. Fig. 4.15(c) shows a part of a sequence where all the possible amplitudes are generated. Note that in this example, T_{Sy} is equal to

$6 \cdot T_S$. Fig. 4.15(d) shows the results obtained when a phase transition is performed. The phase step is equal to -90º. As in the previous case, the maximum error appears during the transition.

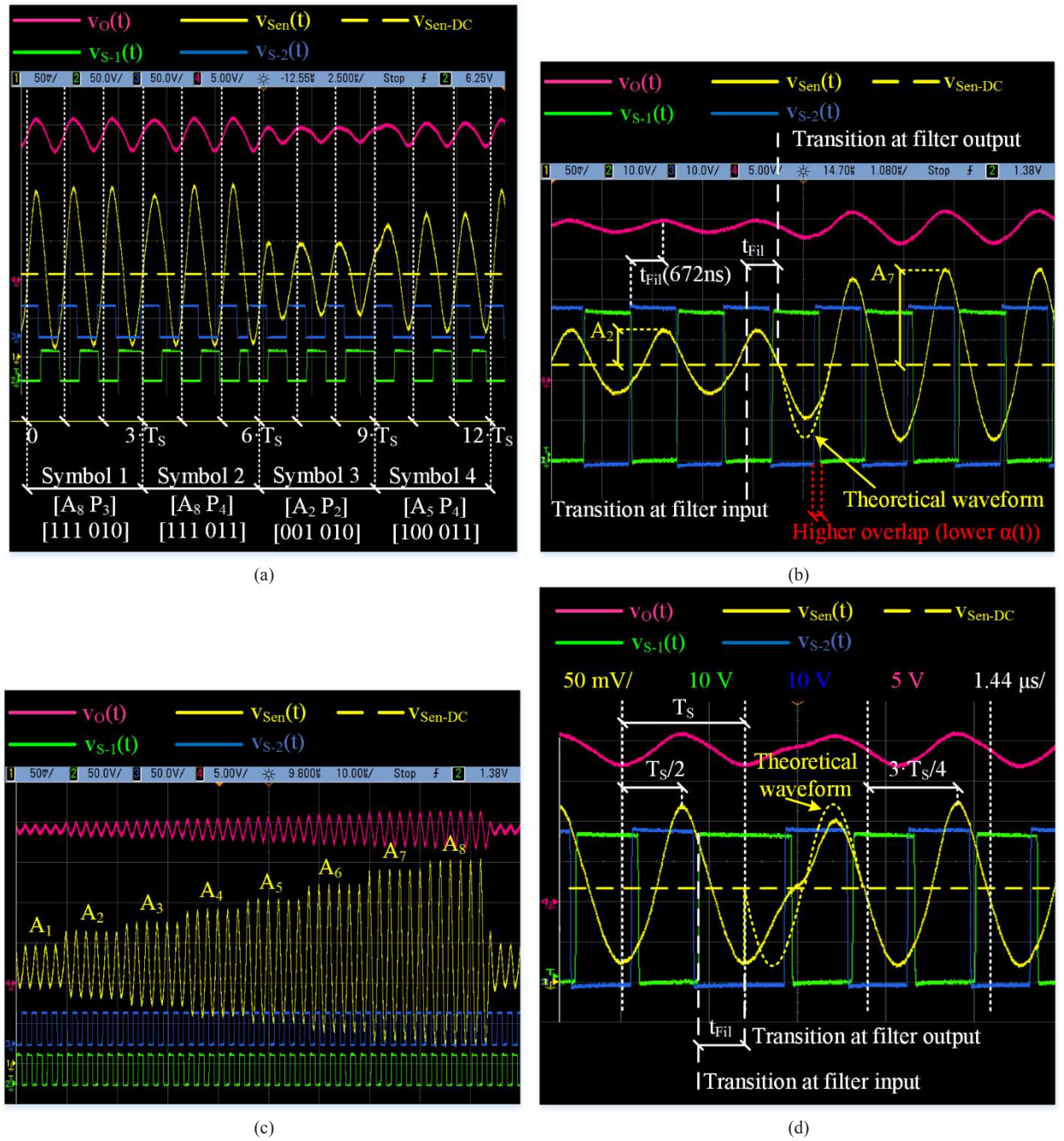

Fig. 4.15. Main experimental waveforms of the prototype that reproduces SCM schemes by using the RM technique: (a) Portion of the experimental 64-QAM sequence where four symbols are highlighted. (b) Detail of a transition when a change in the amplitude is performed. Instants in which the transition occurs at the output and at the input of the filter are highlighted. (c) Sequence where all the possible amplitudes are generated. Note that in this case, the amplitude keeps constant during $6 \cdot T_S$. (d) Detail of a transition when a change in the phase is performed. The phase step is equal to -90º. Instants in which the transition occurs at the output and at the input of the filter are highlighted.

Finally, the VLC system is evaluated by receiving the transmitted signal using the setup shown in Fig. 4.16(a). The commercial receiver PDA10A-EC is utilized during the tests. The distance between the VLC transmitter prototype and the receiver is around 60 cm. Fig. 4.16(b) shows the main waveforms involved in the test when a sequence is transmitted and received. Note that $v_{RX}(t)$ is the signal at the receiver.

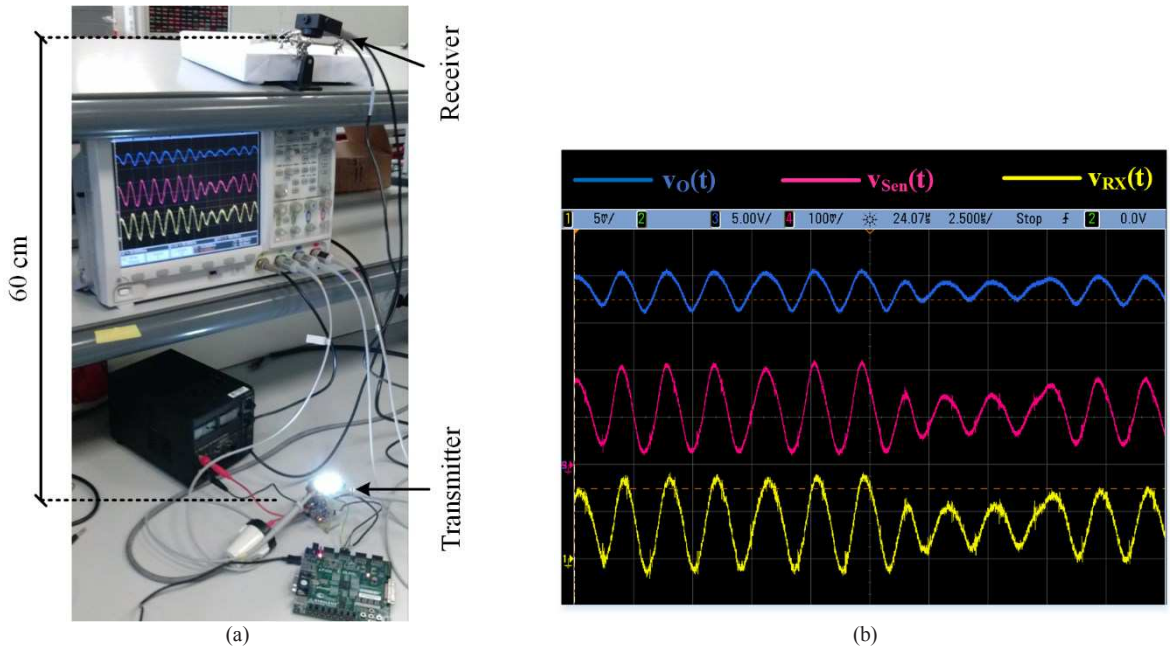

Fig. 4.16. VLC link: (a) Setup. (b) Main waveforms involved in the test of the VLC system.

4.3.2 Evaluation of the Communication Capability

In order to test the communication capability, the received signal is demodulated with Matlab. At this point, the definition of the in-phase and quadrature components is necessary. In the theoretical explanations of this dissertation, the symbols are described according to the polar coordinates (i.e., a combination of a certain amplitude with a certain phase):

$$\bar{V}(t) = A_V(t) \cdot e^{j \cdot \phi_V(t)}. \tag{4.46}$$

However, the traditional architecture of the QAM demodulator (see Fig. 4.17) is based on the Cartesian coordinates:

$$\bar{V}(t) = A_V(t) \cdot cos(\phi_V(t)) + j \cdot A_V(t) \cdot sin(\phi_V(t)). \tag{4.47}$$

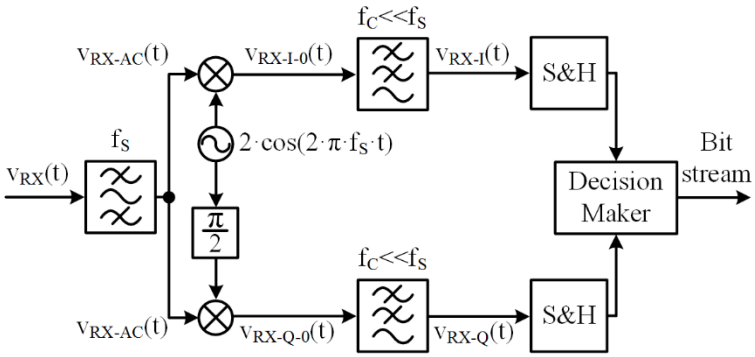

Fig. 4.17. Diagram of the QAM demodulator implemented in Matlab.

Thus, the in-phase component (i.e., horizontal component in Fig. 4.14) is:

$$V_I(t) = A_V(t) \cdot cos(\phi_V(t)). \tag{4.48}$$

Similarly, the quadrature component (i.e., vertical component in Fig. 4.14) is:

$$V_Q(t) = A_V(t) \cdot sin(\phi_V(t)). \tag{4.49}$$

The expression of the voltage at the output of the transimpedance amplifier is:

$$v_{RX}(t) = v_{RX-DC} + A_{RX}(t) \cdot cos(2 \cdot \pi \cdot f_S \cdot t + \phi_{RX}(t)). \tag{4.50}$$

where $A_{RX}(t)$ and $\phi_{RX}(t)$ are the received amplitude modulation and phase modulation, respectively. Since $v_{RX\text{-}DC}$ does not provide any information related to the communication, it is removed with a pass-band filter. Then, this signal is processed through two different paths. In the upper one, $v_{RX\text{-}AC}(t)$ is multiplied by the local oscillator, whose frequency is equal to f_S:

$$\begin{aligned} v_{RX-I-0}(t) &= v_{RX-AC}(t) \cdot 2 \cdot cos(2 \cdot \pi \cdot f_S \cdot t) \\ &= A_{RX}(t) \cdot [cos(\phi_{RX}(t)) + cos(4 \cdot \pi \cdot f_S \cdot t + \phi_{RX}(t))]. \end{aligned} \tag{4.51}$$

After that, the frequency component at $2 \cdot f_S$ is removed with a low-pass filter, obtaining the in-phase component of the received signal:

$$v_{RX-I}(t) = A_{RX}(t) \cdot cos(\phi_{RX}(t)). \tag{4.52}$$

In the lower path, $v_{RX\text{-}AC}(t)$ is multiplied by the local oscillator with a phase-shift of 90º:

$$\begin{aligned} v_{RX-Q-0}(t) &= v_{RX-AC}(t) \cdot 2 \cdot cos\left(2 \cdot \pi \cdot f_S \cdot t + \frac{\pi}{2}\right) \\ &= A_{RX}(t) \cdot [sin(\phi_{RX}(t)) - sin(4 \cdot \pi \cdot f_S \cdot t + \phi_{RX}(t))]. \end{aligned} \tag{4.53}$$

After that, the frequency component at $2 \cdot f_S$ is removed with a low-pass filter, obtaining the quadrature component of the received signal:

$$v_{RX-Q}(t) = A_{RX}(t) \cdot sin(\phi_{RX}(t)). \tag{4.54}$$

Both $v_{RX\text{-}I}(t)$ and $v_{RX\text{-}Q}(t)$ are sampled and sent to the decision maker block, which estimates that the received symbol is the closest one considering the constellation diagram depicted in Fig. 4.14. Fig. 4.18 exemplifies the demodulation process using the sequence portion shown in Fig. 4.15(a).

Finally, to measure the accuracy of the communications system, the error vector (i.e., $\bar{e}$) is employed:

$$\bar{e} = \bar{W} - \bar{V}, \tag{4.55}$$

where $\bar{W}$ is the received symbol and $\bar{V}$ is the ideal symbol (see Fig. 4.19).

The Root Mean Square value of the Error Vector Magnitude (i.e., EVM_{RMS}) is a widely used figure-of-merit that evaluates the performance of the communication system. EVM_{RMS} is based on calculating $\bar{e}$ for a sequence symbols, considering the average power of the involved symbols:

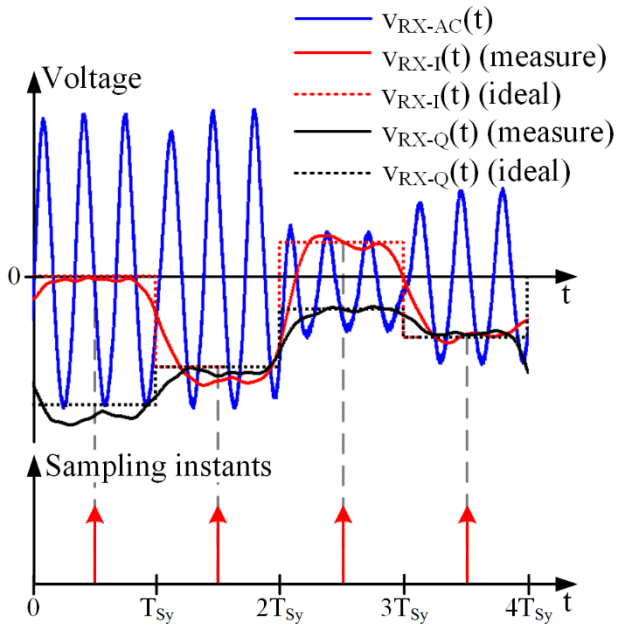

Fig. 4.18. Demodulation process example.

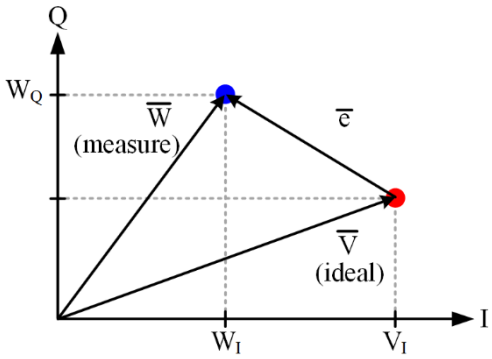

Fig. 4.19. Graphical interpretation of the error vector.

$$EVM_{RMS} = \sqrt{\frac{\sum_{k=1}^{NS} |\overline{e_k}|^2}{\sum_{k=1}^{NS} |\overline{V_k}|^2}}, \tag{4.56}$$

where NS is the number of symbols considered for the calculation.

The measured EVM_{RMS} of the implemented communication system is 14.6% when considering the sequence of four symbols (i.e., 24 bits) depicted in Fig. 4.18. Typically, EVM_{RMS} is evaluated for longer sequences and a value around 5%-15% is usually required to fulfill the requirements of wireless communication systems [4.6].

4.4 Evaluating the Output Voltage Accuracy

As was explained in Section 2.1, the high output voltage accuracy is one of the most challenging requirements for driving the HB-LEDs of a VLC transmitter. In the case of a RM-SMPC, the output voltage accuracy must be evaluated by means of the minimum voltage amplitude change (ΔA_V) and minimum voltage phase change ($\Delta\phi_V$) that can be performed. According (4.32), ΔA_V of a two-phase buck converter based on the RM technique can be calculated as follows:

$$\begin{aligned} \Delta A_V &= \left|A_V\left((\alpha_{OP}+\Delta\alpha), d_{OP}\right) - A_V(\alpha_{OP}, d_{OP})\right| \\ &= \frac{2\cdot V_G}{\pi}\cdot sin(\pi\cdot d_{OP})\cdot\left|cos\left(\pi\cdot(\alpha_{OP}+\Delta\alpha)\right) - cos(\pi\cdot\alpha_{OP})\right|, \end{aligned} \tag{4.57}$$

where α_{OP} and d_{OP} are the $\alpha(t)$ value and the $d(t)$ value in the operating point, respectively. Moreover, $\Delta\alpha$ is the minimum change of $\alpha(t)$ that can be performed. It is important to note that $\Delta\alpha$ depends on the minimum change of a pulse position that can be carried out ($\Delta\gamma$), which can be calculated by considering the temporal resolution (i.e., Δt) of the RM-SMPC control system:

$$\Delta\gamma = f_S\cdot\Delta t. \tag{4.58}$$

In order to perform a phase-shift change without modifying the average phase, the distance of the pulses position change of each phase of the buck converter must be the same, but they must be moved in opposite direction. Therefore, $\Delta\alpha$ can be calculated as follows:

$$\Delta\alpha = 2\cdot\Delta\gamma = 2\cdot f_S\cdot\Delta t. \tag{4.59}$$

Substituting (4.59) into (4.57) leads to:

$$\Delta A_V = \frac{2\cdot V_G}{\pi}\cdot sin(\pi\cdot d_{OP})\cdot|cos[\pi(\alpha_{OP}+2\cdot f_S\cdot\Delta t)] - cos(\pi\alpha_{OP})|. \tag{4.60}$$

The loss of accuracy for reproducing $A_V(t)$ (i.e., the increase of ΔA_V) with the increase of Δt is shown in Fig. 4.20(a). According to (4.60) and as Fig. 4.20(a) shows, ΔA_V depends on the operating point. It can be seen that accuracy for reproducing $A_V(t)$ rises if α_{OP} and d_{OP} are far from 0.5. However, this strategy has some drawbacks, such as an increase of the distortion caused by the second switching harmonic.

According to (4.33), $\Delta\phi_V$ of a two-phase buck converter based on the RM technique can be calculated as follows:

$$\Delta\phi_V = |\phi_V(\beta_{OP}+\Delta\beta) - \phi_V(\beta_{OP})| = 2\cdot\pi\cdot\Delta\beta, \tag{4.61}$$

where $\Delta\beta$ is the minimum change of $\beta(t)$ that can be performed. $\Delta\beta$ also depends on $\Delta\gamma$, but in this case, both the distance and the direction of the pulses position change of each phase of the buck converter must be the same to perform a change of the average phase without modifying the phase-shift. Hence, $\Delta\beta$ can be calculated as follows:

$$\Delta\beta = \Delta\gamma = f_S\cdot\Delta t. \tag{4.62}$$

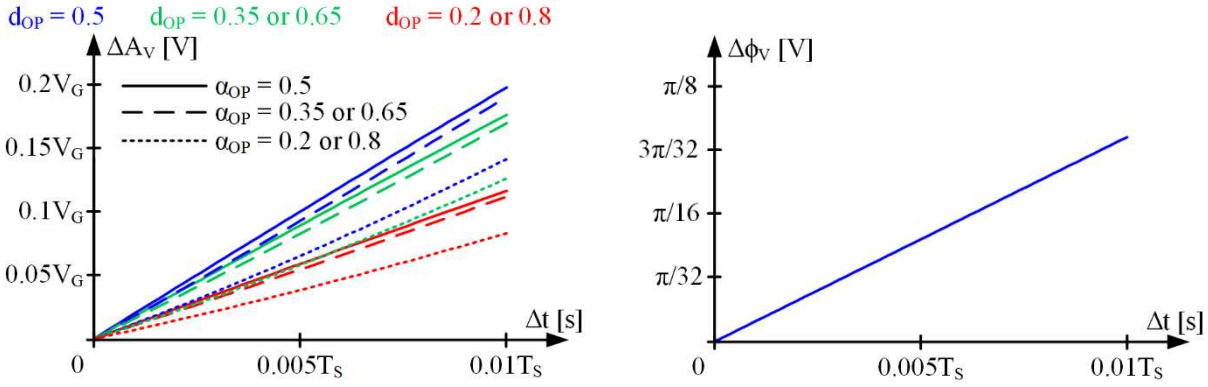

Fig. 4.20. Evaluation of the output voltage accuracy when the RM technique is implemented with a two-phase synchronous buck converter. (a) Accuracy of the voltage amplitude modulation. (b) Accuracy of the voltage phase modulation.

Substituting (4.62) into (4.61) leads to:

$$\Delta\phi_V = 2 \cdot \pi \cdot f_S \cdot \Delta t. \tag{4.63}$$

Fig. 4.20(b) shows the loss of accuracy for reproducing $\phi_V(t)$ (i.e., the increase of $\Delta\phi_V$) with the increase of Δt. Note that in this case, the accuracy does not depend on the operating point.

4.5 Evaluating the Improvement of the RM Technique

As was indicated in Section 4.1, the RM technique was developed to reduce the ratio between the required f_S and the maximum frequency that can be reproduced. In other words, the target is to provide a given bit rate by using a lower f_S value in the power stage of the HB-LED driver. Thus, improving the power efficiency and facilitating the practical implementation. The bit rate achieved by a VLC transmitter divided by f_S of the HB-LED driver is a suitable figure-of-merit to evaluate and to compare different approaches. In this section, the main VLC transmitters based on the use of SMPCs that have been reported in the literature are compared. The comparison includes the drivers based on switching on and off the HB-LEDs that are reported in [4.7] and [4.8], the driver based on PWM-SMPCs that are reported in [4.9] (Chapter 3 approach) and [4.10] (described in Chapter 3) and the RM-SMPC described in Section 4.3. It is important to note that the bit rate achieved by each approach can be evaluated as follows:

$$Bit\ rate = \frac{N \cdot log_2(NS)}{T_{Sy}}, \tag{4.64}$$

where N is the number of carriers (1 if the modulation scheme is not a MCM scheme) and NS is the number of symbols of the modulation scheme. Table IV.IV includes all the data of the comparison. It can be seen that the proposed RM-SMPC provides the highest ratio between bit rate and f_S. The achieved ratio is 20 times higher than that of the approaches reported in [4.7] and [4.9]. The improvement with respect the solution reported in [4.8] and [4.10] is lower. However, it is important to note that communication error should be taken into account. According to (4.64), the higher the NS value, the higher the bit rate because each symbols transmits more bits. Moreover, the lower the T_{Sy} value, the higher the bit rate because less time is spent transmitting each symbol. The maximum NS value and the minimum T_{Sy} that can be used in practice are determined by the error of the communication link. In general, the error rises if NS is increased or/and if T_{Sy} is decreased. In the case of the RM-SMPC prototype, the bit rate achieved is 1 Mbps because a

64-QAM scheme (i.e., NS is 64) is reproduced and T_{Sy} is equal to 6 μs (i.e., $3 \cdot T_S$). According to Section 4.3.2, the communication error is low enough in these conditions. As was explained in Section 3.3.5.3, the PWM-SMPC prototype reported in [4.10] needs to reduce the bit rate from 17.4 Mbps to 7.5 Mbps to accomplish with most extended communication standards. Therefore, its practical ratio between bit rate and f_S is 0.75. Moreover, the communication error of [4.8] is not evaluated and, consequently, its figure of merit is not very representative from a practical point of view.

TABLE IV.IV. COMPARISON BETWEEN VLC TRANSMITTERS BASED ON THE USE OF SMPCS.

	f_S (MHz)	Modulation scheme	NS	T_{Sy}	Bit rate (Mbps)	Bit rate/f_S (bps/Hz)
Driver based on switching on and off the HB-LEDs that is reported in [4.7]	0.5	VPPM	2	$10 \cdot T_S$	0.05	0.1
Driver based on switching on and off the HB-LEDs that is reported in [4.8]	2	VPPM	2	T_S	2	1
PWM-SMPC reported in [4.9] (Chapter 3 approach)	4.5	16-QAM	16	$36 \cdot T_S$	0.5	0.1111
PWM-SMPC reported in [4.10] (described in Chapter 3)	10	64-QAM-OFDM (N = 29)	64	$100 \cdot T_S$	17.4	1.74
RM-SMPC described in Section 4.3	0.5	64-QAM	64	$3 \cdot T_S$	1	2

4.6 Using the Ripple Modulation Technique for Reproducing MCM Schemes

As is explained in the previous sections, the RM technique provides interesting characteristics: the power stage is quite simple and the required f_S is much lower than in the case of PWM-SMPCs, which reduces the impact of the switching losses. However, it has an important drawback: the RM technique was proposed for reproducing SCM schemes and it has not been reported how to reproduce MCM schemes (i.e., the most recommended modulation schemes for VLC) [4.1]-[4.2]. As was shown in Section 4.2.2, reproducing SCM schemes by means of a the RM technique is straightforward: equation (4.1) (i.e., the voltage waveform that is required for reproducing a SCM scheme) can be compared to (4.30) (i.e., the voltage waveform provided by a two-phase buck converter based on the RM technique) in order to identify terms.

The analysis for MCM schemes is not as trivial as in the case of SCM schemes. Since MCM schemes are made up of several cosine waveforms with different frequencies (check equations (1.15)-(1.16)), identifying the references that $A_V(t)$ and $\phi_V(t)$ must track for reproducing such schemes is not straightforward. The voltage waveform that is required for reproducing a MCM scheme can be expressed as follows:

$$v_{O-MCM}(t) = v_{O-DC} + \frac{1}{N}\sum_{k=1}^{N} A_{V-MCM-k}(t) \cdot cos(2 \cdot \pi \cdot f_{MCM-k} \cdot t + \phi_{V-MCM-k}(t)), \quad (4.65)$$

where $A_{V\text{-}MCM\text{-}k}(t)$ and $\phi_{V\text{-}MCM\text{-}k}(t)$ are the voltage amplitude modulation and the voltage phase modulation of the k^{th} carrier, respectively. Each component can obtained from the light intensity amplitude modulation and light intensity phase modulation of the k^{th} carrier:

$$A_{V-MCM-k}(t) = \frac{A_{S-MCM-k}(t)}{K_{S-V}}, \tag{4.66}$$

$$\phi_{V-MCM-k}(t) = \phi_{S-MCM-k}(t). \tag{4.67}$$

As can be seen, a comparison between (4.65) and (4.30) does not allow us to identify the references that $A_V(t)$ and $\phi_V(t)$ must track. In order to obtain those references, (4.65) must be manipulated to reach an expression where only a single cosine waveform changes the amplitude and the phase over time. The first step is to calculate the center frequency of the MCM:

$$f_{MCM} = \frac{1}{N}\sum_{k=1}^{N} f_{MCM-k}. \tag{4.68}$$

After that, the difference between f_{MCM} and the frequency of each cosine waveform can be expressed as follows (see Fig. 4.21):

$$\Delta f_{MCM-k} = f_{MCM-k} - f_{MCM}. \tag{4.69}$$

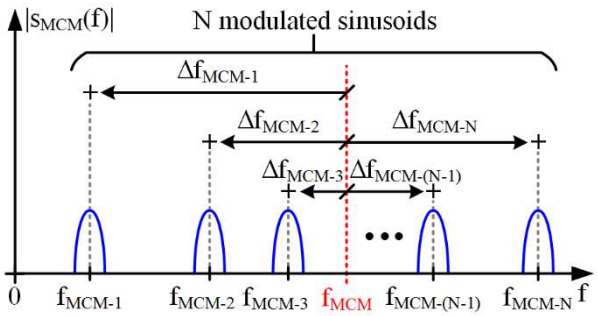

Fig. 4.21. MCM scheme in the frequency domain.

Taking into account (4.69), the k^{th} voltage carrier can be expressed as:

$$\begin{aligned} v_{O-MCM-k}(t) &= A_{V-MCM-k}(t)\cdot cos\big(2\cdot\pi\cdot(f_{MCM}+\Delta f_{MCM-k})\cdot t + \phi_{S-MCM-k}(t)\big) \\ &= A_{V-MCM-k}(t)\cdot cos(2\cdot\pi\cdot f_{MCM}\cdot t)\cdot cos\big(2\cdot\pi\cdot\Delta f_{MCM-k}\cdot t + \phi_{S-MCM-k}(t)\big) \\ &- A_{S-MCM-k}(t)\cdot sin(2\cdot\pi\cdot f_{MCM}\cdot t)\cdot sin\big(2\cdot\pi\cdot\Delta f_{MCM-k}\cdot t + \phi_{S-MCM-k}(t)\big). \end{aligned} \tag{4.70}$$

Substituting (4.70) into (4.65) leads to:

$$v_{O-MCM}(t) = v_{O-DC} + v_{O-MCM-I}(t)\cdot cos(2\cdot\pi\cdot f_{MCM}\cdot t) - v_{O-MCM-Q}(t)\cdot sin(2\cdot\pi\cdot f_{MCM}\cdot t), \tag{4.71}$$

where $v_{O\text{-}MCM\text{-}I}(t)$ and $v_{O\text{-}MCM\text{-}Q}(t)$ are the in-phase and quadrature component of the MCM scheme with respect to a cosine waveform whose frequency is f_{MCM}. These two components are formulated as:

$$v_{O-MCM-I}(t) = \frac{1}{N}\sum_{k=1}^{N} A_{V-MCM-k}(t)\cdot cos\big(2\cdot\pi\cdot\Delta f_{MCM-k}\cdot t + \phi_{V-MCM-k}(t)\big), \tag{4.72}$$

$$v_{O-MCM-Q}(t) = \frac{1}{N}\sum_{k=1}^{N} A_{V-MCM-k}(t) \cdot sin\left(2 \cdot \pi \cdot \Delta f_{MCM-k} \cdot t + \phi_{V-MCM-k}(t)\right). \quad (4.73)$$

Finally, the MCM signal can be expressed as a function of a single cosine waveform that changes the amplitude and the phase over time:

$$v_{O-MCM}(t) = v_{O-DC} + A_{V-MCM}(t) \cdot cos\left(2 \cdot \pi \cdot f_{MCM} \cdot t + \phi_{V-MCM}(t)\right), \quad (4.74)$$

$$A_{V-MCM}(t) = \sqrt{v_{O-MCM-I}(t)^2 + v_{O-MCM-Q}(t)^2}, \quad (4.75)$$

$$\phi_{V-MCM}(t) = \tan^{-1}\left(\frac{v_{O-MCM-Q}(t)}{v_{O-MCM-I}(t)}\right) \quad (4.76)$$

It is important to note that $A_{V\text{-}MCM}(t)$ and $\phi_{V\text{-}MCM}(t)$ are the envelope and the instantaneous phase of the pass-band signal considering a cosine waveform with frequency equal to f_{MCM} as the carrier (see Fig. 4.22) [4.11]. The relationship with $\alpha(t)$ and $\beta(t)$ is explained in Section 4.7.2 and Section 4.7.3, respectively.

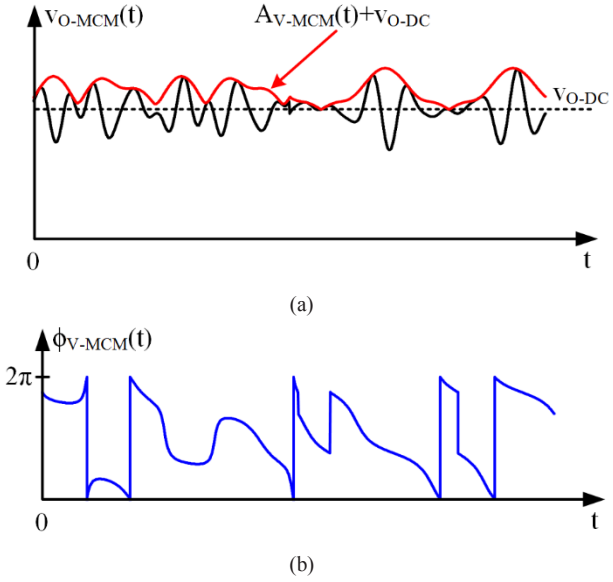

Fig. 4.22. References that must be tracked in order to reproduce a MCM scheme with the RM technique: (a) $A_V(t)$ must track the envelope of the communication signal. (b) $\phi_V(t)$ must track the instantaneous phase of the communication signal.

As a conclusion, the RM technique can be used to reproduce MCM schemes. In this case, f_S must be equal to f_{MCM}, $A_V(t)$ must track the envelope of the MCM signal and $\phi_V(t)$ must be equal to its instantaneous phase. The process described from (4.70) to (4.73) is analogous to the low-pass equivalent of a band-pass signal [4.11]. In fact, the process described in (4.75) and (4.76) is the polar representation of the I-Q components of the MCM scheme. Moreover, the method can be used to reproduce any band-pass communication signal. Note that any signals can be used in (4.75) and (4.76) instead of the I-Q components of a MCM scheme. Then, $\alpha(t)$ and $\beta(t)$ can be calculated following the process described in Section 4.7.2 and Section 4.7.3. In this way, a carrier whose frequency is f_S of the RM-SMPC would be modulated by an arbitrary waveform defined by the arbitrary signals used in (4.75) and (4.76).

4.7 Control System of a Two-Phase Synchronous Buck Converter with High Order Output Filter Based on the RM Technique

As previously explained, the RM technique is based on the PWPPM technique. It implies that the control system aims to control not only the width of the voltage pulses at the input of the filter (i.e., the duty cycles of $v_{S\text{-}1}(t)$ and $v_{S\text{-}2}(t)$), but also their phases. As a consequence, the control system of the proposed two-phase buck converter based on the RM technique is very different from that of PWM-SMPCs. Fig. 4.23 shows the power stage and the main blocks of the control system. The inputs are the voltage envelope reference ($A_{V\text{-}Ref}(t)$) and the instantaneous phase voltage reference ($\phi_{V\text{-}Ref}(t)$) that must be tracked by $A_V(t)$ and $\phi_V(t)$, respectively; the measurement of the current that flows through the HB-LEDs (i.e., $i_O(t)$) and the DC current reference (i.e., $i_{O\text{-}DC\text{-}Ref}$), which, in turns, determines the lighting level. The outputs of the control system are the pulse voltage waveforms that feed the gates of the MOSFETs: $v_{G1\text{-}1}(t)$, $v_{G1\text{-}2}(t)$, $v_{G2\text{-}1}(t)$ and $v_{G2\text{-}2}(t)$ for $Q_{1\text{-}1}$, $Q_{1\text{-}2}$, $Q_{2\text{-}1}$ and $Q_{2\text{-}2}$, respectively. A general description of the main blocks can be found below.

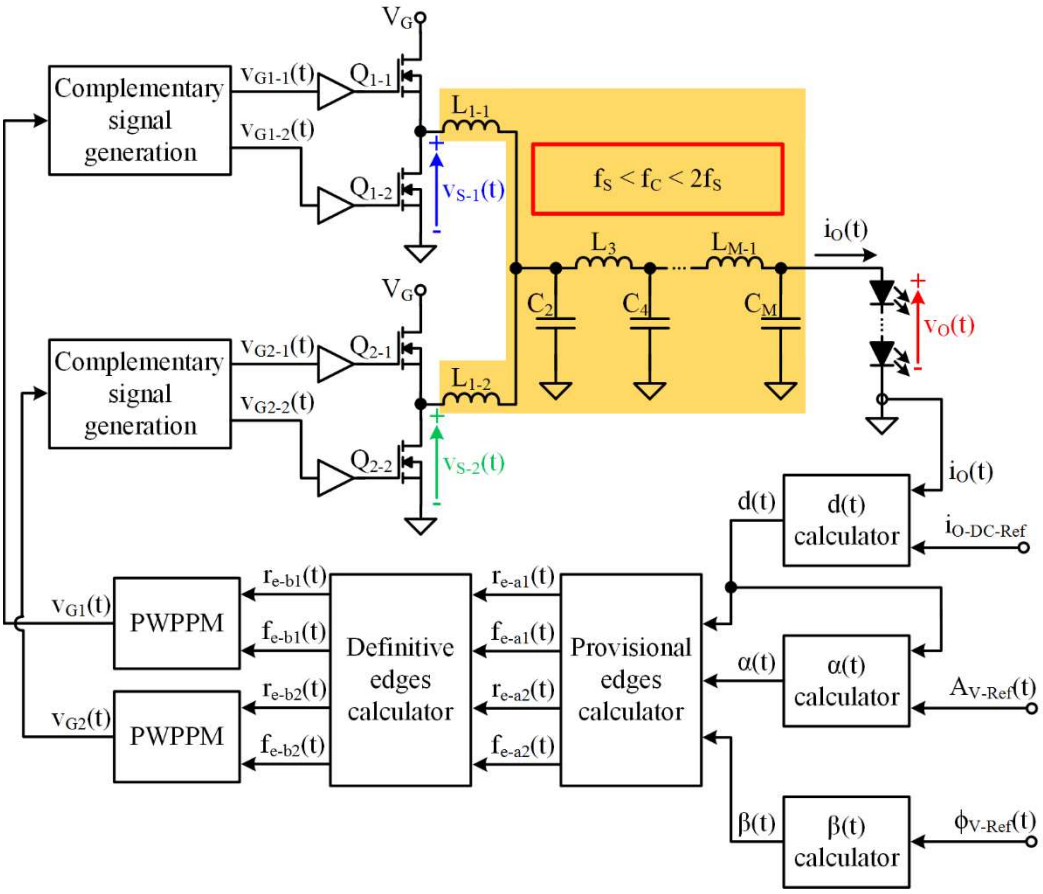

Fig. 4.23. Power stage and blocks diagram of the control system used to apply the RM technique.

4.7.1 d(t) Calculator

This block calculates the d(t) value that is required for properly biasing the HB LEDs (see Fig. 4.24). $i_O(t)$ is sensed and filtered to measure $i_{O\text{-}DC}$. Since this value determines the lighting level, $i_{O\text{-}DC\text{-}Ref}$ is compared to $i_{O\text{-}DC}$. After that, the EA provides the d(t) value that ensures the desired lighting level.

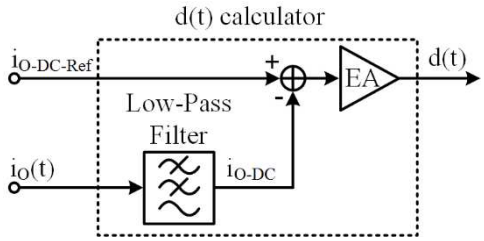

Fig. 4.24. d(t) calculator block.

4.7.2 α(t) Calculator

The calculation that the block must carried out can be obtained following (4.32):

$$\alpha(t) = \frac{1}{\pi} \cdot cos\left(\frac{\pi \cdot A_{V-Ref}(t)}{2 \cdot V_G \cdot \sin(d(t) \cdot \pi)}\right). \tag{4.77}$$

As can be seen, the α(t) calculation is not straightforward because the expression is quite complex and it depends not only on $A_{V\text{-}Ref}(t)$ (i.e., the amplitude of the cosine waveform that must be tracked), but also on the current d(t) value. As a consequence, both $A_{V\text{-}Ref}(t)$ and d(t) must feed the α(t) calculator block (see Fig. 4.23).

Fortunately, (4.77) can be simplified since, in practice, $A_V(t)$ is much smaller than V_G. This is because of the relationship between the light intensity emitted by a HB-LED, the current that flows through it and the applied voltage. As is explained in Section 2.1, once the HB-LED is properly biased, small voltage changes lead to both big current changes and big light intensity changes. As Fig. 4.25 shows, the relationship between α(t) and $A_V(t)$ is almost linear when $A_V(t) << V_G$ and, consequently, the following approximation is quite accurate:

$$\alpha(t) \cong \alpha_O - m_O(d(t)) \cdot A_{V-Ref}(t). \tag{4.78}$$

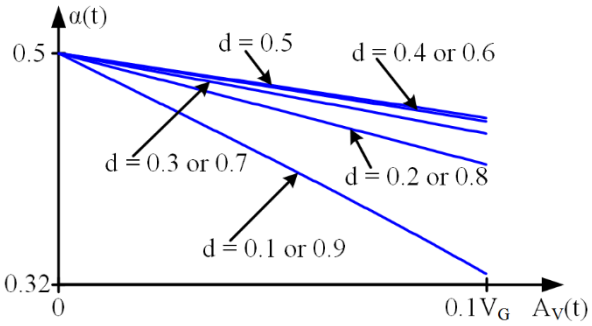

Fig. 4.25. α(t) versus $A_V(t)$ when $A_V(t) << V_G$.

Note that α_O is the α(t) value when $A_V(t)$ is 0 V, and $m_O(d(t))$ is the derivate of α(t) with respect to $A_V(t)$ and evaluated in $A_V(t)$ = 0 V:

$$\alpha_O = 0.5, \tag{4.79}$$

$$m_O(d(t)) = \frac{1}{2 \cdot V_G \cdot \sin(d(t) \cdot \pi)}. \tag{4.80}$$

Since $m_O(d(t))$ depends on d(t) and the function is not trivial, it is calculated by means of a look-up table (see Fig. 4.26).

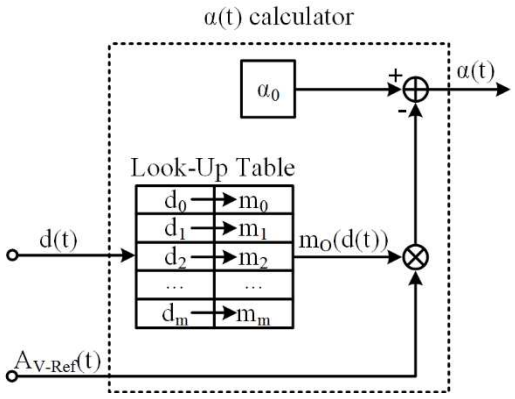

Fig. 4.26. α(t) calculator block.

4.7.3 β(t) Calculator

Differently form the α(t) calculation, the β(t) calculation is straightforward following (4.33) (see Fig. 4.27):

$$\beta(t) = \frac{-\phi_V(t)}{2 \cdot \pi}. \tag{4.81}$$

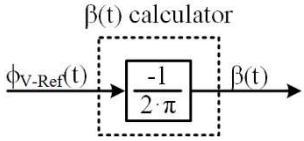

Fig. 4.27. β(t) calculator block.

4.7.4 Provisional Edges Positions Calculator

Once α(t), β(t) and d(t) are calculated, the generation of the pulses can be addressed. In the particular case of the two-phase buck converter, both $v_{S\text{-}1}(t)$ and $v_{S\text{-}2}(t)$ are proportional to the gate signals that feed $Q_{1\text{-}1}$ and $Q_{2\text{-}1}$. Obviously, the gate signals that feed $Q_{1\text{-}2}$ and $Q_{2\text{-}2}$ are the complementary ones. Therefore, and as will be shown below, the remaining part of the control system is focused on generating the gate signals that feed $Q_{1\text{-}1}$ and $Q_{2\text{-}1}$. As Fig. 4.23 shows, the last stage of the control system is the generation of the complementary gate signals that feed $Q_{1\text{-}2}$ and $Q_{2\text{-}2}$.

The first step is to calculate the provisional rising and falling edges positions of the pulses. The reason that explains why they are provisional values is detailed in Section 4.7.5. The provisional edges positions can be calculated as follows (see Fig. 4.28):

$$r_{e-a1}(t) = \beta(t) - \frac{\alpha(t)}{2} - \frac{d(t)}{2}, \tag{4.82}$$

$$f_{e-a1}(t) = \beta(t) - \frac{\alpha(t)}{2} + \frac{d(t)}{2}, \tag{4.83}$$

$$r_{e-a2}(t) = \beta(t) + \frac{\alpha(t)}{2} - \frac{d(t)}{2}, \tag{4.84}$$

$$f_{e-a2}(t) = \beta(t) + \frac{\alpha(t)}{2} + \frac{d(t)}{2}, \tag{4.85}$$

where $r_{e\text{-}a1}(t)$, $f_{e\text{-}a1}(t)$, $r_{e\text{-}a2}(t)$ and $f_{e\text{-}a2}(t)$ are the provisional rising edge position of phase 1, the provisional falling edge position of phase 1, the provisional rising edge position of phase 2 and the provisional falling edge position of phase 2, respectively (see Fig. 4.29(a)).

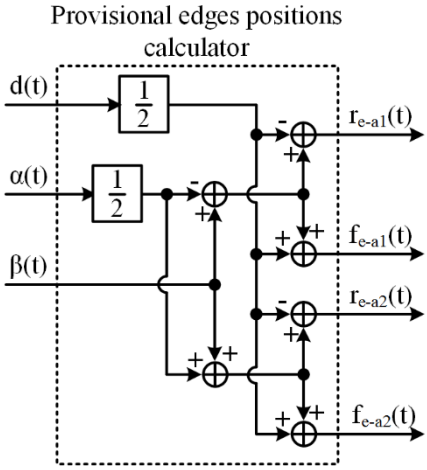

Fig. 4.28. Provisional edges positions calculator block.

4.7.5 Definitive Edges Positions Calculator

The aforementioned rising and falling edges positions are provisional values because they are only valid if the pulse that must be generated does not exceed the limits of its switching period. Note that if a provisional edge positions is lower than 0 or higher than 1, it means that the pulse exceeds its switching period. Considering the maximum and minimum values of α(t), β(t) and d, there are five possible situations:

Situation 1: $r_{e\text{-}a}(t)>0$ and $f_{e\text{-}a}(t)<1$. The pulse does not exceed its switching period (see Fig. 4.29(a)). In this situation, the definitive rising and falling edges positions ($r_{e\text{-}b}(t)$ and $f_{e\text{-}b}(t)$) are equal to the provisional ones:

$$r_{e-b}(t) = r_{e-a}(t), \tag{4.86}$$

$$f_{e-b}(t) = f_{e-a}(t). \tag{4.87}$$

Situation 2: $r_{e\text{-}a}(t)<0$ and $f_{e\text{-}a}(t)<1$. The pulse exceeds its switching period and a part of it tries to invade the previous one (see Fig. 4.29(b)). In this situation, the part of the pulse that tries to appear in the previous switching period must be moved to the end of the correct one:

$$r_{e-b}(t) = r_{e-a}(t) + 1, \tag{4.88}$$

$$f_{e-b}(t) = f_{e-a}(t). \tag{4.89}$$

Situation 3: $r_{e\text{-}a}(t)<1$ *and* $f_{e\text{-}a}(t)>1$. The pulse exceeds its switching period and a part of it tries to invade the next one (see Fig. 4.29(c)). In this situation, the part of the pulse that tries to appear in the next switching period must be moved to the beginning of the correct one:

$$r_{e-b}(t) = r_{e-a}(t), \tag{4.90}$$

$$f_{e-b}(t) = f_{e-a}(t) - 1. \tag{4.91}$$

Situation 4: $r_{e\text{-}a}(t)<0$ *and* $f_{e\text{-}a}(t)<0$. The pulse exceeds its switching period and tries to invade completely the previous one (see Fig. 4.29(d)). In this situation, the pulse must be moved to the correct switching period:

$$r_{e-b}(t) = r_{e-a}(t) + 1, \tag{4.92}$$

$$f_{e-b}(t) = f_{e-a}(t) + 1. \tag{4.93}$$

Situation 5: $r_{e\text{-}a}(t)>1$ *and* $f_{e\text{-}a}(t)>1$. The pulse exceeds its switching period and tries to invade completely the next one (see Fig. 4.29(e)). In this situation, the pulse must be moved to the correct switching period:

$$r_{e-b}(t) = r_{e-a}(t) - 1, \tag{4.94}$$

$$f_{e-b}(t) = f_{e-a}(t) - 1. \tag{4.95}$$

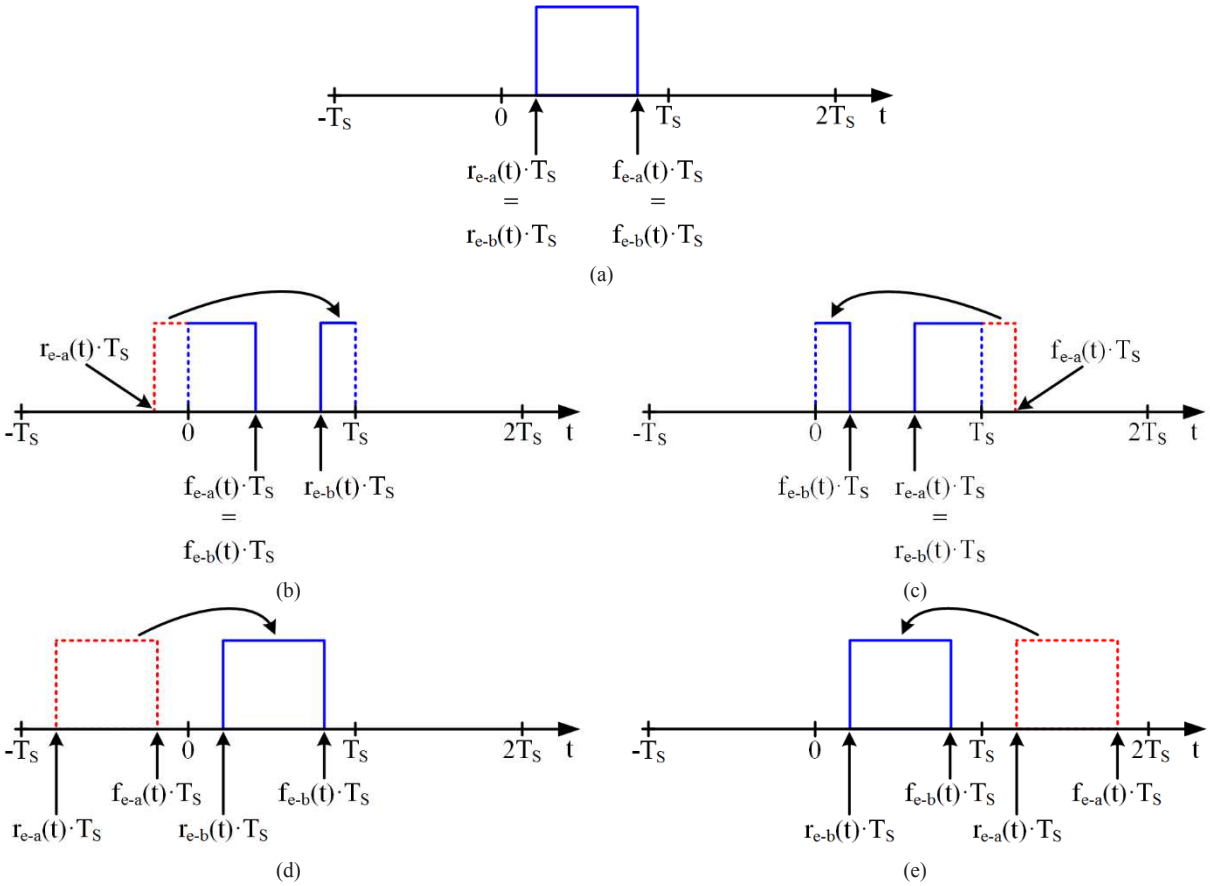

Fig. 4.29. Situation that could appear according to the possible values of the provisional rising and falling edges positions: (a) Situation 1, (b) Situation 2. (c) Situation 3. (d) Situation 4. (e) Situation 5.

Fig. 4.30 shows the definitive edges calculator block.

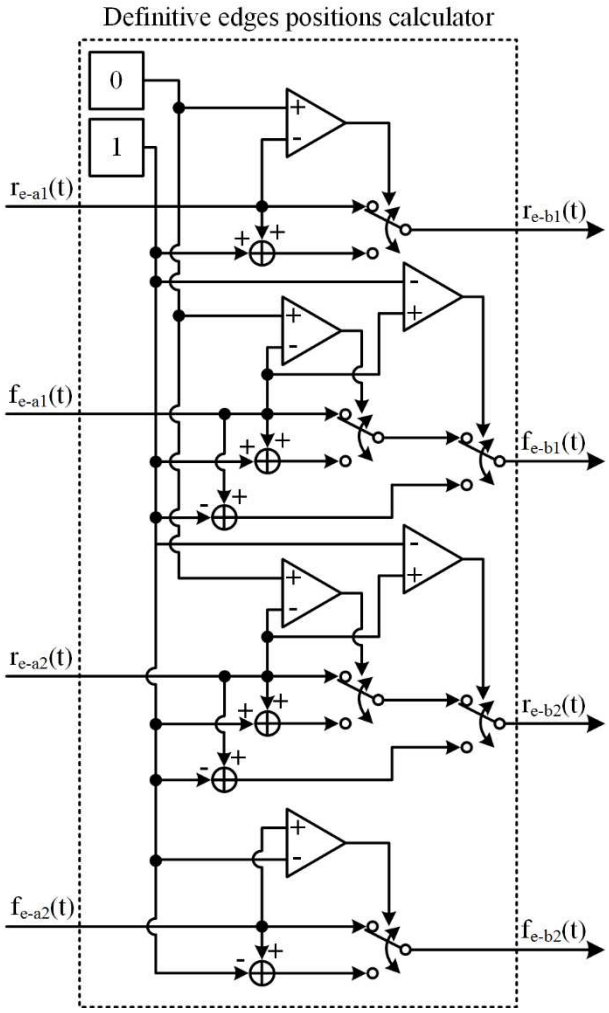

Fig. 4.30. Definitive edges positions calculator block.

4.7.6 Pulse-Width and Pulse-Phase Modulation (PWPPM)

The PWPPM block is responsible for generating the gate pulses of $Q_{1\text{-}1}$ or $Q_{2\text{-}1}$ by knowing their definite rising and falling edges positions. As in the case of the PWM technique, the pulse generation is performed by making a comparison with a sawtooth signal ($s_w(t)$) whose frequency is f_S and whose maximum and minimum values are 1 and 0, respectively. However, in the case of the PWPPM technique, $s_w(t)$ is compared to two references: the definitive rising ($r_{e\text{-}b}(t)$) and falling edges ($f_{e\text{-}b}(t)$). In addition, the output depends on the aforementioned situations. When the situation is 1, 4 or 5 (see Fig. 4.31(a)); $f_{e\text{-}b}(t)$ is higher than $r_{e\text{-}b}(t)$ and the output is (note that is a logical equation):

$$v_G(t) = \left(s_w(t) > r_{e-b}(t)\right) AND \left(s_w(t) < f_{e-b}(t)\right). \tag{4.96}$$

On the other hand, when the situation is 2 or 3 (see Fig. 4.31(b)); $f_{e\text{-}b}(t)$ is lower than $r_{e\text{-}b}(t)$ and the output is:

$$v_G(t) = \left(s_w(t) > r_{e-b}(t)\right) OR \left(s_w(t) < f_{e-b}(t)\right). \tag{4.97}$$

The PWPPM block can be implemented by defining the following logical variables:

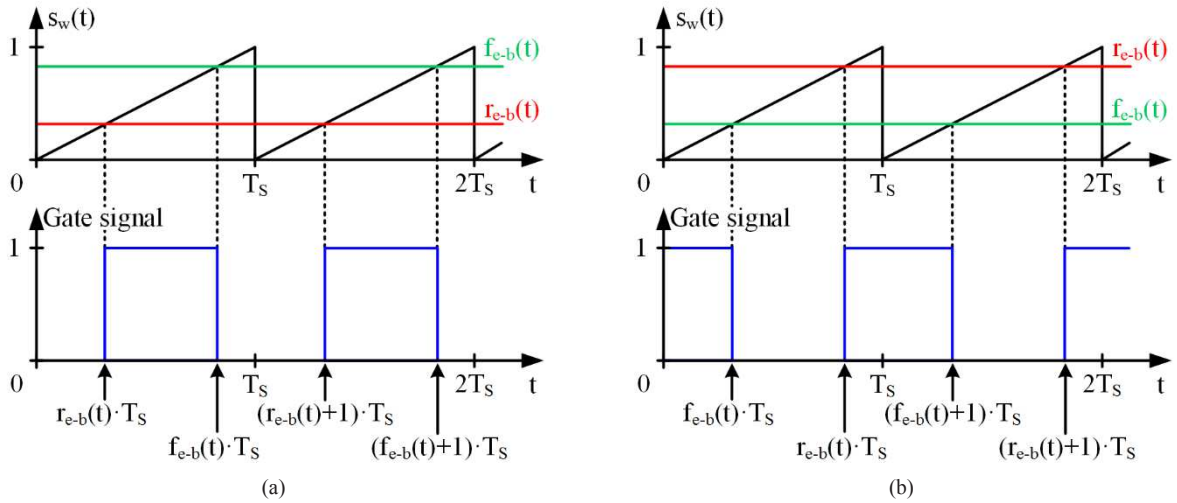

Fig. 4.31. Output of the PWPPM block depending on the situation: (a) Situation 1, 4 or 5. (b) Situation 4 or 5.

$$A = s_w(t) < f_{e-b}(t), \tag{4.98}$$

$$B = s_w(t) > r_{e-b}(t), \tag{4.99}$$

$$C = f_{e-b}(t) > r_{e-b}(t). \tag{4.100}$$

Following (4.96)-(4.97), $v_G(t)$ can be calculated as:

$$v_G(t) = (A \cdot B \cdot C) + (A + B) \cdot \bar{C}. \tag{4.101}$$

Fig. 4.32 shows the scheme of the PWPPM block.

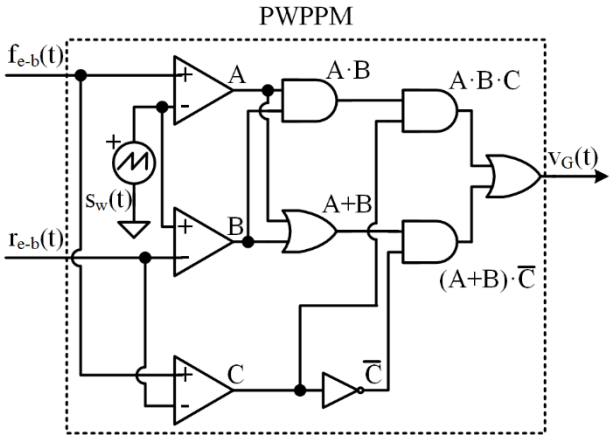

Fig. 4.32. Scheme of the PWPPM block.

4.8 Prototype 2: MCM Transmitter based on the RM Technique

A two-phase synchronous buck converter with 10th order Butterworth filter (f_C = 650 kHz) was built in order to validate the proposed technique (see Fig. 4.33). The increase of the filter order with respect to the SCM transmitter based on the RM technique reported in Section 4.3 is performed to enable d(t) values different from 0.5. In this way, the higher rejection of the filter compensates the increase of the second switching harmonic.

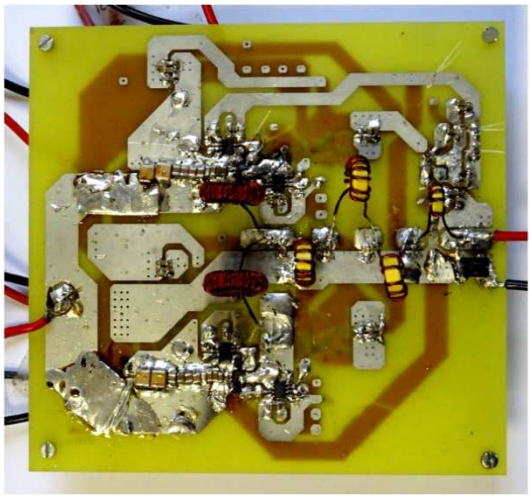

Fig. 4.33. Prototype of the MCM transmitter based on the RM technique.

The RM-SMPC supplies a string of five HB-LEDs (W42180 Seoul Semiconductor). The switching frequency is 500 kHz, the input voltage is 30 V and the maximum power is around 10 W. SSM3K361R MOSFETs are used driven by EL7156 ICs. Fig. 4.34 shows that the efficiency of the proposed RM-SMPC ranges between 95% and 96.5% depending on the dimming level. It must be pointed out that the efficiency is quite independent of $A_V(t)$.

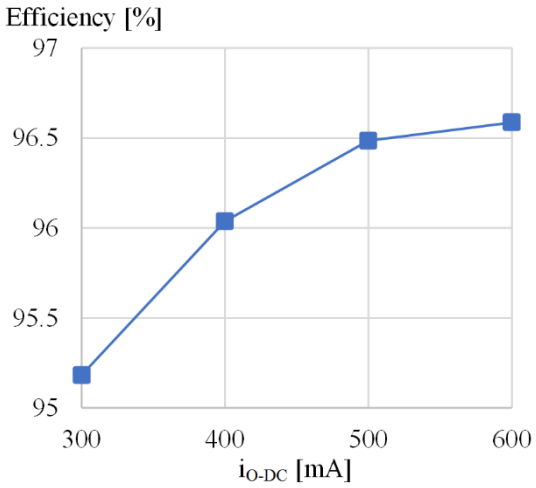

Fig. 4.34. Efficiency versus dimming level.

4.8.1 Main Experimental Waveforms

Fig. 4.35 shows the main experimental waveforms of the RM-SMPC in steady-state conditions (i.e., constant $A_V(t)$ and $\phi_V(t)$) in two situations: $A_V(t)$ is much higher in Fig. 4.35(a) than in Fig. 4.35(b). As can be seen, the cosine waveform is reproduced with high accuracy in both cases. As was indicated in Section 4.7.2, the high output voltage accuracy demanded by the VLC application is translated into high α(t) accuracy: the control system uses α(t) values

that are very close to 0.5 because $A_V(t) << V_G$. Note the small difference between the phase-shift in Fig. 4.35(a) and that of Fig. 4.35(b); and that both values are close to 180º.

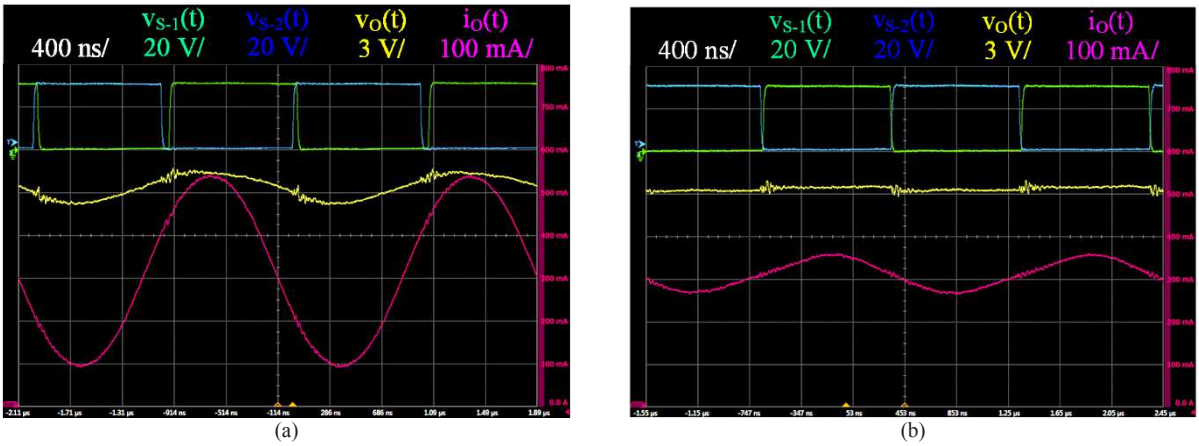

(a) (b)

Fig. 4.35. Main experimental waveforms of the HB-LED driver for VLC in steady-state conditions (i.e., constant $A_V(t)$ and $\phi_V(t)$) for two $A_V(t)$ values: (a) High $A_V(t)$ value. (b) Low $A_V(t)$ value.

In order to evaluate the capability to reproduce a MCM scheme, a signal that is made up of six carriers is reproduced. Each carrier keeps its amplitude, phase and frequency constant over time. Table IV.V shows the characteristics of each carrier (c_1, c_2, …, c_6). Note that the amplitude information is normalized: parameter A depends on the communication signal power that is used for performing the transmission.

TABLE IV.V. MAIN PARAMETERS OF THE MCM SCHEME.

	c_1	c_2	c_3	c_4	c_5	c_6
Frequency (kHz)	475	485	495	505	515	525
Amplitude	1·A	4·A	2·A	1·A	3·A	2·A
Phase (rad)	π/2	0	π	π/2	3·π/2	0

As in Section 4.3, the commercial receiver PDA10A-EC provides $v_{RX}(t)$. Fig. 4.36(a) shows the main waveforms of the VLC setup in the time domain when the aforementioned MCM scheme is reproduced. Fig. 4.36(b) the magnitude of $v_{RX}(t)$ in the frequency domain. As in any transmission system, the received signal is made up of the information (i.e., the modulated carriers) and noise that damages the communication. At this point, it is very important to study the robustness of the communication link by evaluating the error of the waveforms and by analyzing how that error damages the communication capability.

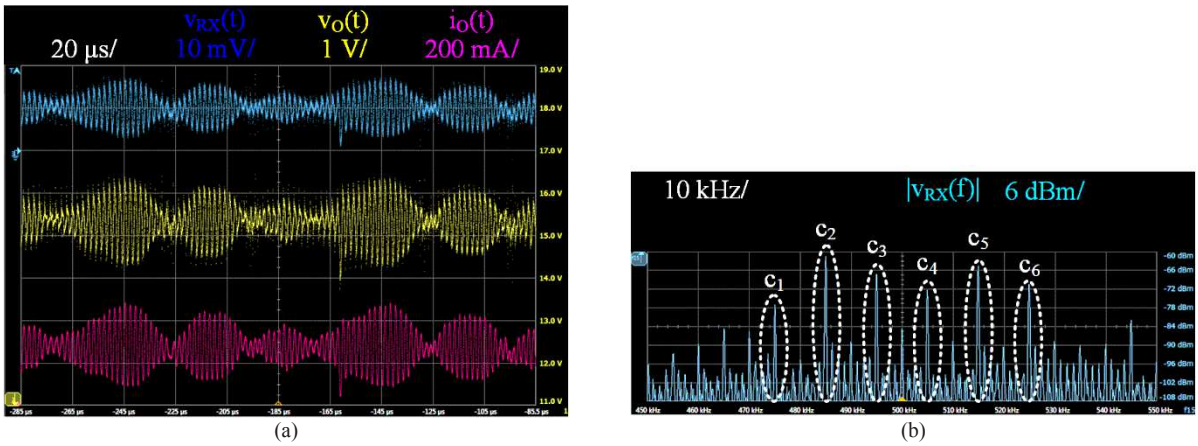

(a) (b)

Fig. 4.36. Main experimental waveforms of the VLC link (distance: 40 cm): (a) Time domain. (b) Frequency domain.

4.8.2 Analysis of the Communication Link Error

The evaluation of the VLC link robustness starts by analyzing how accurately $v_O(t)$ is reproduced. As a first step, the accuracy of the proposed HB-LED driver for VLC is evaluated by studying $A_V(t)$ and $\phi_V(t)$ with Matlab. Fig. 4.37(a) shows the envelope of the theoretical signal ($A_{Th\text{-}Nor}(t)$) and the envelope of $v_{O\text{-}AC}(t)$ ($A_{V\text{-}Nor}(t)$). In order to enable a comparison, both waveforms are scaled to have a communication signal with energy equal to 1 J. Both the instantaneous phase of the theoretical signal ($\phi_{Th}(t)$) and $\phi_V(t)$ can be seen in Fig. 4.37(b). As a conclusion, $A_V(t)$ and $\phi_V(t)$ track quite well their references. However, it is important to note that the error that appears at this point is very important because it will be propagated during the rest of the link.

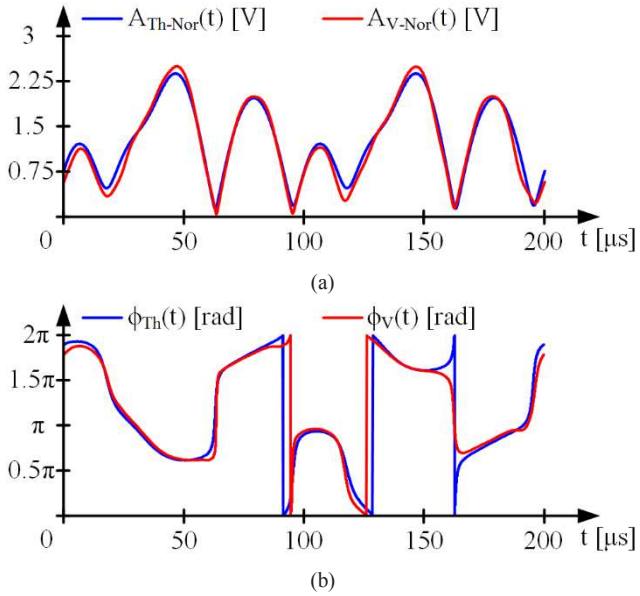

Fig. 4.37. Accuracy evaluation of the proposed HB-LED driver for VLC: (a) Comparison between the theoretical envelope and the envelope of $v_{O\text{-}AC}(t)$ when they are scaled to have a communication signal with energy equal to 1 J. (b) Comparison between the theoretical instantaneous phase and the instantaneous phase of $v_{O\text{-}AC}(t)$.

The next step is to evaluate the conversion between voltage and light intensity that is performed by the HB-LEDs. Fig. 4.38 shows the comparison between the envelopes and the instantaneous phases of both $v_{O\text{-}AC}(t)$ and $v_{RX\text{-}AC}(t)$. Note that as in the previous case, the envelopes are normalized in order to have a communication signal with energy equal to 1 J. As is indicated in Section 2.1, the relationship between the $v_{O\text{-}AC}(t)$ and $s_{AC}(t)$ is quite linear and, consequently, the conversion between voltage and light intensity does not add a remarkable error.

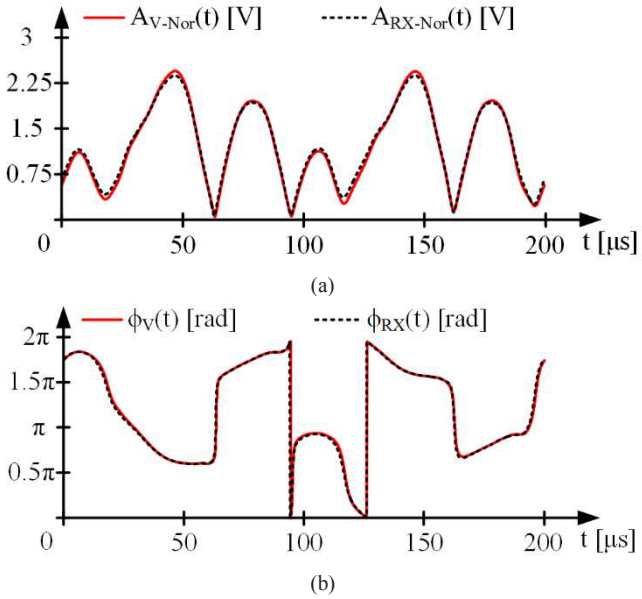

Fig. 4.38. Conversion from voltage to light intensity (link distance: 20 cm): (a) Comparison between the envelope of $v_{O\text{-}AC}(t)$ and the envelope of $v_{RX\text{-}AC}(t)$ (both waveforms are normalized in order to have a signal with energy equal to 1 J. (b) Comparison between the instantaneous phase of $v_{O\text{-}AC}(t)$ and the instantaneous phase of $v_{RX\text{-}AC}(t)$.

As in any communication system, the increase of the link distance leads to an increase of the error. As an example, Fig. 4.39 shows how $A_{RX}(t)$ and $\phi_{RX}(t)$ are deteriorated when the link distance rises from 20 cm to 100 cm.

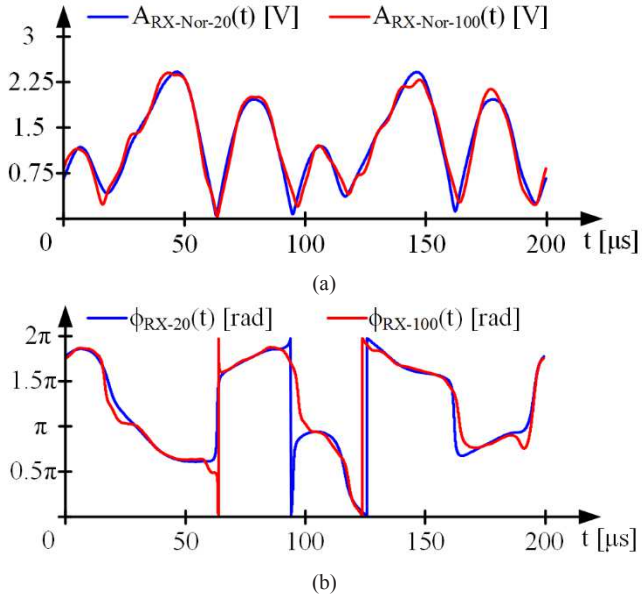

Fig. 4.39. Deterioration of the signal with the link distance rises from 20 cm to 100 cm: (a) Envelope of $v_{RX\text{-}AC}(t)$. (b) Instantaneous phase of $v_{RX\text{-}AC}(t)$.

In order to evaluate the error taking into account both the amplitude and the phase error, the following normalized temporal error vector is used:

$$\bar{e}_{Nor}(t, L_D) = A_{Th}(t) \cdot e^{j \cdot \phi_{Th}(t)} - A_{RX-Nor}(t, L_D) \cdot e^{j \cdot \phi_{RX}(t, L_D)}. \quad (4.102)$$

where L_D is the link distance.

At this point, the energy of the normalized temporal error vector allows us to evaluate the deterioration of the communication signal. That energy can be calculated as follows:

$$E_e(L_D) = \frac{1}{T}\int_{t=0}^{T} |\bar{e}_{Nor}(t, L_D)|^2 dt, \tag{4.103}$$

where T is the period of the signal (200 μs in our case).

Fig. 4.40 exemplifies the calculation of $E_e(L_D)$ when L_D is 20 cm or 100 cm. Moreover, Fig. 4.41 shows the $E_e(L_D)$ when L_D is 20 cm, 40 cm, 60 cm, 80 cm and 100 cm. As espected, $E_e(L_D)$ rises with L_D. It is important to note that according to Fig. 4.37 and to Fig. 4.38, $E_e(L_D)$ is mainly the error caused by the non-perfect reproduction of the target $v_{O\text{-}AC}(t)$ (i.e., the error caused by the HB-LED driver).

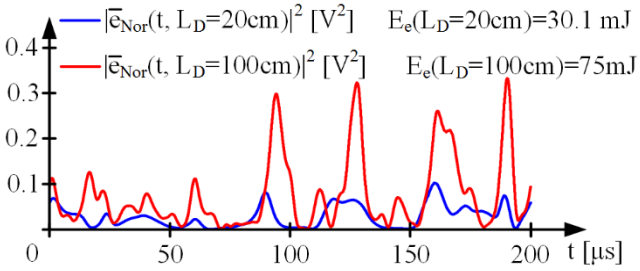

Fig. 4.40. Example of the error calculation when L_D is 20 cm or 100 cm.

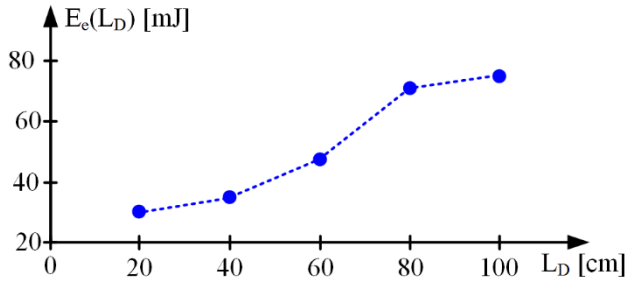

Fig. 4.41. Increase of $E_e(L_D)$ with L_D. Note that the error definition considers signals with energy equal to 1 J.

$E_e(L_D)$ allows us to evaluate the error in a general way because its definition is valid for any kind of communication signal. However, as was indicated before, it is important to analyze how that error damages the communication capability. In the particular case of a MCM scheme, that analysis is translated into the study of how the error affects the different carriers. In order to address that point, $v_{RX}(t)$ is demodulated and the amplitude and phase of each carrier is evaluated. Fig. 4.42 shows the demodulator implemented in Matlab. It is derived from the QAM demodulator explained in Section 4.3.2 and it is based on obtaining the in-phase component ($v_{O\text{-}MCM\text{-}I\text{-}k}(t)$) and the quadrature component ($v_{O\text{-}MCM\text{-}Q\text{-}k}(t)$) of each carrier. Then, these components are used to calculate the amplitude and the phase of each carrier (i.e., $A_{V\text{-}MCM\text{-}k}(t)$ and $\phi_{V\text{-}MCM\text{-}k}(t)$).

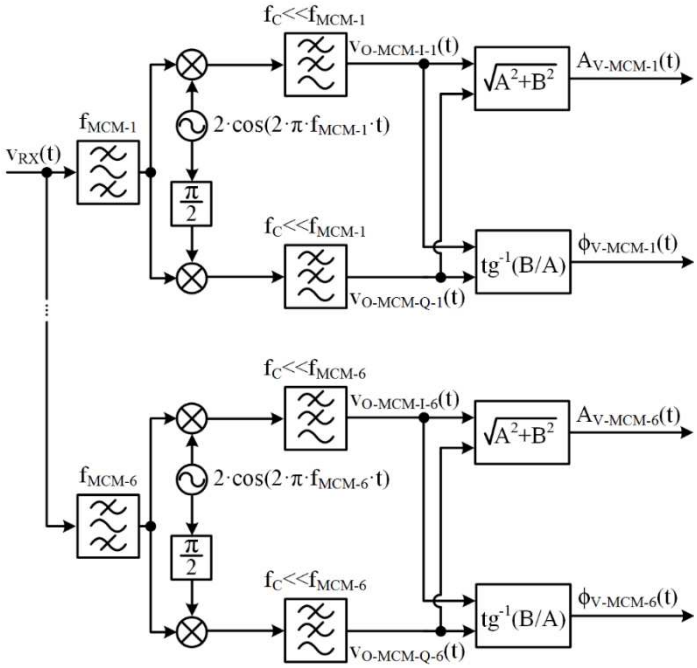

Fig. 4.42. Diagram of the MCM demodulator implemented in Matlab.

Fig. 4.43 shows the amplitude and the phase of the received modulated carriers for the different link distances (i.e., from 20 cm to 100 cm). Note that the results are given in polar form with the amplitude normalized to have a communication signal with energy equal to 1 J. As can be seen, the error causes that the amplitude and the phase of the received carriers do not match perfectly with the theoretical ones. Basically, it determines how many symbols can be distinguished by the receiver: the lower the error, the closer the symbols can be placed and, consequently, a higher number of symbols can be considered. Note that the bit rate rises with the number of symbols (see (4.64)).

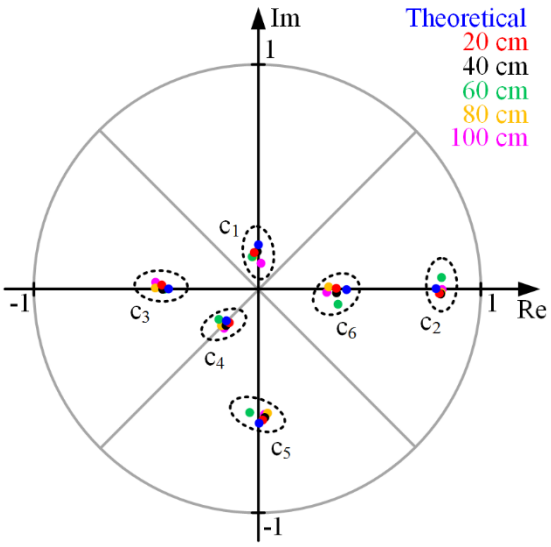

Fig. 4.43. Polar representation of the demodulated carriers normalized to have a signal with energy equal to 1 J. Note that the results of C_4 are $3\cdot\pi/4$ phase-shifted in order to avoid the overlap with the results of C_1.

In this case, a normalized temporal error vector can be calculated for each carrier an for each L_D:

$$\bar{e}_{k-Nor}(t, L_D) = A_{k-Th}(t) \cdot e^{j\cdot\phi_{k-Th}(t)} - A_{k-RX-Nor}(t, L_D) \cdot e^{j\cdot\phi_{k-RX}(t, L_D)}, \quad (4.104)$$

where $A_{k\text{-}Th}(t)$ is the theoretical amplitude of the k^{th} carrier when the communication signal is normalized to have energy equal to 1 J, $\phi_{k\text{-}Th}(t)$ is the theoretical phase of the k^{th} carrier, $A_{k\text{-}RX\text{-}Nor}(t, L_D)$ is the amplitude of the received k^{th} carrier when the communication signal is normalized to have energy equal to 1 J and $\phi_{k\text{-}RX}(t, L_D)$ is the phase of the received k^{th} carrier. Then, the energy of the normalized temporal error vector can be evaluated as follows:

$$E_{e-MCM-k}(L_D) = |\bar{e}_{k-Nor}(L_D)|^2. \tag{4.105}$$

Finally, the average energy of the normalized temporal error vector per carrier can be calculated as follows (see Fig. 4.44):

$$E_{e-MCM}(L_D) = \frac{1}{6}\sum_{k=1}^{6} E_{e-MCM-k}(L_D). \tag{4.106}$$

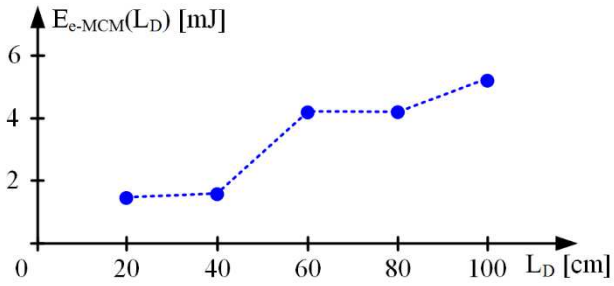

Fig. 4.44. Average energy of the normalized temporal error vector per carrier versus L_D. Note that the error definition considers signals with energy equal to 1 J.

4.9 Conclusion

The RM technique allows us to reproduce a communication signal by using the output voltage ripple of a SMPC. Hence, it is an interesting approach to be used for driving the HB-LEDs of a VLC transmitter. In this chapter, a two-phase synchronous buck converter with high order output filter is proposed to implement the RM technique. In particular, this RM-SMPC is based on controlling the amplitude and the phase of the first switching harmonic of the output voltage ripple. The proposed HB-LED driver for VLC offers two main benefits with respect to the approaches based on the use of PWM-SMPCs (i.e., the approaches described in Chapter 2 and Chapter 3). The first one is that the f_S required for reproducing a given modulation scheme is lower. In this way, the impact of the switching losses is mitigated and the problems derived from operating with high f_S values, such as the generation of the gate signals, are alleviated. The second benefit is that the power stage is quite simple in comparison to the PWM-SMPC reported in Section 3.3. However, this benefit is not so clear when the RM-SMPC enables d(t) values different from 0.5. In that case, the increase of the second switching harmonic must be compensated with an increase of the filter order.

The key points of the RM technique are described in this chapter: the operating principle of the proposed RM-SMPC, how $A_V(t)$ and $\phi_V(t)$ can be controlled, how to reproduce SCM schemes and MCM schemes, description of the control system, etc. However, since it is a very recent idea, there a lot points that, according to the early results, should be studied in the future: implementation of the RM technique with other topologies, use of the second or higher switching harmonics, maximum communication bandwidth achievable, optimization of the output filter, etc.

4.10 References

[4.1] J. Rodriguez, D. G. Lamar, J. Sebastian and P. F. Miaja, "Taking advantage of the output voltage ripple of a two-phase buck converter to perform quadrature amplitude modulation for visible light communication," 2017 IEEE Applied Power Electronics Conference and Exposition (APEC), Tampa, FL, 2017, pp. 2116-2123.

[4.2] J. Rodríguez, D. G. Lamar, P. F. Miaja and J. Sebastián, "Reproducing single-carrier digital modulation schemes for VLC by controlling the first switching harmonic of the DC–DC power converter output voltage ripple," in IEEE Transactions on Power Electronics, vol. 33, no. 9, pp. 7994-8010, Sept. 2018.

[4.3] B. Sklar, *Digital communications*. Vol. 2. Upper Saddle River: Prentice Hall, 2001.

[4.4] G. L. Stüber, *Principles of mobile communication*. Springer Science & Business Media, 2011.

[4.5] J. R. Barry, E. A. Lee, and D. G. Messerschmitt. *Digital communication*. Springer Science & Business Media, 2012.

[4.6] E. McCune, *Practical digital wireless signals*. Cambridge University Press, 2010.

[4.7] S. Zhao, J. Xu and O. Trescases, "Burst-mode resonant LLC converter for an LED luminaire with integrated visible light communication for smart buildings," in IEEE Transactions on Power Electronics, vol. 29, no. 8, pp. 4392-4402, Aug. 2014.

[4.8] K. Modepalli and L. Parsa, "Dual-purpose offline LED driver for illumination and visible light communication," in IEEE Transactions on Industry Applications, vol. 51, no. 1, pp. 406-419, Jan.-Feb. 2015.

[4.9] J. Rodríguez, D. G. Lamar, D. G. Aller, P. F. Miaja and J. Sebastián, "Efficient visible light communication transmitters based on switching-mode dc-dc converters," in Sensors, vol. 18, no. 4, 2018.

[4.10] J. Rodriguez, D. G. Lamar, P. Fernandez Miaja, D. G. Aller and J. Sebastian, "Power efficient VLC transmitter based on pulse-width modulated DC-DC converters and the split of the power," in IEEE Transactions on Power Electronics.

[4.11] J. G. Proakis, *Digital communications*, 4th ed. New York: McGrawHill, 2000.

Chapter 5:
Conclusions, Contributions and Future Work

The main conclusions of the dissertation are included in this chapter. Moreover, the contributions of the research are also described. Finally, different points that could be studied in the future are explained in order to stablish a possible roadmap to continue the research line.

5.1 General Conclusions

VLC has gained relevance recently because of the saturation of wireless communication systems that is predicted for the upcoming years. Unfortunately, this technology has several weak points that are slowing down its implementation. One of the major bottlenecks is the low power efficiency achieved by the HB-LED drivers that have been proposed for providing high data rates. Reproducing advanced modulation schemes, such as SCM and MCM schemes, is mandatory for enabling the massive data traffic predicted for the future. This dissertation aimed to developed power efficient solutions that are able to reproduce such modulation schemes by means of designing HB-LED drivers for VLC that are fully-based on the use of SMPCs. However, this target is not trivial because driving the HB-LEDs of VLC transmitters leads to very challenging requirements. Providing a bandwidth of units to tens of MHz and the capability to perform very small voltage changes are two critical points.

From a theoretical point of view, a buck converter can be used to drive the HB-LEDs of the VLC transmitter. However, it has several drawbacks that limit its employment. The high f_S required for providing a bandwidth high enough for reproducing the communication signals makes the practical implementation very difficult because of the high switching losses, the difficulty of driving the MOSFETs, etc. Moreover, the capability to perform very small voltage changes with a SMPC falls with f_S. Regulating $i_{O\text{-}DC}$ with a feedback loop instead of $i_O(t)$, and reproducing the communication signal in open loop is an interesting approach for reducing the required f_S. However, the required f_S keeps being unaffordable and, as a consequence, more complex PWM-SMPCs were explored. The multi-phase structure, the floating structure and the high order filter are three buck-derived converters that have very interesting features for driving the HB-LEDs of VLC transmitters. They reduce the required f_S with respect to a conventional buck converter, which increases the power efficiency and facilitates the practical implementation. Moreover, the floating structure minimizes the power processed with high f_S, which increases the power efficiency even more. In addition, this structure also facilitates the reproduction of the communication signal since it increases the operating range of the duty cycle with respect to a conventional buck converter.

Therefore, using PWM-SMPCs is an interesting approach for driving the HB-LEDs of a VLC transmitter avoiding the use of a power inefficient LPA. However, the recommended topologies for enabling an affordable f_S and for fulfilling the required output voltage accuracy lead to quite complex designs. The RM technique is a method specially conceived for VLC that reproduces the communication signal by using the output voltage ripple of a SMPC. This technique can be implemented by means of a two-phase synchronous buck converter with high order output filter that passes not only the DC component, but also the 1st switching harmonic of the switch-node voltages. The RM-SMPC controls the amplitude and the phase of the first switching harmonic of the output voltage ripple by using the PWPPM technique in each phase of the converter. The RM technique offers two main benefits with respect to the approaches based on the use of PWM-SMPCs: the required f_S is lower, which mitigates the impact of the switching losses and alleviates the problems derived from operating with high f_S values; and the power stage is quite simple.

5.2 Contributions

The contributions of the work can be summarized as follows:

- Studying the role that power electronics can play in VLC in order to maintain the high efficiency of HB-LED lighting. The power inefficient HB-LED driver that is based on the use of a LPA can be replaced by different solutions that are fully or partially based on the use of SMPCs.
- Identifying the requirements for driving the HB-LEDs of a VLC transmitter and the main design challenges that appear when a SMPC is designed to fulfill that task. It is concluded that both the high bandwidth and the high output voltage accuracy that is required for reproducing properly the communication signal are the two main design challenges.
- Studying design strategies for reducing both the required f_S and the required duty cycle accuracy when using PWM-SMPCs. The use of multi-phase structures, floating structures and high order filters are interesting approaches for addressing the aforementioned design challenges.
- Proposing a method for reproducing SCM schemes by using the output voltage ripple of a SMPC in order to reduce the required f_S and the complexity of the power stage.
- Extending the previous method in order to reproduce MCM schemes (i.e., the most recommended modulation schemes for VLC) by using the output voltage ripple of a SMPC.

As the outcome of this dissertation, several scientific papers have been published in international journals, international conferences and national conferences (see Section 5.2.1, Section 5.2.2 and Section 5.2.3). Moreover, other contributions to the power electronics field have been made during the development of the work (see Section 5.2.4, Section 5.2.5 and Section 5.2.6).

5.2.1 Contributions of the Dissertation that Are Published in International Journals

[1] J. Sebastián, D. G. Lamar, D. G. Aller, **J. Rodríguez** and P. F. Miaja, "On the role of power electronics in visible light communication," in IEEE Journal of Emerging and Selected Topics in Power Electronics.

[2] **J. Rodríguez**, D. G. Lamar, D. G. Aller, P. F. Miaja and J. Sebastián, "Efficient visible light communication transmitters based on switching-mode dc-dc converters," in Sensors, vol. 18, no. 4, 2018.

[3] **J. Rodríguez**, D. G. Lamar, P. F. Miaja and J. Sebastián, "Reproducing single-carrier digital modulation schemes for VLC by controlling the first switching harmonic of the DC–DC power converter output voltage ripple," in IEEE Transactions on Power Electronics, vol. 33, no. 9, pp. 7994-8010, Sept. 2018.

[4] **J. Rodríguez**, D. G. Lamar, P. Fernández Miaja, D. G. Aller and J. Sebastián, "Power efficient VLC transmitter based on pulse-width modulated DC-DC converters and the split of the power," in IEEE Transactions on Power Electronics.

5.2.2 Contributions of the Dissertation that Are Published in International Conferences

[5] **J. Rodríguez**, D. G. Lamar, J. Sebastián and P. F. Miaja, "Taking advantage of the output voltage ripple of a two-phase buck converter to perform quadrature amplitude modulation for visible light communication," 2017 IEEE Applied Power Electronics Conference and Exposition (APEC), Tampa, FL, 2017, pp. 2116-2123.

[6] J. Sebastián, D. G. Aller, **J. Rodríguez**, D. G. Lamar and P. F. Miaja, "On the role of the power electronics on visible light communication," 2017 IEEE Applied Power Electronics Conference and Exposition (APEC), Tampa, FL, 2017, pp. 2420-2427.

[7] **J. Rodríguez**, D. G. Aller, D. G. Lamar and J. Sebastián, "Energy efficient visible light communication transmitter based on the split of the power," 2017 IEEE Energy Conversion Congress and Exposition (ECCE), Cincinnati, OH, 2017, pp. 217-224.

[8] **J. Rodríguez**, D. G. Aller, D. G. Lamar and J. Sebastián, "Performance evaluation of a VLC transmitter based on the split of the power," 2018 IEEE Applied Power Electronics Conference and Exposition (APEC), San Antonio, TX, 2018, pp. 1179-1186.

[9] **J. Rodríguez**, D. G. Lamar, D. G. Aller, P. F. Miaja and J. Sebastián, "Power-efficient VLC transmitter able to reproduce multi-carrier modulation schemes by using the output voltage ripple of the HB-LED driver," 2018 IEEE 19th Workshop on Control and Modeling for Power Electronics (COMPEL), Padova, 2018.

5.2.3 Contributions of the Dissertation that Are Published in National Conferences

[10] **J. Rodríguez**, P. F. Miaja, D. G. Lamar y J. Sebastián, "Aprovechamiento del rizado de la tensión de salida de un convertidor CC/CC para reproducir esquemas QAM en VLC", Seminario Anual de Automática, Electrónica Industrial e Instrumentación 2017 (SAAEI'17), Valencia (Spain), 2017.

[11] J. Sebastián, D. G. Aller, **J. Rodríguez**, P. F. Miaja y D. G. Lamar, "El papel de los convertidores CC/CC en las comunicaciones por luz visible", Seminario Anual de Automática, Electrónica Industrial e Instrumentación 2017 (SAAEI'17), Valencia (Spain), 2017.

[12] D. G. Aller, **J. Rodríguez**, J Sebastián y D. G. Lamar, "Desarrollo de un transmisor para comunicaciones en luz visible (VLC) basado en un convertidor CC/CC conmutado de respuesta rápida", Seminario Anual de Automática, Electrónica Industrial e Instrumentación 2017 (SAAEI'17), Valencia (Spain), 2017.

[13] **J. Rodríguez**, D. G. Lamar, D. G. Aller, P. F. Miaja y J. Sebastián, "Transmisor VLC eficiente basado en el reparto de la potencia entre convertidores CC/CC modulados por ancho de pulso", Seminario Anual de Automática, Electrónica Industrial e Instrumentación 2018 (SAAEI'18), Barcelona (Spain), 2018.

[14] D.G. Aller, D. G. Lamar, **J. Rodríguez**, P. F. Miaja and J. Sebastián, "Diseño de transmisores VLC eficientes basados en convertidores CC/CC de respuesta rápida", Seminario Anual de Automática, Electrónica Industrial e Instrumentación 2018 (SAAEI'18), Barcelona (Spain), 2018.

5.2.4 Other Contributions that Are Published in International Journals

[15] **J. Rodríguez**, J. Roig, A. Rodríguez, D. G. Lamar and F. Bauwens, "Evaluation of superjunction MOSFETs in cascode configuration for hard-switching operation," in IEEE Transactions on Power Electronics, vol. 33, no. 8, pp. 7021-7037, Aug. 2018.

[16] **J. Rodríguez**, D. G. Lamar, J. Roig, A. Rodríguez and F. Bauwens, "Improving the third quadrant operation of superjunction MOSFETs by using the cascode configuration," in IEEE Transactions on Power Electronics.

5.2.5 Other Contributions that Are Published in International Conferences

[17] **J. Rodríguez**, A. Rodríguez, D. G. Lamar, J. Roig and F. Bauwens, "Modeling the switching behaviour of superjunction MOSFETs in cascode configuration with a low voltage silicon MOSFET," 2016 IEEE 17th Workshop on Control and Modeling for Power Electronics (COMPEL), Trondheim, 2016, pp. 1-8.

[18] A. López, **J. Rodríguez**, M. R. Rogina, I. Castro and A. Rodríguez, "Switching performance comparison of a power switch in a cascode configuration using a superjunction MOSFET," 2016 51st International Universities Power Engineering Conference (UPEC), Coimbra, 2016, pp. 1-6.

[19] **J. Rodríguez**, A. Rodríguez, I. Castro, D. G. Lamar, J. Roig and F. Bauwens, "Superjunction cascode, a configuration to break the silicon switching frequency limit," 2016 IEEE Energy Conversion Congress and Exposition (ECCE), Milwaukee, WI, 2016, pp. 1-8.

[20] **J. Rodríguez**, A. Rodríguez, D. G. Lamar, J. Roig and F. Bauwens, "Reducing Qrr in high-voltage superjunction MOSFETs by using the cascode configuration," 2017 IEEE Applied Power Electronics Conference and Exposition (APEC), Tampa, FL, 2017, pp. 1970-1977.

[21] J. Roig, G. Gómez, F. Bauwens, B. Vlachakis, **J. Rodríguez**, M. R Rogina, A. Rodríguez, D. G. Lamar "Series-connected GaN transistors for ultra-fast high-voltage switch (>1kV)," 2017 IEEE Applied Power Electronics Conference and Exposition (APEC), Tampa, FL, 2017, pp. 3043-3048.

5.2.6 Other Contributions that Are Published in National Conferences

[22] I. Castro, J. Roig, F. Bauwens, D. G. Lamar, **J. Rodríguez** and A. Vázquez, "Verificacion del modelo analítico de pérdidas en conmutación para MOSFET de superunión con modelado de capacidades no-lineales y diversificacion de corrientes," Seminario Anual de Automática, Electrónica Industrial e Instrumentación 2015 (SAAEI'15), Zaragoza (España), 2015.

[23] A. Vázquez, A. Rodríguez, **J. Rodríguez**, D. G. Lamar and M. M. Hernando, "Técnica de maestro-esclavo aplicada a la agrupación modular en paralelo para la mejora del rendimiento," Seminario Anual de Automática, Electrónica Industrial e Instrumentación 2015 (SAAEI'15), Zaragoza (España), 2015.

[24] D. G. Lamar, M. Arias, A. Rodríguez, K. Martín and **J. Rodríguez**, "Colaboración del Grupo SEA con empresas para la propuesta y realizacion de PFC," Tecnología, Aprendizaje y Enseñanza de la Electrónica (TAEE) 2016, Sevilla (España), 2016.

[25] **J. Rodríguez**, J. Roig, A. Rodríguez, A. López, D. G. Lamar and F. Bauwens, "Cascodo de super union, una configuración para Romper el límite de frecuencia de conmutacion del silicio," Seminario Anual de Automática, Electrónica Industrial e Instrumentación 2016 (SAAEI'16), Elche (España), 2016.

[26] **J. Rodríguez**, J. Roig, A. Rodríguez, A. Lopez, D. G. Lamar and F. Bauwens, "Reducción de Qrr en MOSFETs de superunión mediante la configuración en cascodo," Seminario Anual de Automática, Electrónica Industrial e Instrumentación 2017 (SAAEI'17), Valencia (España), 2017.

[27] M. R. Rogina, A. Rodríguez, J. Roig, **J. Rodríguez** and D. G. Lamar, "Dispositivo de alta tensión (>1kV) formado por Transistores de GaN en configuración super-cascodo," Seminario Anual de Automática, Electrónica Industrial e Instrumentación 2017 (SAAEI'17), Valencia (España), 2017.

[28] A. Rodríguez, M. Rodríguez-Rogina, **J. Rodríguez**, D. González-Lamar, A. Vázquez and J. Sebastián, "Planificación de prácticas de laboratorio basadas en un amplificador de radiofrecuencia de bajo coste orientadas a la enseñanza de asignaturas de Electrónica de Comunicaciones," Congreso Universitario de Innovación Educativa en las Enseñanzas Técnicas (CUIEET), Gijón (España), 2018.

[29] D. González-Lamar, A. Rodríguez, M. Arias, A. Vázquez, **J. Rodríguez**, M. Rodríguez-Rogina, F. Fernández-Linera, M. M. Hernando y J. Sebastián, "Una evolución natural hacia la aplicación del aprendizaje basado en diseños en las asignaturas de la mención de sistemas electrónicos del grado en Ingeniería en Tecnologías y Servicios de Telecomunicación de la Universidad de Oviedo. Una experiencia docente desde la EPI de Gijón," Congreso Universitario de Innovación Educativa en las Enseñanzas Técnicas (CUIEET), Gijón (España), 2018.

[30] A. López, **J. Rodríguez**, M. R. Rogina and A. Rodríguez, "Análisis del funcionamiento de un IGBT en configuración cascodo," Seminario Anual de Automática, Electrónica Industrial e Instrumentación 2018 (SAAEI'18), Barcelona (España), 2018.

[31] D. G. Lamar, M. Arias, K. Martín, **J. Rodríguez**, M. R. Rogina and J. Sebastián, "Aplicación de aprendizaje basado en diseños en la asignatura de Diseño de Sistemas Electrónicos de Potencia," Seminario Anual de Automática, Electrónica Industrial e Instrumentación 2018 (SAAEI'18), Barcelona (España), 2018.

5.3 Suggestions for Future Work

There are several points that could be addressed in the future in order to continue the research line of this dissertation:

- Evaluating the use of a PWM-SMPC for performing envelope tracking with the LPA of the conventional HB-LED driver proposed for VLC.
- Replacing the LPA of the conventional HB-LED driver proposed for VLC by a switching-mode power amplifier.
- Improving the implementation of the RM technique that is proposed in this dissertation by considering other topologies, the use of the second or higher switching harmonics, the optimization of the output filter, etc.

5.4 Dissertation Funding

This work was supported in part by the Spanish Government under Project MINECO-17-DPI2016-75760-R, Project DPI2013-47176-C2-2-R, in part by the Scholarship FPU14/03268 and the Principality of Asturias under Project FC-15-GRUPIN14-143, the Project SV-PA17-RIS3-4, and in part by the European Regional Development Fund grants.

Capítulo 5:
Conclusiones, Contribuciones y Trabajo Futuro

Las principales conclusiones de esta tesis doctoral se recogen en este capítulo, además de una descripción de las contribuciones logradas por la investigación que se ha llevado a cabo. Finalmente, se explican diferentes puntos que pueden ser estudiados en el futuro para continuar con la línea de investigación.

5.1 Conclusiones Generales

La saturación de los sistemas de comunicación inalámbricos que se prevé para los próximos años ha aumentado el interés por VLC. Desafortunadamente, esta tecnología presenta varios puntos débiles que están ralentizando su implantación. Uno de los mayores cuellos de botella es el bajo rendimiento energético de los *drivers* de HB-LEDs que han sido propuestos para ofrecer altos valores de *bit rate*. Para posibilitar las enormes tasas de tráfico previstas para los próximos años es imprescindible reproducir esquemas de modulación avanzados, como los esquemas SCM y MCM. Esta tesis doctoral se ha centrado en desarrollar soluciones eficientes energéticamente que sean capaces de reproducir dichos esquemas de modulación. Para ello, se ha optado por el diseño de *drivers* de HB-LEDs para VLC basados exclusivamente en el uso de SMPCs. Sin embargo, este objetivo no es trivial puesto que gobernar los HB-LEDs de un transmisor VLC implica cumplir una serie de requisitos muy exigentes. Los dos puntos críticos son la necesidad de proporcionar un ancho de banda de unidades o decenas de MHz y tener la capacidad de realizar cambios muy pequeños de la tensión sobre los HB-LEDs.

Desde un punto de vista teórico, se podría utilizar un convertidor reductor para gobernar los HB-LEDs del transmisor VLC. Sin embargo, esta opción presenta varios inconvenientes que limitan su uso. Uno de los mayores problemas es la elevada frecuencia de conmutación requerida para proporcionar un ancho de banda suficientemente grande como para reproducir las señales de comunicación, lo que dificulta enormemente la implementación debido a las altas pérdidas de conmutación, la dificultad para gobernar los MOSFETs, etc. Además, la capacidad de realizar cambios muy pequeños de la tensión de salida de un SMPC disminuye al aumentar la frecuencia de conmutación. Un método interesante para reducir la frecuencia de conmutación requerida es regular el valor medio de la corriente que circula por los HB-LEDs en lugar de toda la corriente de salida, y reproducir la señal de comunicación en lazo abierto. Sin embargo, la frecuencia de conmutación requerida sigue siendo demasiado elevada y, como consecuencia, se optó por explorar PWM-SMPCs más complejos. La estructura multi-fase, la estructura flotante y los filtros de alto orden son tres variantes del convertidor reductor cuyas características hacen que estos convertidores sean muy interesantes para ser utilizados como *drivers* de HB-LEDS para VLC. Las tres opciones permiten reducir la frecuencia de conmutación con respecto a un convertidor reductor convencional, lo cual conlleva un aumento del rendimiento energético y facilita la implementación práctica. Además, la estructura flotante minimiza la potencia procesada a alta frecuencia, incrementando el rendimiento energético aún más. Por otro lado, esta estructura también facilita la reproducción de la señal de comunicación dado que incrementa el rango de operación del ciclo de trabajo con respecto a un convertidor reductor convencional.

Por tanto, el uso de PWM-SMPCs es una opción interesante para gobernar los HB-LEDs de un transmisor VLC evitando el uso de LPAs, los cuales ofrecen bajos rendimientos energéticos. Sin embargo, las topologías recomendadas para poder operar con una frecuencia de conmutación asumible (es decir, suficientemente baja) y tener la capacidad de hacer cambios en la tensión de salida suficientemente pequeños son muy complejas, lo que dificulta su implantación. La técnica de RM es un método especialmente concebido para VLC que reproduce la señal de comunicación a partir del rizado de la tensión de salida del SMPC. Esta técnica puede ser implementada por medio de un convertidor reductor de dos fases con un filtro de alto orden que permite el paso tanto de la componente continua como del primer armónico de conmutación de las tensiones en los nodos de conmutación. El RM-SMPC logra controlar la amplitud y la fase del primer armónico de conmutación del rizado de la tensión de salida aplicando la técnica PWPPM en cada fase del

convertidor reductor. La técnica RM ofrece dos grandes ventajas con respecto a la opción basada en el uso de PWM-SMPCs: la frecuencia de conmutación requerida es menor, lo que reduce el impacto de las pérdidas de conmutación y alivia los problemas derivados de operar con frecuencias de conmutación muy elevadas; y la etapa de potencia es bastante simple.

5.2 Contribuciones

Las contribuciones de este trabajo se resumen a continuación:

- Estudiar el papel que la electrónica de potencia puede jugar en VLC para mantener el alto rendimiento energético de la iluminación HB-LED. Los *drivers* para HB-LEDs basados en LPAs ofrecen un bajo rendimiento energético, pero pueden ser reemplazados por drivers basados total o parcialmente en el uso de SMPCs.
- Identificar los requisitos para gobernar los HB-LEDs de un transmisor VLC y los mayores retos de diseño que surgen cuando se plantea el uso de un SMPC. Se ha concluido que el elevado ancho de banda demandado y la alta precisión requerida para reproducir la forma de onda de tensión que se debe aplicar a los HB-LEDs son las dos mayores dificultades.
- Estudiar estrategias de diseño que permitan reducir tanto la frecuencia de conmutación requerida como la precisión necesaria en el ciclo de trabajo al emplear PWM-SMPCs. El uso de estructuras multi-fase, estructuras flotantes y filtros de alto orden son tres opciones interesantes para afrontar estos dos retos de diseño.
- Proponer un método para reproducir esquemas SCM utilizando el rizado de la tensión de salida de un SMPC con el objetivo de reducir la frecuencia de conmutación requerida y la complejidad de la etapa de potencia.
- Extender el método anterior para reproducir esquemas MCM (es decir, los esquemas de modulación más recomendados para VLC) utilizando el rizado de la tensión de salida de un SMPC.

Como resultado de esta tesis doctoral se han publicado varios artículo científicos en revistas internacionales, congresos internacionales y congresos nacionales (ver Sección 5.2.1, Sección 5.2.2 and Sección 5.2.3). Además, se han realizado otras contribuciones al campo de la electrónica de potencia durante el desarrollo de este trabajo (ver Sección 5.2.4, Sección 5.2.5 and Sección 5.2.6).

5.2.1 Contribuciones de la Tesis Doctoral Publicadas en Revistas Internacionales

[1] J. Sebastián, D. G. Lamar, D. G. Aller, **J. Rodríguez** and P. F. Miaja, "On the role of power electronics in visible light communication," in IEEE Journal of Emerging and Selected Topics in Power Electronics.

[2] **J. Rodríguez**, D. G. Lamar, D. G. Aller, P. F. Miaja and J. Sebastián, "Efficient visible light communication transmitters based on switching-mode dc-dc converters," in Sensors, vol. 18, no. 4, 2018.

[3] **J. Rodríguez**, D. G. Lamar, P. F. Miaja and J. Sebastián, "Reproducing single-carrier digital modulation schemes for VLC by controlling the first switching harmonic of the DC–DC power converter output voltage ripple," in IEEE Transactions on Power Electronics, vol. 33, no. 9, pp. 7994-8010, Sept. 2018.

[4] **J. Rodríguez**, D. G. Lamar, P. Fernández Miaja, D. G. Aller and J. Sebastián, "Power efficient VLC transmitter based on pulse-width modulated DC-DC converters and the split of the power," in IEEE Transactions on Power Electronics.

5.2.2 Contribuciones de la Tesis Doctoral Publicadas en Congresos Internacionales

[5] **J. Rodríguez**, D. G. Lamar, J. Sebastián and P. F. Miaja, "Taking advantage of the output voltage ripple of a two-phase buck converter to perform quadrature amplitude modulation for visible light communication," 2017 IEEE Applied Power Electronics Conference and Exposition (APEC), Tampa, FL, 2017, pp. 2116-2123.

[6] J. Sebastián, D. G. Aller, **J. Rodríguez**, D. G. Lamar and P. F. Miaja, "On the role of the power electronics on visible light communication," 2017 IEEE Applied Power Electronics Conference and Exposition (APEC), Tampa, FL, 2017, pp. 2420-2427.

[7] **J. Rodríguez**, D. G. Aller, D. G. Lamar and J. Sebastián, "Energy efficient visible light communication transmitter based on the split of the power," 2017 IEEE Energy Conversion Congress and Exposition (ECCE), Cincinnati, OH, 2017, pp. 217-224.

[8] **J. Rodríguez**, D. G. Aller, D. G. Lamar and J. Sebastián, "Performance evaluation of a VLC transmitter based on the split of the power," 2018 IEEE Applied Power Electronics Conference and Exposition (APEC), San Antonio, TX, 2018, pp. 1179-1186.

[9] **J. Rodríguez**, D. G. Lamar, D. G. Aller, P. F. Miaja and J. Sebastián, "Power-efficient VLC transmitter able to reproduce multi-carrier modulation schemes by using the output voltage ripple of the HB-LED driver," 2018 IEEE 19th Workshop on Control and Modeling for Power Electronics (COMPEL), Padova, 2018.

5.2.3 Contribuciones de la Tesis Doctoral Publicadas en Congresos Nacionales

[10] **J. Rodríguez**, P. F. Miaja, D. G. Lamar y J. Sebastián, "Aprovechamiento del rizado de la tensión de salida de un convertidor CC/CC para reproducir esquemas QAM en VLC", Seminario Anual de Automática, Electrónica Industrial e Instrumentación 2017 (SAAEI'17), Valencia (Spain), 2017.

[11] J. Sebastián, D. G. Aller, **J. Rodríguez**, P. F. Miaja y D. G. Lamar, "El papel de los convertidores CC/CC en las comunicaciones por luz visible", Seminario Anual de Automática, Electrónica Industrial e Instrumentación 2017 (SAAEI'17), Valencia (Spain), 2017.

[12] D. G. Aller, **J. Rodríguez**, J Sebastián y D. G. Lamar, "Desarrollo de un transmisor para comunicaciones en luz visible (VLC) basado en un convertidor CC/CC conmutado de respuesta rápida", Seminario Anual de Automática, Electrónica Industrial e Instrumentación 2017 (SAAEI'17), Valencia (Spain), 2017.

[13] **J. Rodríguez**, D. G. Lamar, D. G. Aller, P. F. Miaja y J. Sebastián, "Transmisor VLC eficiente basado en el reparto de la potencia entre convertidores CC/CC modulados por ancho de pulso", Seminario Anual de Automática, Electrónica Industrial e Instrumentación 2018 (SAAEI'18), Barcelona (Spain), 2018.

[14] D.G. Aller, D. G. Lamar, **J. Rodríguez**, P. F. Miaja and J. Sebastián, "Diseño de transmisores VLC eficientes basados en convertidores CC/CC de respuesta rápida", Seminario Anual de Automática, Electrónica Industrial e Instrumentación 2018 (SAAEI'18), Barcelona (Spain), 2018.

5.2.4 Otras Contribuciones Publicadas en Revistas Internacionales

[15] **J. Rodríguez**, J. Roig, A. Rodríguez, D. G. Lamar and F. Bauwens, "Evaluation of superjunction MOSFETs in cascode configuration for hard-switching operation," in IEEE Transactions on Power Electronics, vol. 33, no. 8, pp. 7021-7037, Aug. 2018.

[16] **J. Rodríguez**, D. G. Lamar, J. Roig, A. Rodríguez and F. Bauwens, "Improving the third quadrant operation of superjunction MOSFETs by using the cascode configuration," in IEEE Transactions on Power Electronics.

5.2.5 Otras Contribuciones Publicadas en Congresos Internacionales

[17] **J. Rodríguez**, A. Rodríguez, D. G. Lamar, J. Roig and F. Bauwens, "Modeling the switching behaviour of superjunction MOSFETs in cascode configuration with a low voltage silicon MOSFET," 2016 IEEE 17th Workshop on Control and Modeling for Power Electronics (COMPEL), Trondheim, 2016, pp. 1-8.

[18] A. López, **J. Rodríguez**, M. R. Rogina, I. Castro and A. Rodríguez, "Switching performance comparison of a power switch in a cascode configuration using a superjunction MOSFET," 2016 51st International Universities Power Engineering Conference (UPEC), Coimbra, 2016, pp. 1-6.

[19] **J. Rodríguez**, A. Rodríguez, I. Castro, D. G. Lamar, J. Roig and F. Bauwens, "Superjunction cascode, a configuration to break the silicon switching frequency limit," 2016 IEEE Energy Conversion Congress and Exposition (ECCE), Milwaukee, WI, 2016, pp. 1-8.

[20] **J. Rodríguez**, A. Rodríguez, D. G. Lamar, J. Roig and F. Bauwens, "Reducing Qrr in high-voltage superjunction MOSFETs by using the cascode configuration," 2017 IEEE Applied Power Electronics Conference and Exposition (APEC), Tampa, FL, 2017, pp. 1970-1977.

[21] J. Roig, G. Gómez, F. Bauwens, B. Vlachakis, **J. Rodríguez**, M. R Rogina, A. Rodríguez, D. G. Lamar "Series-connected GaN transistors for ultra-fast high-voltage switch (>1kV)," 2017 IEEE Applied Power Electronics Conference and Exposition (APEC), Tampa, FL, 2017, pp. 3043-3048.

5.2.6 Otras Contribuciones Publicadas en Congresos Nacionales

[22] I. Castro, J. Roig, F. Bauwens, D. G. Lamar, **J. Rodríguez** and A. Vázquez, "Verificacion del modelo analítico de pérdidas en conmutación para MOSFET de superunión con modelado de capacidades no-lineales y diversificacion de corrientes," Seminario Anual de Automática, Electrónica Industrial e Instrumentación 2015 (SAAEI'15), Zaragoza (España), 2015.

[23] A. Vázquez, A. Rodríguez, **J. Rodríguez**, D. G. Lamar and M. M. Hernando, "Técnica de maestro-esclavo aplicada a la agrupación modular en paralelo para la mejora del rendimiento," Seminario Anual de Automática, Electrónica Industrial e Instrumentación 2015 (SAAEI'15), Zaragoza (España), 2015.

[24] D. G. Lamar, M. Arias, A. Rodríguez, K. Martín and **J. Rodríguez**, "Colaboración del Grupo SEA con empresas para la propuesta y realizacion de PFC," Tecnología, Aprendizaje y Enseñanza de la Electrónica (TAEE) 2016, Sevilla (España), 2016.

[25] **J. Rodríguez**, J. Roig, A. Rodríguez, A. López, D. G. Lamar and F. Bauwens, "Cascodo de super union, una configuración para Romper el límite de frecuencia de conmutacion del silicio," Seminario Anual de Automática, Electrónica Industrial e Instrumentación 2016 (SAAEI'16), Elche (España), 2016.

[26] **J. Rodríguez**, J. Roig, A. Rodríguez, A. Lopez, D. G. Lamar and F. Bauwens, "Reducción de Qrr en MOSFETs de superunión mediante la configuración en cascodo," Seminario Anual de Automática, Electrónica Industrial e Instrumentación 2017 (SAAEI'17), Valencia (España), 2017.

[27] M. R. Rogina, A. Rodríguez, J. Roig, **J. Rodríguez** and D. G. Lamar, "Dispositivo de alta tensión (>1kV) formado por Transistores de GaN en configuración super-cascodo," Seminario Anual de Automática, Electrónica Industrial e Instrumentación 2017 (SAAEI'17), Valencia (España), 2017.

[28] A. Rodríguez, M. Rodríguez-Rogina, **J. Rodríguez**, D. González-Lamar, A. Vázquez and J. Sebastián, "Planificación de prácticas de laboratorio basadas en un amplificador de radiofrecuencia de bajo coste orientadas a la enseñanza de asignaturas de Electrónica de Comunicaciones," Congreso Universitario de Innovación Educativa en las Enseñanzas Técnicas (CUIEET), Gijón (España), 2018.

[29] D. González-Lamar, A. Rodríguez, M. Arias, A. Vázquez, **J. Rodríguez**, M. Rodríguez-Rogina, F. Fernández-Linera, M. M. Hernando y J. Sebastián, "Una evolución natural hacia la aplicación del aprendizaje basado en diseños en las asignaturas de la mención de sistemas electrónicos del grado en Ingeniería en Tecnologías y Servicios de Telecomunicación de la Universidad de Oviedo. Una experiencia docente desde la EPI de Gijón," Congreso Universitario de Innovación Educativa en las Enseñanzas Técnicas (CUIEET), Gijón (España), 2018.

[30] A. López, **J. Rodríguez**, M. R. Rogina and A. Rodríguez, "Análisis del funcionamiento de un IGBT en configuración cascodo," Seminario Anual de Automática, Electrónica Industrial e Instrumentación 2018 (SAAEI'18), Barcelona (España), 2018.

[31] D. G. Lamar, M. Arias, K. Martín, **J. Rodríguez**, M. R. Rogina and J. Sebastián, "Aplicación de aprendizaje basado en diseños en la asignatura de Diseño de Sistemas Electrónicos de Potencia," Seminario Anual de Automática, Electrónica Industrial e Instrumentación 2018 (SAAEI'18), Barcelona (España), 2018.

5.3 Sugerencias para el Trabajo Futuro

Existen varios puntos que pueden ser estudiados en el futuro para continuar la línea de investigación de esta tesis doctoral:

- Evaluar el uso de un PWM-SMPC para realizar seguimiento de envolvente con el LPA utilizado en el *driver* convencional de HB-LEDs de un transmisor VLC.
- Remplazar el LPA del *driver* convencional de HB-LEDs de un transmisor VLC por un amplificador conmutado de potencia.
- Mejorar la implementación de la técnica RM propuesta en esta tesis doctoral explorando el uso de otras topologías, el aprovechamiento del segundo y superiores armónicos de conmutación, la optimización del filtro de salida, etc.

5.4 Entidades Financiadoras del Presente Trabajo

Este trabajo ha sido financiado en parte por el Gobierno de España bajo la beca FPU14/03268, el proyecto MINECO-17-DPI2016-75760-R y el proyecto DPI2013-47176-C2-2-R, por el Principado de Asturias bajo el proyecto FC-15-GRUPIN14-143, el proyecto SV-PA17-RIS3-4, y en parte por las becas European Regional Development Fund.

Appendices

A.1 From the Buck Converter to the Floating Multi-Phase Buck Converter

The process to obtain the floating multi-phase buck converter (i.e., the HB-LED driver that is proposed in Section 3.3) from a buck converter could be not trivial. This appendix describes the methodology followed by the author of the dissertation. For the sake of simplicity, two phases and a fourth order filter will be considered in the explanation.

Fig. A.1.1 shows three different ways of implementing a buck converter. In the conventional buck converter (see Fig. A.1.1(a)), the current that flows through the MOSFET ($i_Q(t)$ in the high side) is equal to the current that entries through the negative terminal of V_G ($i_Q(t)$ in the low side). Hence, the MOSFET can be connected between the anode of D and the negative terminal of V_G instead of between the positive terminal of V_G and the cathode of D (see Fig. A.1.1(b)). Obviously, in practice, there is a capacitor in parallel with V_G in order to filter $i_Q(t)$, but the reasoning is similar. The schematic depicted in Fig. A.1.1(b) allows us to supply the driver of Q with V_G since both V_G and Q are referred to the same point. The drawback is that the negative terminal of the load (i.e., ground) must be isolated from the negative terminal of V_G.

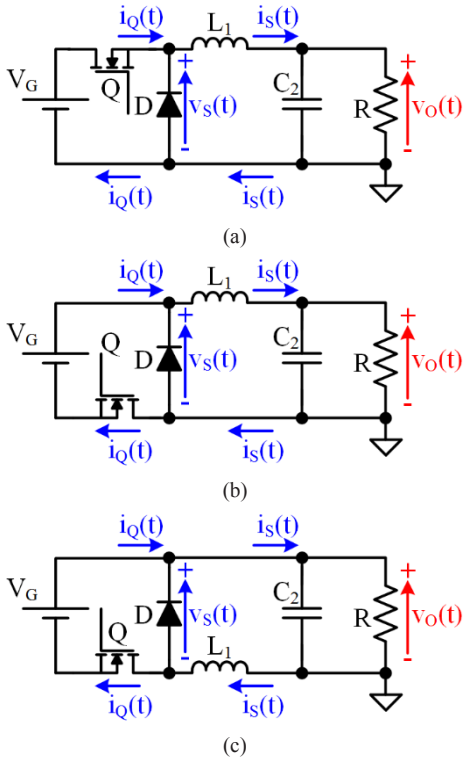

Fig. A.1.1. Different implementations of a buck converter: (a) Conventional buck converter. (b) Buck converter with the MOSFET source connected to the negative terminal of the input voltage. (c) Buck converter with the MOSFET source connected to the negative terminal of the input voltage and with the inductor connected between the switch-node and the negative terminal of the load (ground).

Similarly to the previous reasoning, the current that flows from the cathode of D to the positive terminal of the load ($i_S(t)$ in the high side) is equal to the current that flows from the negative terminal of the load to the anode of D ($i_S(t)$ in the low side). Therefore, the inductor can be connected between the negative terminal of the load and the anode of D instead of between the cathode of D and the positive terminal of the load (see Fig. A.1.1(c)). Note that this modification does not have any major benefit or drawback.

Fig. A.1.2 shows the two-phase version of the buck converter depicted in Fig. A.1.1(c). Obviously, the connection of the phases is carried out by using the phase inductors. Similarly to the reasoning related to the inductor position of Fig. A.1.1(c), a fourth order filter can be implemented having two possible positions of the additional inductor (see L_3 in Fig. A.1.3).

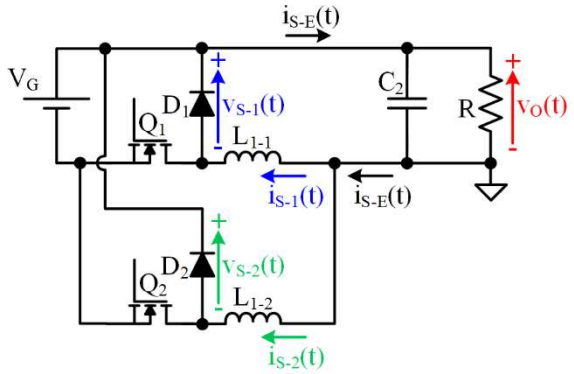

Fig. A.1.2. Two-phase version of the buck converter depicted in Fig. A.1.1(c).

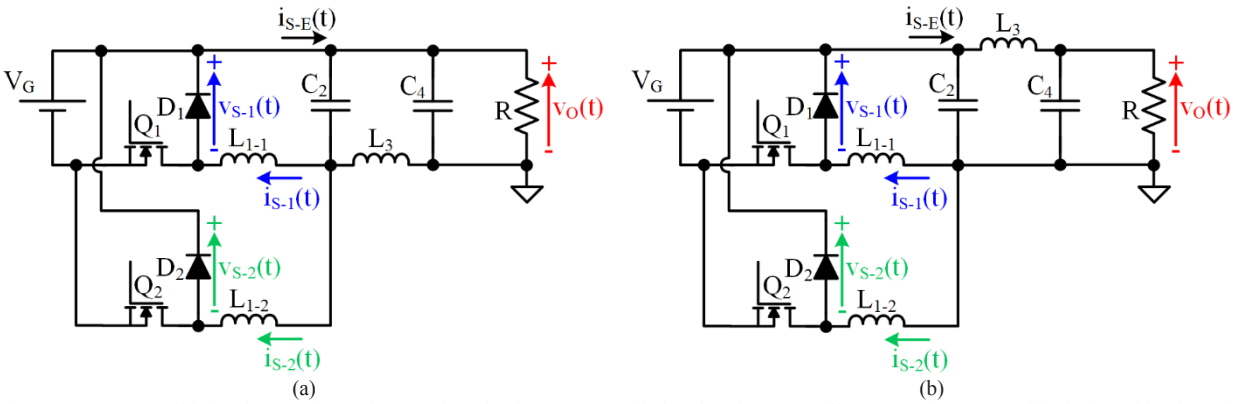

Fig. A.1.3. Two possible implementations of a two-phase buck converter with fourth order output filter: (a) L_3 is connected in the low side. (b) L_3 is connected in the high-side.

Finally, a constant voltage source can be connected between the output of the converter and the load to implement a floating two-phase buck converter with fourth order filter (see Fig. A.1.4). Obviously, this constant voltage source can be the output of another SMPC (as in the case of the topology proposed in Section 3.3 of Chapter 3).

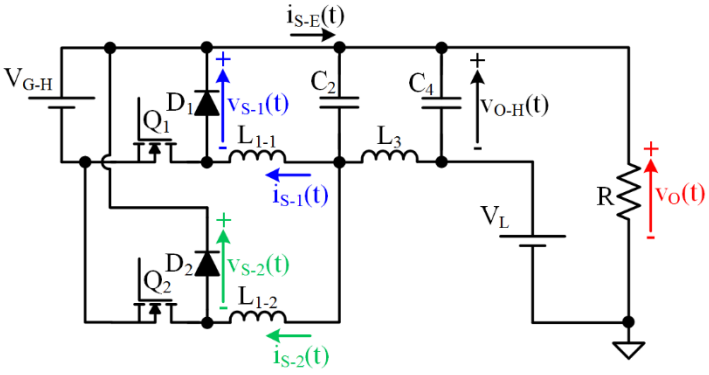

Fig. A.1.4. Floating version of the converter depicted in Fig. A.1.3(a).